MODELLING PORE-LEVEL PROPERTIES OF POROUS MATERIALS

by

CATHERINE JEAN RIDGWAY

A thesis submitted to the University of Plymouth
in partial fulfilment for the degree of

DOCTOR OF PHILOSOPHY

Department of Environmental Sciences
Faculty of Science

August 1995

ABSTRACT

by

Catherine Jean Ridgway

Pore-Cor is a 1.2 Mbyte Fortran 77 software package, which uses information from mercury porosimetry curves, supported by image-analysed electron micrographs, to generate a three-dimensional representational model of the pore-space within a porous material. As a result of this project, a much-improved version has been produced. The mercury intrusion curves for the simulated structures now converge automatically onto the experimental curves, so reducing the simulation time from several days to less than an hour. A further time economy has been provided by the incorporation of an improved permeability routine, reducing the calculation time from 10 minutes to 30 seconds.

Modifications have allowed non-homogeneous structures to be modelled, in simulation of real samples of banded, vuggy and clay-included sandstones. Porosimetry measurements have been made for Fontainebleau sandstone into which small amounts of illite, a simulated clay deposit, had been introduced by hydrothermal crystallisation. Despite having no effect on porosity, the effects on simulated permeability could be successfully assessed. The causes of hysteresis, i.e. the trapping of a non-wetting fluid in a porous medium, were also investigated.

The need for higher quality experimental data to feed into the Pore-Cor software has led to improved measurement and analysis methods for the porosimetry. A new spreadsheet-based iterative programme, named Pore-Comp, provides a unique method of measuring the compressibility (or bulk modulus) of the solid phase of a porous medium, and this has been used to examine the effects of silicate micro-crystallinity and latex binders on the compressibility of paper-coating formulations. Using the cryo-stage of the electron microscope, the retention of mercury in some paper coating formulations has been investigated further.

LIST OF CONTENTS

LIST OF TABLES

Chapter 5

Chapter 6

LIST OF FIGURES

LIST OF PLATES

ACKNOWLEDGEMENTS

I would like to thank my supervisor, Dr. G. Peter Matthews, for his continuous help, support, encouragement and friendship throughout the last three years. John Kettle has also been a great support and I thank him for his sense of humour and help with mercury porosimetry measurements and paper coating information.

For their inputs to the advancement of Pore-Cor my thanks go to Dr. John Dowd, Georgia, who found the much faster Dinic routine for calculating the maximum capacity of the unit cell, and to Joseph and James Matthews, sons of Dr. G. Peter Matthews, who have programmed the new interface system and designed a new logo for Pore-Cor respectively.

I would like to thank David Griffiths for taking photographs of the computer screen and preparing all the prints for this thesis. For their time, explanations and demonstrations I would like to thank Roy Moate and Jane Green from the electron microscopy unit and also Mike Ashton for his help with sample preparation. I would like to thank Joe Small from Manchester University for his Fontainebleau samples with and without clay precipitations; British Gas for the Clashach sandstone and reservoir sandstone samples; Corex Aberdeen for the week-long course entitled "Core Analysis - Measurement and Use in Reservoir Evaluation"; English China Clay International, St Austell for the use of their mercury porosimeter; and also the Polytechnic and College Funding Council who funded this project. I am grateful to the Digital Equipment Corporation for their free maintenance and advice regarding both the software and the hardware used for this project.

I would like to thank Dave Dowdell, Adam Moss, Eva Nägelsbach and Toby Mathews with whom I have worked and shared the lab. My thanks also go to Pete Sutton who has kept my spirits up, been a great friend and took the close up sample photographs. Finally I would like to thank my parents for their encouragement, support and for just being there.

AUTHORS DECLARATION

At no time during the registration for the degree of Doctor of Philosophy has the author been registered for any other University award.

This study was financed with the aid of a studentship from the Polytechnic and College Funding Council.

A programme of advanced study was undertaken, which included supervised study in Workstation programming, scanning electron microscopy, image analysis, mercury porosimetry and the courses listed on page xix.

Relevant scientific seminars and conferences were regularly attended at which work was often presented; external institutions were visited for consultation purposes, and several papers prepared for publication.

Publications arising from this project

1. A New Dimension in Mercury Porosimetry, by Matthews G.P. *The microReport* :1-4.(4th Quarter 1994)

2. Void Space Modelling of Mercury Intrusion Hysteresis in Sandstone, Paper Coating and Other Porous Media, (9000 words, 25 figs, 1 table) by Matthews G.P., Ridgway C.J., Spearing M.C. *Journal of Colloid and Interface Science* 171(1):8-27.(April 1995)

3. The Effects of Correlated Networks on Mercury Intrusion Simulations and Permeabilities of Sandstone and Other Porous Media, (6700 words, 20 figs, 1 table) by Matthews G.P., Moss A.K., Ridgway C.J. *Powder Technology* 83(1):61-77.(April 1995)

4. Modelling of Simulated Clay Precipitation Within Reservoir Sandstones, (4450 words, 8 figs, 3 plates) by Matthews G.P., Ridgway C.J., Small J.S. *Marine and Petroleum Geology* submitted for publn (March 1995)

5. Void Space Structure of Compressible Polymer Spheres and Consolidated Calcium Carbonate Paper-Coating Formulations, (7400 words, 12 figs, 2 tables) by Gane P.A.C.,

Kettle J.P., Matthews G.P., Ridgway C.J. *Industrial and Engineering Chemistry Research* submitted for publn (June 1995)

6. Evaluation of the Void Space Structure of Paper Using Combined Mercury and Hexa-decane Porosimetry, by Kettle J.P., Matthews G.P., Ridgway C.J., Wagberg L. *Measurement Science and Technology* in preparation (1995)

7. Measurement of Void Space Correlation in Sandstones and Other Porous Media, by Adams J.M., Mathews T., Matthews G.P., Moss A.K., Ridgway C.J. *Transport in Porous Media* in preparation (1995)

Consultancy Reports arising from this project

8. Matthews, G.P. and Ridgway, C.J. Computer Modelling of the Void Structure of a Non-Bonded Fibrous Network. 1994; PEP Contract no.1367 AB.

9. Matthews, G.P. and Ridgway, C.J. Preliminary Mercury Porosimetry Study of Building Materials to Test Feasibility of Use in the Study of Sealer Pigment Migration. May 1995; PEP Contract no.1444 AB.

10. Matthews, G.P. and Ridgway, C.J. Feasibility Study of the Void Space Modelling of AVX Tantalum Capacitors Using Pore-Cor. June 1995; PEP Contract no.3207 AB.

11. Matthews, G.P. and Ridgway, C.J. AVX Tantalum Capacitor Efficiency Study. July/August 1995;

Presentations, Conferences and Courses associated with this project

(A = attendance, P = poster presentation, L = lecture presentation)

Sandstone Reservoir Geology: Techniques and Applications, JAPEC course no. 123, Imperial College, London, September 1992.(A)

Core Analysis - Measurement and Use in Reservoir Evaluation, 1 week residential course. Corex, Aberdeen. January 1993. (A)

Effects of Pore-Throat Coordination Number and Throat Size Distribution on Mercury Intrusion into a Porous Solid, by Cathy J. Ridgway and G.Peter Matthews, Second UK Colloid and Surface Science Student Meeting, organised by SCI Colloid and Surface Science Group and the RSC Colloid and Interface Science Group, University of Nottingham, 18 -21 April 1993.(P)

Computer Modelling of Pore Structure and Permeability of Reservoir Sandstones, by G.Peter Matthews and Adam K. Moss, Geofluids 93 (International Conference on Fluid Evolution, Migration and Interaction in Rocks), Torquay, 4th to 7th May 1993. (A)

Mercury Porosimetry as a Probe of the Three Dimensional Pore Network within a Porous Solid, COPS - III, IUPAC Symposium on the Characterization of Porous Solids, Marseille, France, May 9-12, 1993. (P).

A Three Dimensional Model of the Pore Structure of Outcrop and Reservoir Sandstones, by A.K.Moss, G.P.Matthews and C.J.Ridgway, British Organic Geochemistry Society meeting, University of Plymouth, July 1993. (A)

Roth Microstructure Products Seminar, Farnborough, November 1993. (A)

The Pore Structure and Permeability of Calcium Carbonate Coated Substrate, by J.Kettle, G.P.Matthews and C.Ridgway, ECCI research seminar, December 1993. (A)

Correlation of the Pore-level Properties of Rock, by G.P.Matthews and C.J.Ridgway, European Geophysical Society, XIX General Assembly, Grenoble, 25-29 April 1994. (L)

A Computer Model for the Pore Structure of Porous Materials, by G.P.Matthews and C.J.Ridgway, Silsoe College research seminar, November 1994, and to David Scholfield from North Wyke, and 2nd supervisors of other projects, December 1994. (L)

Void Space Modelling of Homogeneous, Inhomogeneous and Compressible Porous Media, by G.P.Matthews, Loughborough University Chemical Engineering Department research seminar, March 1995. (A)

Computer Modelling of the Pore-level Properties of Clashach, Fontainebleau and

Morecambe Bay Sandstone, by G.P.Matthews, British Gas R&D, Loughborough, March 1995. (A)

Void Space Modelling of Homogeneous, Inhomogeneous and Compressible Porous Media, by G.P.Matthews, Royal Society of Chemistry Particle Characterisation Group Meeting, March 1995. (A)

Transport in Porous Media, Society of Chemical Industry International Conference, London, March 1995. (A)

Introduction to Scanning Electron Microscopy - two day course at the Electron Microscopy Unit, University of Plymouth with Brian Lakey, January 1995. (A)

Signed....Cathy Ridgway.....

Date.....10th August 1995

CHAPTER 1

INTRODUCTION

1.1 Work carried out in this project

The work reported in this thesis is the latest part of a large on-going project, the characterisation of the void space of porous materials, that has been running at the University of Plymouth in the Environmental Science department since the late 1980's. Porous naturally-occurring mediums such as sandstone and limestone are industrially important materials. In the oil industry, the crude petroleum often occurs in porous geological strata, from which it must be displaced by injecting water under pressure: the success of the extraction process is governed by the pore structure of the containing rock.

In the paper industry, coatings made from fine China clay are applied as a liquid suspension to the paper surface. The structure of the deposited layer, on the microscopic scale, is a three-dimensional array of particles, from which fluid is removed by drainage and evaporation. The functionality of the coating depends upon its initial and final void structures, which control both the removal of the suspending liquid and the properties of the final coating.

A useful technique for the study of void space structure and configuration in porous materials is mercury porosimetry. A sample is immersed in mercury, and the pressure gradually increased. The amount of mercury intruding the void space of the sample is measured: the amount increases as the pressure increases and the mercury is forced into successively smaller voids. The result is a mercury intrusion curve, which, knowing the interfacial tension and contact angle of mercury with the solid, can be converted into a void-size distribution. A similar procedure, with pressure reduction, allows the drainage curve to be obtained, as the mercury emerges from the sample. The intrusion and extrusion curves differ, due to the hysteresis caused by the pressure needed to force

mercury into a larger void space, a *pore*, through a connecting narrower void space, a *throat*, being greater than that at which it will come out again. (i.e. small throats can shield large pores)

There is a large amount of information potentially derivable from such curves. The average pore diameter is readily obtained as that diameter at which 50 % of the mercury has been intruded, but other useful structural determinations are possible. A very successful method has been to determine a structure for the pore/throat distribution, and to perform a computer simulation, endeavouring to match the simulated behaviour of the modelled structure to the experimental behaviour of the actual sample, improving the fit by successive approximation.

Such a simulation program was written by Dr. Michael Spearing in 1991. He started by investigating various types of void space, such as that of an array of spherical particles, progressing to a pore-throat-pore structure. Programming was based upon cubic pores arranged on a simple cubic lattice linked by cylindrical throats running from one lattice point (i.e. pore) to the next. The first graphical views were of two dimensional layers, an example of which is shown in Fig. 1.1. Further programming led to the unit cell as a whole being illustrated, however, the throats could only be shown as diamond shaped or of hexagonal cross-section, as in Fig. 1.2. After further advancement in the programming it was possible to show the cylindrical throats as they should be as seen in Fig. 1.3. The computation and drawing of the black and white diagrams of the arrangements of pores and throats on the lattice, as seen in Figs. 1.2 and 1.3, could take up to twelve hours. With the installation of Gino graphics the 10 x 10 x 10 three dimensional unit cell could be produced in colour, Plate 1.1, and in a matter of minutes.

The present writer's part in the departmental project has been to bring about a wide range of improvements in the computer program. Improvements have been made to the model, the speed of convergence, the overall accuracy and to the presentation of the final

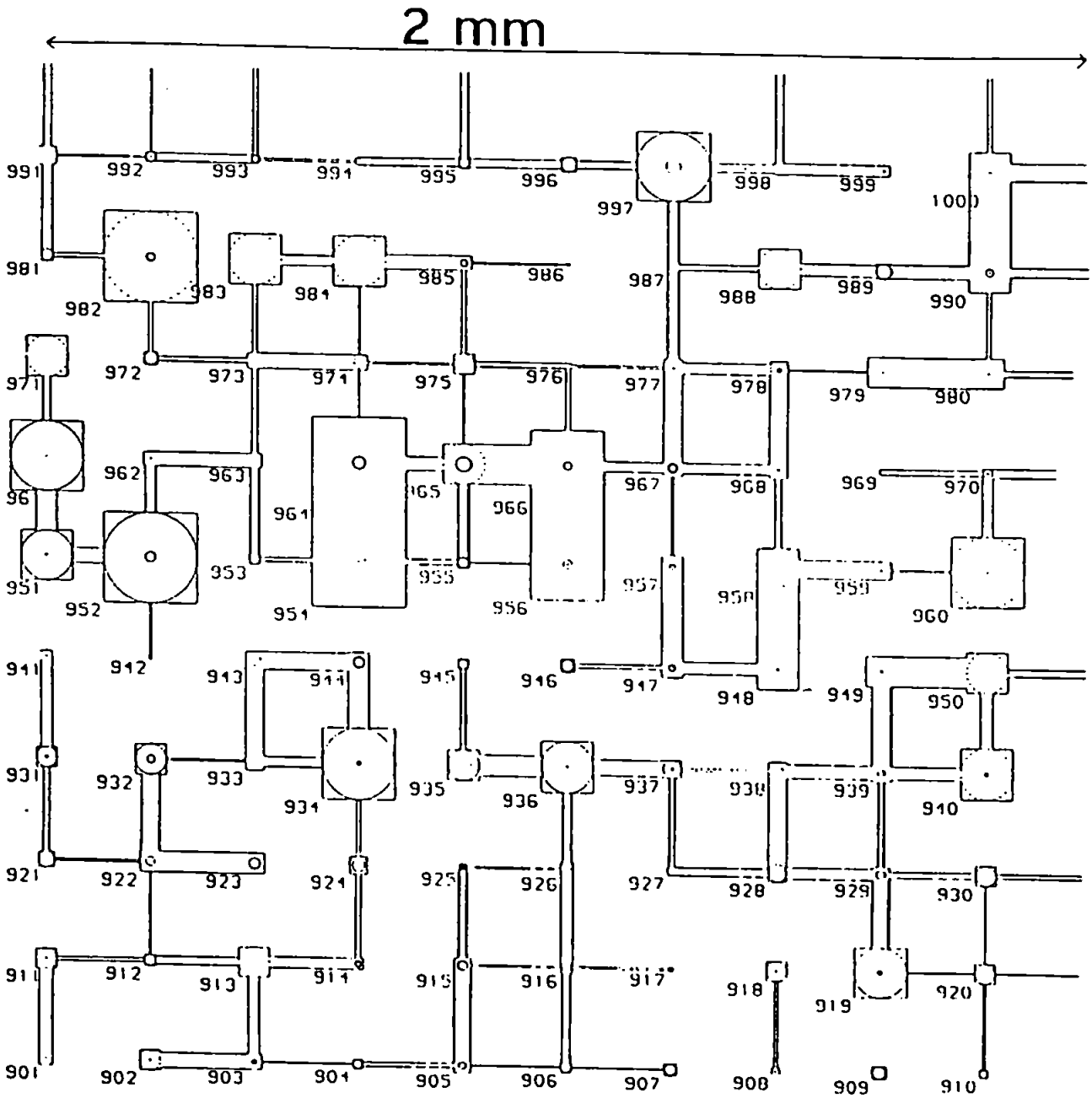

Figure 1.1 Black and white two dimensional layer of unit cell

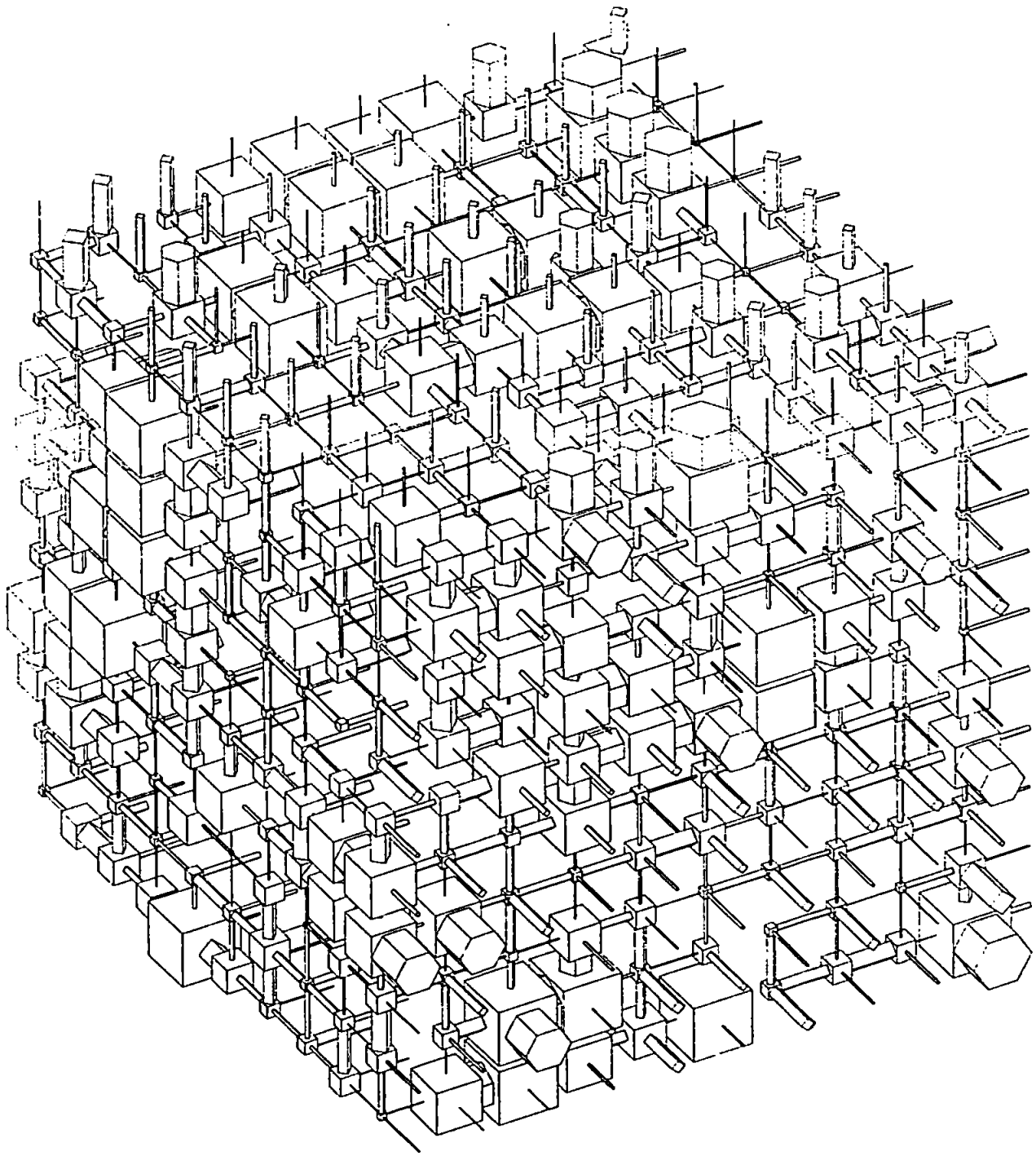

Figure 1.2 Black and white unit cell with hexagonal pores and diamond shape throats

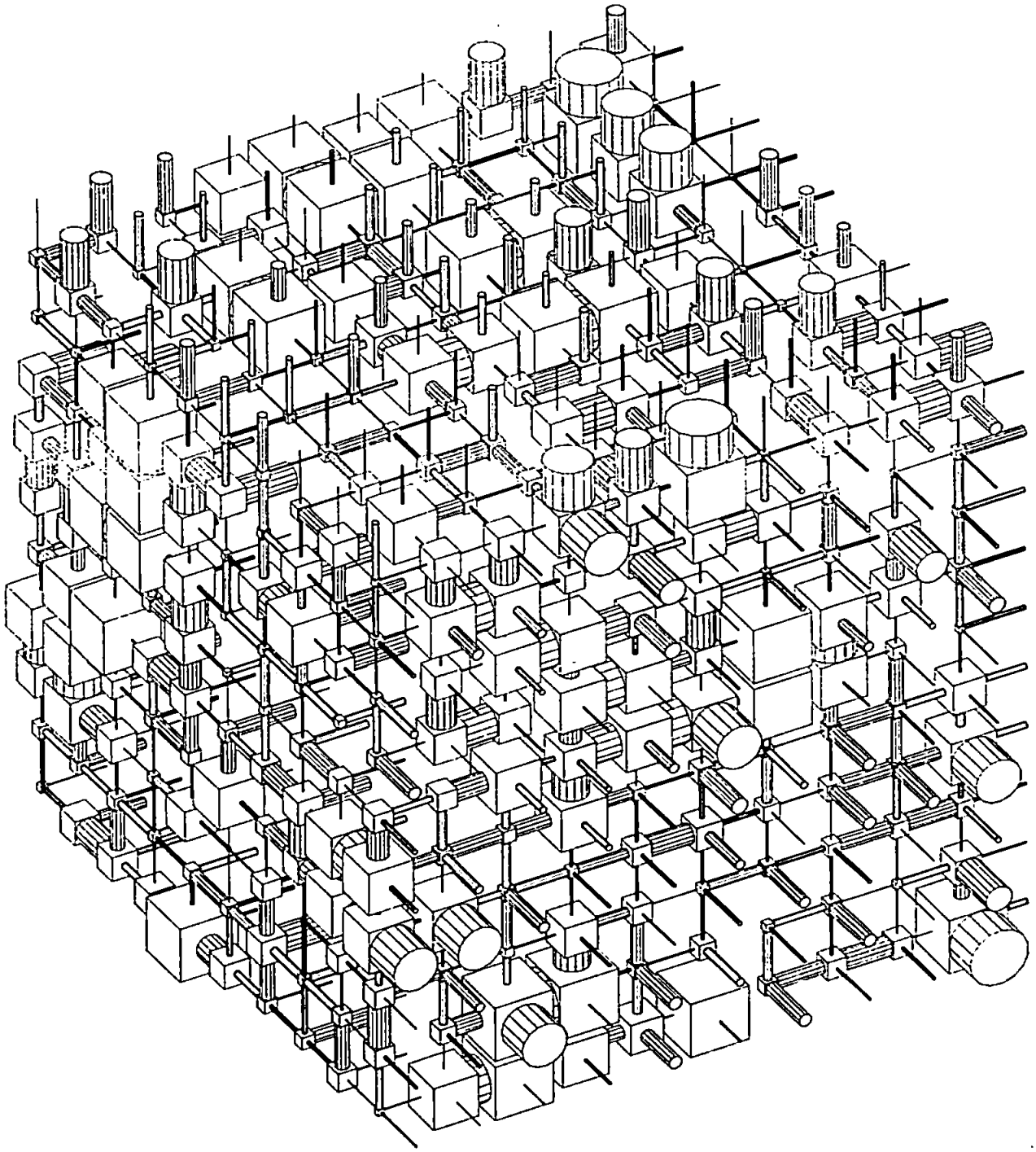

Figure 1.3 Black and white unit cell with cubic pores and cylindrical throats

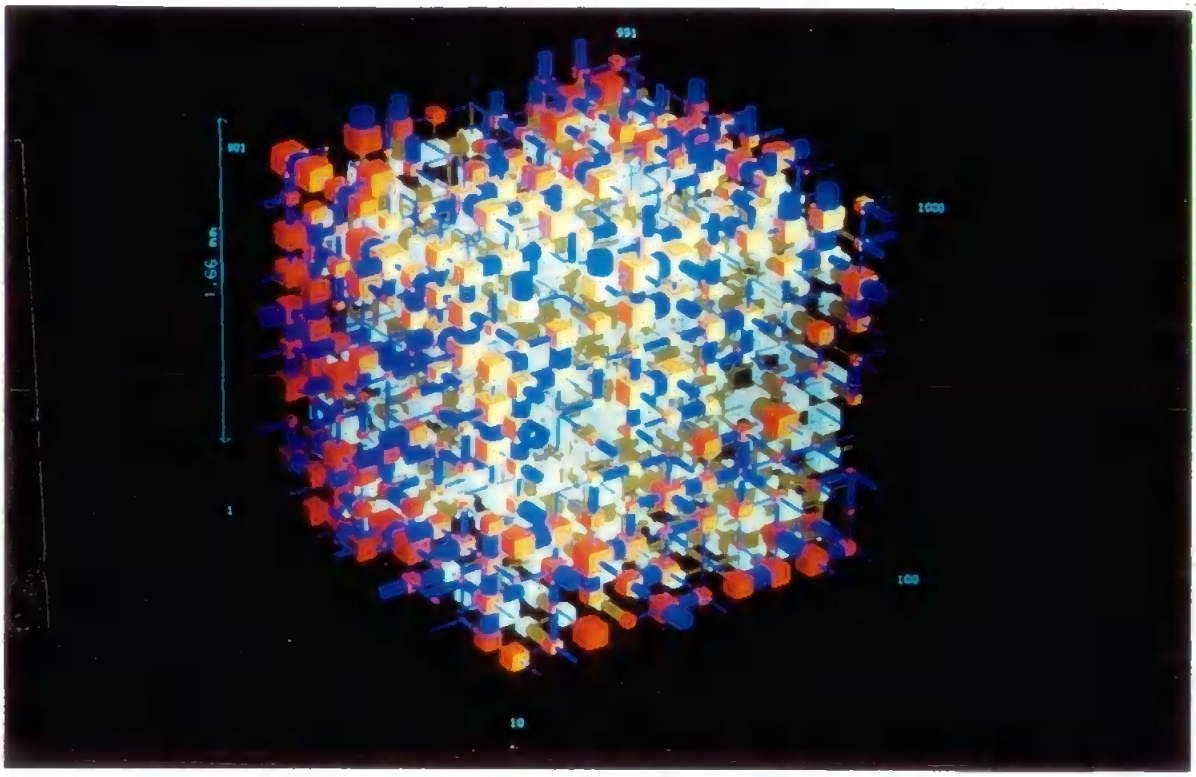

Plate 1.1 First colour unit cell using Gino graphics

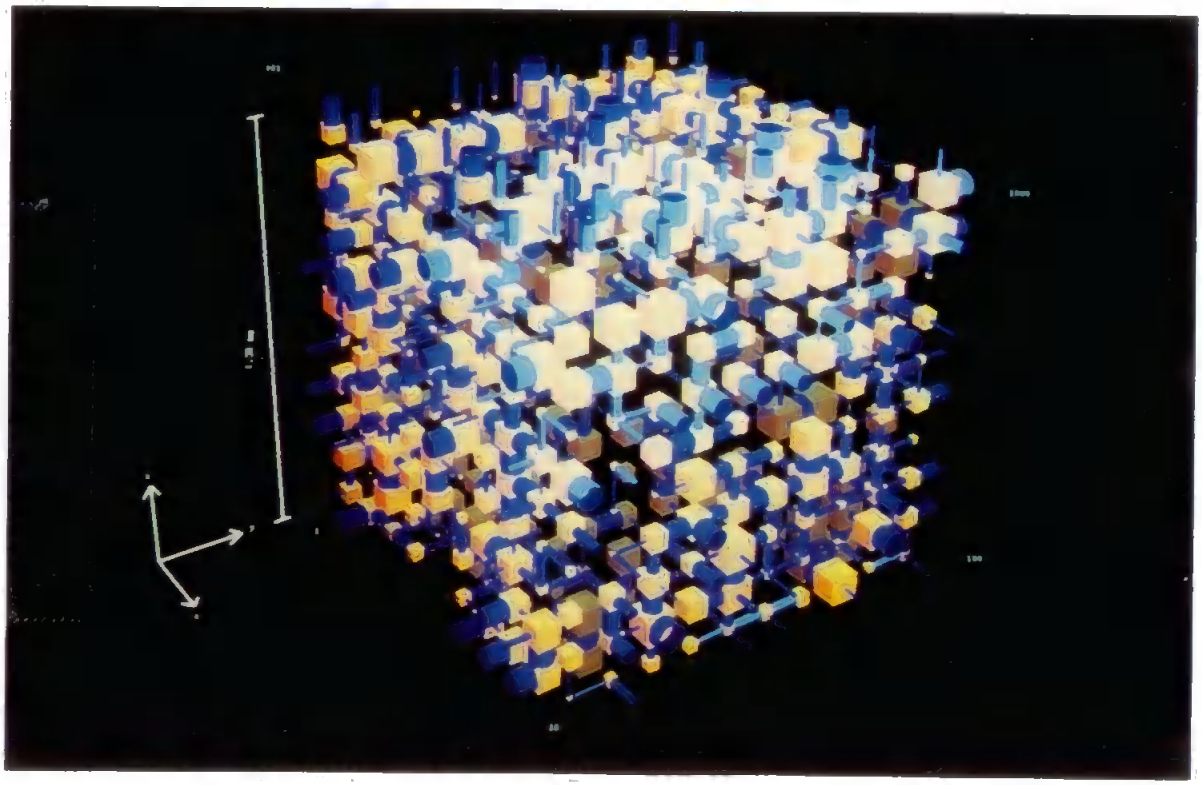

Plate 1.2 Improved shading and colour scheme of unit cell

results. The colours of the unit cell have been improved, Plate 1.2, and also a specified cube size can be illustrated as shown in Plate 1.3. This shows the repeating of the unit cell and also where the mercury retention has occurred after the extrusion simulation.

At the outset, Pore-Cor, the simulation program, had been applied with some success to an outcrop sandstone, and some progress had been made with reservoir sandstones. It has now been successfully applied not only to these materials, but also to ground calcite, plastic pigments, pure kaolin and kaolin mixed with latex and/or starch binder, high voidage porous fibrous mats, a wide range of building materials, car battery separators and sintered tantalum slugs used in electronic capacitors. The effects of the deposition of clay in Fontainebleau sandstone, which cannot be assessed by traditional methods of porosity change measurement, have been simulated. The mercury porosimetry data-correction program, Pore-Comp, has enabled the compressibility or bulk modulus of solid phases to be measured.

This degree of advancement has been made possible by the following improvements

(a) automatic parameter adjustment and convergence of the simulation onto the experimental mercury intrusion curve, reducing the running time from days to less than one hour

(b) the invention and use of banded or clustered structures to simulate inhomogeneous materials, clay-included sandstones and high-voidage fibrous mats

(c) an improved permeability calculation routine

(d) better measurement and analysis methods in mercury porosimetry

Time was also spent during this project installing and establishing the Reference Manager database which is a personal reference management system. This database now contains 750 references, 100 of which are quoted as part of this thesis.

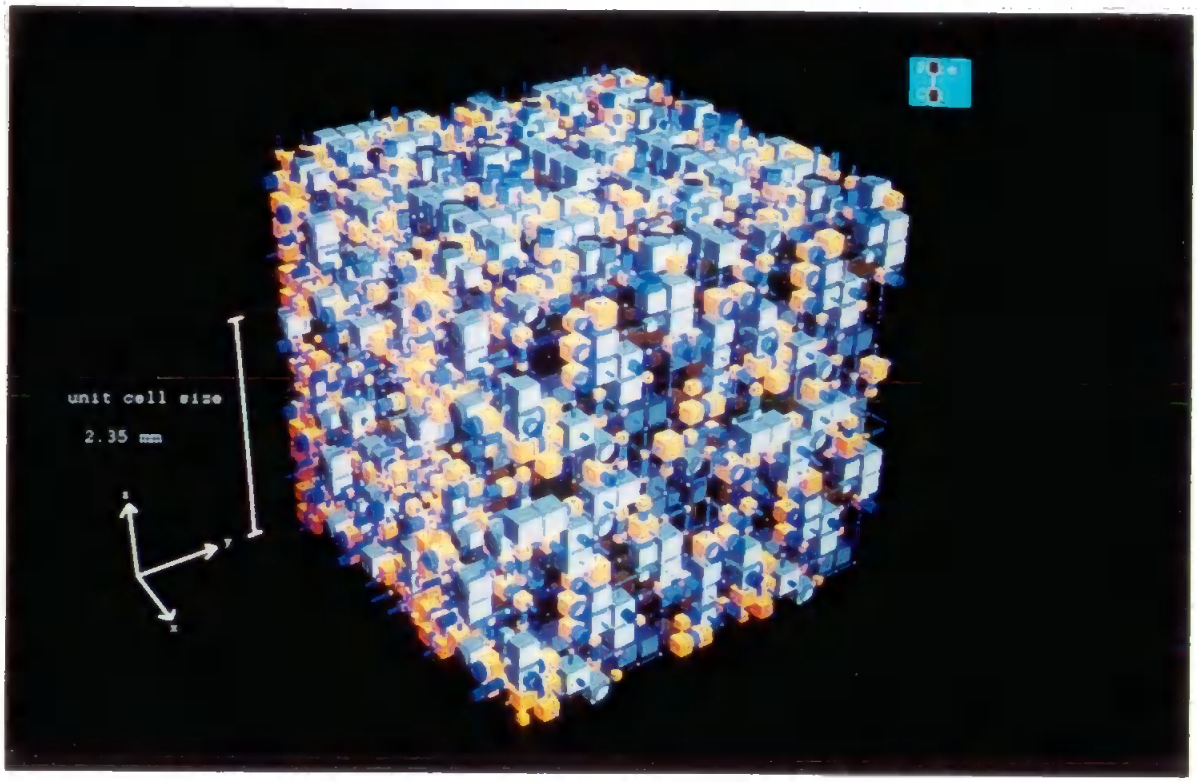

Plate 1.3 Multiple unit cell showing mercury retention

1.2 Characterisation and development of the Pore-Cor void space model

The network consists of a three-dimensional cubic unit cell which repeats infinitely in each direction, each cell containing 1000 nodes on a regular 10 x 10 x 10 matrix. Fig. 1.4 shows the two outermost layers of pores and throats in a unit cell representing the void space of a reservoir sandstone (Sample 212B). As can be seen, the nodes are positioned using Cartesian coordinates x, y and z, although, since the sample is isotropic, the allocation of these axes is arbitrary. The origin of the axes is at the corner of the unit cell adjacent to the first node, and the pores are numbered as indicated. The void volume in the unit cell consists of up to 1000 cubic pores centred on the nodes. Connected to each pore are up to six cylindrical throats along the line of the arcs in the positive and negative x, y and z directions. We refer to the number of throats connected to a particular pore as the *pore co-ordination number*, and the arithmetic mean of this quantity over the whole unit cell as the *connectivity*. Individual pore coordination numbers may range from 0 to 6, while the connectivity of sandstone is around 3 (Yanuka *et al.* 1986; Koplik *et al.* 1984).

The network model presented here has three main characteristics: (i) it has a physically realisable geometry, (ii) the same network with precisely the same geometry can be used to model a wide range of properties, and (iii) all fitting parameters are property dependent. The networks developed by other workers, described below, rarely display more than one of these three characteristics.

The first characteristic, the model's real pore-space geometry, has been described above. The second feature, the wide range of properties which have been modelled with the same network, is detailed in the box diagram, Fig. 1.5. It has been shown in previous publications that the network reproduces the experimental mercury intrusion curve, porosity, connectivity, pore : throat size correlation, tortuosity, gaseous diffusion through a dry sample, permeability and colloidally induced formation damage (Spearing *et al.*

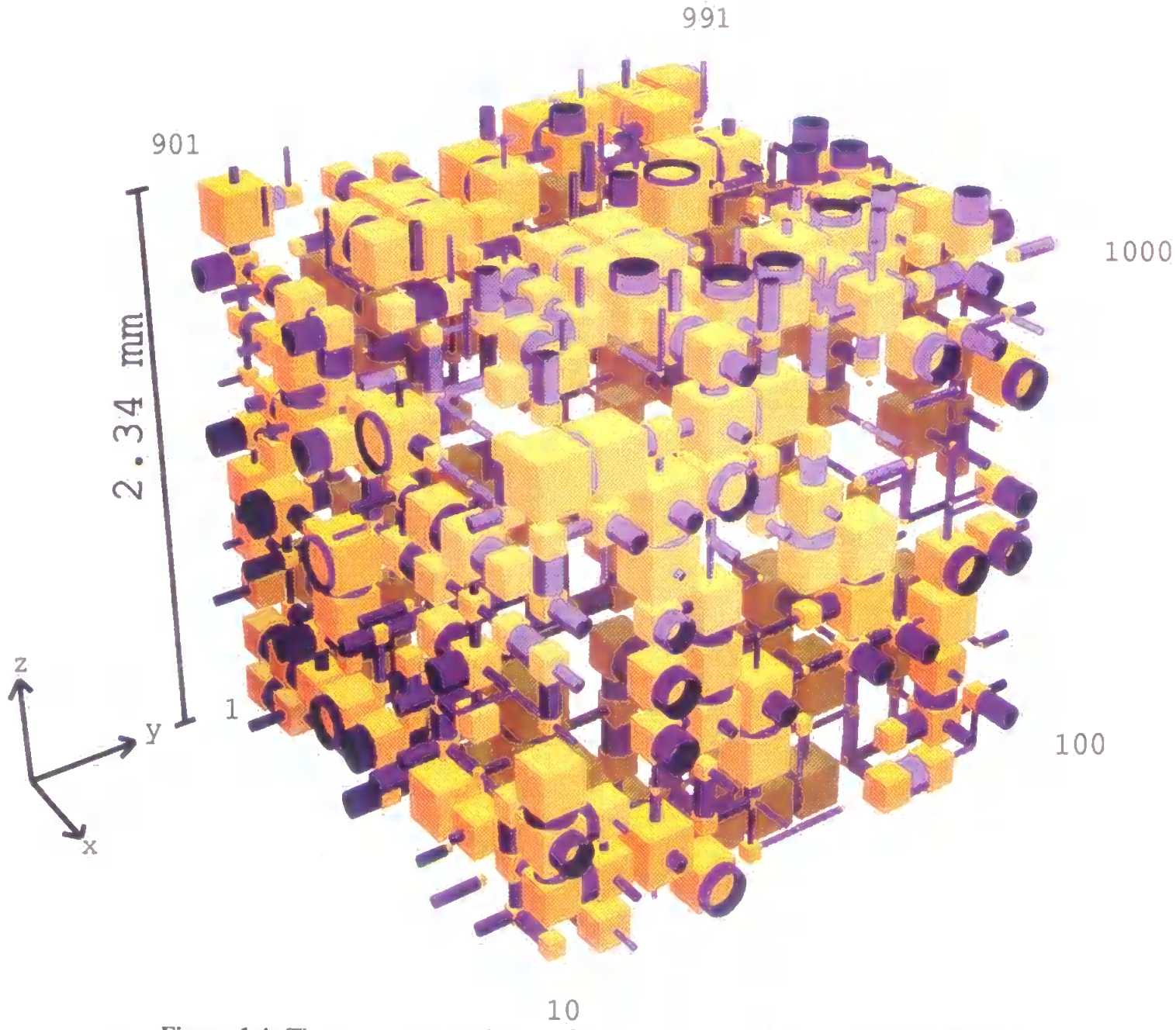

Figure 1.4 The two outermost layers of the unit cell of reservoir sandstone sample 212B

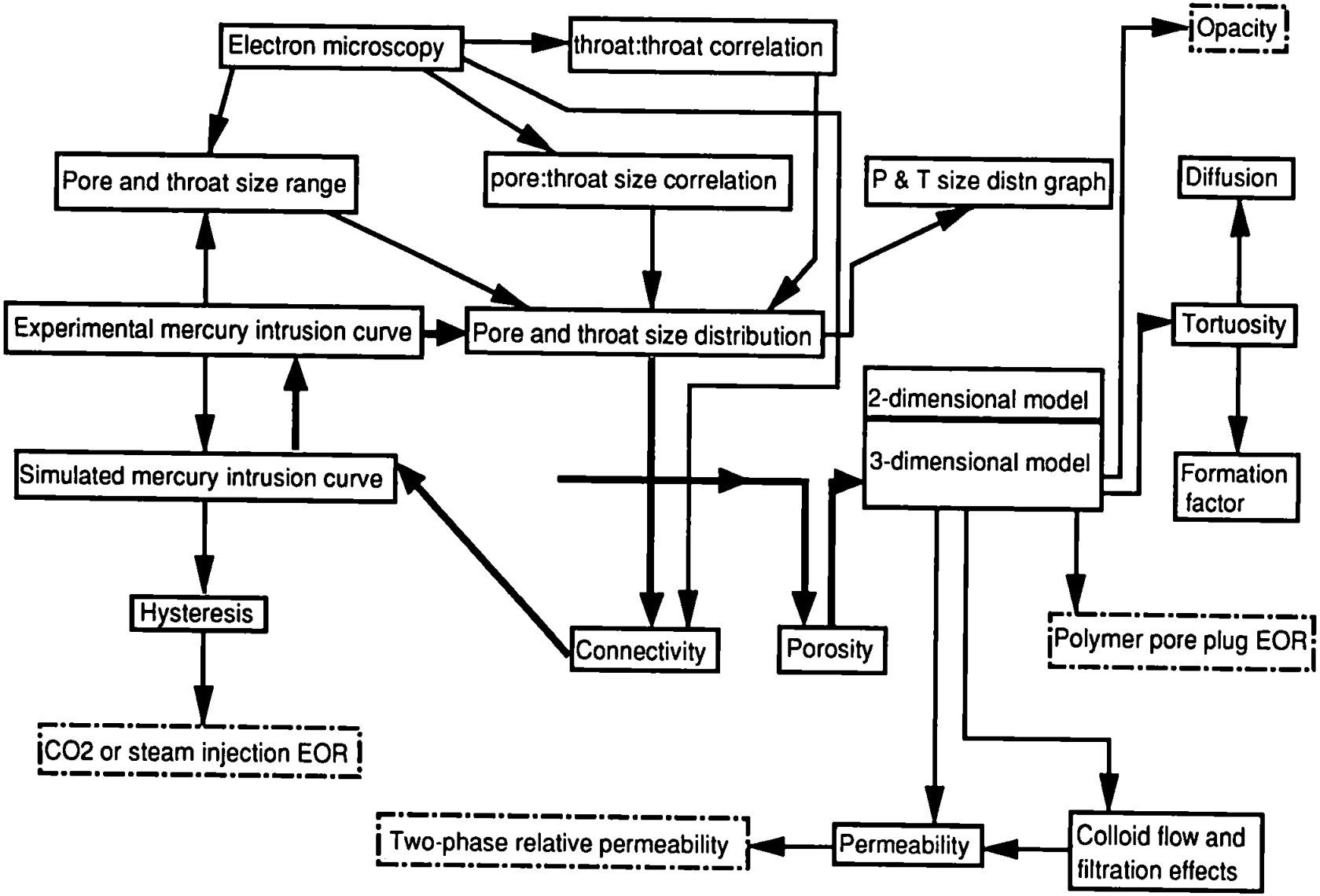

Figure 1.5 Scope and data flow of Pore-Cor: solid boxes show work to date, dashed boxes show future work, bold arrows show route of manual and automatic calculation methods.

1991b; Matthews *et al.* 1992; Matthews *et al.* 1993; Mathews *et al.* 1994). The surface of the simulated void space is too smooth by up to two orders of magnitude, but this can be roughened to match experiment (Spearing *et al.* 1991b). The model has a higher fractal dimension than sandstone (Spearing *et al.* 1991a). The modelling technique has been successfully used on outcrop sandstone (Moss *et al.* 1993), reservoir sandstone (Matthews *et al.* 1993), paper coatings (Kettle *et al.*1993), fibrous mats (Matthews *et al.* 1994), building materials (Matthews *et al.* 1995c) and tantalum capacitors (Matthews *et al.* 1995d).

The third feature of the modelling is that the fitting parameters are property-dependent. These parameters, in particular the skew of the throat diameter distribution and the connectivity, are actual properties of the sample, and can be checked as having realistic values. No entirely arbitrary, property-independent fitting parameters are needed to make the simulation fit experiment. Thus there are no hidden features in the model specific to any particular porous solid, and Pore-Cor can therefore be applied to any porous medium for which appropriate experimental measurements are available.

Although the Pore-Cor model is closely associated with experimental parameters, it is nevertheless a representation, or mapping, of the true structure rather than an exact replica of that structure. This raises the question of whether the mapping is unique, an issue which is investigated and discussed later.

In this thesis, there is an investigation of the effect of additionally including positive and negative correlations between throat sizes (and hence pore sizes) in different parts of the unit cell of the void space model, thus producing structures which are banded, or which contain clusters of small pores and throats, or clusters of large pores and throats. The effect of such correlation on absolute permeability has also been investigated, in structures which have been arbitrarily generated, and also in structures which have been additionally constrained to simulate experimental mercury intrusion curves. The modelling

method has been applied to banded sandstone samples (212B and 212C) from Morecambe Bay. Another structure for Pore-Cor was developed when fibrous mats were being modelled. These samples had porosities of about 80 %, which could not be modelled by the usual random structure. A unit cell which had all the pores the same size, the size of the largest throat diameter, was used. An example of this type of model is shown later. Hysteresis has been investigated, and a new program, Pore-Comp, has been developed which corrects mercury intrusion readings for mercury compression and penetrometer expansion. This program is illustrated with the modelling of nine paper-coating formulations. The fundamental theory for the analysis of all mercury porosimetry data is the same for all samples and is described below.

1.3 Mercury porosimetry

As is normal in this field, the Washburn (or Laplace) equation is used in the present work to relate throat diameter to mercury pressure:

$$d = -\frac{4\gamma\cos\theta}{P} \qquad [1.1]$$

where γ is the interfacial tension between mercury and air (0.48 N m^{-1}), P is the applied pressure, θ is the contact angle and d is the throat diameter. Van Brakel *et al.* (1981) discuss the limitations on the use of this equation and the uncertainties in the values of γ and θ. For example, surface roughness may cause the contact angle to increase to 180°. In this study the commonly accepted value of 140° for mercury intruding into sandstone against residual air is used, so that eqn [1.1] reduces to:

$$d = \frac{1470}{P} \qquad [1.2]$$

where d is the throat diameter in μm and P the applied mercury pressure in kPa.

The mercury intrusion curve of a porous sample consists of measurements of the volume of mercury intruded, V, plotted against applied mercury pressure, P. The volume of mercury intruded is often converted to a percentage of the total void volume (= 100 % x volume intruded at pressure P / volume intruded at highest attainable pressure), and the applied mercury pressure converted to a throat diameter via eqn [1.1] or [1.2]. An example of a curve plotted in this format is shown in Fig. 1.6. It can be seen that the intrusion curve is sigmoid in shape. Traditionally, it has been assumed that the distribution of throat diameters (not distinguished from pore sizes) can be equated to the first derivative of an intrusion curve, dV/dd. This results in a distribution which has a peak at the point on the intrusion curve which has the highest gradient, i.e. the point of inflection. The Washburn throat diameter at this point is then often referred to as the characteristic throat diameter. However, the use of the first derivative is only valid for a porous solid which consists of a bundle of non-interconnecting capillary tubes, which can be tortuous, but each of which must be of a single diameter throughout its length or monotonically tapering from the point of external mercury contact. Fig. 1.7 shows the unit cell which is generated by the application of these assumptions to the reservoir sandstone 212B.

Porosimeter control software usually incorporates the first derivative assumption and such software sometimes extends this assumption to derive a particle size distribution for the solid. The first derivative assumption is also inherent in the derivation of fractal dimension from mercury intrusion curves using equations such as Friesen *et al.* (1993) as discussed by Spearing *et al.* (1991a):

$$\log\left[\frac{dV}{dr}\right] \sim (2 - D)\log(r) \qquad [1.3]$$

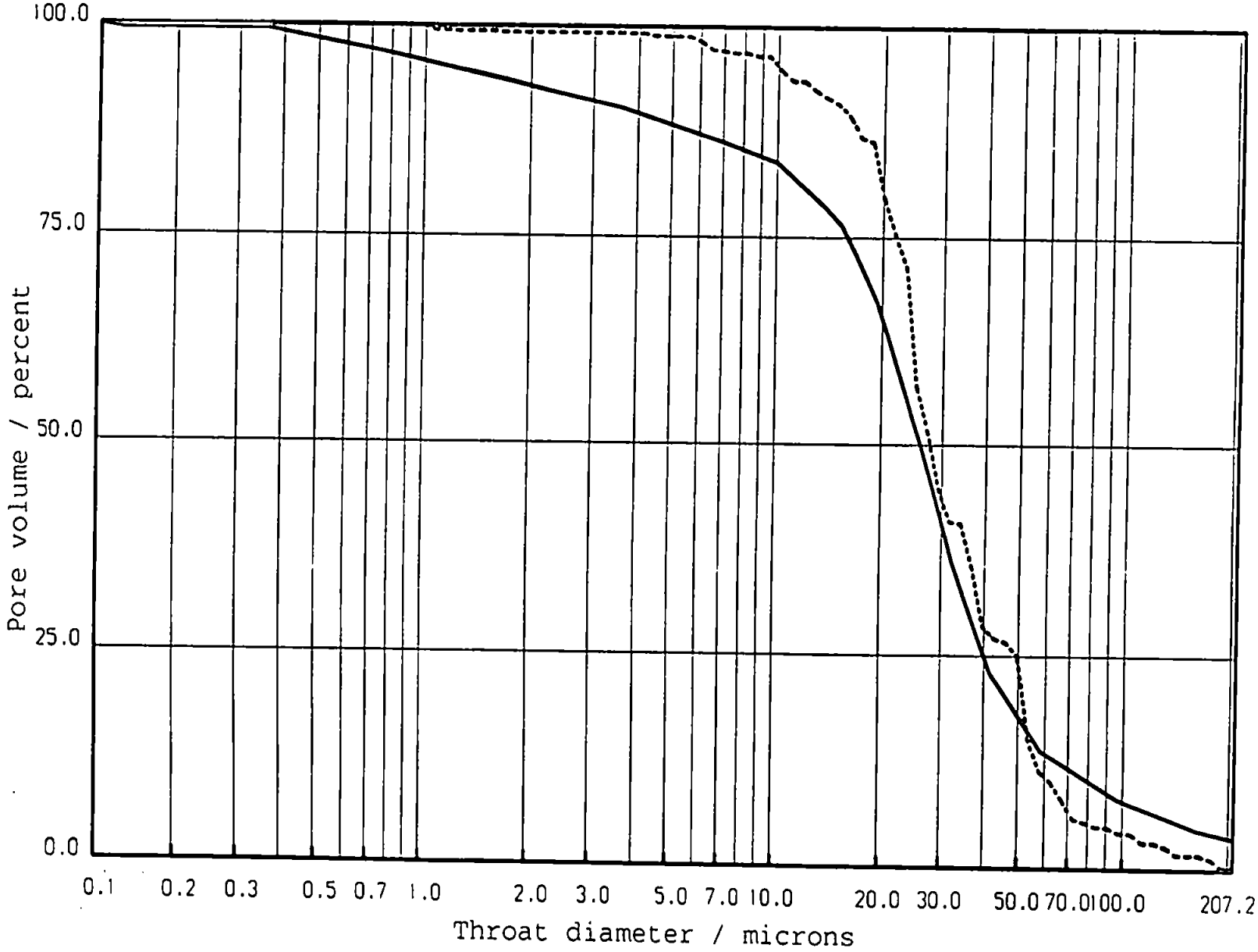

Figure 1.6 Mercury intrusion for sample 212B: —— experimental, ----- simulation

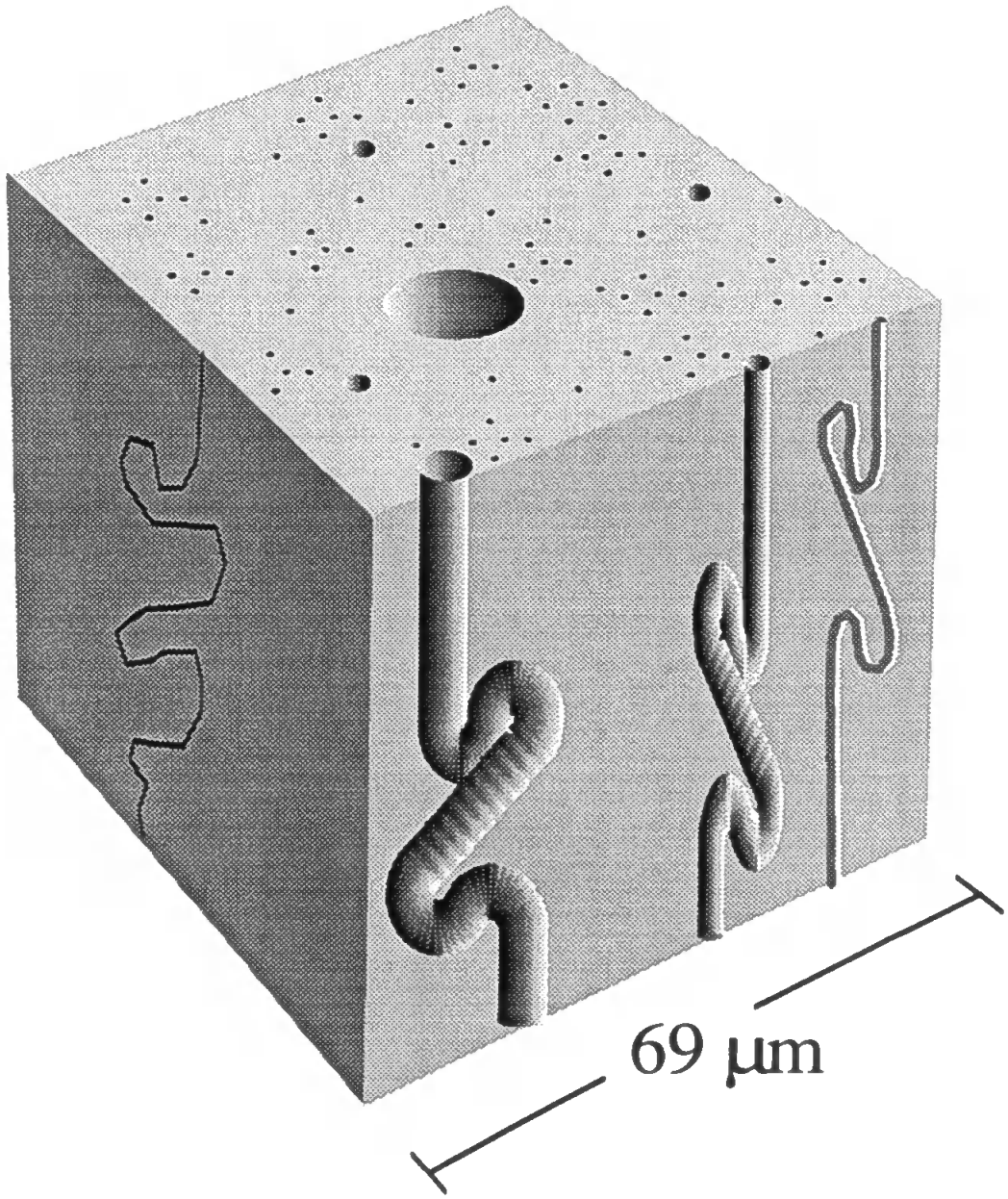

Figure 1.7 Unit cell for sandstone sample with first derivative assumption

where the r is the Washburn throat radius = $d/2$ and D is the fractal dimension. This equation may in fact be written without recourse to the Washburn throat diameter, but the capillary bundle assumption is still present.

The unit cell of the simulation presented here consists of a 10 x 10 x 10 array of pore sites connected by throats. The size of the unit cell has been limited by computing power, particularly with regard to the calculation of permeability (Matthews *et al.* 1993). A typical unit cell applied to sandstone represents about a 2 mm cube, (Fig. 1.4). Whereas the unit cell repeats infinitely in every direction, an experimental sample tends to have larger throats at its surface, which allow intrusion at lower pressures than for an infinitely large sample (Wardlaw *et al.* 1976). Account of these edge effects can be taken when fitting mercury intrusion curves either by extending the experimental mercury intrusion curve down from the point of inflection or by giving a lower statistical weighting to the fit at larger throats sizes.

1.4 Other simulations

1.4.1 *Random structures*

Garboczi (1991) has pointed out that the two main limitations of using a percolation algorithm based on the Washburn equation are (i) that the throats are all considered to be cylindrical, and (ii) that the mapping of the effective network derived from the mercury porosimetry curve is not necessarily the same as the real network. Calculations on specific shapes of pores have been carried out by Mason *et al,* 1988, who have also modelled the intrusion and extrusion of mercury in an array of packed spheres (Mason *et al.* 1991) by using the Haines in-sphere approximation (Haines, 1927) to model the void spaces between them. Conner *et al.* (1988a) have used a range of rod- and plate-like structures to demonstrate that there is a relationship between shape of pores and throats, and the shapes of the intrusion and extrusion mercury hysteresis curves. Yanuka *et al.* (1986) have also

used different void shapes, in the form of a three-dimensional network of intersecting ellipsoids, for their simulation of percolation processes, and Kloubek (1994) uses a pore with a conical termination. However, Garboczi (1991) showed that a range of pores and throats of different shapes and sizes could be adequately represented by a random network of interconnecting elliptical cylinders. The elliptical cylinders can range from circular (major and minor axes equal) through to cracks (minor axis negligible). As will be demonstrated, the mercury intrusion curve can be simulated using only throat diameter distribution, pore size : throat diameter correlation, and connectivity. The resulting sizes incorporate the effect of the shapes of the void spaces (Cebeci 1980). The close fit to experiment which can be generated by very simple pore and throat geometries suggests that it might not necessarily be valid for other workers to interpret the discrepancy between their simple models and experiment as arising from more subtle information such as pore and throat shape and formation damage.

A survey of networks used by other workers up to 1975, ranging from bundles of capillary tubes through to three-dimensional interconnecting networks, is given by Van Brakel (1975). The network presented here is based on actual samples, although not on any form of tomography (Lymberopoulos *et al.* 1992), and so is closer to an actual representation of void volume than it is to a mathematical network. Lenormand *et al.* (1988,1989) have used 100 x 100 x 1 and 25 x 25 x 1 networks to simulate two-phase displacement effects, namely capillary fingering, viscous fingering and stable displacements. Blunt *et al.* (1990,1991) generated 2-D and 3-D networks of up to 80000 pores of equal volume, with pore coordination numbers in the range 3 to 12, and a connectivity of 6. The throat diameters followed a uniform, linear distribution. Chatzis *et al.* (1985) used 33 x 33 x 1 and 18 x 18 x 12 networks formed from angular capillary tubes with angular bulges to represent pores. The pore volume network was fitted to experimental data, which deviated from one another by up to 8 % above about 70 % pore

volume. Conner *et al.* (1988b) used a 10 x 10 x 10 matrix, with all pores being of the same volume, and the throats having zero volume, with a connectivity of 6. Li *et al.* (1990) used a 16 x 16 x 48 network, with pore and throat diameter distributions based on uniform diameter intervals, throats of negligible volume, and connectivities of 4, 6 and 8. Payatakes and coworkers (Tsakiroglou *et al.* 1991; Constantinides *et al.* 1989) used 20 x 20 x 20 and 30 x 30 x 2 networks for the simulation of mercury intrusion and extrusion curves. They used an invasion percolation algorithm which was very similar to that used in this work, but also included resistance effects due to pore shape, Tsakiroglou *et al.* (1990).

All the networks mentioned above have some geometrical point of weakness, e.g. arbitrary pore and throat size distribution, arbitrary or fixed connectivity, an undrawable structure or the use of arbitrary fitting parameters. The networks used by Payatakes and coworkers (Tsakiroglou *et al.* 1990, 1991, 1993; Vizika *et al.* 1994), generally have a more sophisticated geometry than the present Pore-Cor network, and a very similar percolation algorithm is used. The advantage of Pore-Cor, however, is that it models a wide range of pore-level properties from the same simulated unit cell structure.

1.4.2 *Correlated structures*

In Chapter 2 of this thesis, there is an investigation of the effect of additionally including positive and negative correlations between throat sizes (and hence pore sizes) in different parts of the unit cell of the void space model, thus producing structures which are banded, or which contain clusters of small pores and throats, or clusters of large pores and throats. The effect of such correlation on absolute permeability has been investigated, in structures which have been arbitrarily generated, and also in structures which have been additionally constrained to simulate experimental mercury intrusion curves. The modelling method has been applied to banded sandstone samples (212B and 212C) from Morecambe

Bay.

Uncorrelated networks developed by other workers range from parallel bundle models which do not take any shielding effects into account (Yamazaki *et al.* 1993), through two dimensional models that model shielding effects and hysteresis (Androutsopoulos *et al.* 1979; Mann *et al.* 1981; Gavrilenko *et al.* 1989; Hirasaki 1990; Mason *et al.* 1991; Hampton *et al.* 1993), to more complicated three dimensional models (Koplik *et al.* 1984; Blunt *et al.* 1991; Portsmouth *et al.* 1991; Zgrablich *et al.* 1991; Garboczi 1991; Bryant *et al.* 1993). The void space network of the present thesis has been compared with the networks of other workers in a recent publication (Matthews *et al.* 1993).

In studies of correlation effects, other workers have generated void space networks with pore and throat size distributions and correlation levels obeying pre-set mathematical functions. These models can be very precise in themselves but are often only loosely related to experimental samples. Li *et al.* (1986a,1990) showed how correlation effects reduced shielding and brought about intrusion at a lower pressure. This in turn caused a reduction of entrapment during secondary imbibition. This effect has also been demonstrated by Wardlaw (1990) in multiple intrusion/extrusion scanning loops. Tsakiroglou *et al.*, (1991) generated 30 x 30 x 2 and 20 x 20 x 20 networks of cylindrical throats and spherical pores with shaped necks, and demonstrated that the points of inflection of the simulated mercury intrusion curves were less pronounced within pore-pore and pore-throat correlated models compared to uncorrelated structures. Ioannidis *et al.* (1993a, 1993b) represented porous media by a 50 x 50 x 50 array of cubes with different grey levels representing different pore sizes, and showed that mercury intrusion became slightly more gradual with increasing pressure as the structure was correlated. The retention of mercury after secondary imbibition decreased because of a reduction in shielding and snap-off effects. Day *et al.* (1994) pointed out that a two-step mercury

intrusion curve would result from extreme positive and negative pore : pore size correlation if such correlation produced a bimodal distribution. Jerauld *et al.* (1990) used a 20 x 20 x 20 Voronoi network to demonstrate that increasing the extent of correlation between throats increased non-wetting phase relative permeability and slightly decreased wetting phase relative permeability.

Image analysis of serial sections of resin- or Woods metal-impregnated samples has been used for the experimental study of the correlated void space. Adler *et al.* (1990) studied resin-filled Fontainebleau sandstone sections and 'reconstructed' the porous medium using a 27 x 27 x 27 array of either solid or void cubes. The array had the same porosity and correlation factor as the two dimensional sections of sandstone, although connectivity could not be modelled and it was found that unrealistic blocking of flow was caused by individual solid cubes. Wardlaw *et al.* (1987) injected samples of Berea sandstone and Indiana limestone with Woods metal, and used electron microscopy to examine the void space. Lymberopoulos *et al.* (1992) have used serial tomography to measure correlation effects and also set up algorithms to interpolate the void volumes between the serial sections and to distinguish pores from throats. Their work also suggests that the mercury intrusion curve is spread over a wider range of pressures in correlated structures. Ringrose *et al.* (1992) have discussed the problems in the study of permeability correlations in clastic sediments on a scale up to 1000 times larger than in the present thesis.

1.4.3 *Edge effects*

Wardlaw *et al.* (1976) have shown that there was a difference between the mercury intrusion curve of two almost identical 9 cm^3 cylinders of Indiana Limestone, one sealed with a thin coat of epoxy resin except for one end, and the other uncoated. In the uncoated sample, intrusion commenced at lower pressures and was up to 15 % pore volume higher

in the low pressure region, a change attributed to surface throat enlargement. The intrusion curve for the coated sample, however, increased much more abruptly from the zero pore volume axis up towards the point of inflection. The intrusion curves for the coated and uncoated samples were identical above around 20 % pore volume. Experiments were also carried out on samples of different bulk volume, from 1.7 to 25.0 cm^3. The smallest sample volume produced an intrusion curve up to 3 % pore volume higher than the other curves at low pressures, but converged at 10 % pore volume. These intrusion curves highlight the problems involved with edge effects.

1.5 Paper coatings

All the networks so far described have been applied to fairly coarse-grained porous materials such as sandstone. However, recently it has been realised that the technique can be usefully applied to the very much finer particulate materials that find use in the paper coating industry, Gane *et al.* (1995) .

Paper is formed on a fine screen from an aqueous suspension of wood fibres (pulp) and fillers known as *mineral pigments*. The mineral pigments are usually made from high brightness calcite (ground marble or limestone) or china clay (kaolin) which has undergone various grinding and separation processes. To improve gloss, shade, opacity and printing characteristics, paper is often coated with a *coating colour*. The coating colour is an aqueous dispersion which contains similar mineral pigments to those used as filler, although with a finer particle size distribution, together with around 10 % by weight of adhesive known as *binder*, frequently in the form of synthetic latex particles, and possibly a small quantity of synthetic *plastic pigment* in the form of polystyrene spheres to increase gloss and/or opacity. Although not considered here, additives may also be present to enhance binding and/or induce a loose form of association known as flocculation, which affects the structure on drying.

The drying of clay-latex coatings has been studied by Watanabe *et al.* (1982). In the first phase of the process, water evaporates or is drawn from a dispersion in which clay and latex particles can move freely. At what is known as the first critical concentration, free motion ceases and a bulky and deformable three-dimensional network forms. The wet coating then shrinks under the increasing capillary forces until, at the second critical concentration, all structural changes stop. From then on, the capillaries are progressively emptied until drying is completed. The dried coating is thus not a continuous film, but a porous structure of pigment particles bound together at their points of contact. The particle diameters of the mineral pigments in the coating range from around 0.01 to 10 μm (10^{-8} - 10^{-5} m), whilst the synthetic pigments, and the latex particles prior to film formation, are in the 0.1 to 1 μm diameter range. The voids within the dried paper coating are therefore in a similar size range. The structure, size and inter-connectivity of these voids affect the optical properties of the paper (Climpson *et al.* 1976; Lepoutre *et al.* 1977; Alince *et al.* 1980b) and also the way in which ink sets on the paper during the very short time period allowed in modern high-speed printing presses (Gane *et al.* 1994). The void structure of the surface has been studied directly by profilometry of the surface and electron microscopy of vertical sections through resin-embedded samples (Kent *et al.* 1986). Other studies have involved the measurement of the change in reflectance of an imbibed ink drop with time (Larrondo *et al.* 1992; Ranger 1983). Hamlen *et al.* (1991) have developed regular and irregular pore models of fibre sheets, and used them in the study of the variation of permeability on compression.

In the present thesis the use of mercury porosimetry is described for the characterisation of the pore structure of paper coatings, i.e. the measurement of the volume of mercury injected and withdrawn from a sample over a range of increasing and then decreasing applied pressures. Mercury porosimetry has been little used for the study of paper coatings, and suffers from two limitations. The first is that some of the samples are

compressible. The compressibility may be due to calcium carbonate particle inter- and/or intra-compaction, the compression of the latex binder, or, in the case of the synthetic pigments, the compression or collapse of the polystyrene spheres. A new method for compensating for these effects is presented, which also gives a measure of the compressibility or bulk modulus of the sample. The second limitation is that the traditional interpretation of mercury porosimetry methods does not take shielding effects into account. Pore-Cor, however, does account for shielding effects, as explained previously.

CHAPTER 2

GENERATION OF PORE-COR STRUCTURES

A general description of the Pore-Cor package will now be given. The void-space model uses a log/linear throat size distribution, i.e. there are 100 sizes equally spaced on a logarithmic axis, as shown in Fig. 2.1. A log/normal distribution can also be used, but gives mercury intrusion curves which are too steep at the point of inflection (Matthews *et al.* 1992). The parameters which can be varied are the range of throat sizes, the skew of the distribution, the relationship between throat and pore size, and the spacing between the rows of pores.

The range of the throat-size distribution (1 to 100 μm in Fig.2.1) is set to the limits of the experimental mercury intrusion curve, calculated from the pressure range of the curve by means of the Washburn equation, eqn [1.2]. The pore-size distribution generated from this throat-size distribution is checked by inspection of scanning electron micrographs, as indicated in Fig. 1.4 and exemplified in Plate 2.1, discussed below. The term 'skew' is defined to be the percentage of throats of the smallest size in a log/linear distribution. In Fig. 2.1, the skew is set to 1.00 % i.e. there are 1.00 % of the smallest of the 100 throat sizes, and hence 1.00 % of all other sizes, to the nearest integral number of throats. The connectivity of the distribution is 3.5, i.e. there are on average 3.5 throats per pore. As there are 1000 nodes in the unit cell, and each throat connects to two nodes, the number of throats in this instance is 1750. Hence there are, to the nearest integer, 17 or 18 throats at each of the 100 sizes, which explains the oscillation of the throat size distribution in Fig. 2.1. Such variations in numbers of throats and pores, due to the relative simplicity of the unit cell, occur throughout the rest of the modelling.

The 1750 throats are randomly positioned within the unit cell. Pores are then assigned to each node that has at least one throat connected to it, the pore being of a size

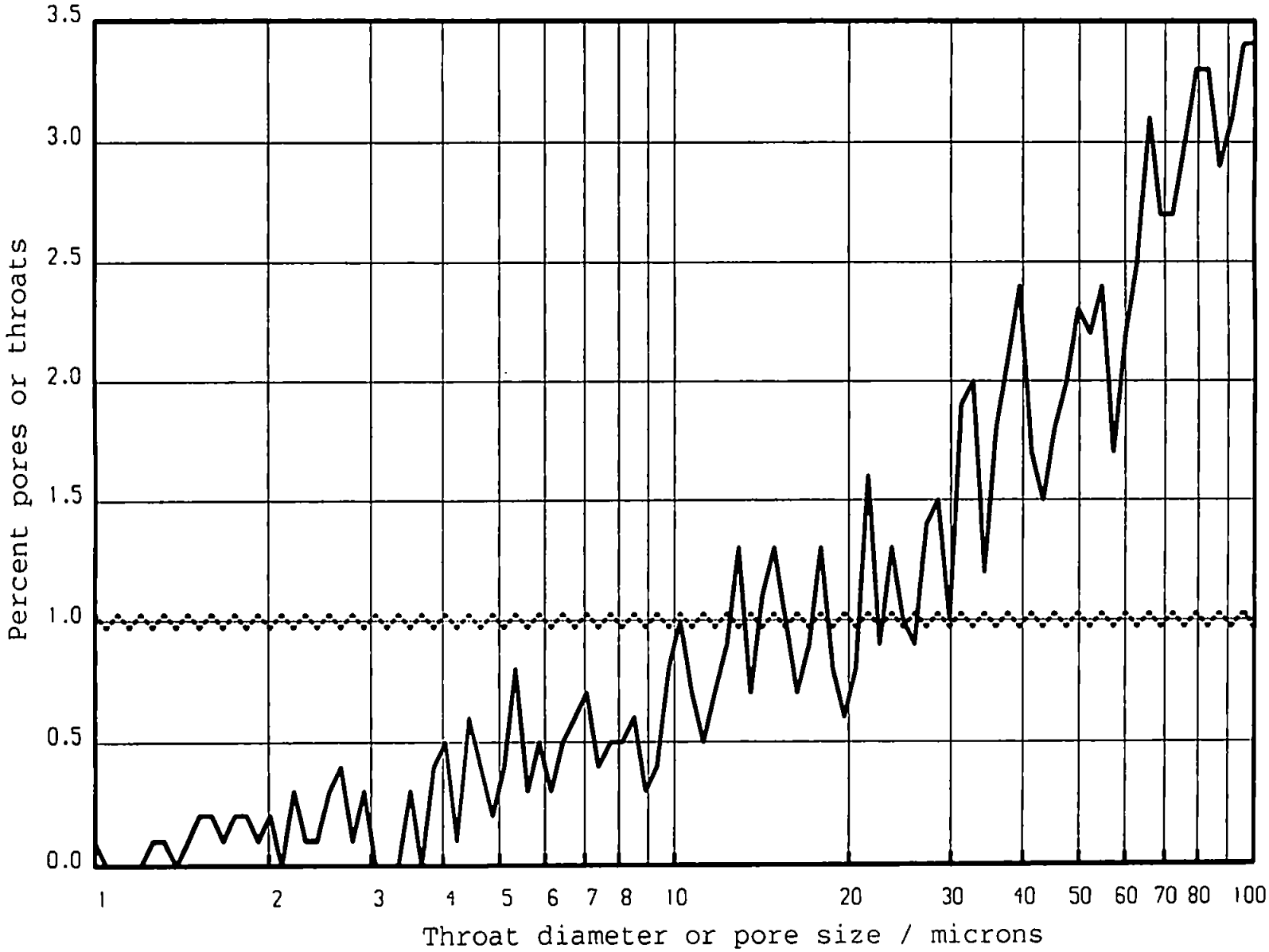

Figure 2.1 Unskewed throat diameter distribution with pore size distribution: —— pores, ----- throats

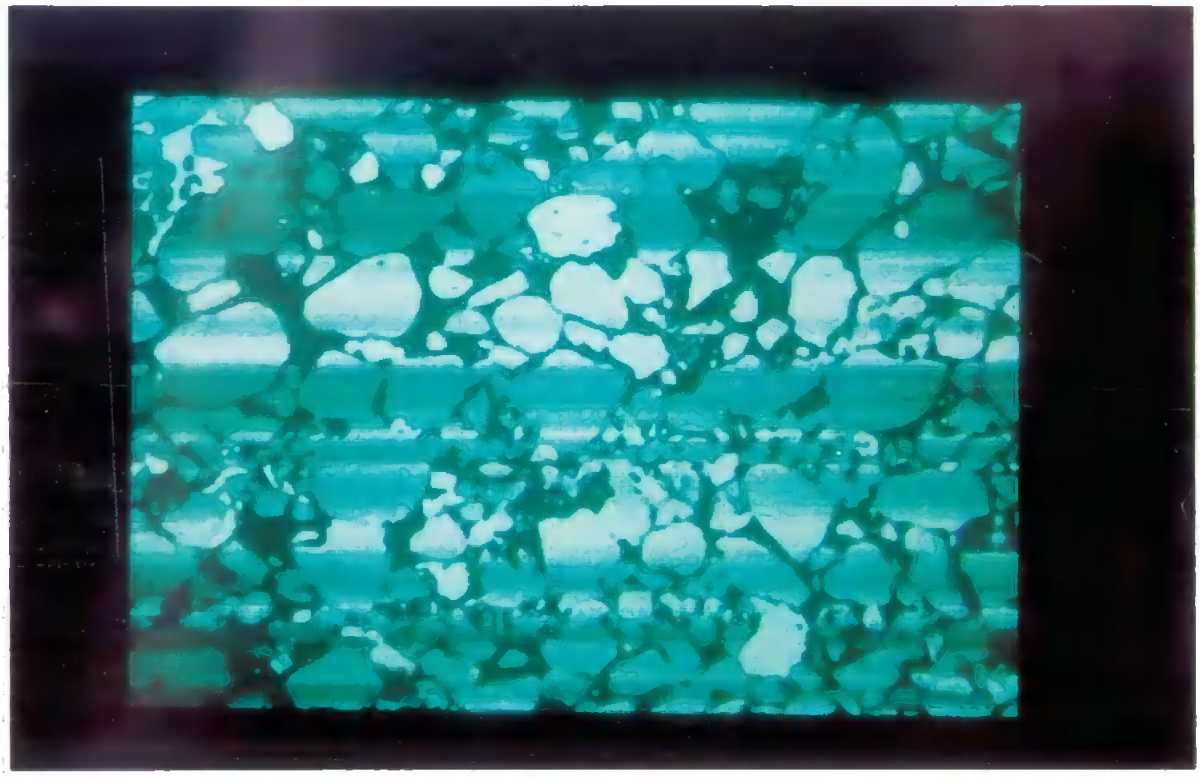

Plate 2.1 An image analysed back scattered electron micrograph of resin-filled sandstone sample 212B

equal to the diameter of the largest throat reaching that node. The random positioning of the throats introduces a degree of randomness into the pore sizes, as shown in Fig.2.1. This pore size : throat size correlation is typical of sandstones but not limestones (Wardlaw *et al.* 1987). Finally, the row spacing of the matrix is set so that the porosity of the simulated network is equal to that of the experimental sample. Increasing the pore row spacing lengthens the throats, increases the unit cell size, and reduces the porosity.

All the above is for a uniform distribution of throat sizes. However, the distribution can also be skewed by rotating the linear throat size distribution about its centre point. A throat size distribution with a skew of 0.19 %, for example, has 0.19 % of the smallest throat size, 1 % of the size in the middle of the logarithmic distribution (10 μm in Fig. 2.1), and 1.81 % of the largest size. Fig. 2.2 shows what is referred to as a 'negative' skew of - 0.42 %, i.e. the linear distribution of throat diameters would intercept the percentage of smallest (0.12 micron) throat diameters at - 0.42 %, were it not for the fact that the distribution is horizontal at 0 % to bring any impossible negative percentages up to zero, and horizontal at 2 % to maintain the total number of throats at 100 %.

If the size model were infinite, then the random positioning of the throats (and hence pores) within a given set of parameters would always produce a uniform isotropic assembly with identical cell properties. However, the present unit cell has only 1000 nodes, so that using different sets of random numbers will produce assemblies with different properties. For a number of typical unit cells adjusted to fit experimental data as explained below but using different seeds to produce the random numbers, the simulated permeabilities can be as large as twice or as small as half of the mean value. The obvious solution to this divergence would be to increase the number of nodes in the unit cell, but this is impossible because of the processing limit of the Dinic network analysis algorithm. The random positioning of throats is therefore carried out by using a pseudo-random number generator with the same seed for every simulated structure. Thus structures with

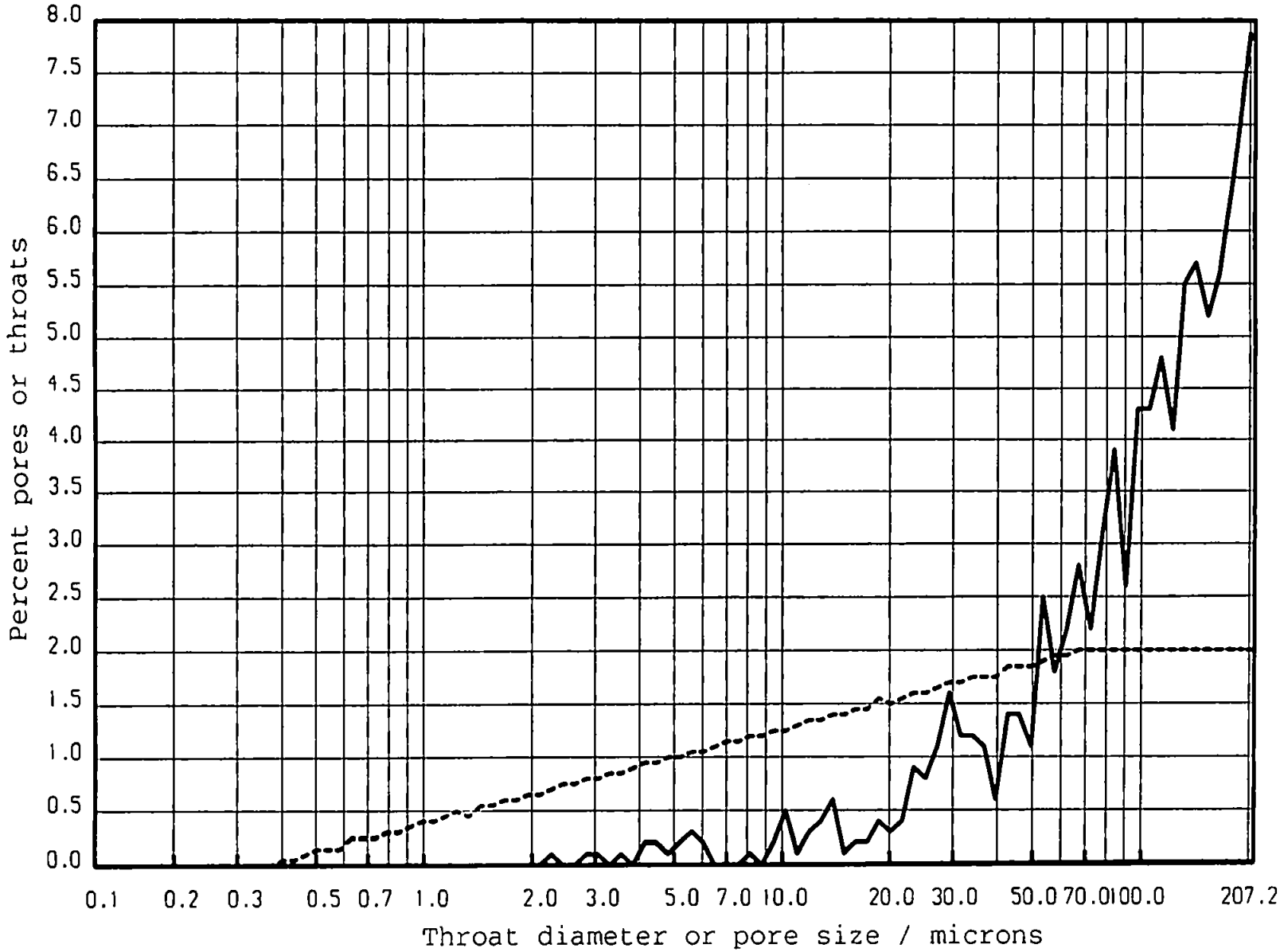

Figure 2.2 Negative skewed (-0.42 %) throat diameter distribution with pore size distribution: —— pores, ----- throats

similar parameter values, such as skew and connectivity, have very similar properties, and the trends induced by the changes in parameter values can be isolated from those resulting from the use of different random number sets.

In the present mercury intrusion simulation, the mercury is always injected from the top of the unit cell (i.e. normal to the *xy* plane at $z = l_{cell}$), so that the injection corresponds to intrusion downwards from the top surface of the cell shown in Fig. 1.3. The mercury pressure applied is related to the diameter of the penetrated throats by the Laplace / Washburn equation mentioned previously, eqn [1.1]. An invasion percolation method is used to calculate the fraction of pore volume occupied at a series of increasing static pressures of mercury. This mimics data available from standard mercury porosimeters, although more precise information can be gained from rate-controlled porosimetry (Yuan *et al.* 1989). The algorithm used has been described in detail in a previous publication (Spearing *et al.* 1991b), and is similar to that of Tsakiroglou *et al.* (1990). Fig. 2.3 shows the simulated mercury intrusion curves for the unskewed distribution of throats and also for the distribution of throats where the skew is 0.45 %.

The gradient of the porosimetry curve at its point of inflection is governed by the connectivity, an experimentally realistic value being 3.5. Higher values shift the curve to the right, and also introduce too high an upper shoulder as a consequence of increasing the gradient at the point of inflection. This is shown in Fig. 2.4, where higher connectivities give a steeper shoulder above the point of inflection due to the greater suddenness with which the mercury invades the network near the breakthrough pressure. Also, breakthrough occurs at a lower pressure (greater throat diameter) because of the increased number of routes available through the network. For the intrusion curve with a connectivity of 4.5, the characteristic throat diameter can be brought back to equality with the experimental one by altering the skew from 0.45 % to 0.90 % (i.e. increasing the number of smaller throats), but the resulting porosimetry curve still has too steep an upper shoulder, and the

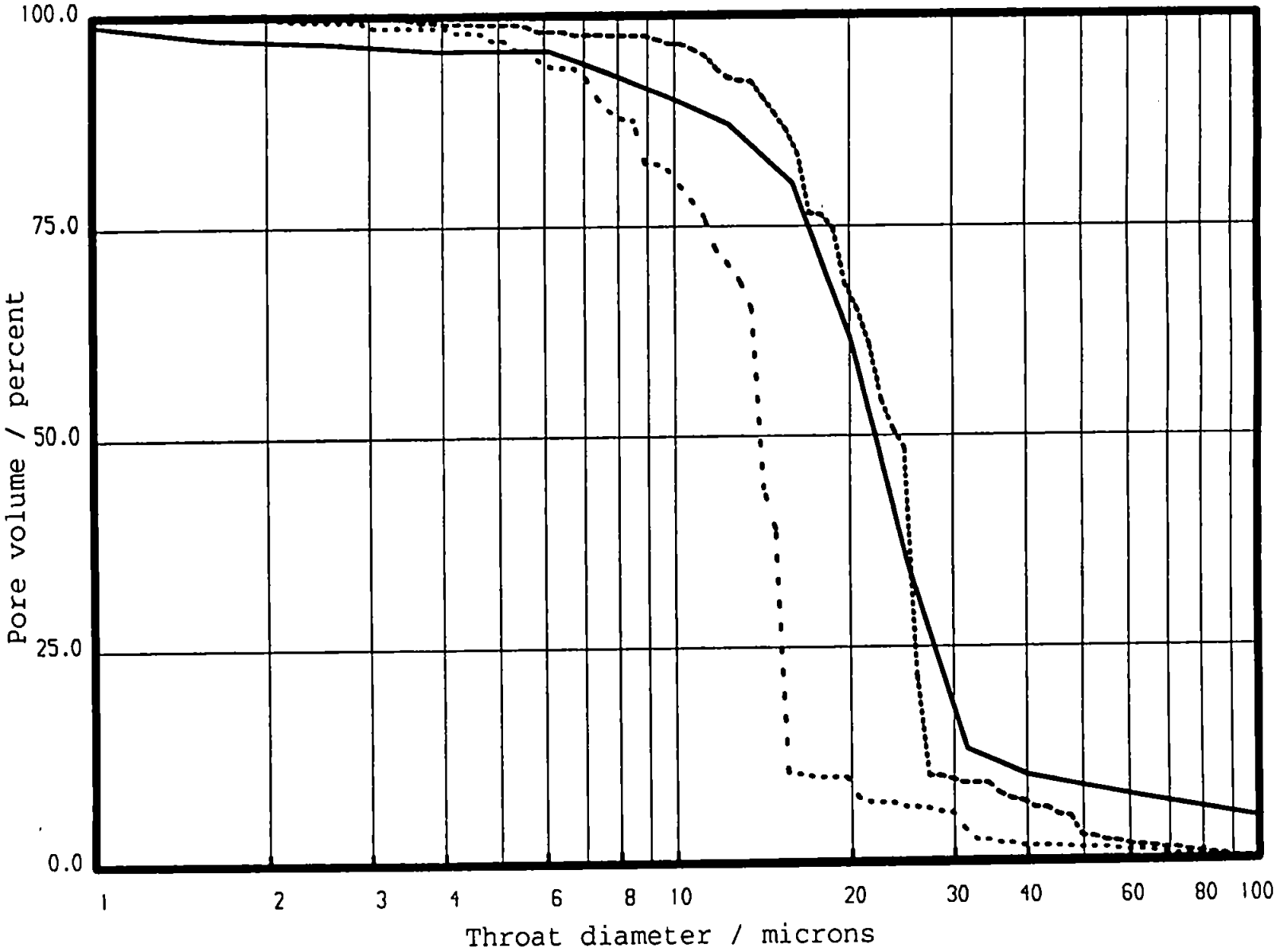

Figure 2.3 Mercury intrusion curves: —— experimental, - - - - unskewed distribution, ----- 0.45 % skewed distribution

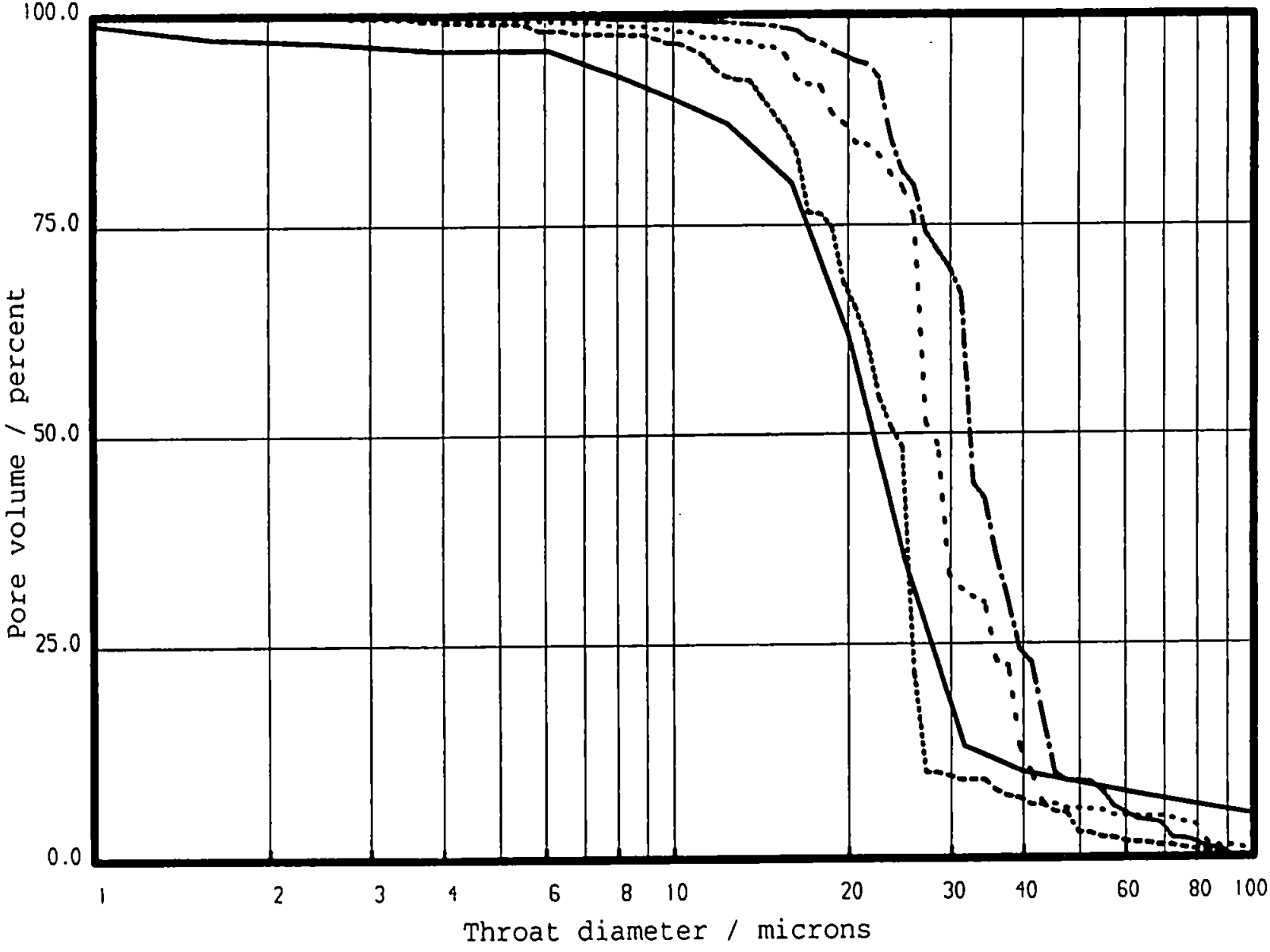

Figure 2.4 Mercury intrusion curves: —— experimental, ----- 0.45 % skewed distribution with connectivity 3.5 - - - - connectivity 4.0 —-—- connectivity 4.5

connectivity of 4.5 is in any case too high for sandstone. A connectivity of 3.5 and a skew of 0.45 % gives a good fit by manual methods.

2.1 Constructing correlated structures

Not all porous materials have truly random structures; many that are met with have regions where large pores and/or regions where small pores occur more frequently. These regions may take the form of layers or bands, or they may be more or less spherical. The three structures dealt with here are banded, structures with small pores and throats at the centre of the cell and structures with large pores and throats at the centre of the cell.

2.1.1 *Banded structures*

Fig. 2.5 shows a structure which is banded vertically, with the smallest throats on one side of the unit cell ranging across to the largest pores and throats on the other side. In such a structure, the numbers and sizes of the throats are determined by the initial data input i.e. minimum throat diameter, maximum throat diameter, skew and connectivity. The total number of throats is divided into ten equal as possible groups starting from the smallest. To obtain a totally correlated structure the whole of the first group must be placed randomly in the *yz* plane (or band) at minimum x, the second group in the band with the next lowest x, and so on until the final group of the largest throats are placed randomly in the final, tenth, band. Once the throats are positioned, pores are constructed equal to the size of the largest throat entering them. The unit cell repeats in all directions, and therefore the 10th band with the largest throats will adjoin the first band of the adjacent, identical unit cell. The first band therefore contains some large pores, as can be seen in Fig. 2.5. The permeability of the banded simulated structure is calculated in the negative z direction, i.e. parallel to the bands, which is in agreement with the experimental tradition of measuring the permeabilities of such banded samples.

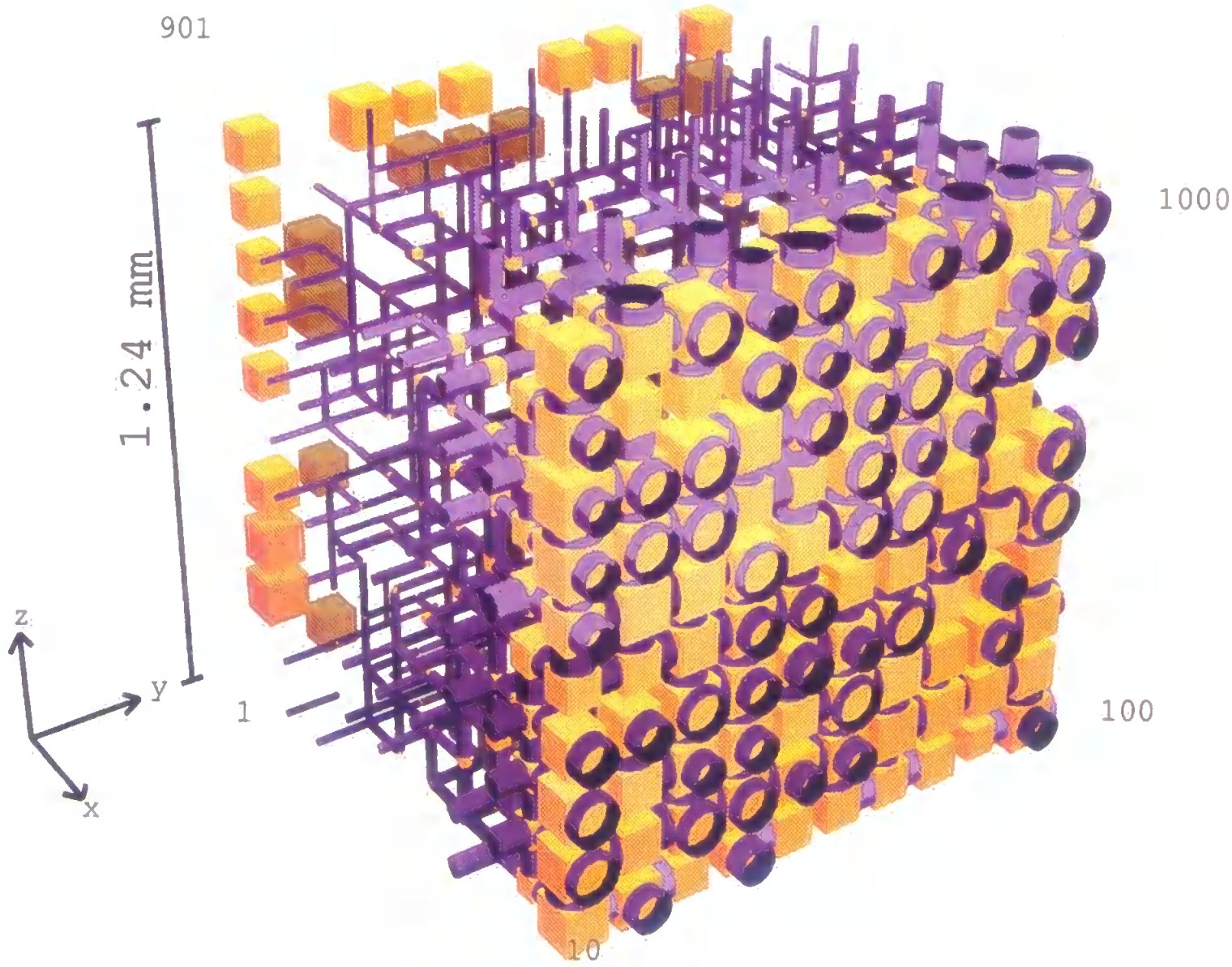

Figure 2.5 Totally correlated banded unit cell

The pore and throat size distribution of this structure is shown in Fig. 2.6. Each pore is the size of the largest throat entering it, and thus within each layer the pore sizes are skewed to the largest throat sizes. In the 6th layer, for example, the pore size distribution increases from 0 % at 10.72 μm to 2.4 % at 15.56 μm.

It is also possible to construct the unit cell with different levels of correlation. If a unit cell is totally correlated then each throat is positioned in a specific *yz* layer according to its size. If the level of correlation is reduced by one step (from 1.0 to 0.8), then a range of positioning is introduced of ±1 layer, i.e. there are now three layers in which a throat of a certain size may appear. In general

$$rowdiff = 5 \times (1 - clev) \qquad [2.1]$$

where *rowdiff* is the additional range of layers for positioning, and *clev* the correlation level Therefore, the total range of layers in which the throat may appear is (2 *rowdiff* + 1). Such a range may cause a throat to be positioned in a neighbouring unit cell. Since all unit cells are identical, the throat is therefore positioned in the corresponding position in the original unit cell.

2.1.2 *Structures with small pores and throats in the centre*

A totally correlated unit cell of this type is shown in Fig. 2.7. It has all its smallest pores and throats in the centre and its largest pores and throats around the outside. It is divided into ten spherical shells each containing an equal number of throat sites. To achieve this, the outer spherical shell, which only occurs at the corners of the cubic unit cell, is much thicker than the other shells. The total number of throats is divided into ten equal groups and, as with the banded structure, each group is placed within a shell designated according to the group number, with the smallest throats at the centre.

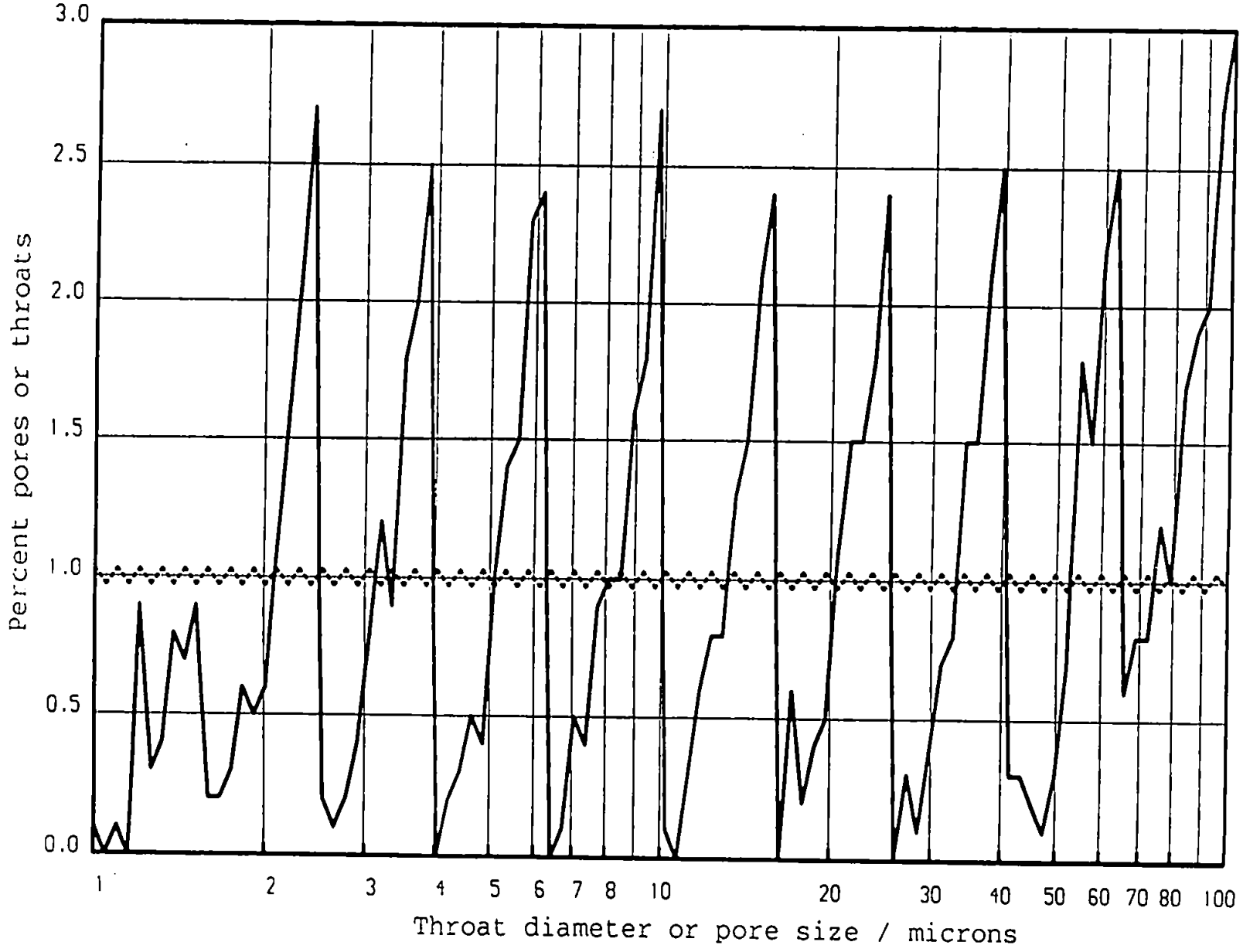

Figure 2.6 Throat diameter distribution with pore size distribution for a totally correlated banded structure: —— pores, ----- throats

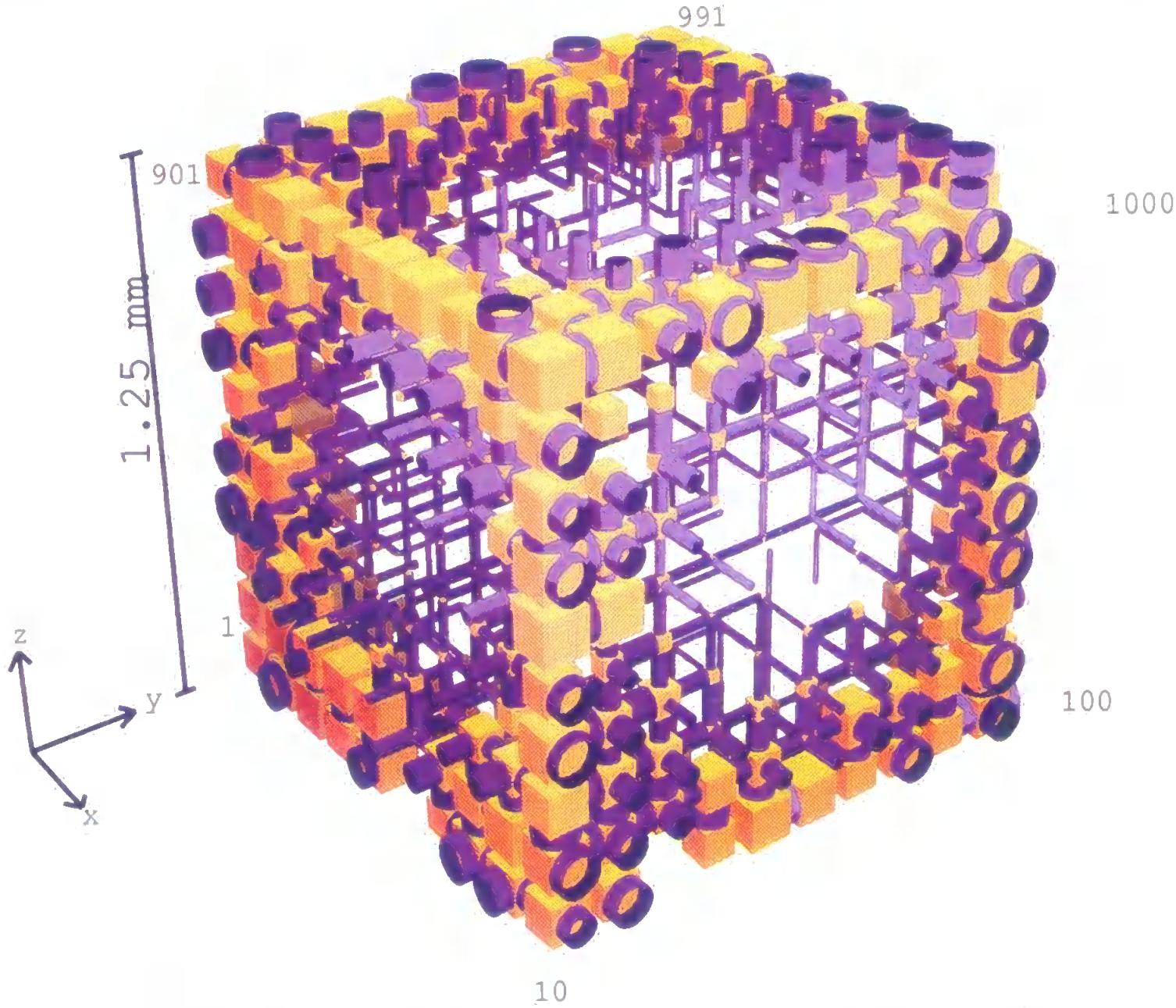

Figure 2.7 Totally correlated unit cell with small pores and throats in the centre

As before, various levels of correlation may be specified according to eqn [2.1]. However, in this case, the siting of throats in neighbouring unit cells is not permitted. The range of (2 *rowdiff* + 1) layers in which the throat may appear is therefore confined within the original ten shells in the unit cell as shown in Fig. 2.8.

The overall simulated structure is made up of an infinite array of these unit cells, and therefore has repeating clusters of smaller pores and throats within a matrix of larger pores and throats. Fig. 2.9 shows the fully correlated unit cell, with the small pores and throats in the centre, repeating to a cubic size of 2.5 mm. An experimental sample analogous to this would be a reservoir sandstone with clay inclusions.

2.1.3 *Structures with large pores and throats in the centre*

Fig. 2.10 shows the outer two layers of a unit cell of this type, in which the largest throats are positioned in the first (central) shell and the smallest throats are positioned in the outer shell. The method of construction and correlation is the same as for the structure described in the previous section. The pore size distribution peaks within each shell as it did with the banded structure (see Fig. 2.11). The overall simulated structure contains repeating clusters of larger pores and throats in a matrix of smaller pores and throats. Fig. 2.12 shows the fully correlated unit cell, with the large pores and throats in the centre, repeating to a cubic size of 2.5 mm. Such non uniform 'vuggy' samples also exist in the real world, for example clumps of soil.

2.2 Structures with all the pore sizes identical and all equal to the largest throat diameter

This structure was developed for the modelling of fibrous mats which have very high porosities. The random structure induces a restriction on the value of porosity due to the row spacing necessary to accommodate the largest pore size. In the fibrous mat

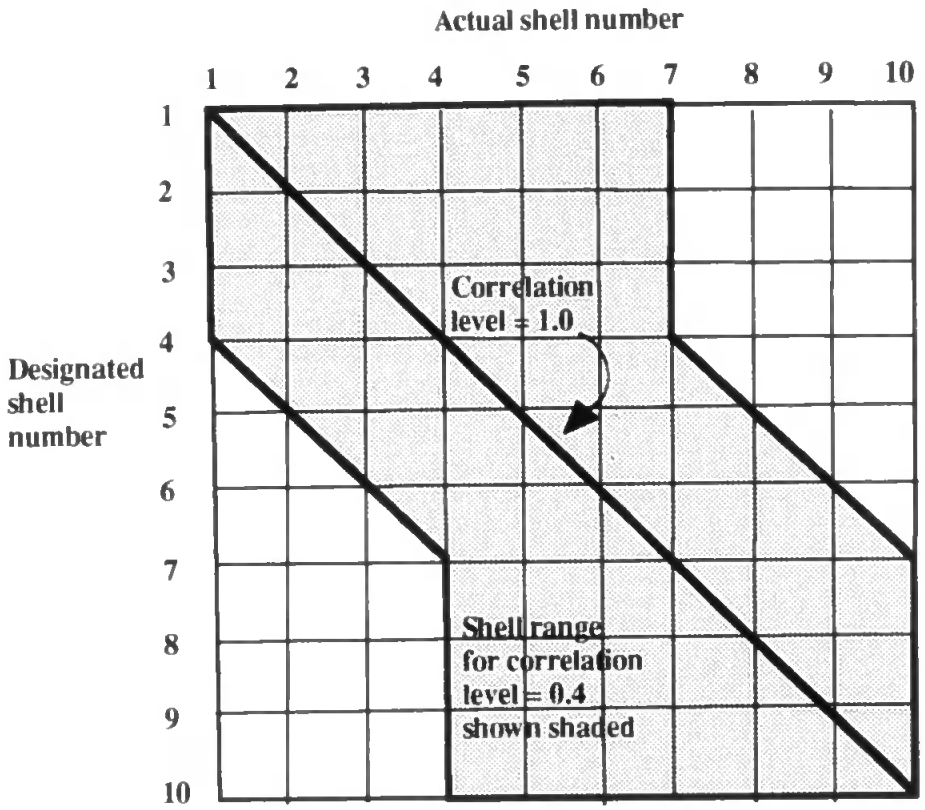

Figure 2.8 Throat shell ranges in spheres

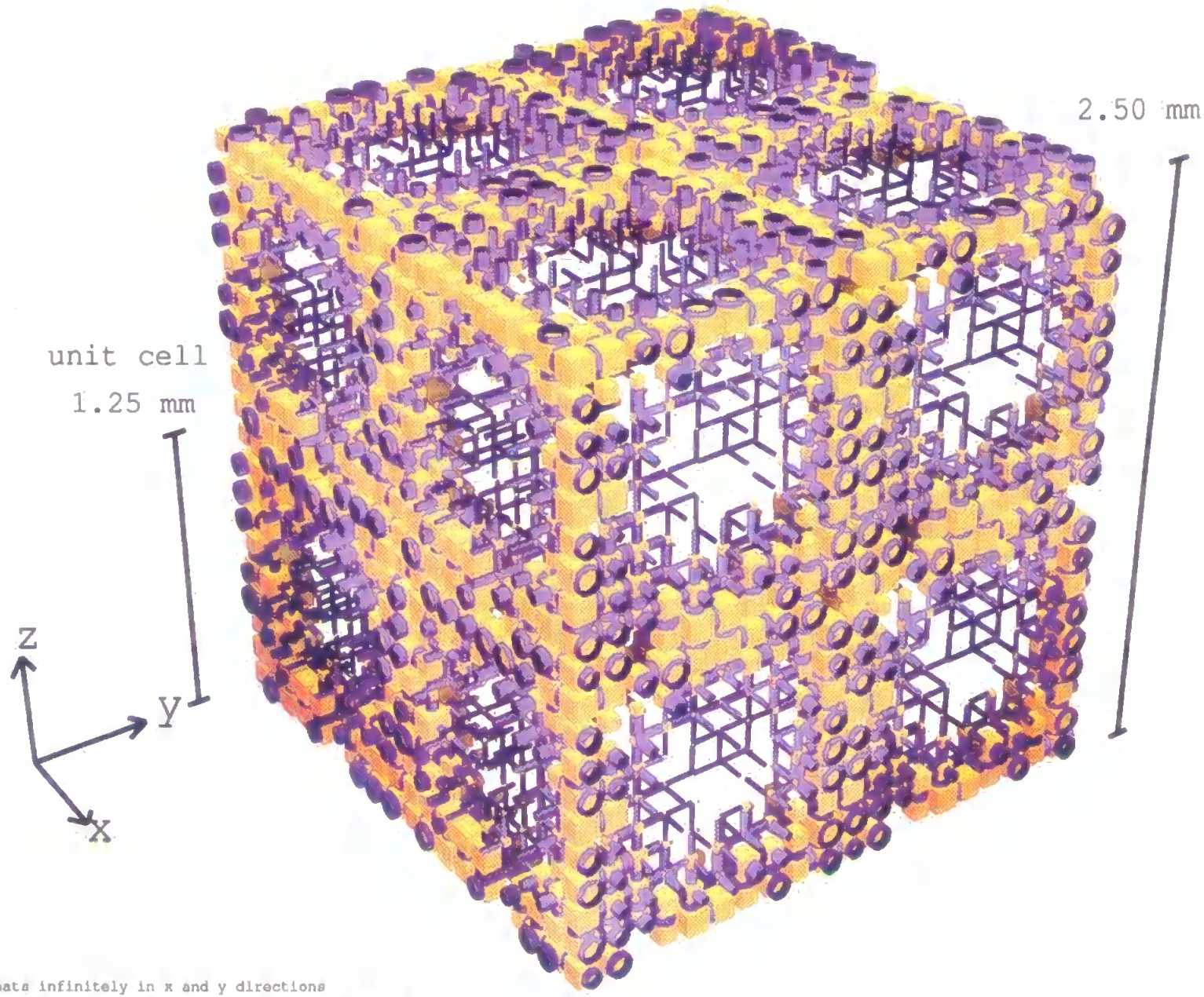

Figure 2.9 Totally correlated unit cell with small pores and throats in the centre repeating to a cubic size of 2.5 mm

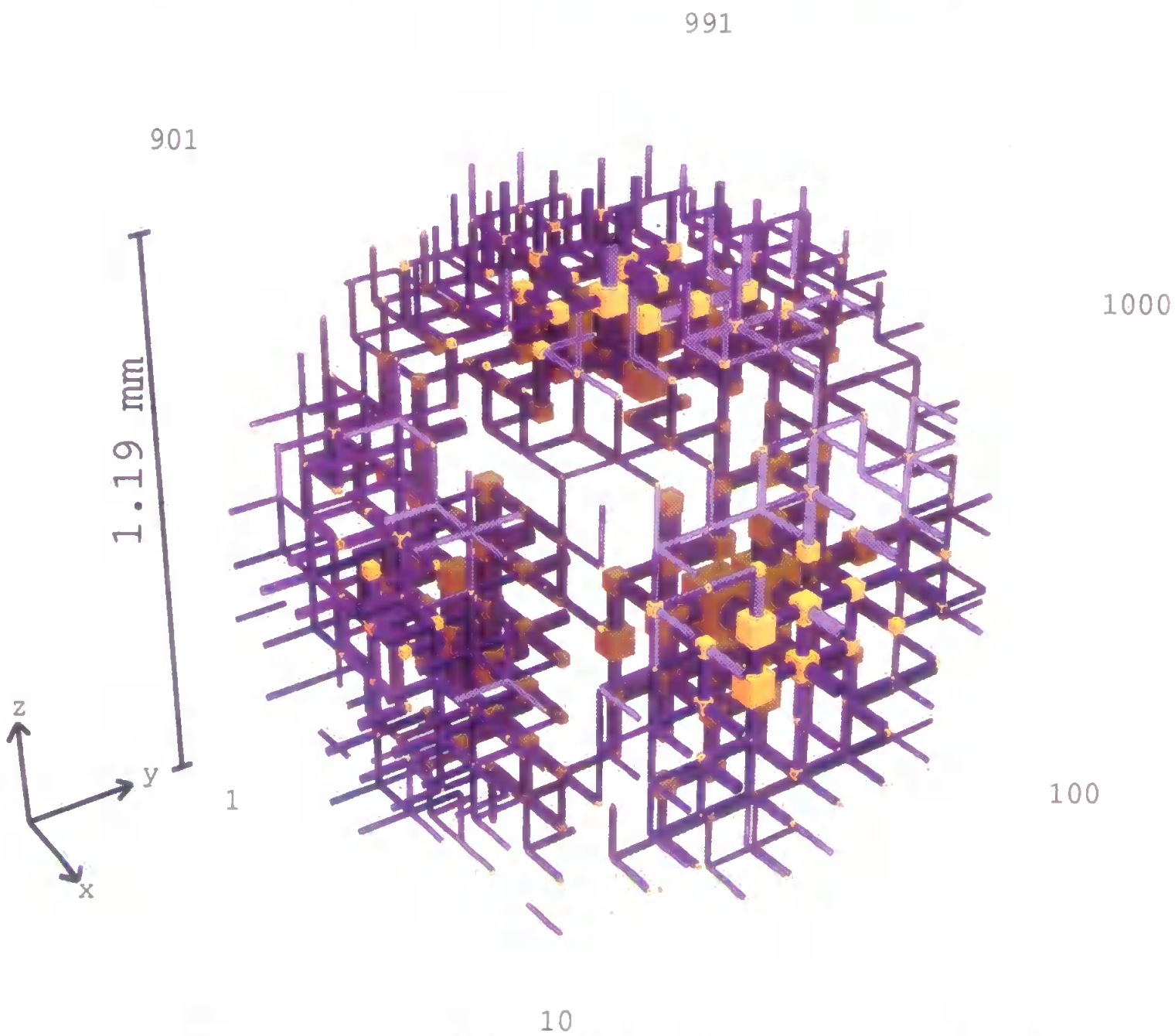

Figure 2.10 Totally correlated unit cell with large pores and throats in the centre

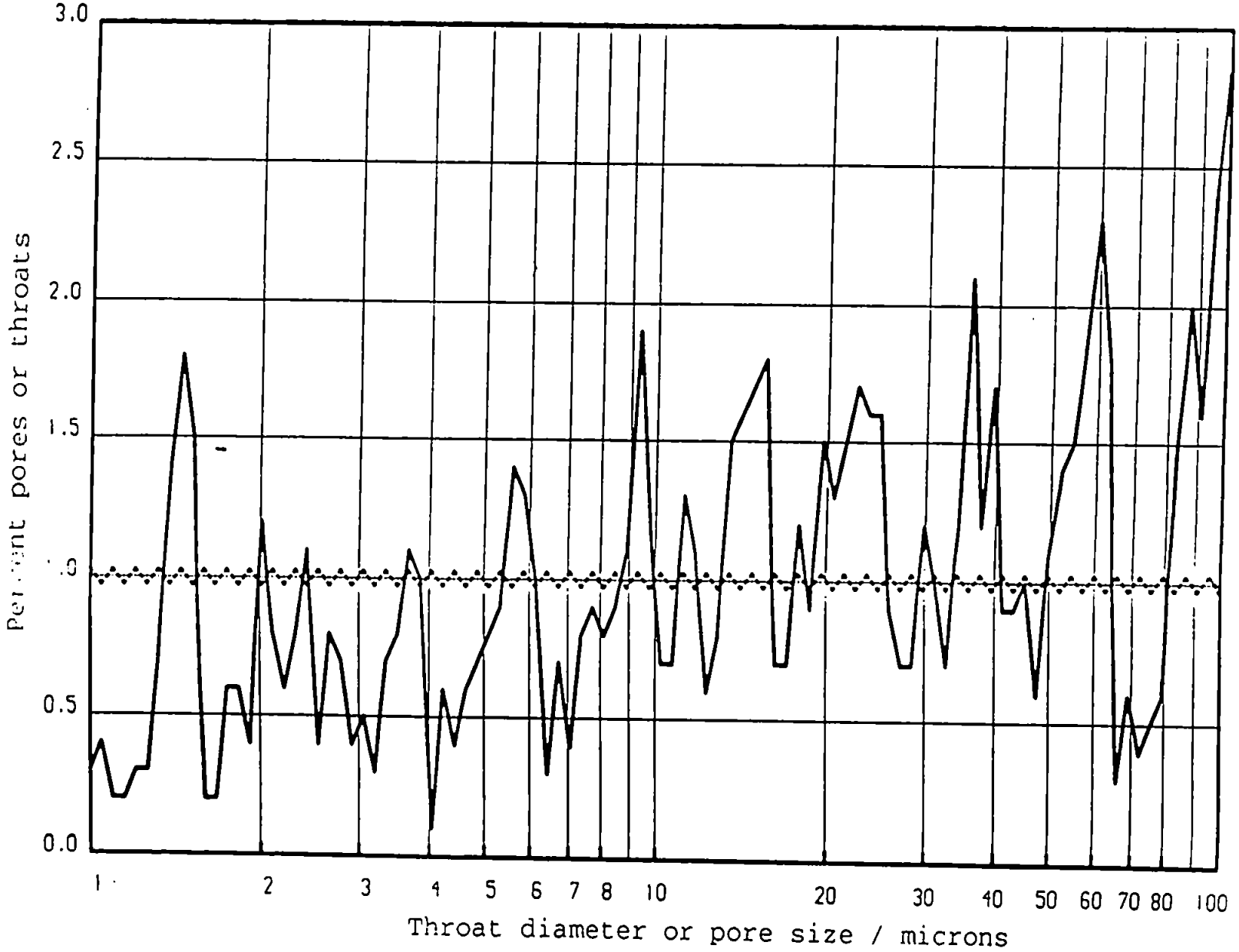

Figure 2.11 Throat diameter distribution with pore size distribution for a totally correlated structure with large pores and throats in the centre: —— pores, ----- throats

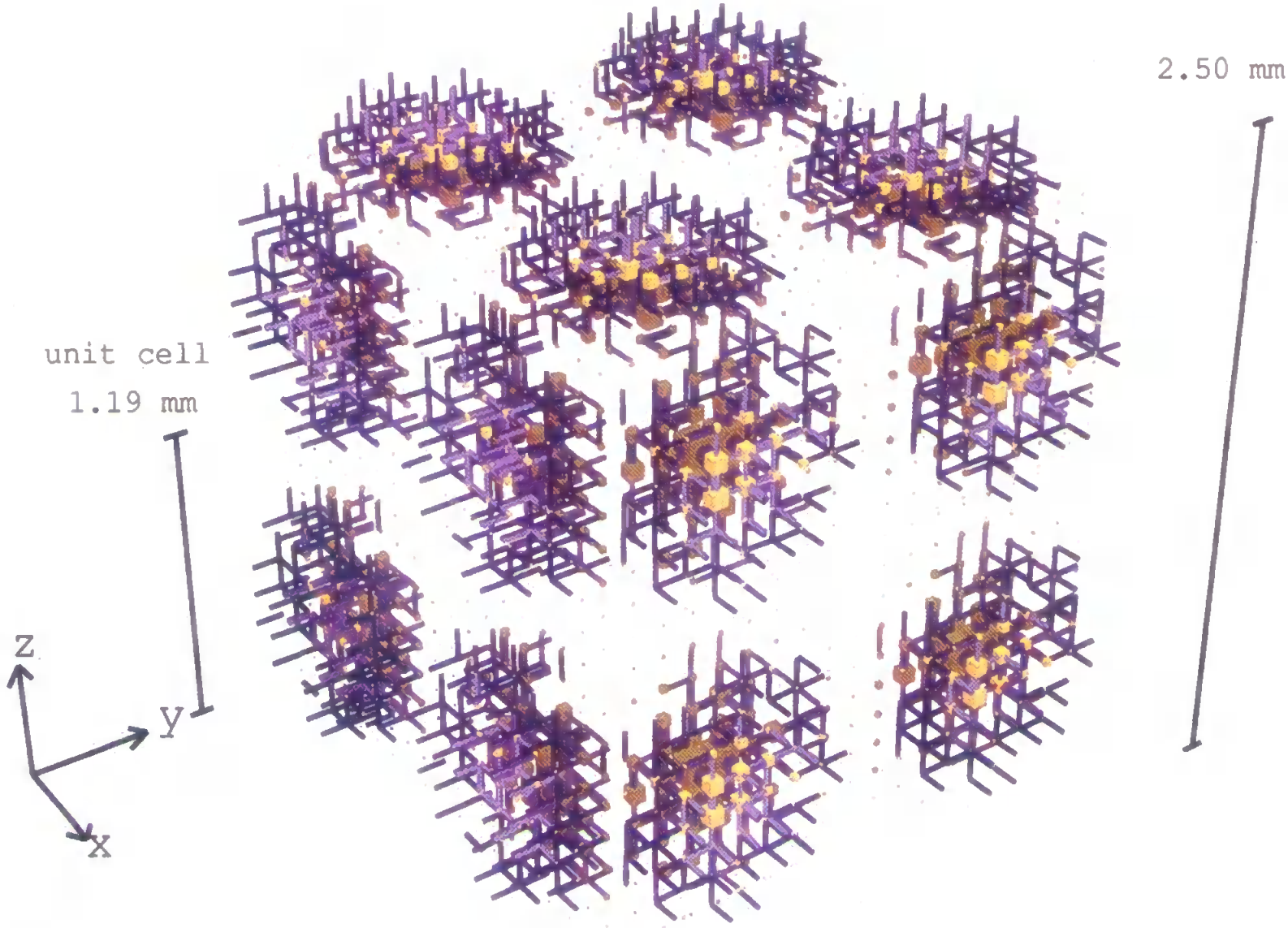

Figure 2.12 Totally correlated unit cell with large pores and throats in the centre repeating to a cubic size of 2.5 mm

structure the throat diameters can be adjusted to model the non-wetting phase intrusion curve, but the pores are all of a maximum size, i.e. equal to the largest of the throat sizes as can be seen in Fig. 2.13.

2.3 Automatic convergence onto experimental intrusion data

In this section, four methods are described in which more powerful programming procedures have been applied. Instead of the initial tedious manual method in which a range of skew and connectivity values had to be tried out, much faster automatic procedures have been introduced to find those values giving the best simulation curve. The first method fits the curve at the point of inflection by adjusting the skew and using a fixed connectivity; the other three methods run through a range of skew and connectivity values and calculate the least squares deviation between the simulated and the experimental curves. The least-squares values are stored in a file and then can then be used, if required, to produce a contour plot, the minimum of which shows the curve which best fits the experimental. For each method, the porosity of the simulation matches the experimental porosity to within 0.1 %.

2.3.1 *Fitting the mercury intrusion curve solely at the 50 % pore volume point*

The simplest method of fitting the mercury intrusion curve is to optimise only a single variable parameter. The variation of skew has been chosen, with the connectivity arbitrarily fixed at 3.5. The only criterion for fit is that the deviation, $\Delta_{50\,\%}$, between the throat diameters for the simulation and experimental curves must lie within 3 % of the total logarithmic range of the graph, at the point where 50 % of the available pore volume has been filled with mercury. This is called the 50 % method; the fit criterion may be expressed as:

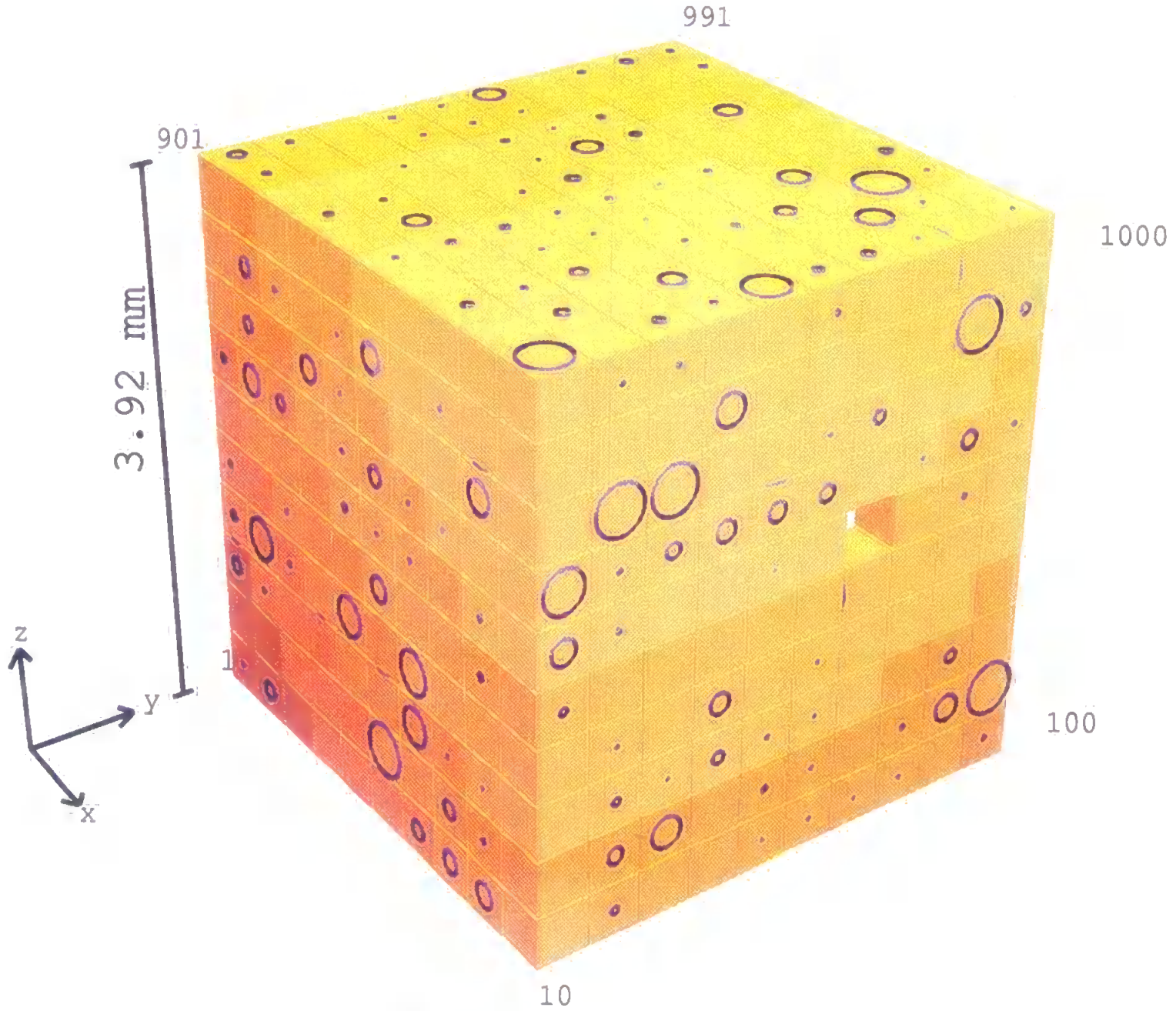

Figure 2.13 Unit cell for fibrous mat

$$\Delta_{50\%} = | \log d_{sim(V=50\%)} - \log d_{exp(V=50\%)} | \quad [2.2]$$
$$< 0.03 (\log d_{max} - \log d_{min})$$

Initially an unskewed throat diameter distribution is used. A second approximation is then made, using a skew of either 0.50 % or 1.50 %, whichever is expected to give the closer fit. A linear interpolation / extrapolation algorithm is then used to obtain a third, best-fit, skew. Further iterations are possible, but for all the samples described in this work, three have been adequate.

2.3.2 *The regular spacing algorithm*

To improve the fit between the simulated and experimental curves, they must be compared not only at the 50 % pore volume point, but also at other positions. One way to do this is to calculate the horizontal difference between them at spaced intervals along the vertical pore-volume axis. This difference represents the divergence between the throat diameters at a particular percentage of pore volume intruded. For each complete run through the optimisation procedure, there must be the same relative weightings of the deviations over different portions of the curves; the easiest way to achieve this is to have the comparison points evenly spaced along the pore-volume axis. There is a problem in that experimental measurements from mercury porosimeters are not usually evenly spaced along the pore-volume axis. An interpolation algorithm could be used to produce an evenly spaced set of points, V_i, V_{i+1}, ..., but this would introduce inaccuracies because the shape of the experimental curve, and hence the appropriate interpolation algorithm, is unknown. A compromise method is employed. Experimental measurements are used whenever possible, but if the pore volume spacing is outside set limits points are either removed or linearly interpolated. The limits are arbitrarily set at a half of, and twice, the

spacing along the pore-volume axis that would have existed if the experimental points had been evenly spaced:

$$\frac{V_{tot}}{2n} < |V_i - V_{i-1}| < \frac{2V_{tot}}{n} \qquad [2.3]$$

where V_{tot} is the volume intruded at the highest experimental pressure, and n is the total number of experimental points. A flow diagram for the selection and calculation of comparison points is given in Fig. 2.14.

Once obtained, the same set of comparison points is used for each simulation of a particular experimental curve. The horizontal difference between experimental and simulation i.e. the difference in Washburn throat diameter, is determined at each appropriate pore volume. Two different measures of deviation are used: the linear deviation, Δ_{lin}, and logarithmic deviation, Δ_{log}, can be defined as:

$$\Delta_{lin} = \frac{\sum_{i=1}^{n} (d_{exp(V_i)} - d_{sim(V_i)})^2}{n} \qquad [2.4]$$

$$\Delta_{log} = \frac{\sum_{i=1}^{n} (\log d_{exp(V_i)} - \log d_{sim(V_i)})^2}{n} \qquad [2.5]$$

The minimisation of Δ_{lin} using the skew and the connectivity is referred to as the linear method, and the corresponding minimisation of Δ_{log} as the logarithmic method. The linear method might be expected to give the most realistic model, and to be most useful for the simulation of other properties such as permeability. However, on the comparison graphs presented in this work, which use logarithmic scales of throat diameters, the linear method

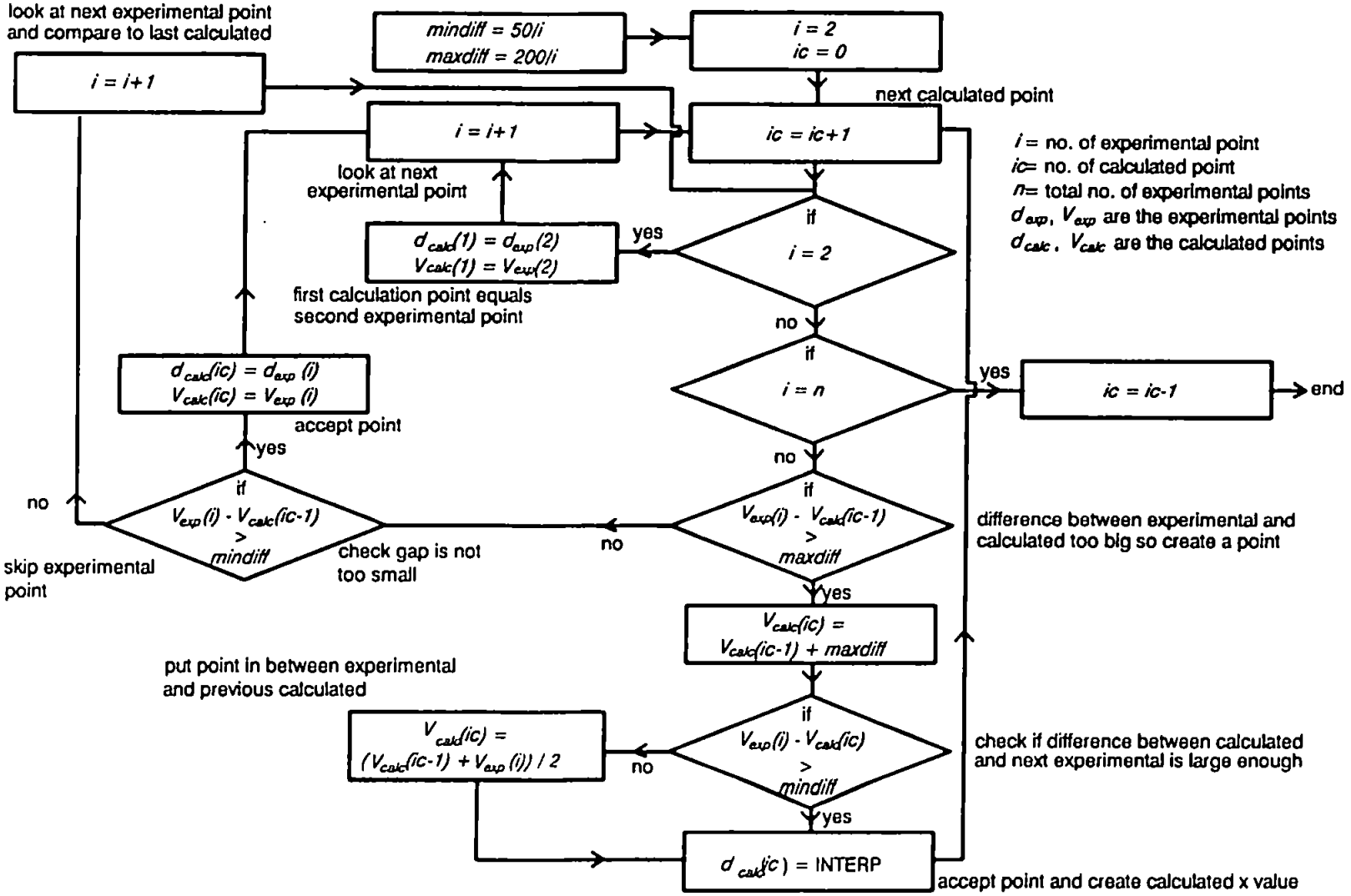

Figure 2.14 Experimental data point selection and interpolation algorithm

appears to give undue weighting to deviations at low pore volume and large throat diameter. The logarithmic method, however, corresponds to the best fit over the whole curve on a logarithmic scale, i.e. the fit that one would tend to perform visually. The reduced statistical weighting which the logarithmic method gives to the fit of large throat diameters, relative to the linear method, is also in accordance with the allowance for edge corrections.

One approach to the edge effect problem (Matthews *et al.* 1995a), is to carry out a straightening and truncation of the intrusion curve below the point of inflection, but the changing of the experimental curve involves a considerable degree of arbitrary subjectivity and cannot account for subtle internal void-space effects in the presence of large edge effects that perhaps have occurred during sample preparation. Because of this a fourth criterion of fit has been used, the 'linear top fit', based on the linear least squares deviation between the experimental and interpolated points above the median point in the equi-spaced experimental curve. This type of fit was developed to model samples where the lower end of the mercury intrusion had been greatly influenced by edge effects.

As can be seen the various fitting methods have different uses, and it is the operators choice as to which type of fitting method will be most appropiate.

2.3.3 *Fitting the mercury intrusion curve using multiple comparison points*

In the 50 % method it is the connectivity that is fixed. In contrast, when using the linear and logarithmic methods, two parameters are varied, the connectivity and the skew. These two parameters have different effects on the simulated curves, as previously discussed and shown in Figs. 2.3 and 2.4. However, in both the linear and logarithmic methods, the skew value that will be a suitable centre for the range of skews to be tested is still found by using the 50 % method. The total skew range is then set as this central

value ±0.70, at intervals of 0.10. The total connectivity range tested is 2.6 to 4.0, at intervals of 0.1. In practice, the lower limit of connectivity is often above 2.6, because connectivities cannot be accepted which cause the formation of isolated pore and throat systems. The method currently being used involves simulating the intrusion curve for every combination of skew and connectivity in the specified ranges. This can take an appreciable length of time (10 minutes on a 25 Mips workstation) and work is in hand to incorporate a Simulated Annealing / Simplex method to speed up the process.

CHAPTER 3

MODELLING OF HYSTERESIS, PERMEABILITY AND TORTUOSITY

Pore-Cor allows the simulation of other properties of porous materials, notably hysteresis, permeability and tortuosity. Hysteresis is the phenomenon that the drainage of mercury from an intruded sample does not follow the same volume/pressure curve as the intrusion prior. Permeability has proved to be one of the more difficult parameters to simulate accurately but, although the attainable precision is not all that could be desired, it is nevertheless perfectly possible to use the obtained values to establish clear trends across ranges of similar samples. Tortuosity is a difficult parameter to measure accurately, but it can be assessed from the Pore-Cor model by making a series of random walks from the upper to the lower surface of the unit cell.

3.1 Hysteresis

3.1.1 *Hysteresis in mercury porosimetry*

At a sufficiently high applied pressure, mercury intrudes all of the accessible pore space within a sample. However, if the applied pressure is then decreased, more mercury stays in the sample at any particular pressure than the amount specified by the intrusion curve, and there is a residual amount of mercury trapped even at the lowest possible applied pressure. These effects are referred to as hysteresis and residual saturation respectively, and are labelled on Fig. 3.1, which shows these effects for the reservoir sandstone sample 212B.

Hysteresis in mercury porosimetry can be compared to the recovery efficiency of oil from a reservoir after displacement by a water flood (Wardlaw *et al.* 1979). Neglecting any wettability effects, the amount of residual oil that remains trapped on a microscopic scale depends on the pore-to-pore displacement capability, which in turn depends on the

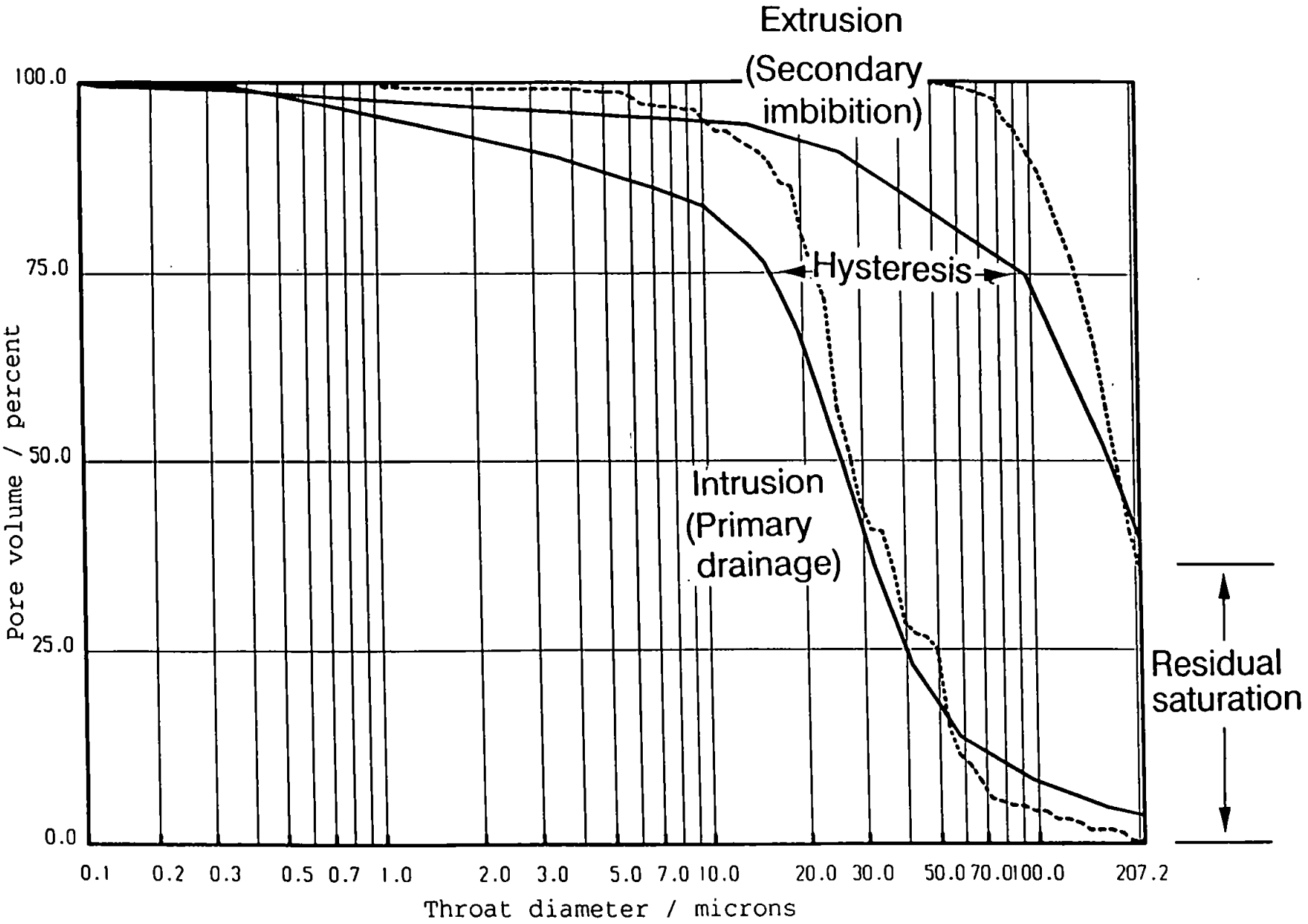

Figure 3.1 Mercury intrusion and extrusion hysteresis for sample 212B: —— experimental, ----- simulation

pore size distribution, the connectivity between pores and the ratio of pore size to throat diameter. Although mercury porosimetry and the flooding of a core by water differ, not least because of the fluids involved, it is possible that data obtained for the trapping of mercury may be usefully applied to the trapping of oil, providing the oil/water system is strongly water-wet (Wardlaw *et al.* 1979).

During the flooding of an oil reservoir by water, it is thought that oil may cease to flow during water displacement because the continuity of the oil is broken. The oil then occupies discrete regions, the volume of which should be proportional to that of the mercury in a mercury porosimetry experiment following secondary imbibition. Results from Pickell *et al.* (1966) support this possibility.

There are various causes of the hysteresis between primary drainage and secondary imbibition mercury porosimetry curves, which are now discussed.

3.1.2 *Structural hysteresis in individual pore and throat chains*

As a non-wetting phase intrudes, the pressure at which any given throat is intruded is controlled by the throat radius. However, the removal of mercury from pores, which is secondary imbibition, is controlled by the size of the pore rather than of the throat. This can be explained by considering Fig. 3.2, which shows a series of cylindrical pores and throats in a single chain. The network is exposed to mercury, to which a pressure P is applied. For simplicity in this explanation, it is assumed that eqn [1.2] is valid. The pressure is increased until it exceeds $1470/d_1$, whereupon the capillary forces within the throat of diameter d_1 are overcome. This throat is then filled; so also is the pore of diameter d_2 whose capillary resistance is less than that of the throat. When the applied pressure reaches a value of $1470/d_3$, the next throat, of diameter d_3, will fill.

Subsequent decrease of the applied pressure causes withdrawal of the mercury and imbibition of the nominal wetting phase. As the pressure decreases below $1470/d_3$, the

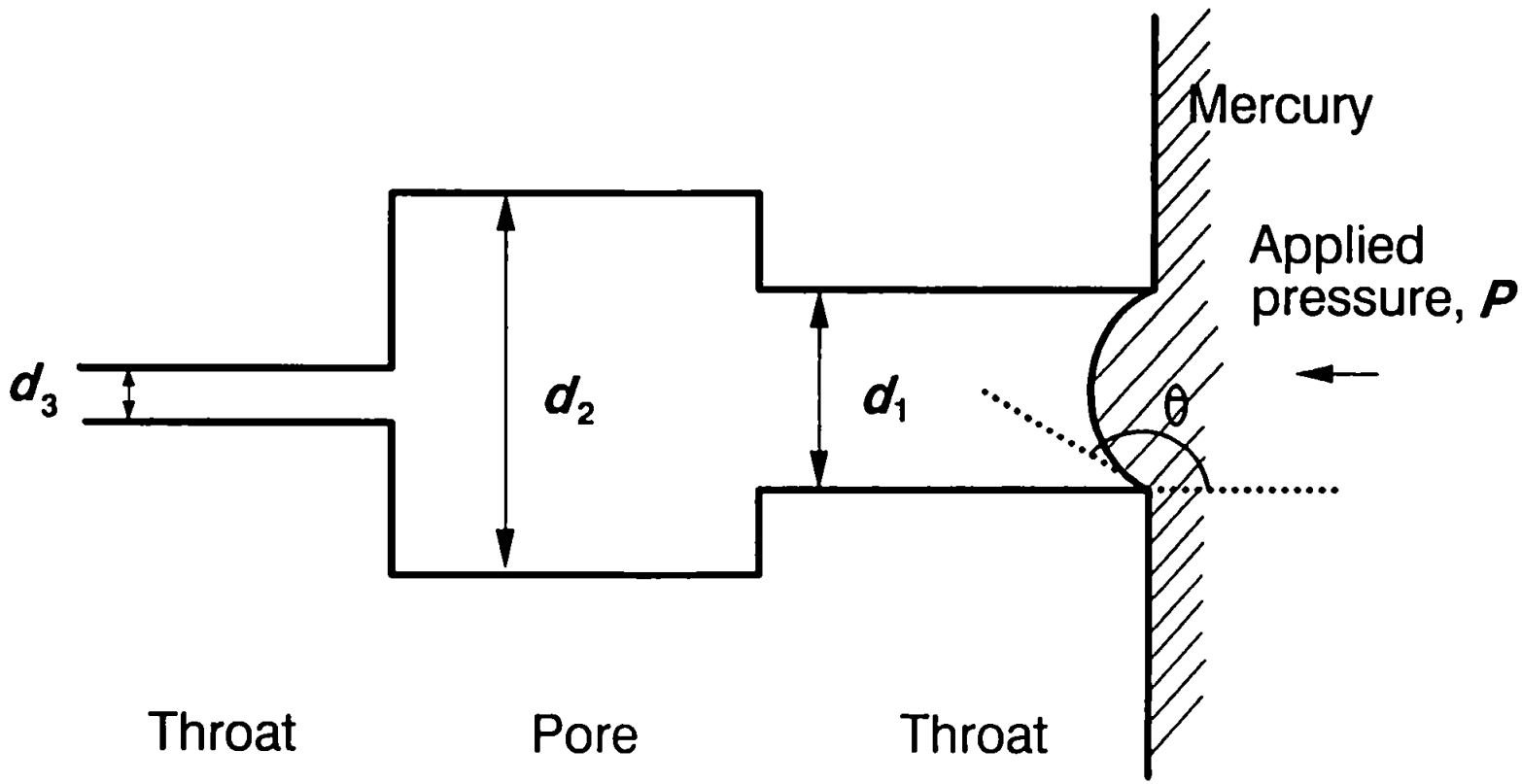

Figure 3.2 A one-dimensional pore and throat network

throat of diameter d_3 will empty back into the pore, and an equivalent amount will extrude to the outer surface. Next to empty is the pore of diameter d_2, which empties when the pressure falls to less than $1470/d_2$. However the higher pressure of $1470/d_1$ was required to fill this pore. The fact that the pore required a high pressure to fill it, whilst a much lower pressure was required to empty it is the phenomenon of hysteresis.

3.1.3 *Snap-off*

There is another complication which occurs during withdrawal of the mercury. If d_2 is very much larger than d_1, it is difficult for the mercury to re-adjust its shape to extrude from the large pore through the narrow throat. Wardlaw *et al.* (1981) have photographed this effect in glass micro-models of pore and throat chains. Trapping occurs when the ratio R of pore size : throat diameter is greater than 6. Trapping in the larger pores of sandstone has been verified experimentally by Chatzis *et al.* (1981). Wardlaw *et al.* (1979) calculated values of R for some 27 sandstone samples. They took the throat diameter d_1 to be that value corresponding to 50 % mercury saturation of a sample from the primary drainage curve of the sample, and they measured the pore size d_2 directly from resin pore casts. Despite the errors associated with mercury porosimetry they obtained values of R ranging from 3 to 94. Their mean value was 11 because they felt that 94 was anomalously high. Wardlaw *et al.* (1987) measured R for Berea sandstone as 7.3 with a possible range upto 86.3. They also obtained R values for Indiana limestone ranging from 4.8 to 148.7.

The reasons for this R-dependent trapping effect have been given a possible explanation by Dawe *et al.* (1978). When an interface travels though an irregularly shaped channel, its meniscus must adopt non-equilibrium shapes. However, the meniscus is always trying to achieve its minimum energy configuration, which can only be achieved by a change in shape which must be sudden. The liquid therefore does not flow uniformly

but moves between pores in jumps known as Haines jumps. For a certain value of R this attainment of minimum energy may result in 'snap-off' of the mercury column. The wetting phase which will have been compressed and possibly occluded in surface undulations or micro-pores during imbibition, can re-expand and act as the seed of such snap-off phenomena. Li *et al.* (1986b, 1986c) have also used glass micromodels to study other pore and throat arrangements of various shapes, explaining their observed effects in terms of theories involving geometry and wetting behaviour.

Snap-off, and consequent trapping, can also occur because of the structure of an interconnected network. For non-wetting phase to empty there must be a continuous unbroken line of non-wetting phase to the outside surface. Consider the two-dimensional network shown in Fig. 3.3. By the time the pressure has dropped sufficiently for pore A to empty, its neighbouring pores B, C and D will have already emptied as they are smaller. There is now no inter-connected route for mercury to escape from A to the surface, so that it will remain trapped. In three-dimensional networks, as presented in this work, the routes available for escape are more complicated, and the trapping effects more subtle than those shown in Fig. 3.3.

3.1.4 *Correlation of pore and throat sizes*

It is evident from the preceding discussion that the relative sizes of adjacent pores and throats affect intrusion and withdrawal. Therefore if these sizes are correlated, i.e. there are regions of large pores and throats together, or small pores and throats together, either as clusters or bands, there is likely to be an effect on intrusion and hysteresis. Constantinides *et al.* (1989) have found that pore size : throat diameter correlation, but with no pore size : pore size correlation in the sense of local clustering of pores of similar size, has only a weak effect on mercury intrusion. However they found that pore size clustering together with pore size : throat diameter correlation had a strong effect on the

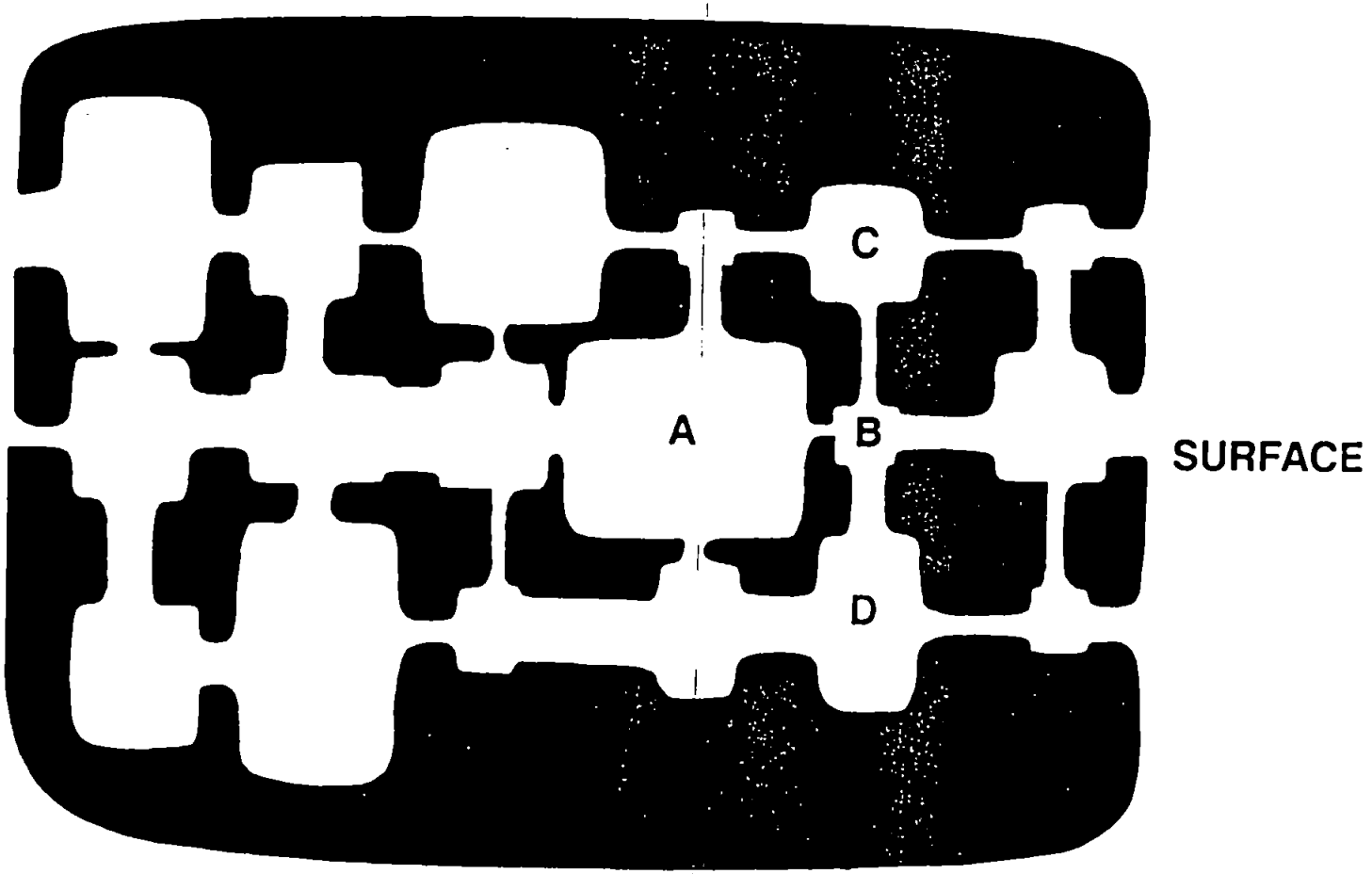

Figure 3.3 A two-dimensional pore and throat network

extrusion curves, spreading them over a wider range of pressures. Li *et al.* (1986a, 1990) demonstrated analytically, for a linear throat size distribution, how correlation effects reduce shielding, thus causing intrusion at lower pressure and a reduction of entrapment during secondary imbibition. Wardlaw (1990) also showed that this effect occurred in multiple intrusion / extrusion scanning loops.

In the present work, the pore and throat sizes are correlated by setting the size of each pore equal to the diameter of the largest throat entering it. It has been shown in a previous work (Spearing *et al.* 1991b) that this produces a pore size : throat diameter correlation similar to that for sandstone, but different from that of other types of porous media such as limestone (Wardlaw *et al.* 1987). The effects of other types of correlation on both mercury intrusion and permeability have been simulated, and the results published (Matthews *et al.* 1995a).

3.1.5 *Dead-end pores*

Structural hysteresis is also caused by dead-end or 'ink bottle' pores, which are pores with only one throat. Indeed, in many fields, dead-end pores are considered to be the only cause of hysteresis. During intrusion, the dead-end pores fill with non-wetting phase. During imbibition of the wetting phase, a situation arises where wetting phase has reached the throat of a dead-end pore. However, it can only enter the dead-end pore by surface flow down the walls of the throat accompanied by withdrawal of the non-wetting phase through the middle of the throat. This process does not usually occur, and therefore dead-end pores cause trapping of the non-wetting phase. The percentage of dead-end pores increases as the connectivity decreases, and hence the relative effect of dead-end pores rises with decreasing connectivity.

3.1.6 *Contact angle hysteresis*

There is much evidence in the literature for contact angle hysteresis, i.e. a difference in contact angle dependent on whether the mercury is advancing during intrusion, or receding during wetting phase imbibition (Bell *et al.* 1981; Kloubek 1981). The angle commonly used in the analysis of mercury porosimetry curves is 140° for both the advancing and receding angle. However, the magnitude of the contact angle has a substantial effect in the analysis of mercury intrusion and extrusion by means of the Laplace equation. Van Brakel *et al.* (1981) have shown in principle that irreversible penetration of mercury may be caused solely by contact angle hysteresis. A possible explanation is given by Wardlaw *et al.* (1976). The mercury intruding into an advancing mercury meniscus tends to clean the meniscus because of the surface expansion, but on withdrawal, impurities may accumulate at the meniscus because of its contraction. It is well known from laboratory experiments using the tilting-plate method for contact angle measurement, (Shaw 1986), that impurities in the liquid or roughness of the surface that the liquid is advancing or receding across, may contribute to hysteresis.

There are many different estimates in the literature of the magnitude of contact angles, which have been summarised by Good *et al.* (1981). Advancing angles of 180° have been quoted for mercury in sandstones, whereas Dunmore *et al.* (1974) and Kloubek (1981) found an advancing angle of 138.4° and a receding angle of 127.4° on smooth quartz.

The processes occurring during secondary imbibition have been explained previously. An algorithm has been developed to simulate these processes, the results of this are presented. The simulation has been kept simple, and deviations between simulation and experiment are discussed in the context of the simple model.

3.1.7 *Simulation*

In order to simulate the secondary imbibition processes, a computer algorithm was originally written by Dr. Michael Spearing. In this work, the routine has been implemented in conjunction with the regular spacing algorithm, applied to sandstone samples and investigated and explained for publication purposes (Matthews *et al.* 1995b).

For convenience in the algorithm , the decreasing applied pressure was converted to a series of increasing Washburn diameters using eqn [1.1]. These diameters were assigned to the program variable *hgsize*. Then two assumptions were made. Firstly, imbibition was entirely determined by the sizes of pores, not throats. Secondly, no withdrawal of mercury occurred anywhere until *hgsize* increased to a value equal to the diameter of the smallest pore on the bottom layer of the unit cell (remembering that mercury is applied to the top layer). These assumptions are shown in the flow diagram of the algorithm, see Fig. 3.4. Also shown are the stages at which tests are made to see if pores will empty. The conditions for such emptying are:

(i) The applied mercury pressure must be below that required to intrude the pore, as determined by the Washburn equation, eqn [1.1].

(ii) There is a connected route for withdrawal of the non-wetting phase back to the plane of injection, modelled by a filled throat-pore-throat-pore system adjacent to the pore in question.

(iii) The pore size relative to its throat diameter is below the ratio which causes snap-off, as described above.

Displacement of mercury from a void was assumed to be complete and piston-like; no fractional emptying was modelled. Dead end pores, described previously, were not included in the modelling, since sufficient trapping occurs without invoking them.

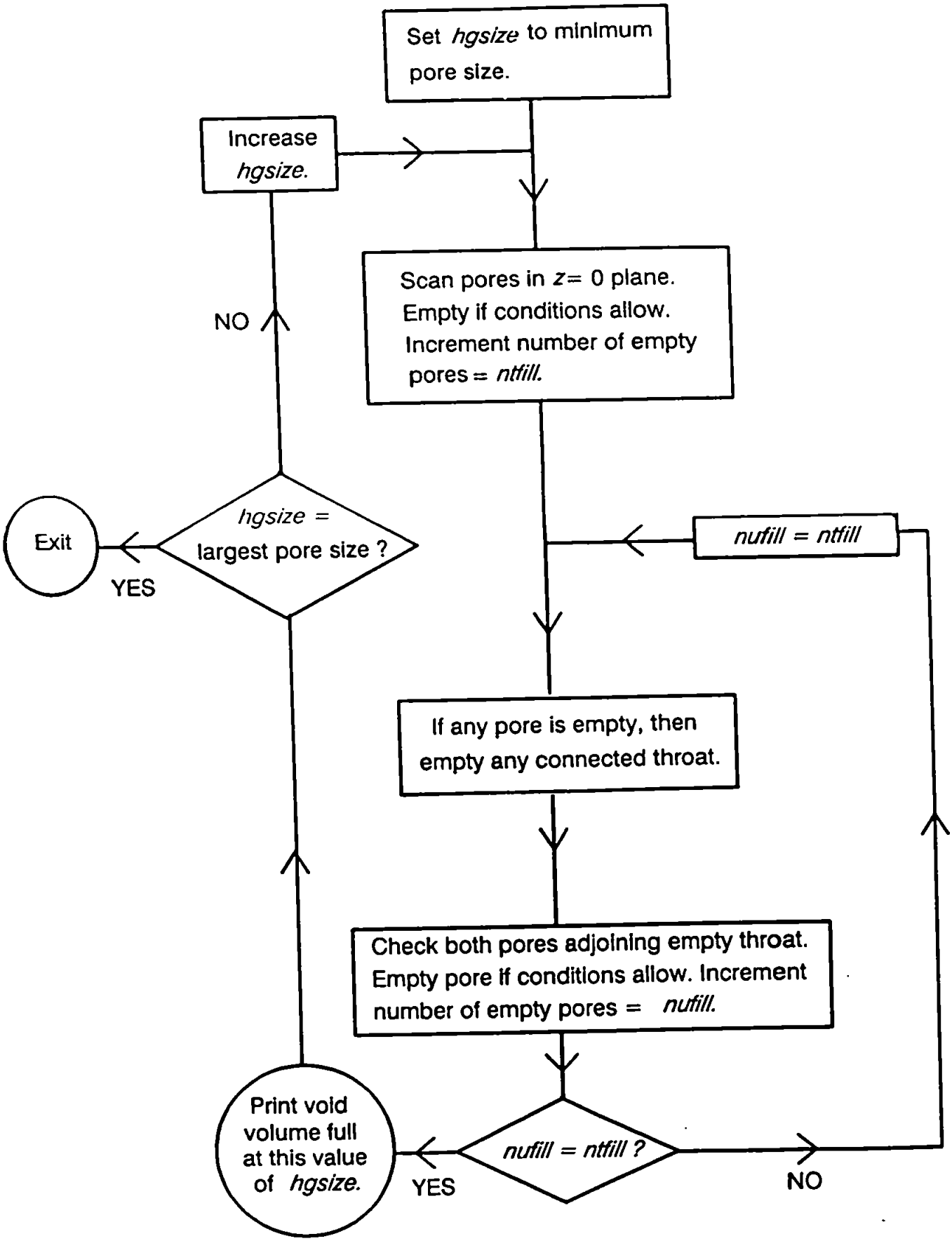

Figure 3.4 Hysteresis algorithm

3.2 The calculation of permeability

A long-standing problem in the study of porous media has been the question of how to calculate the permeability of a solid from a knowledge of the geometry of the void space within it. The absolute permeability k of a porous solid is traditionally defined in terms of Darcy's law. With reference to a cell of the solid of unit volume, this may be written:

$$\left(\frac{dV}{dt}\right)_{cell} = -\frac{k A_{cell}\,\delta P_{cell}}{\mu\, l_{cell}} \qquad [3.1]$$

where $(dV/dt)_{cell}$ is the volumetric flow rate through the cell of cross sectional area A_{cell} when a pressure drop δP_{cell} is applied between the upper and lower surfaces of the cell , which are l_{cell} apart, for a fluid of viscosity μ. Many attempts have been made to calculate k from primary parameters such as the lengths, positions and diameters of the pores and throats. Other workers have described equations based on such characteristics as porosity, the total externally-accessible surface area per unit volume of the solid, the characteristic throat diameter d_c (often loosely referred to as the characteristic pore diameter), the tortuosity τ, and the formation factor F (Matthews *et al.* 1993). One of the most successful attempts to date is the equation of Thompson *et al.*(1987):

$$k = \frac{1}{226}\frac{d_c^2}{F} \qquad [3.2]$$

This predicts permeabilities correct to a factor of 7 for a range of sandstone and limestone samples covering several orders of magnitude of experimental permeability.

An incompressible fluid flowing through a tube takes up a parabolic velocity profile, with maximum flow rate down the centre of the tube. If the flow at the walls is assumed to be zero, integration over the velocity profile yields the Poiseuille equation:

$$\left(\frac{dV}{dt}\right)_{tube} = -\frac{\pi r_{tube}^4 \delta P_{tube}}{8 \mu l_{tube}} \qquad [3.3]$$

in which $(dV/dt)_{tube}$ is the volumetric flow rate, r_{tube} is the radius of the tube and $\delta P_{tube} / l_{tube}$ is the pressure gradient along the tube. Poiseuillian flow has been shown to occur for oil displacement in capillaries down to 4 μm in diameter (Templeton 1954).

If we now assume that Poiseuillian flow occurs across the whole cell in the negative z direction, i.e. from the top to the bottom face of the unit cell in Fig. 1.3, then

$$\left(\frac{dV}{dt}\right)_{cell;-z} = -\frac{\pi}{8\mu} \Omega \left(r_{tubes;z}^4\right)_{cell} \frac{\delta P_{cell}}{l_{cell}} \qquad [3.4]$$

where Ω is an averaging operator over the whole unit cell operating on the fourth power of the individual radii $r_{tube;z}$ of all tubes lying parallel to the z axis. It is calculated by means of the Dinic network analysis algorithm. Ω is defined in such a way that eqn [3.4] is satisfied, and generates a term which is related to the effective Poiseuillian capacity of the cell for flow in the negative z direction. Since, at this stage of the calculation, all the tube lengths $l_{tube;z}$ are identical and $l_{tube;z} = l_{cell} / \beta$, where β is the number of tubes in the z direction in the unit cell (in this case 10), these lengths can be included in the averaging function, so that

$$\left(\frac{dV}{dt}\right)_{cell;-z} = -\frac{\pi}{8\mu} \Omega \left(\frac{r_{tubes;z}^4}{\beta\, l_{tubes;z}}\right)_{cell} \delta P = -\frac{\pi}{8\mu} \Omega \left(\frac{r_{tubes;z}^4}{l_{tubes;z}}\right)_{cell} \frac{\delta P}{\beta} \qquad [3.5]$$

By considering tubes in the $\pm x$ and $\pm y$ directions as well, and comparing with the Darcy equation, eqn [3.1], it follows that

$$k = \frac{\pi}{8\beta}\,\Omega\left(\frac{r_{tube}^4}{l_{tube}}\right)_{cell}\frac{l_{cell}}{A_{cell}} \qquad [3.6]$$

Once this equation is corrected for the square cross-section of the pores, and for slip flow Matthews *et al.* (1993) the permeability may be calculated. The permeability unit is microdarcy: 1 μD = 9.87 x 10^{-19} m^2.

3.3 Tortuosity

Tortuosity has had many definitions in the literature but we have chosen the simplest (Spearing et al. 1991b). The tortuosity (T) of a porous sample is the ratio of the distance through the pore network (L_e) and the length of the sample (L), see Fig. 3.5.

$$T = \frac{L_e}{L} \qquad [3.7]$$

An algorithm to simulate this property was written by Spearing (1991b) and is included on the Pore-Cor package. Both the actual and simulated values for tortuosity have a lower limit of one, and in this work the simulated value has not been seen to rise above four. The tortuosity of the unit cell is measured by carrying out one hundred weighted random walks through it, in the ±*x*, ±*y* and negative *z* directions, starting at the top face and finishing at the bottom face. These random walks occur one at a time, whereas in reality there are a large number of diffusing gas molecules or ions moving around the structure at one time hence the algorithm tends to over estimate both tortuosity itself and changes in tortuosity. The median simulated tortuosity and the upper and lower interquartile ranges are used for comparison purposes between samples.

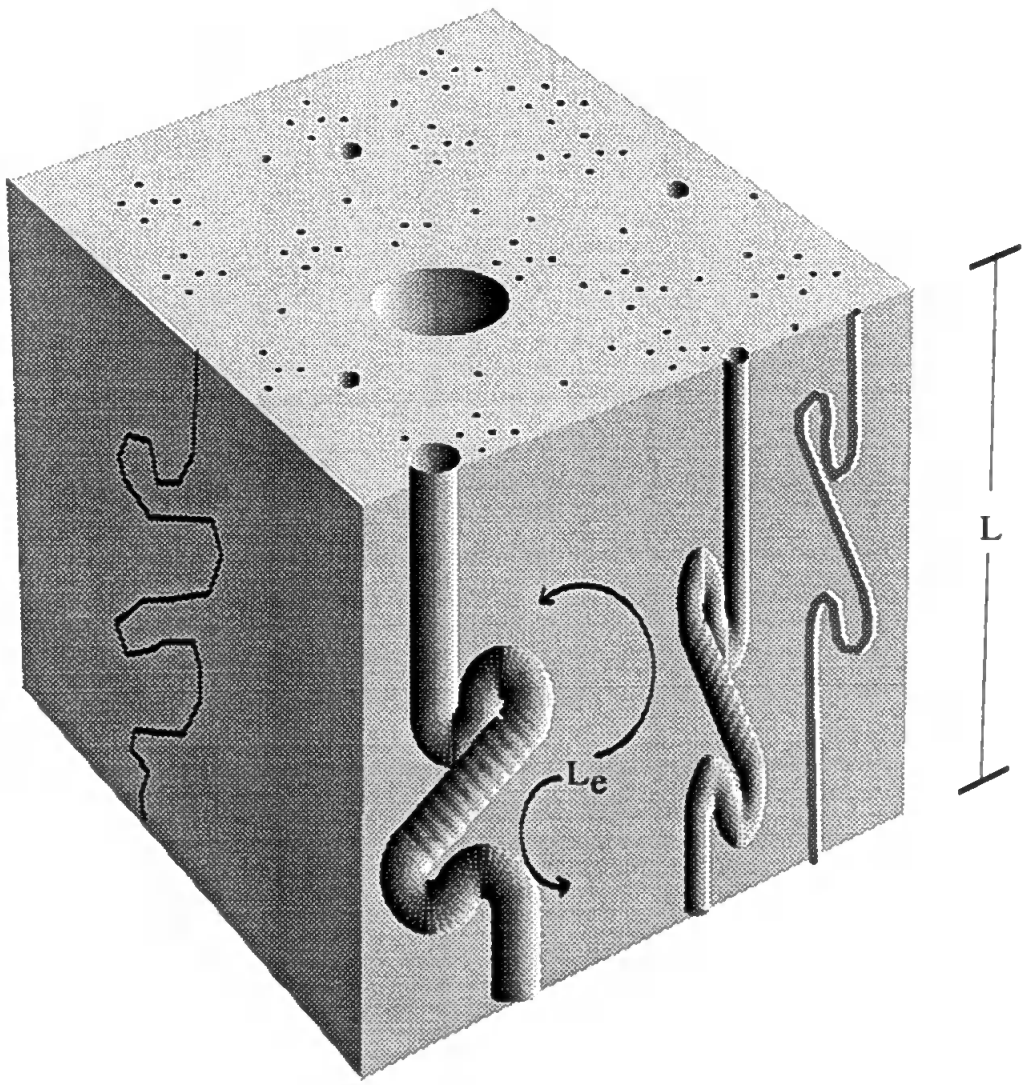

Figure 3.5 A schematic porous medium showing a tortuous capillary

CHAPTER 4

VOID SPACE MODELLING OF COMPRESSIBLE SAMPLES

More recently mercury porosimetry and computer modelling have been applied to a variety of rather specialised materials used in the paper industry. During this work it became apparent that some corrections would have to be applied to the porosimetry measurements. Paper coating materials have throat diameter distributions that range upwardly from 0.007 μm, whilst sandstones have a minimum throat diameter of about 0.12 μm. This means that the pressure that must be applied to produce penetration is approaching two orders of magnitude greater. In addition the available sample sizes are usually quite small, and the materials themselves can be compressible. In the light of these facts, it was decided that a program would have to be written that would include provisions for making additional corrections. Such a program has been written: it has been designated Pore-Comp, runs using Microsoft Excel, and the corrections which it embodies will now be described.

4.1 Correction terms for incompressible samples

The approach described in this section is an extension of that for concrete used by Cook *et al.* (1993). It allows mercury porosimeter measurements to be corrected to obtain a true measure of the increase in intruded volume with pressure.

The intruded mercury volume reading, V_{obs} , observed during a mercury porosimetry experiment is not only a measure of the volume of intrusion into the sample, V_{int} , but also contains significant contributions arising from the expansion of the porosimeter chamber or *penetrometer*, δV_{pen} , and the compression of the mercury δV_{Hg} :

$$V_{obs} = V_{int} + \delta V_{pen} + \delta V_{Hg} \qquad [4.1]$$

(Any terms such as the mercury compression, δV_{Hg}, or the sample compression as described in section 2.3, which make a positive contribution to the observed volume, V_{obs}, are given a positive sign. Small corrections to larger terms are denoted by δ.) The mercury also expands because of heat transfer from the pressurising fluid (oil), but it is assumed that this effect is the same for the sample experiment as for the blank experiment described below, and that the resultant effect is zero.

A *blank* experiment is one carried out under the same temperature and pressure conditions as the sample experiment, but with no sample in the penetrometer. The volume, V^1_{blank}, of mercury used in the blank experiment is equal to the volume of the penetrometer, V^1_{pen}, both at 1 atm pressure:

$$V^1_{blank} = V^1_{pen} \qquad [4.2]$$

(Superscripts are used to denote the value of a particular variable at a specified pressure.)

The change in the blank volume reading, δV_{blank}, is taken as zero at the lowest experimentally attainable applied pressure P. Increases in δV_{blank} with pressure are caused by the compression, δV_{Hgpen}, of the volume of mercury needed to fill the empty penetrometer, and increases in the available volume, δV_{pen}, of the penetrometer due to expansion of the glass chamber:

$$\delta V_{blank} = \delta V_{Hgpen} + \delta V_{pen} \qquad [4.3]$$

When a sample is mounted in the penetrometer, it displaces a volume of mercury, V^1_{Hgbulk}, equal to the sample bulk volume, V^1_{bulk}, at 1 atmosphere pressure. The penetrometer is loaded with mercury to the same calibration mark as for the blank experiment, and thus the total volume of mercury, V^1_{Hg}, now used in the experiment is

$$V^{1}_{Hg} = V^{1}_{Hgpen} - V^{1}_{Hgbulk} \quad [4.4]$$

The same relationship holds for the mercury expansion:

$$\delta V_{Hg} = \delta V_{Hgpen} - \delta V_{Hgbulk} \quad [4.5]$$

Eqns [4.1], [4.3] and [4.5] can be combined to yield:

$$V_{obs} = V_{int} + \delta V_{blank} - \delta V_{Hgbulk} \quad [4.6]$$

The compression, δV_{Hgbulk}, of the additional mercury volume in the blank experiment can be related to its volume, V^{1}_{bulk}, at atmospheric pressure by using a form of the Tait equation Cook *et al.* (1993). This gives an experimentally derived expression for the compression of the mercury, using a mercury compressibility of 0.40×10^{-10} Pa^{-1}:

$$\delta V_{Hgbulk} = 0.175\ (V^{1}_{bulk})\ \log_{10}(1 + P/1820) \quad [4.7]$$

in which P is in MPa (1820 MPa = 264,000 psi). (Note that eqn [4.7] has the wrong asymptote as $P \rightarrow \infty$, but is correct for the smaller pressure changes, and hence small relative compressions, considered here.)

The working equation for incompressible samples may, therefore, be derived from eqns [4.6] and [4.7]:

$$V_{int} = V_{obs} - \delta V_{blank} + 0.175\ (V^{1}_{bulk})\ \log_{10}(1 + P/1820) \quad [4.8]$$

4.2 Corrections for compressible samples

Mercury at a high applied pressure will not only intrude into a porous compressible sample, but will also compress it so as to reduce its volume by an amount δV_{sample}. Compression effects typically become important above pressures of 40 MPa (at which pressure mercury penetrates throats with diameters down to 0.04 μm), and cause an increase in apparent intruded volume. For compressible samples, eqn [4.6] becomes:

$$V_{obs} = V_{int} + \delta V_{blank} - \delta V_{Hgbulk} + \delta V_{sample} \qquad [4.9]$$

where δV_{sample} is the (positive) increase in observed mercury volume caused by the compression of the sample.

The compressibility ψ_{ss} of a homogeneous, continuous solid sample may be expressed in terms of its bulk modulus M_{ss}:

$$M_{ss} = \frac{1}{\psi_{ss}} = dP \Big/ \left(\frac{-dV_{ss}}{V_{ss}}\right) \qquad [4.10]$$

(For an incompressible sample, ψ_{ss} is zero, and M_{ss} is infinite.) However, the compression of a porous sample by intruding mercury is more complicated. If the mercury entirely surrounds the continuous solid phase, it will compress it according to eqn [4.10] above. This type of compression will occur above a pressure P^z (the *zero void pressure)* at which all the accessible void space has been intruded by mercury, up to the maximum experimentally attainable applied pressure P^{max}, provided that no other changes in the sample are induced. Increasing the applied mercury pressure P above P^z causes the continuous solid phase of the porous sample to compress from a volume of V^z_{ss} to a volume $(V^z_{ss} - \delta V_{ss})$, and the apparent volume of mercury intruded to increase by an amount δV_{ss}. Integrating eqn [4.10] to find δV_{ss}:

$$\int_{P^z}^{P} dP = M_{ss} \int_{V_{ss}^z}^{V_{ss}^z - \delta V_{ss}} -\frac{dV_{ss}}{V_{ss}} \qquad [4.11]$$

and thus

$$\delta V_{ss} = V_{ss}^z \left(1 - \exp\left[\frac{(P^z - P)}{M_{ss}}\right]\right) \qquad [4.12]$$

The zero void pressure P^z may be identified from experimental curves as the point above which the corrected intrusion curve continues to indicate an increase in intruded mercury volume, but the extrusion curve, measured during subsequent pressure decrease, is identical to the intrusion curve. The coincidence of the two curves indicates an absence of mercury trapping, and therefore demonstrates that the only cause of the corrected mercury volume increase, δV_{sample}, is compression of the continuous solid phase of the sample. (Incompressible samples show no increase in mercury volume above P^z.) Thus,

$$\text{for } P > P^z, \quad \delta V_{sample} = \delta V_{ss} \quad \text{, and} \quad \frac{dV_{int}}{dP} = 0 \qquad [4.13]$$

However, at applied mercury pressures below P^z, there are unintruded voids in the sample, and the sample can undergo an additional type of compression, δV_{su}, because of compression into this void space (Warren *et al.* 1976). Both this compression into the void space and the compression of the solid phase contribute to the increase, δV_{sample}, in the observed intruded volume of mercury, and the effects are impossible to distinguish as they proceed:

$$\text{for } P < P^z, \quad \delta V_{sample} = \delta V_{ss} + \delta V_{su} \qquad [4.14]$$

Thus it must be assumed that the compression of the solid into unintruded void space, δV_{su} , eqn [4.14], is negligible, an approximation which is also implicit in the work of Cook *et al.* (1993).

The maximum compressions of the samples in the present work are mostly less than 1 % of the sample bulk volume, rising to 6 % for the most compressible sample. For these small relative compressions, the compression may be related to the volume, V^1_{ss} , of the solid phase at atmospheric pressure P^1 to an approximation much better than the experimental uncertainty. Thus eqn [4.11] becomes:

$$\int_{P^1}^{P} dP \approx M_{ss} \int_{V^1_{ss}}^{V^1_{ss}-\delta V_{su}} -\frac{dV_{ss}}{V_{ss}} \qquad [4.15]$$

Also, at atmospheric pressure, the solid state volume is, to a similarly good approximation, calculable from the bulk volume and the porosity ϕ^1:

$$V^1_{ss} = V^1_{bulk} \cdot (1 - \phi^1) \qquad [4.16]$$

Applying these approximations to eqn [4.12]:

$$\delta V_{sample} = V^1_{bulk} (1 - \phi^1) \left(1 - \exp\left[\frac{(P^1 - P)}{M_{ss}}\right]\right) \qquad [4.17]$$

The working equation for compressible samples is then derived from eqns [4.7], [4.9] and [4.17]:

$$V_{int} = V_{obs} - \delta V_{blank} + \left[0.175\,(V^{1}_{bulk})\,\log_{10}(1 + P/1820)\right]$$

$$- V^{1}_{bulk}\,(1 - \phi^{1})\left(1 - \exp\left[\frac{(P^{1} - P)}{M_{ss}}\right]\right) \qquad [4.18]$$

The determination of ϕ^{1} can be carried out as described below, so that all the terms on the right of eqn [4.18] can be measured, except for M_{ss} , which can be found by constraining eqn [4.18] to obey eqn [4.13].

4.3 Correction terms for samples with unintrudable compressible space

In this work the mercury porosimetry curves of two types of samples containing unintrudable compressible space have been determined. The first type are samples which are microcrystalline, i.e. the particles contain mosaics of crystals in close proximity to each other, with imperfections and discontinuities between the crystals which are much too small to be intruded by mercury, but which nevertheless contribute to the compressibility of the sample (Deer *et al.* 1980). If the sample is ground to produce finer particles, the grinding causes cleavages at these microcrystal boundaries. The smaller particles then contain relatively fewer microcrystal boundaries, and are less compressible (Shinohara 1990).

The second type of unintrudable compressible space occurs in the centres of the hollow plastic spheres of the Ropaque pigment. At a sufficiently high applied mercury pressure, which is above P^{z}, the spheres collapse irreversibly.

4.4 Measurement of porosity

If no correction is made for the compressibility of a sample, its porosity appears to increase with pressure because more mercury is intruded than expected. Conversely, if a proper correction has been made for compressibility, the corrected porosities at atmospheric pressure and at elevated pressure should be the same, and their equality can be used as a verification of the correction procedure.

At atmospheric pressure

$$\phi^1 = (V^1_{bulk} - V^1_{solid}) / V^1_{bulk} \qquad [4.19]$$

where V^1_{solid} is the volume of the solid phase at atmospheric pressure, calculated from the known compositions and densities of the sample constituents by means of a relationship which for a coating colour is:

$$V^1_{solid} = \frac{m_{sample}}{(w_{pigment} + w_{binder})} \left(\frac{w_{pigment}}{\rho_{pigment}} + \frac{w_{binder}}{\rho_{binder}} \right) \qquad [4.20]$$

where m_{sample} is the mass of the sample, $w_{pigment}$ and w_{binder} are the weights of pigment and binder respectively, and $\rho_{pigment}$ and ρ_{binder} are the respective (relative) densities. In the present work the weights are measured on a parts per hundred of pigment scale, i.e. w_{binder} relates to $w_{pigment} = 100$. At higher pressures, the porosity, uncorrected for compressibility, ϕ_{uncorr}, is given by

$$\phi_{uncorr} = (V_{int} + \delta V_{sample}) / (V_{int} + \delta V_{sample} + V_{solid}) \qquad [4.21]$$

whereas the porosity corrected for compressibility is given by the simpler equation

$$\phi_{corr} = V_{int} / (V_{int} + V_{solid}) \qquad [4.22]$$

CHAPTER 5

MODELLING OF INCOMPRESSIBLE CORRELATED STRUCTURES

Mercury intrusion curves and permeabilities have been calculated for networks with banding, with clustering of small pores and throats, or with clustering of large pores and throats. The modelling method has been applied to banded sandstone samples with edge corrections. The constraint of fitting to experimental mercury intrusion data suppressed the permeability differences induced by structural changes alone. The water drainage curve of a fibrous mat structure has been modelled, the structure being mounted in such a way as to prevent compression. The effects of different optimisation methods are illustrated by modelling four samples: Clashach sandstone, which is an outcrop sandstone, 212B, a reservoir sandstone, 490E a reservoir sandstone with clay inclusions and J7 an incompressible paper coating material. Also modelled are two samples of Fontainebleau sandstone, one an untreated sample and the other a sample with simulated clay inclusions.

5.1 Correlated structures

5.1.1 *Structural effects on mercury intrusion*

The distribution of pores and throats incorporating an unskewed distribution of throats of diameter 1 to 100 μm, a connectivity of 3.5 and a porosity of 11.3 % (parameters typical of outcrop sandstone) is used to generate four unit cells: one is a random structure, the other three are types of correlated structure described previously in Chapter 2. Fig. 5.1 shows the simulated mercury intrusion curves for all four of these. The curve for a random structure has the typical sigmoidal shape of an ordinary mercury intrusion curve. However, for the banded structure, intrusion occurs at much larger throat diameters (lower pressures). This can be explained by the fact that correlation of the pore structure introduces a band of large pores and throats clustered together, and removes

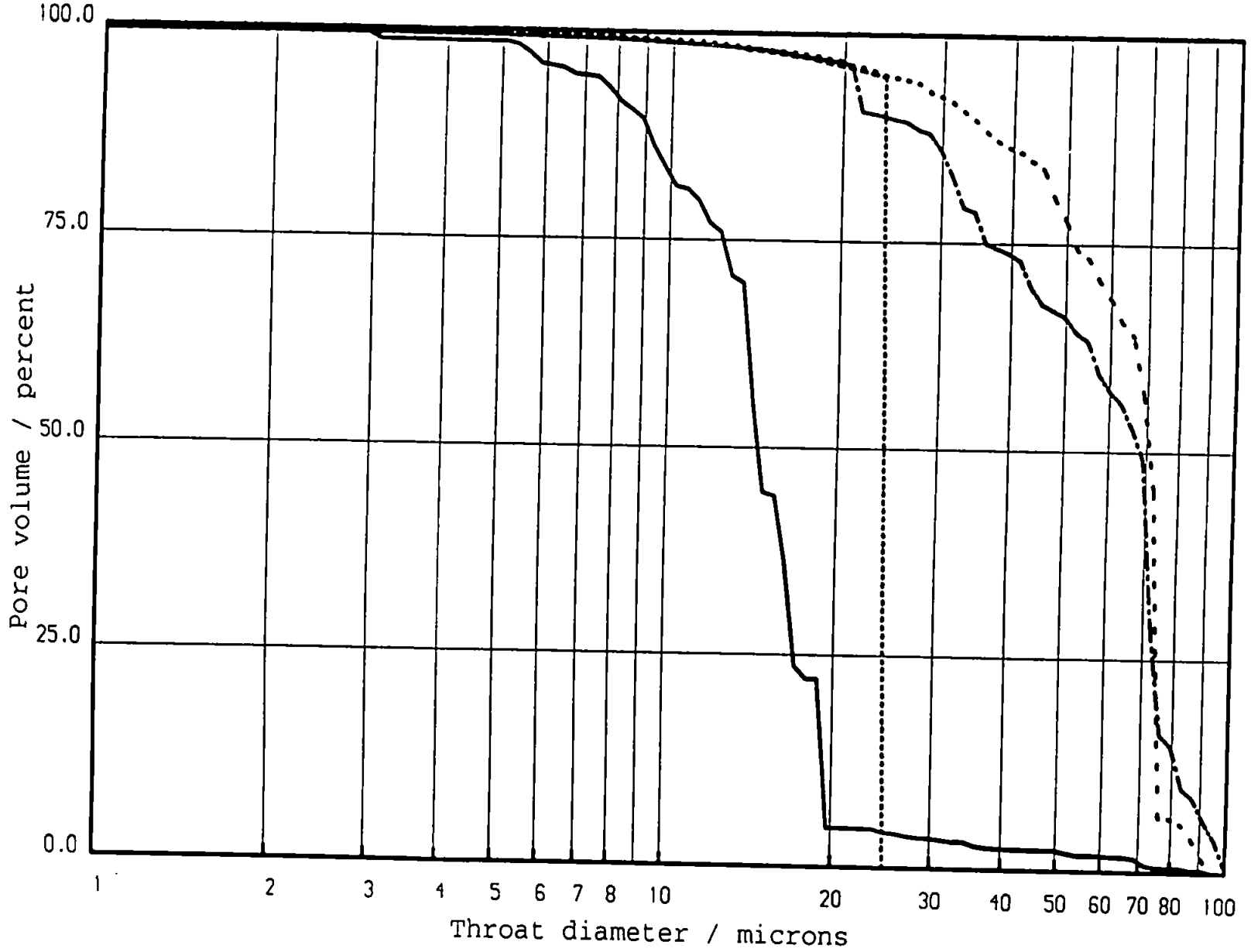

Figure 5.1 Mercury intrusion curves of correlated structures : —— random, ----- large centred structure, - - - - banded structure, – – – – small centred structure

many of the shielding effects of small throats around large pores which are seen in the random structure. In the small-centred structure, intrusion into the clusters of large pores and throats near the top ($z = l_{cell}$) surface of the unit cell occurs at relatively low pressures. At higher pressures, the mercury invades the other large pores and throats, and also the small pores and throats in the centre of the unit cell, giving the shape of intrusion curve shown in the figure. In the large-centred structure, once the mercury has penetrated the outer layers of small pores and throats, it can invade the whole of the centre of the structure, resulting in an almost entirely vertical intrusion curve.

As discussed previously in Chapter 1, the networks developed by other workers generally show that correlation effects cause a less pronounced point of inflection in the mercury intrusion curve, as has been shown for banded structures and structures containing small-centred unit cells. In contrast, the large-centred structures have a much steeper gradient at the point of inflection.

5.1.2 *Structural effects on permeability*

With regard to permeability, the unit cell investigated has the same minimum and maximum throat diameter and porosity as the mercury intrusion simulations. Four different structures have been investigated, with different combinations of skew and connectivity, to show the individual effects of these two parameters on permeability. The combinations of skew and connectivity are 1.0 and 3.5, 1.0 and 2.8, 0.2 and 3.5, and 0.2 and 2.8. The three types of correlation have been investigated with these structures at every level of correlation from totally random to totally correlated.

When offering an explanation of these effects, it must be borne in mind that the method of generating the correlated structures produces fewer large pores in them than it does in random structures with the same throat size distribution. The effect of this artefact on permeability is compensated for by an automatic alteration of throat lengths,

and hence unit cell size, to keep the porosity constant. In the case of banded structures (and others discussed below), the permeability increases with correlation, showing that these two effects are dominated by considerations of shielding.

5.1.2.1 *Banded structures*

The permeabilities for each level of correlation are shown in Fig 5.2. It is clear that the introduction of banding into the structure causes the permeabilities to increase dramatically. It can also be seen that high connectivities and low skews (giving fewer small throats and more large ones), enhance the already-existing increase in permeability with correlation level. The correlation effects are not significant until a correlation level of 0.8 is attained. It may be concluded that structures with correlations of 0.6 and below (i.e. positional ranges of 5 layers or above) are effectively random as far as permeability is concerned.

5.1.2.2 *Structure with small pores and throats in the centre*

From Fig. 5.3 it can be seen that the effects of the skew and connectivity are the same as those for the banded structure: a higher connectivity or a lower skew will give a higher permeability. For structures with a connectivity of 3.5, the overall trend is for the permeabilities to increase as the correlation is introduced. However, the permeabilities of structures with connectivities of 2.8 start to increase as the correlation is introduced, but then reduce again as a totally correlated structure is reached. A structure with connectivity 2.8 has fewer pathways through the unit cell than a structure with connectivity 3.5, so that flow is directed through the central, small-pore-and-throat zone. As the correlation level is increased, this central zone contains fewer and fewer large pores or throats, so that permeability decreases.

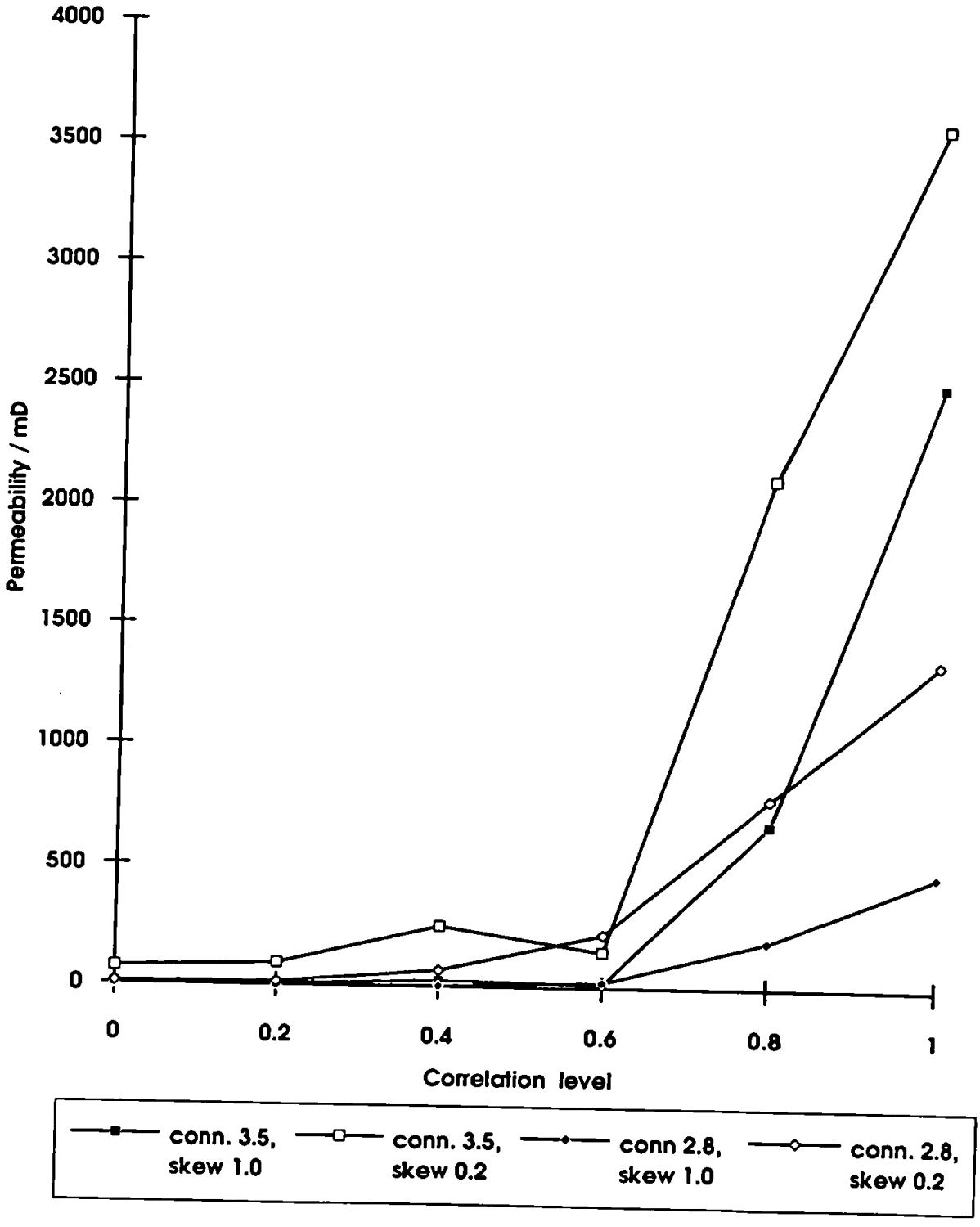

Figure 5.2 Permeabilities of banded structures against correlation level

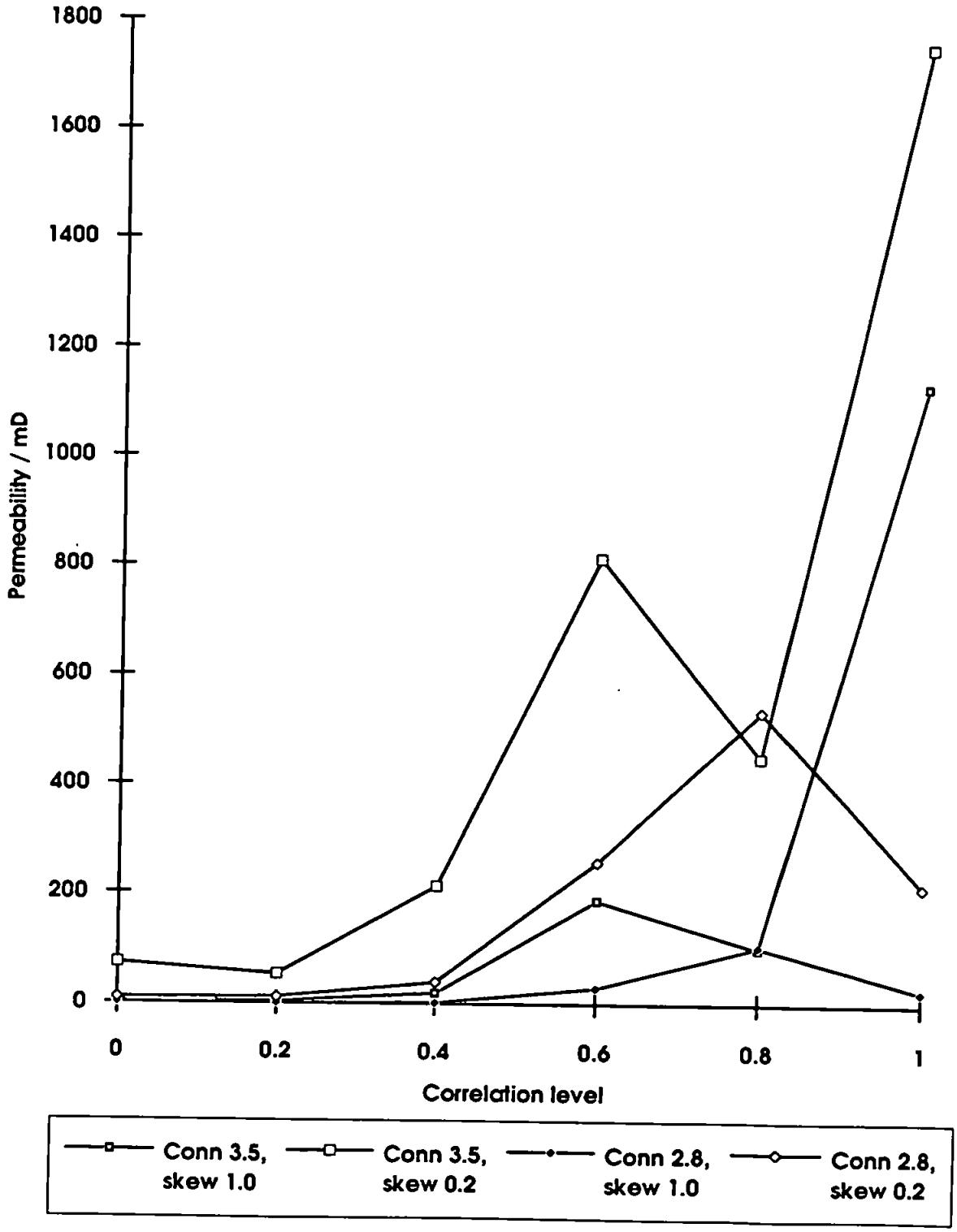

Figure 5.3 Permeabilities of small centred structures against correlation level

5.1.2.3 *Structures with large pores and throats in the centre*

Fig. 5.4 shows the permeabilities for the different structures and the different levels of correlation for structures with the large pores and throats in the centre. In this case, the permeabilities go through a maximum at a correlation level of 0.6 for all the combinations of skew and connectivity investigated. It can be seen from Fig. 5.5 that at a correlation level of 0.6, the small pores and throats have begun to gather at the corners of the unit cell, thus reducing their overall impedance effect and increasing the permeability. However, at higher correlation levels, the central zone of large pores and throats becomes shielded by a shell of smaller pores and throats, as shown in Fig. 2.10 for a correlation level of 1.0, and the permeability decreases again.

5.1.3 *Permeability of structures constrained by fit to experimental mercury intrusion curve*

The structures that have been looked at so far have been purely theoretical structures with a minimum throat diameter of 1 μm, a maximum throat diameter of 100 μm and a porosity of 11.3 %. However, when using the program to model actual samples it is necessary to fit the simulated mercury intrusion curve to the experimental mercury intrusion curve. Under these circumstances, the type and level of correlation are still specified, but the skew and connectivity become variable parameters in the fitting of the simulated curve to experiment. For example, increasing the specified correlation in a large-centred model increases the suddenness of intrusion with pressure, and the fitting routine may consequently decrease the connectivity or increase the skew to compensate for this.

The experimental sample used to illustrate these effects is a reservoir sandstone sample 212B. An image-analysed back-scatter electron micrograph of a resin-filled sample was shown in Plate 2.1. The width of the Plate is 3.28 mm. The horizontal stripes

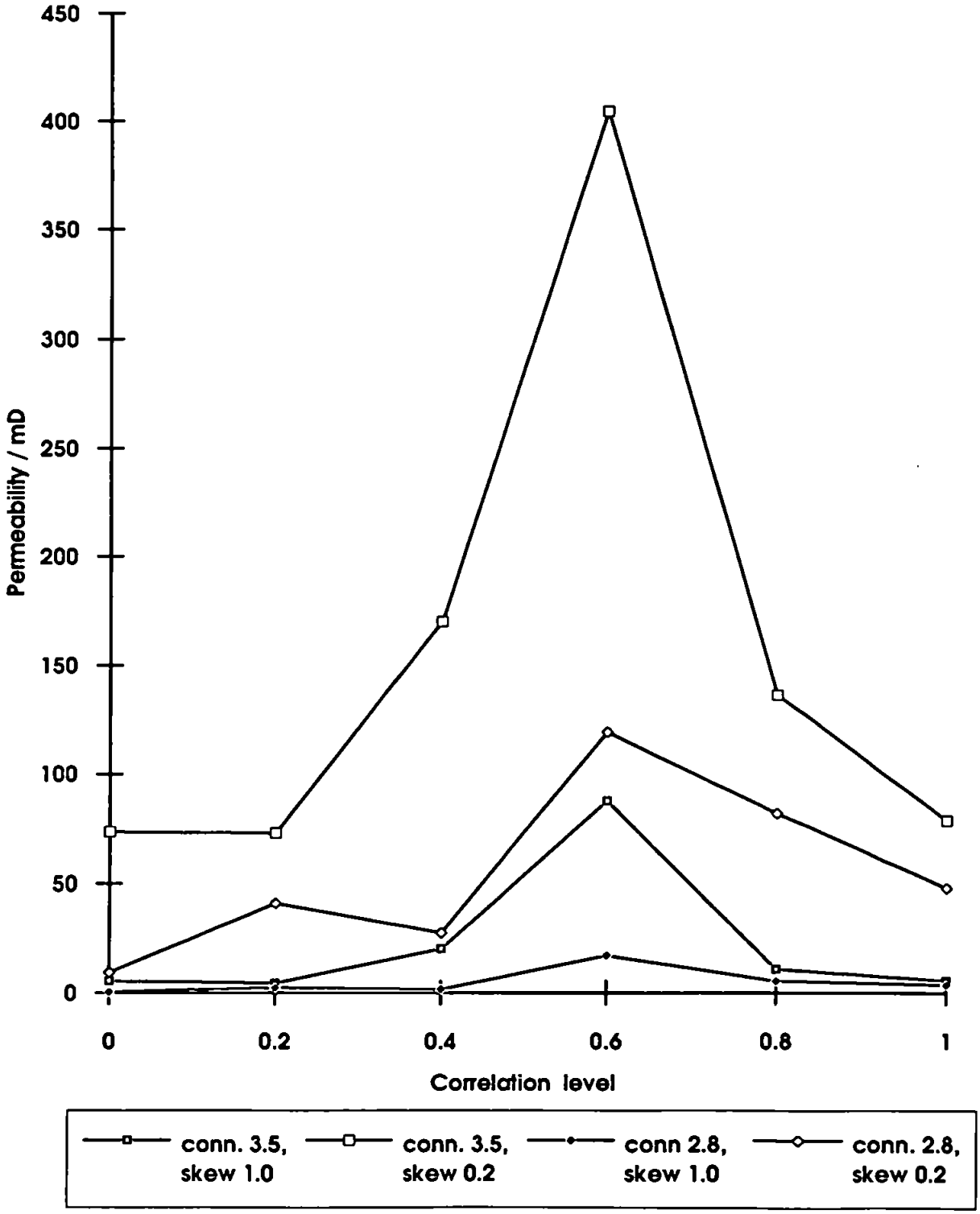

Figure 5.4 Permeabilities of large centred structures against correlation level

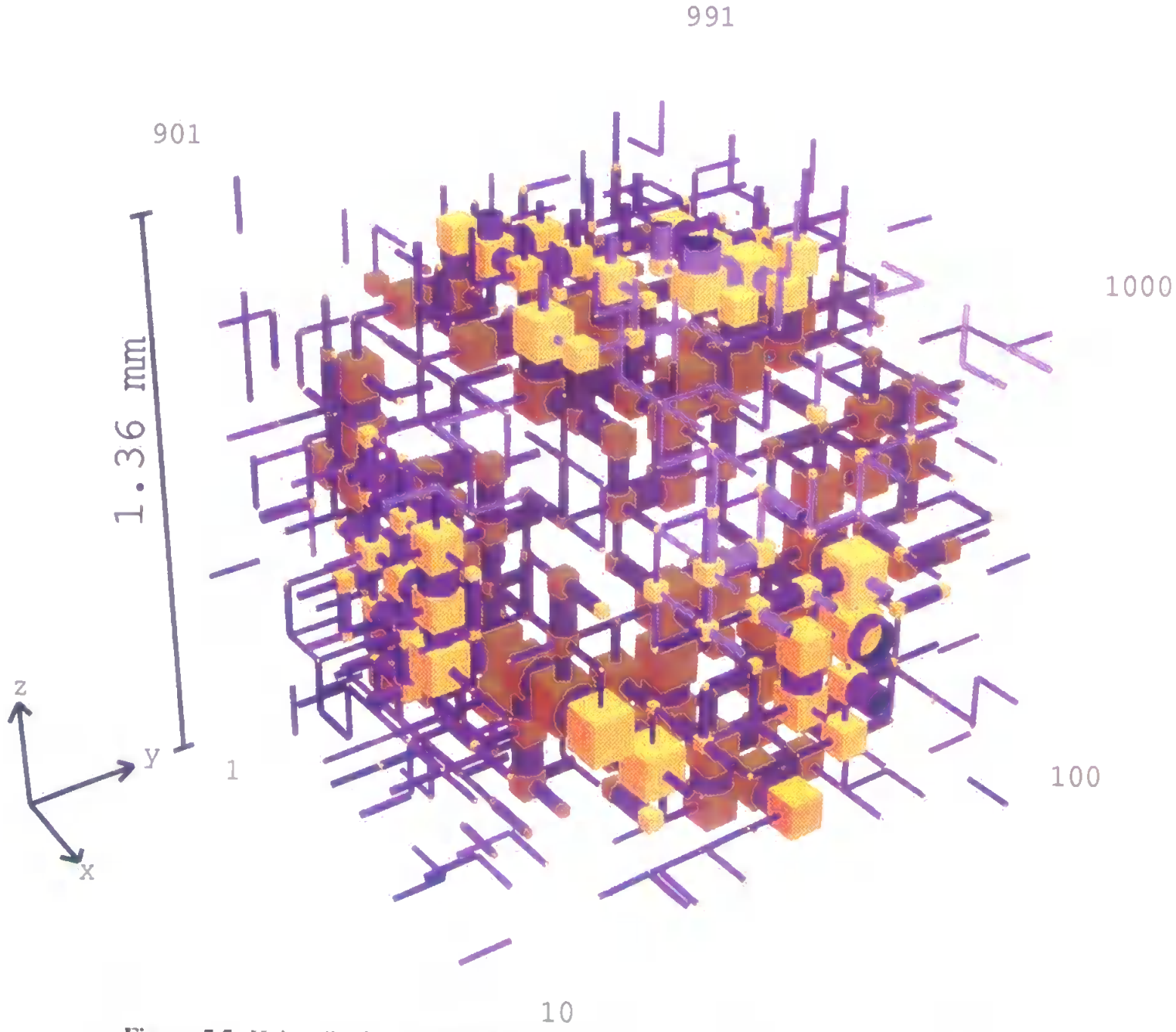

Figure 5.5 Unit cell with large pores and throats in the centre for a correlation level of 0.6

on the Plate are due to rastering effects and are ignored. Void spaces appear dark. Visual inspection suggests that there is a band of smaller grains across the middle of the sample, and that these grains also cluster in places: the banding is in fact easily visible to the naked eye. Mercury porosimetry experiments give a minimum throat diameter of 0.12 μm and a maximum throat diameter of 207.16 μm via eqn [1.2]. The Boyle's law gas porosity of the sample was found to be 21.1 %.

Fig. 5.6 shows the permeabilities for correlated structures at all correlation levels, using the logarithmic fit method. It can be seen that the range of permeabilities in this figure is much smaller than those in Figs. 5.2, 5.3 and 5.4, and that the constraint of fitting to the experimental mercury intrusion curve has entirely masked the effects of correlation on permeability. The effects of the small-centred and large-centred structures are shown for interest, although these are less realistic representations of sample 212B. Fig. 5.6 shows that the same constraining effect on permeability exists for all three types of correlated structure.

5.1.4 *Edge corrections*

The studies carried out by Wardlaw *et al.* (1976), discussed earlier, show that in the low pressure region, edge corrections cause changes of up to 15 % in pore volume and sample-size corrections affect the intrusion curve by up to 3 % pore volume. The discrepancies between the simulated and experimental intrusion curves are often of the order of 15 % pore volume as can be seen in Fig. 1.5, so it is worthwhile to correct for edge effects but not for sample-size effects. The edge-effect correction has been made by changing the shapes of the intrusion curves so that they increase linearly from zero to the take-off point below the point of inflection, as can be seen by comparing Figs. 1.5 and 5.7.

Figs. 5.7 and 5.8 show the results of modelling the edge-corrected intrusion curves for two sandstone samples, 212B and 212C. The results of the modelling are shown in

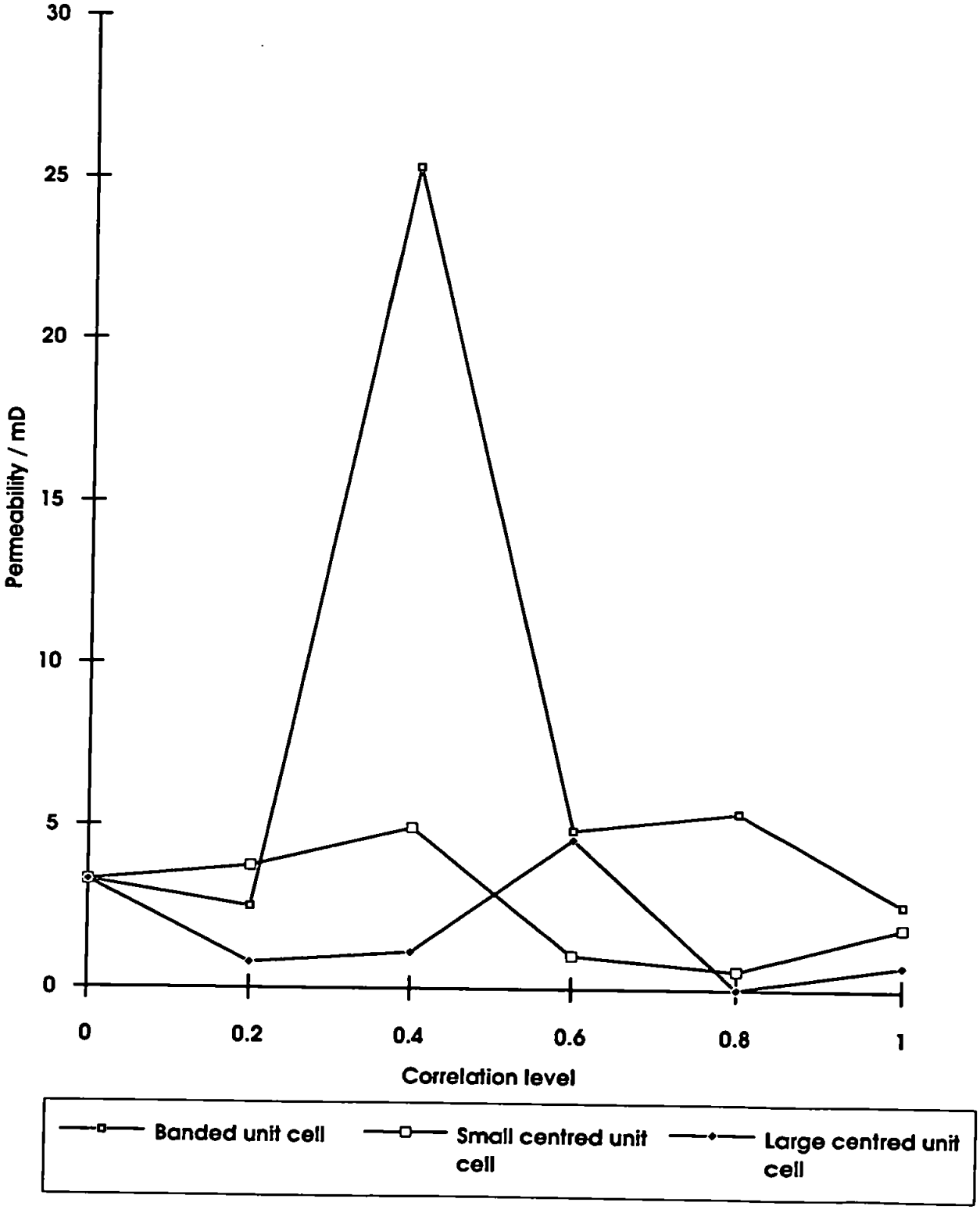

Figure 5.6 Permeability against correlation level for each structure using the logarithmic fit method

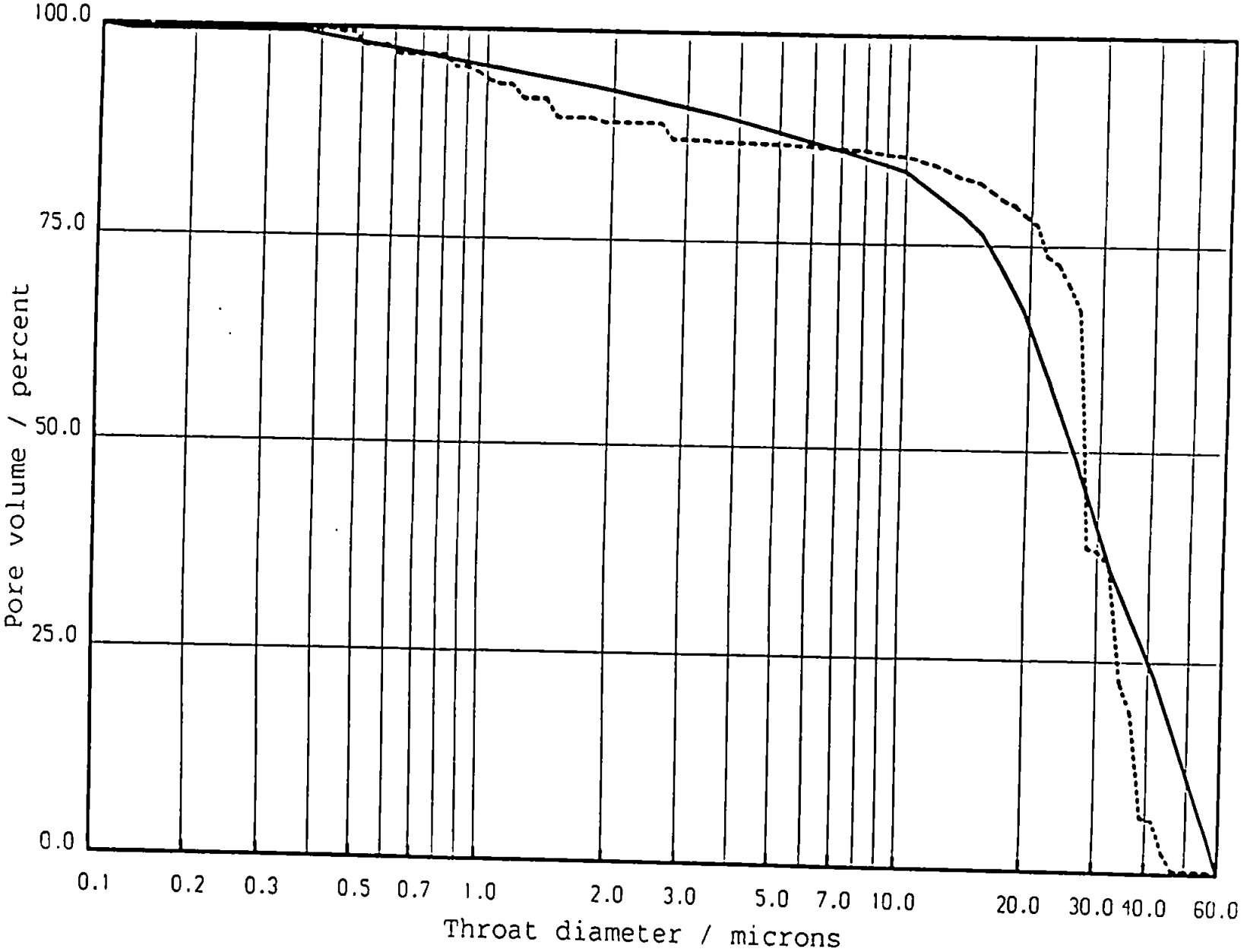

Figure 5.7 Edge-corrected mercury intrusion curve for banded structure for 212B using logarithmic fit and correlation level 1.0: —— experimental, ----- simulation

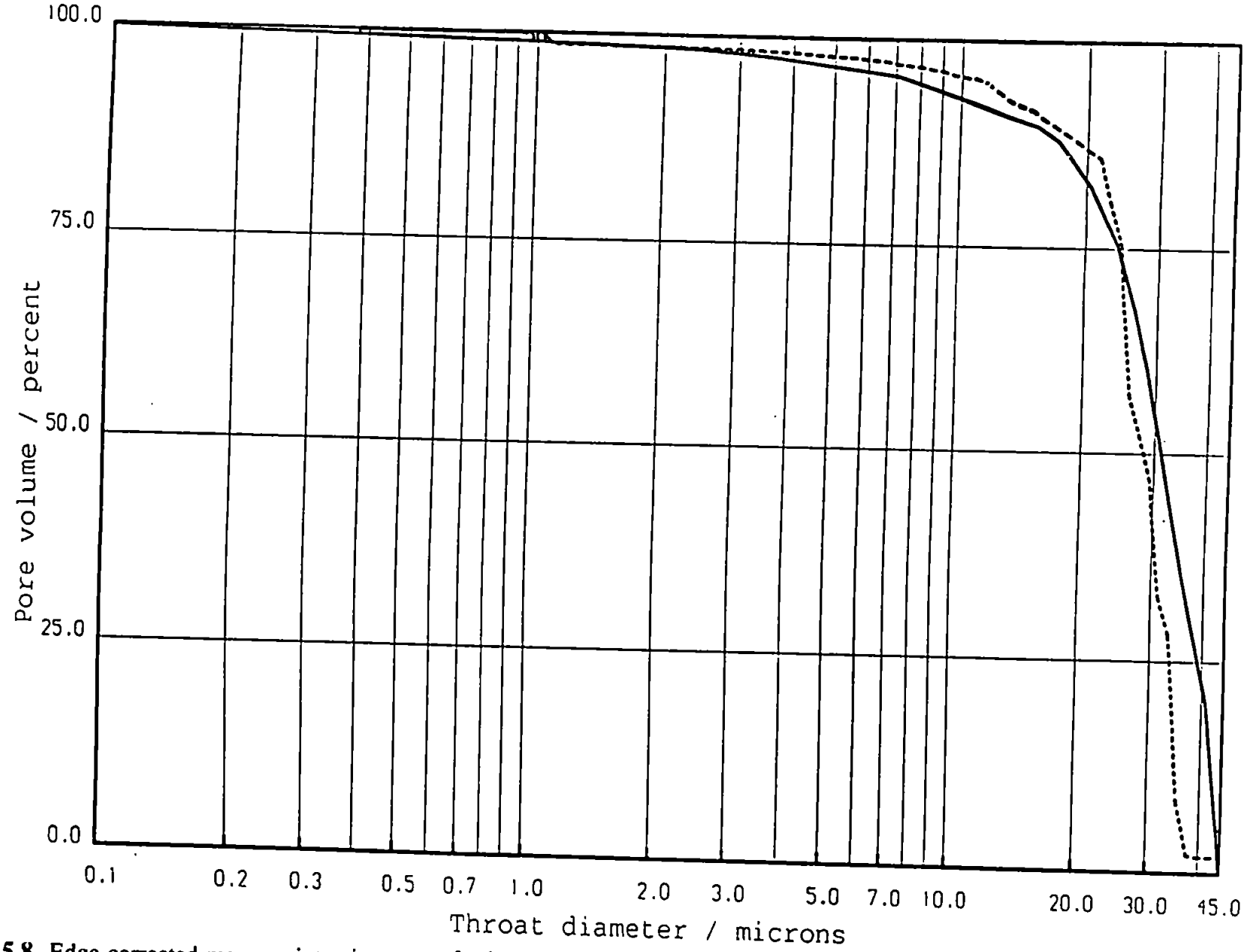

Figure 5.8 Edge-corrected mercury intrusion curve for banded structure for 212C using logarithmic fit and correlation level 0.8: —— experimental, ----- simulation

Table 5.1, which cover a wide range of properties. The permeabilities calculated from the model are within a factor of 3 of the experimental values. This agreement is well within the factor of 7 agreement of Thompson *et al.* (1987), mentioned earlier, eqn [3.2].

The agreement with experimental is gratifying, and gives some support to the choice of the set of fitting parameters, namely the skew, connectivity, and the type and extent of correlation. However, the general characteristics of the network, such as the shape and regular spacing of pores and throats, are arbitrary, and it is obviously an imperfect representation of the true void space. Convergence onto the ultimate goal of perfect representation would require a very large number of experimental data in order to fix all parameters in the model. However, the experimental data must implicitly include some averaging over the experimental sample if the resulting simulated structure is to be a representation of the whole sample. Two steps on this very long road are the modelling of the full mercury porosimetry hysteresis curve, and the inclusion of an experimental measure of correlation effects such as banding. A hysteresis algorithm has been developed, and the details have recently been published Matthews *et al.* (1995b). The image-analysed structure shown in Plate 2.1 is part of a method which has been developed to measure banding, and will be the subject of a forthcoming paper. The next stage of the work is to include these two effects in the modelling of correlated structures.

5.2 Very high porosity structures

The high porosity structure modelled in this thesis is an unbonded dry formed network, fibrous mat, which has been formed from a hard wood material. This material is mixed with water until a pulp is produced, and this is then dried out on a screen. The water drains out through the screen, and a fibrous mat remains on the surface. The modelling is based on the water extrusion data in Table 5.2, which was supplied by SCA Research. It was already converted to throat diameters using the Laplace/Washburn

Sample	Sample volume cm^3	Throat diameter from mercury intrusion (μm)		Skew	Connectivity	Correlation level	Porosity (%)		Permeability (mD)		Tortuosity	
		Minimum	Maximum	sim.	sim.	sim.	expt.	sim.	expt.	sim.	expt.	sim.
212B	0.24	0.12	60.0	0.19	2.9	1.0	21.1	21.1	1413	560	1.75	2.3
212C	2.40	0.10	45.0	0.29	4.0	0.8	24.4	24.4	3161	1010	1.83	2.2

Table 5.1 Modelling of reservoir sandstone samples 212B and 212C

Supplied data				Data ignoring 'gel' water at < 7 microns		
Mean Radius / microns	Mean Diameter / microns	Cumulative volume wp in sample / cm3 g-1	volume wp in sample / %	Adjusted volume wp in sample / cm3 g-1	Adjusted volume wp extruded / cm3 g-1	Adjusted volume wp extruded / %
3.5	7	1.128	19.07	0	4.786	100.00
4.5	9	1.251	21.15	0.123	4.663	97.43
5.5	11	1.343	22.71	0.215	4.571	95.51
6.5	13	1.428	24.15	0.3	4.486	93.73
7.5	15	1.507	25.48	0.379	4.407	92.08
8.5	17	1.587	26.83	0.459	4.327	90.41
9.5	19	1.667	28.19	0.539	4.247	88.74
10.5	21	1.751	29.61	0.623	4.163	86.98
11.5	23	1.838	31.08	0.71	4.076	85.17
12.5	25	1.929	32.62	0.801	3.985	83.26
13.5	27	2.032	34.36	0.904	3.882	81.11
14.5	29	2.14	36.19	1.012	3.774	78.85
15.5	31	2.255	38.13	1.127	3.659	76.45
16.5	33	2.376	40.18	1.248	3.538	73.92
17.5	35	2.496	42.20	1.368	3.418	71.42
18.5	37	2.624	44.37	1.496	3.29	68.74
19.5	39	2.75	46.50	1.622	3.164	66.11
21	42	2.904	49.10	1.776	3.01	62.89
23	46	3.17	53.60	2.042	2.744	57.33
25	50	3.425	57.91	2.297	2.489	52.01
27	54	3.687	62.34	2.559	2.227	46.53
29	58	3.953	66.84	2.825	1.961	40.97
32.5	65	4.198	70.98	3.07	1.716	35.85
37.5	75	4.728	79.95	3.6	1.186	24.78
42.5	85	5.018	84.85	3.89	0.896	18.72
27.5	55	5.168	87.39	4.04	0.746	15.59
52.5	105	5.265	89.03	4.137	0.649	13.56
57.5	115	5.345	90.38	4.217	0.569	11.89
62.5	125	5.411	91.49	4.283	0.503	10.51
67.5	135	5.471	92.51	4.343	0.443	9.26
72.5	145	5.516	93.27	4.388	0.398	8.32
77.5	155	5.554	93.91	4.426	0.36	7.52
82.5	165	5.593	94.57	4.465	0.321	6.71
87.5	175	5.627	95.15	4.499	0.287	6.00
92.5	185	5.657	95.65	4.529	0.257	5.37
97.5	195	5.687	96.16	4.559	0.227	4.74
112.5	225	5.714	96.62	4.586	0.2	4.18
137.5	275	5.827	98.53	4.699	0.087	1.82
162.5	325	5.878	99.39	4.75	0.036	0.75
187.5	375	5.914	100.00	4.786	0	0.00

Table 5.2 Fibrous mat air intrusion data set

equation with contact angle θ of zero and a value if the interfacial tension γ in the range 32-34 mN m^{-1}. The modelling is carried out in terms of the intrusion of a non-wetting phase (air), which is equated to the extrusion of the wetting phase, i.e. water. 'Gel' water, equivalent to throat diameters of less than 7 μm is ignored for purposes of modelling the non-wetting phase intrusion as shown in Table 5.2.

The gel water is also ignored in the calculation of porosity. The density (specific gravity) of cellulose is assumed to be 1.5 g cm^{-3}, which thus occupies a volume of 0.667 cm^3 g^{-1}. The total volume of wetting phase (water) in the sample is 4.786 cm^3 g^{-1}, ignoring the gel water as shown in Table 5.2. The porosity is 4.786 / (0.667+4.786) = 87.8 %. The minimum precision in this calculation is in the density of the cellulose; a density of cellulose = 1.5 ± 0.1 g cm^{-3} corresponds to a porosity of 87.8 ± 0.8 %, a level of uncertainty which has no significant effect on the modelling.

Automatic convergence onto the experimental air intrusion curve produces the fit shown in Fig. 5.9, at a throat diameter distribution skew of 0.99 % and connectivity of 3.2. With regard to the pore and throat size distribution, all the pores are of diameter 375 μm, and the throats are numerically almost equally distributed over 100 sizes in the logarithmic series 7.00, 7.29, ... 360.22, 375.00 μm. This structure is considered the optimum obtainable because it has the same porosity as the experimental sample, as well as providing good fit to the air intrusion curve, and thus matches all the supplied experimental data.

The void space structure is shown in Fig. 2.11. It can be seen that all pores are of the same size (375 μm), but that some pore sites such as 570 in the front right hand face, where there are no connecting throats, are vacant. This represents the site of a knot of fibres. The unit cell size is 3.92 mm, and it follows that the planes in the x, y and z axes representing loci of the fibre positions are 17 μm thick, a reasonable thickness for cellulose fibre. Breakthrough of air occurs at an absolute pressure of 23 kPa, corresponding to a

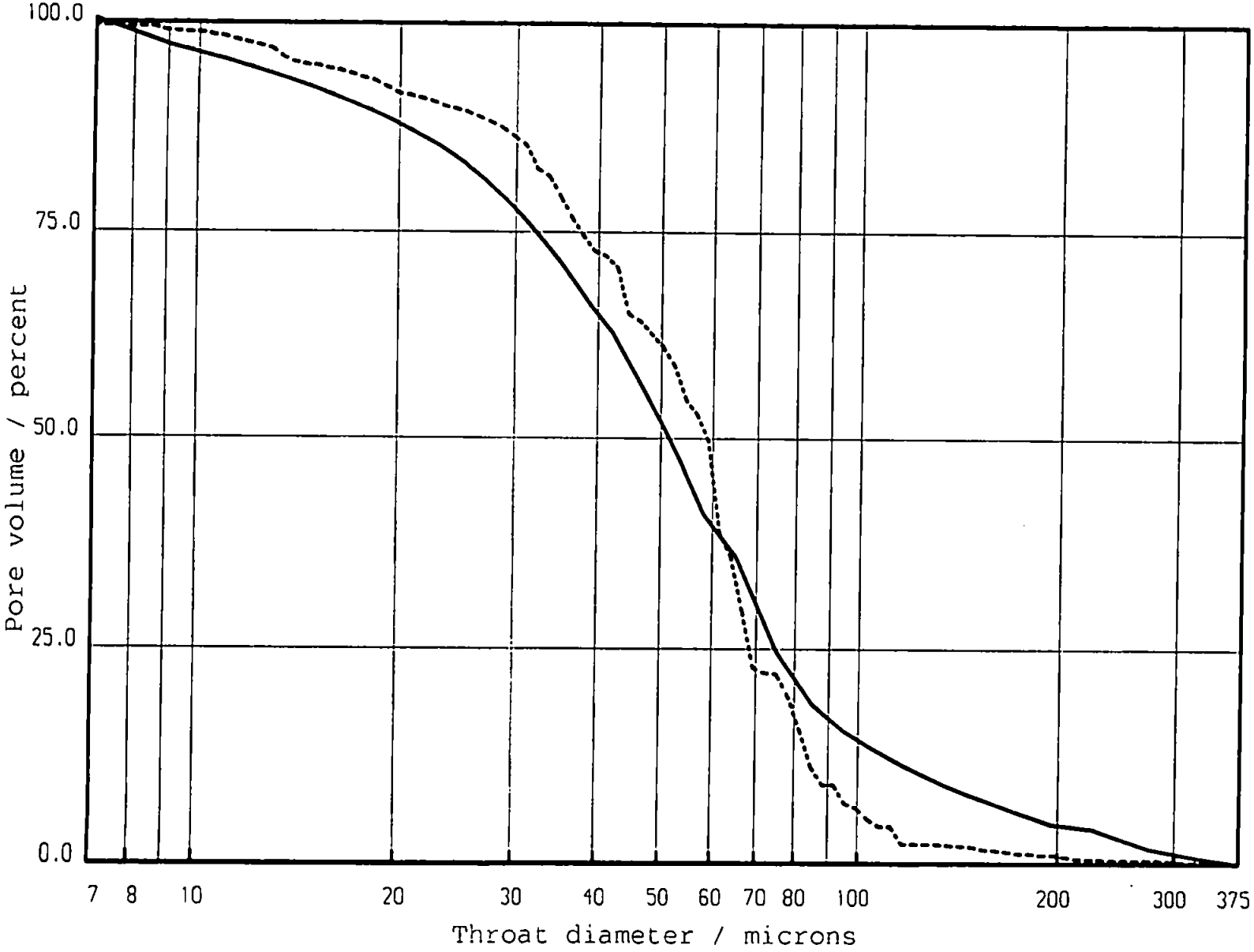

Figure 5.9 Experimental and simulated air intrusion curves, skew 0.99 % and connectivity 3.2: —— experimental, ----- simulation

throat diameter of 63.9 μm. The pores and throats containing air at the breakthrough pressure are shown in black in Fig. 5.10.

A structure has been presented which matches all the supplied data for water extrusion and corresponding air intrusion into a fibrous network, these data being the water extrusion curve and the porosity calculated from the maximum water content using an assumed density of cellulose.

5.3 Optimised fit mercury intrusion curves

5.3.1 *The 50 % fit method*

This method of fitting the mercury intrusion curve has been used for four different types of sample. The long-dashed curve in Fig. 5.11 shows the result for a sample of Clashach outcrop sandstone, which is a relatively well-characterised clay-free sandstone. The simulated and experimental mercury intrusion curves fit closely at 50 % pore volume, but the upper and lower shoulders of the curve do not match. Fig. 5.12 shows the pore size and throat diameter distributions used, the skew for this best fit being 0.60 %. The same method has been used on three other samples: the wide dashed curve in Fig. 5.13 shows the data for a relatively clean reservoir sandstone known as 212B, whilst Fig. 5.14 shows the results for a reservoir sandstone, 490E, that contains some included clay. Fig. 5.15 is for a paper-coating China clay material, J7.

All these curves are forced to fit at the 50 % pore volume level, but they do not fit well at the extremes. The mercury porosimetry curve of samples such as 490E tend to be shallower because the clay obstructs the path of the mercury and causes it to invade more gradually as the pressure is increased. The 50 % method uses a connectivity of 3.5, which gives a simulated curve that is too steep for a good fit as can be seen from Fig. 5.14. The porosities, connectivities and skews of the best fitting curves using the 50 % method are listed in Table 5.3.

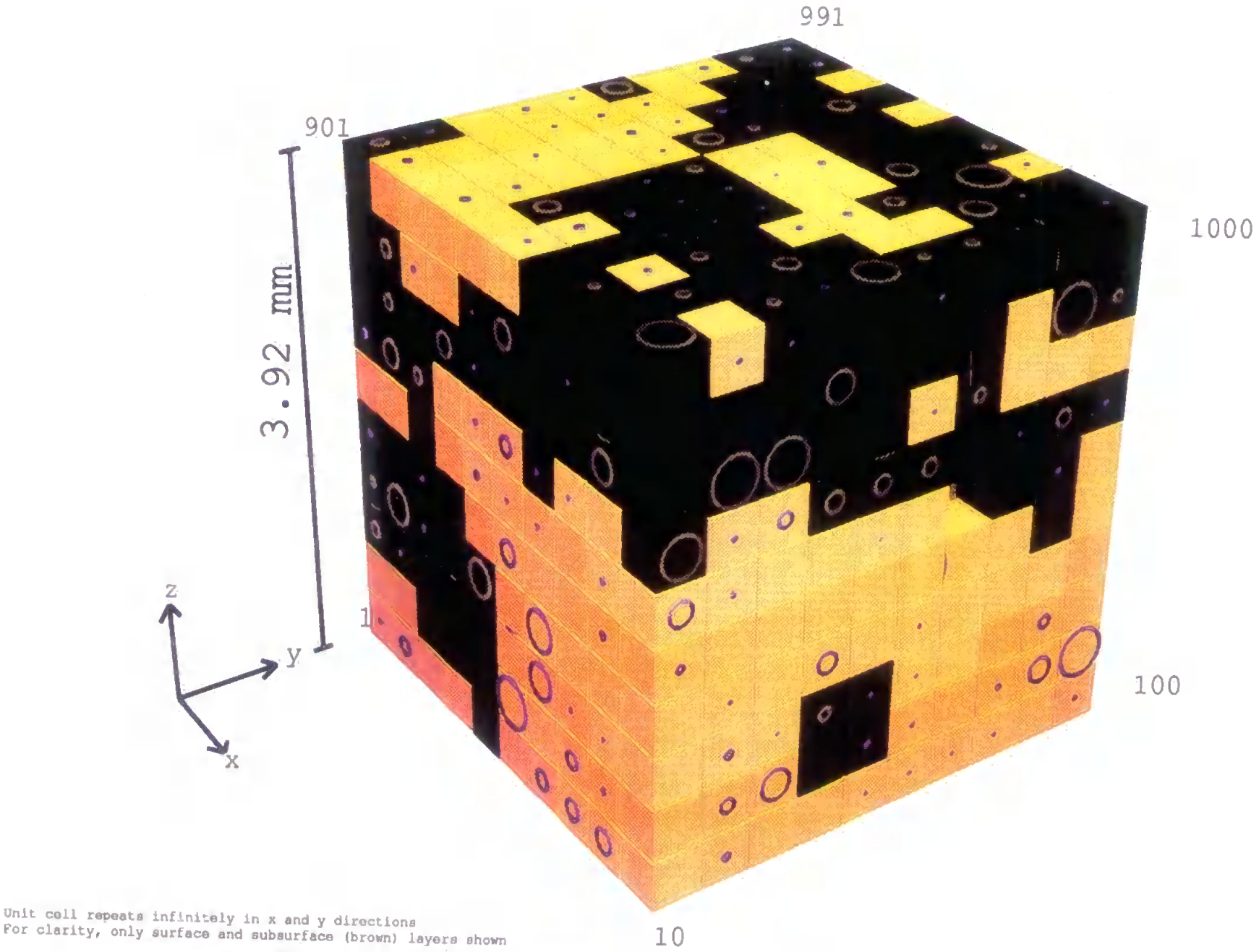

Figure 5.10 Unit cell for fibrous mat showing non-wetting phase in black

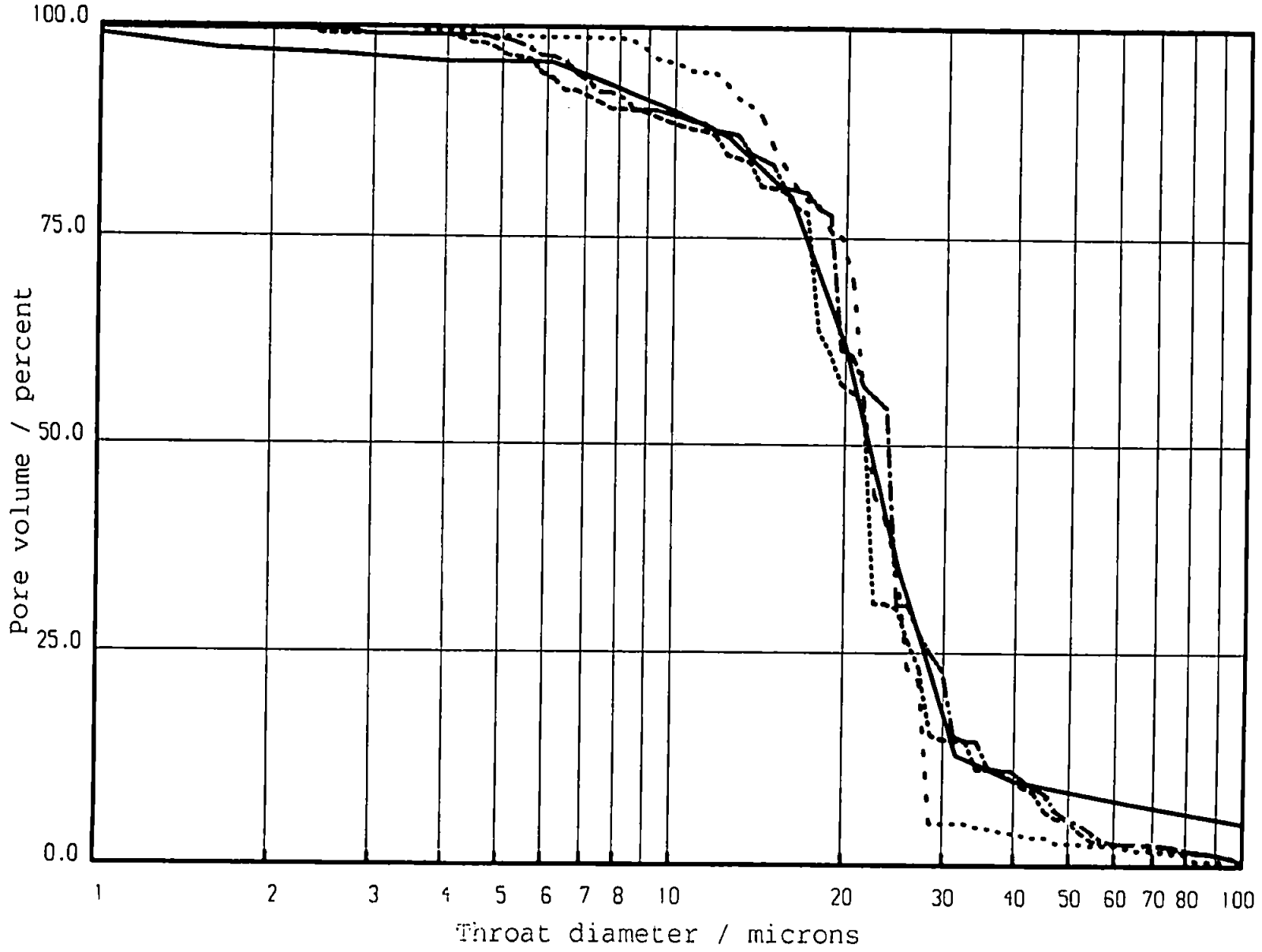

Figure 5.11 Mercury intrusion curve of Clashach sandstone; —— experimental, - - - - 50 % method, – – – – linear method, ----- logarithmic method.

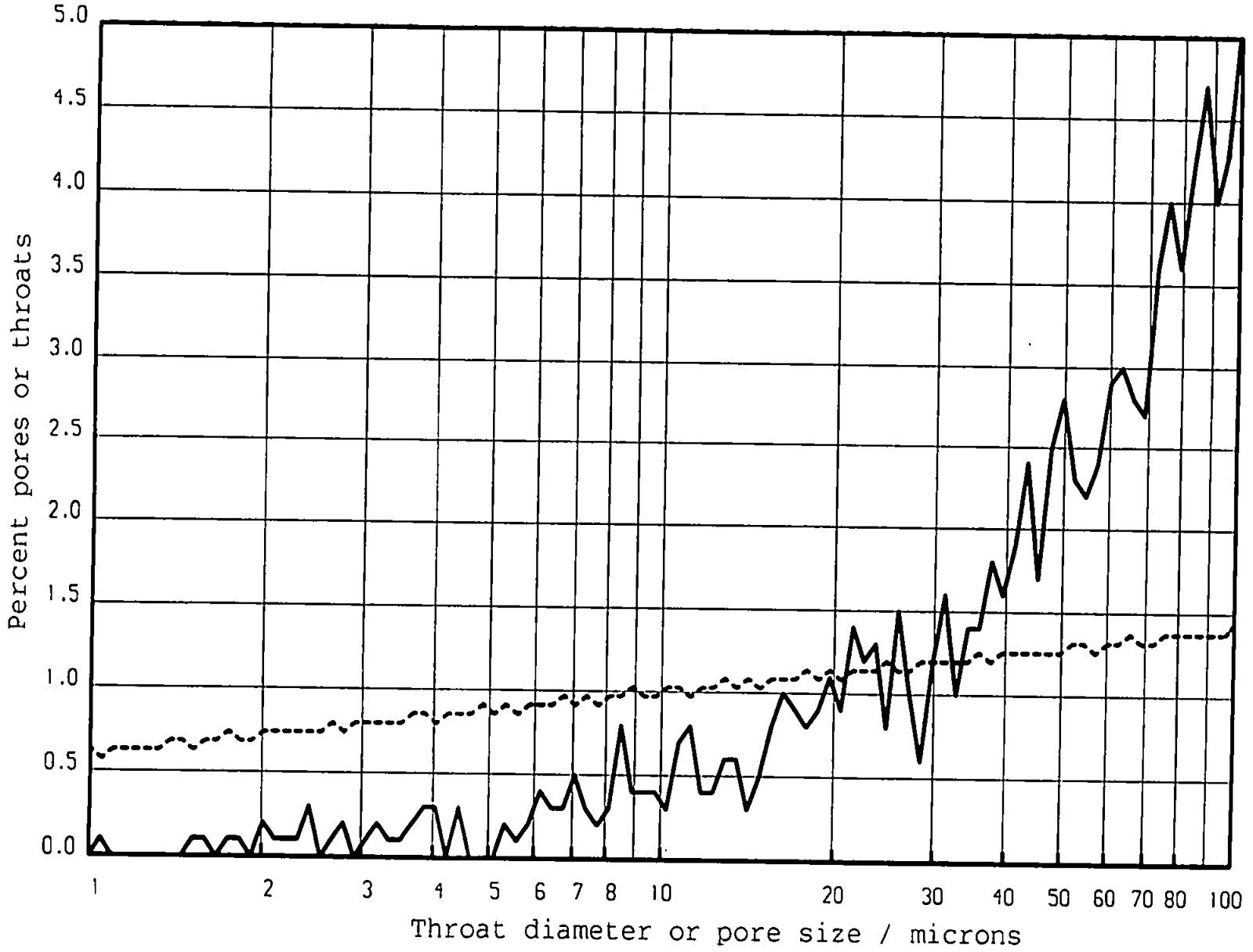

Figure 5.12 Clashach throat diameter distribution with pore size distribution using 50 % method: —— pores, ----- throats

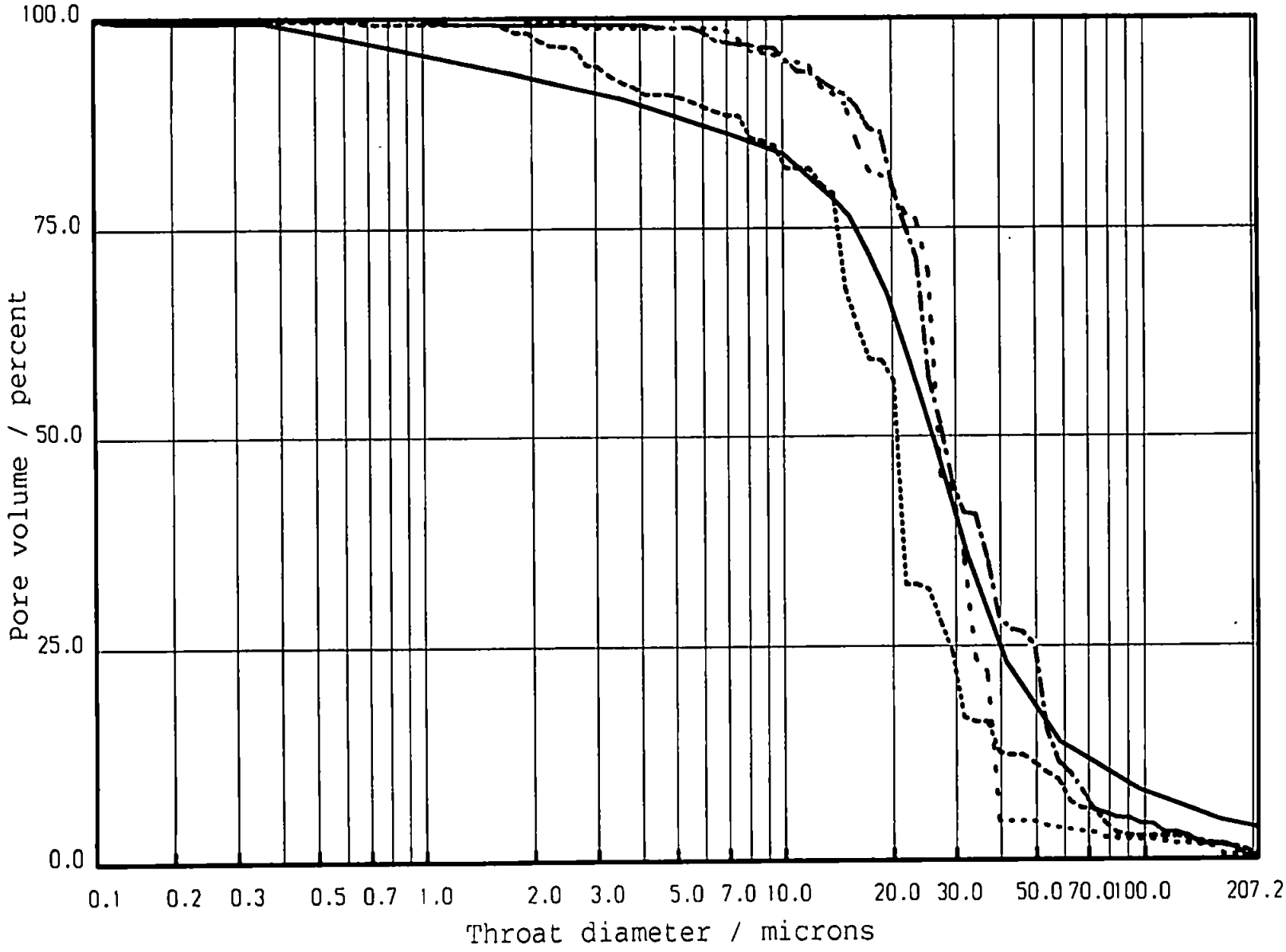

Figure 5.13 Mercury intrusion curve of reservoir sandstone 212B; —— experimental, - - - - 50 % method, – – – – linear method, ----- logarithmic method

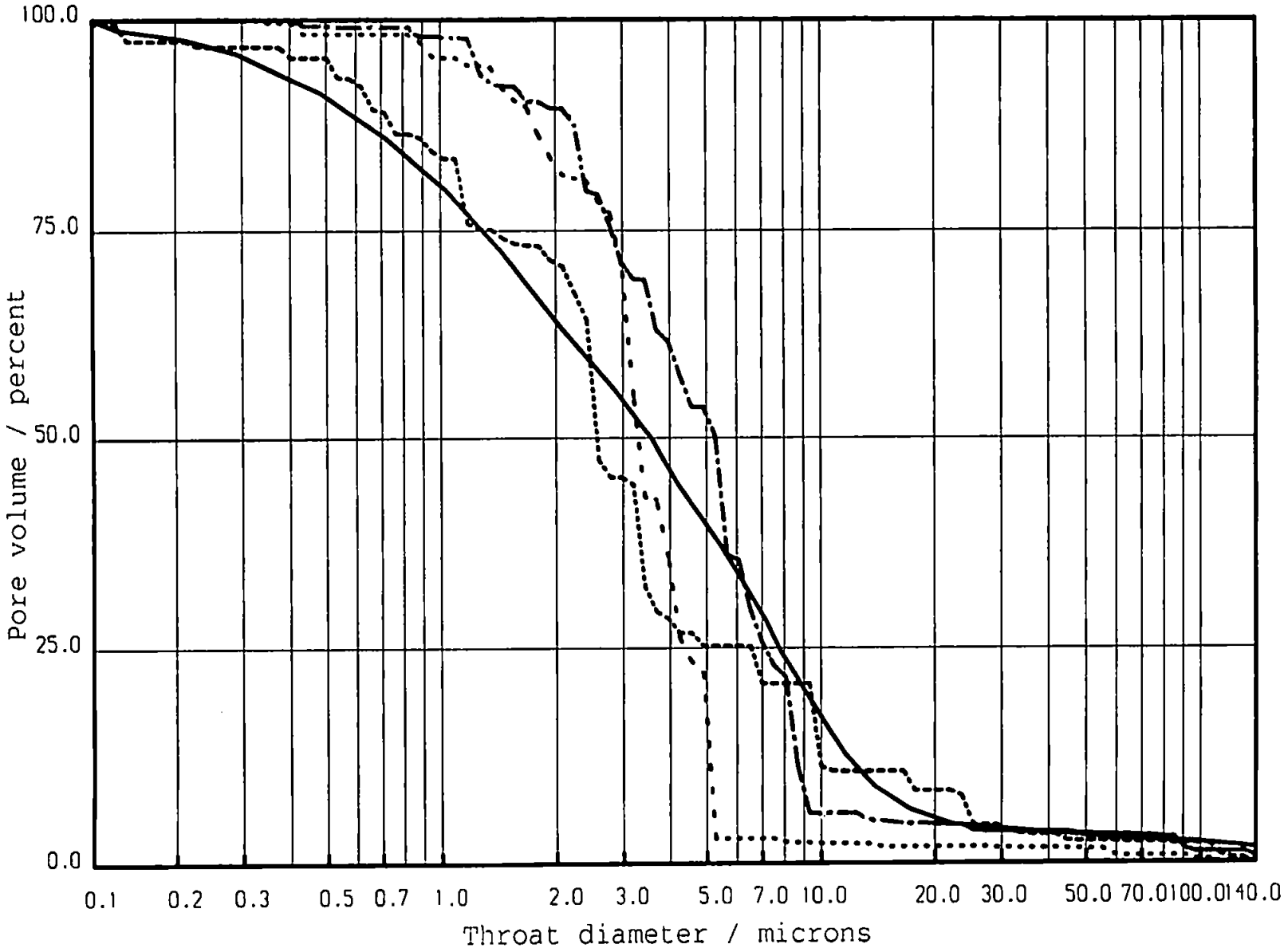

Figure 5.14 Mercury intrusion curve of reservoir sandstone 490E; —— experimental, - - - - 50 % method, – – – – linear method, ----- logarithmic method

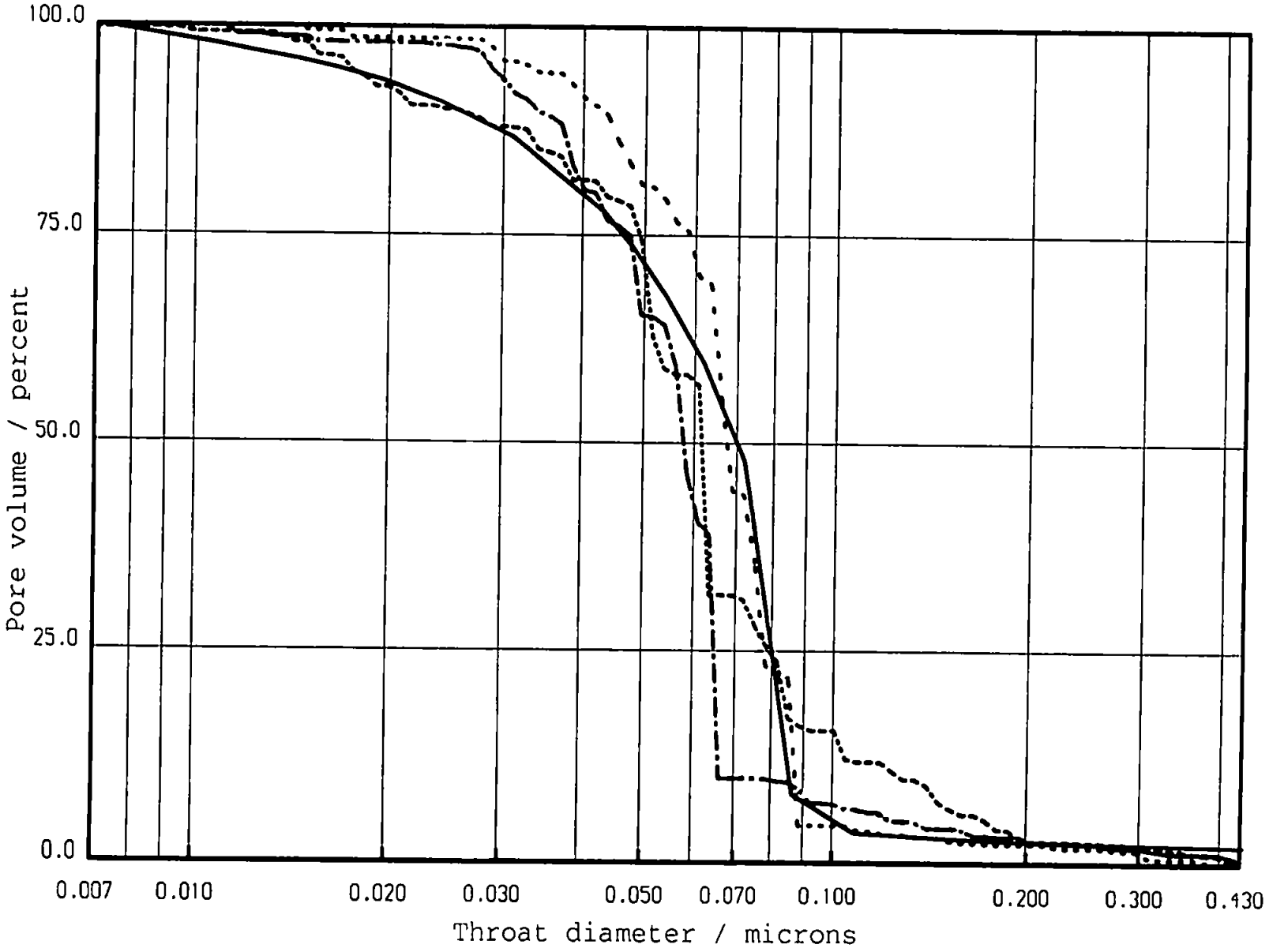

Figure 5.15 Mercury intrusion curve of paper coating J7; —— experimental, - - - - 50 % method, – – – – linear method, ----- logarithmic method

Sample	Method of optimisation	Porosity	Connectivity	Skew
Clashach outcrop sandstone	50%	11.3	3.5	0.60
	linear	11.3	2.8	0.10
	logarithmic	11.3	2.8	0.20
Reservoir sandstone 212B	50%	21.1	3.5	0.28
	linear	21.1	4.0	0.38
	logarithmic	21.1	2.8	0.08
Reservoir sandstone 490E	50%	15.1	3.5	1.42
	linear	15.1	3.4	1.22
	logarithmic	15.1	2.6	0.82
Paper coating J7	50%	22.3	3.5	1.12
	linear	22.3	3.6	1.32
	logarithmic	22.3	2.8	0.82

Table 5.3 Optimised data for Clashach, 212B, 490E and J7

5.3.2 *The logarithmic method and linear method*

Figs. 5.11, 5.13, 5.14 and 5.15 illustrate the application of the linear and logarithmic methods to the previous four samples. Table 5.3 lists the porosities, connectivity and skew values for the best-fitting simulation curves. It was explained previously in Chapter 2 that on the logarithmically scaled graphs used in this work, the linear method appears to give a worse fit to experiment at lower throat diameters than the logarithmic method. This can be seen by comparing the 212B linear model with the 212B logarithmic model in Fig. 5.13. It can also be seen with samples 490E in Fig. 5.14, and J7 in Fig. 5.15. The closer fitting at smaller throat diameters by the logarithmic method entails the use of a lower connectivity value in all cases except Clashach sandstone, (Fig. 5.11), as can be seen in Table 5.3.

It is of interest to compare the best fit simulations produced by the 50 % method with those produced by the linear and logarithmic methods. The 50 % method on the Clashach sample, (Fig. 5.11), produced an intrusion curve which, though fitting experiment at 50 % pore volume, is too steep overall with too high an upper shoulder and too low a lower shoulder. Using the linear method, the upper and lower shoulders fit and the curve is less steep. The logarithmic method uses the same connectivity but increases the skew slightly. This alters the throat distribution, so that there are more small throats, and so moves the curve slightly towards the smaller throat diameters. Similar comparisons can be made for the reservoir sandstone 212B (Fig. 5.13), the reservoir sandstone 490E (Fig. 5.14), and the paper coating J7 (Fig. 5.15).

The connectivity and skew values shown in Table 5.3 are those which produce a minimum deviation between simulation and experiment. Examples of deviations resulting from simulations within the connectivity and skew ranges are shown for the sandstone samples Clashach and 212B respectively in Figs. 5.16 and 5.17, in which the deviations are in units of μm, but since they depend on the number of comparison points, the throat

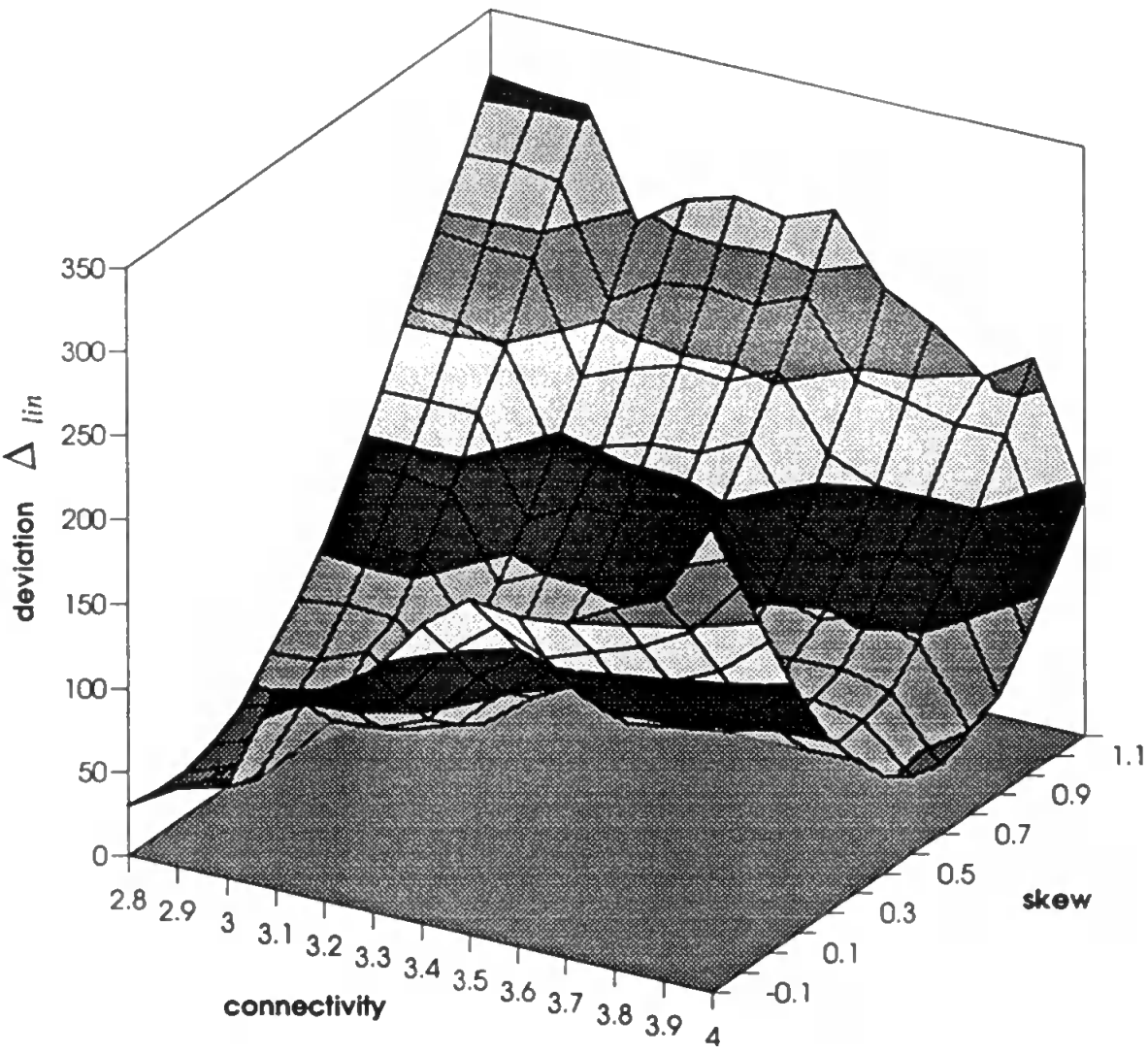

Figure 5.16 Deviations of combinations of skew and connectivity for the linear method for Clashach

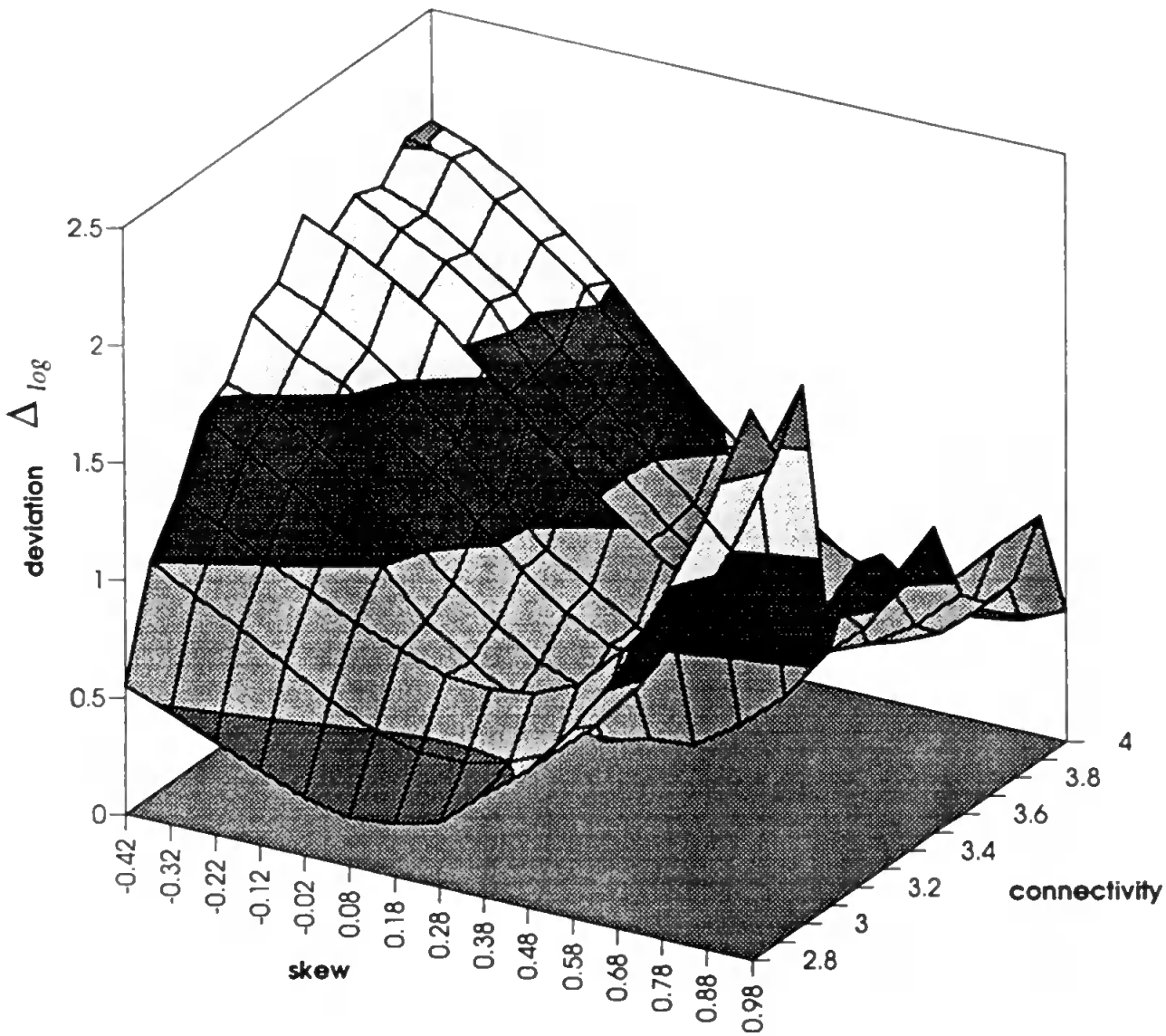

Figure 5.17 Deviations for combinations of skew and connectivity for the logarithmic method for 212B

diameter range and the comparison method used, they are not comparable as between different samples and methods. Ideally, a deviation surface would be hoped for which decreased monotonically to a minimum value, which would lie away from the boundary values. In practice, no surface has ever met both these criteria. Fig. 5.16 shows a fairly smooth surface produced using the linear method with a minimum at a skew of 0.1 and a boundary connectivity of 2.8, as is also noted in Table 5.3. At connectivities below 2.8, isolated pore and throat systems appear. Fig. 5.17 shows a surface with local minima and maxima arising from the application of the logarithmic method to reservoir sandstone sample 212B.

Close investigation of the causes of the local maxima and minima in surfaces such as are shown in Fig 5.17 shows that they arise partly from the lack of complexity of the unit cell. The global minima which occur at the boundaries of the surfaces in Figs. 5.16 and 5.17, also suggest that the unit cell might not be sufficiently versatile. Any increase in the size and complexity of the unit cell would involve the introduction of an additional range of geometric parameters to construct it. This new cell could then usefully be matched with additional experimental data such as scanning loops (repeated intrusion / extrusion cycles) (Wardlaw 1990) and time-dependent porosimetry (Yuan *et al.* 1989). However, such experiments require large, usually unacceptable, amounts of operator time, and can give rise to accumulative errors. Thus for the time being the philosophy has been to keep the model geometry relatively simple, whilst investigating the simulation of a wide range of properties.

5.3.3 *Linear top fit*

The linear top fit method was developed for samples whose mercury intrusion curves are influenced by edge effects, or for samples where the upper part only of the mercury intrusion curve is of interest. Previous results have shown an edge correcting

method of extending the experimental mercury intrusion curve down from the point of inflection. This method is very arbitrary and so the linear top fit method has been developed so that no alteration to the experimental data needs to be made. The measure of fit concentrates on data above the point of inflection. The inclusion of clay in samples affects the smaller pores and throats more than the larger ones. This next section describes how clay precipitation was simulated in Fontainebleau sandstone, the effect it had on the mercury intrusion curve and how Pore-Cor could simulate the void-space of the samples.

5.4 Clay included samples

Pore-Cor has been used to simulate the small but important changes in void-space dimensions which occur when small amounts of illite and kaolinite are artificially deposited inside Fontainebleau sandstone samples. Such clay minerals, when they occur in sandstones, have a detrimental effect on the reservoir properties (Wilson *et al.* 1977), so that an understanding of their effects is of great importance in oil and gas reservoir engineering. However, because of the complex nature of the void space in sandstones, researchers and engineers have had few theories with which to interpret their measurements of the extent to which clay inclusions affect permeability, and to interpret their studies of formation damage, i.e. the alteration and destruction of these inclusions.

Experimental methods have recently been developed whereby clay minerals can be artificially precipitated within the pore space of sandstones (Small *et al.*1992a, 1992b). Illite, illite-smectite and kaolinite formed by these methods have chemical compositions and crystal morphologies indistinguishable from clay inclusions in reservoir sandstones. A direct evaluation of the effect of deposited clays on reservoir properties can be made by comparing the pore-level properties of clay-free sandstones with the properties of equivalent samples in which clay minerals have been artificially precipitated. The effect of the precipitated minerals on the mercury intrusion curves of the samples can then be

related back to changes in the void structure by means of the computer model (Matthews *et al.* 1995b).

A comparison of the mercury intrusion curve of an untreated plug of Fontainebleau sandstone with that of a similar plug in which small amounts of illite and kaolinite have been precipitated has been made. The Pore-Cor model is used to generate void space structures from these intrusion curves and the sample porosities, and then to generate and analyse the differences in tortuosity (Spearing *et al.* 1991b) and permeability (Matthews *et al.* 1993) between the untreated and clay precipitated plugs.

5.4.1 *Artificial clay precipitation*

The actual clay precipitation was carried out at Manchester University by Dr. Joe Small. Some of the electron microscopy and all of the mercury porosimetry experiments and structure simulations were part of this PhD project.

Clay minerals were precipitated in the void space of a 12.5 mm diameter core of Fontainebleau sandstone using a method based on that of Small *et al.* (1992a, 1992b). Fontainebleau sandstone is an exceptionally pure quartzite from the Eocene of the Paris Basin. The sandstone is cemented exclusively by quartz overgrowths and has virtually no clay content (Thiry *et al.* 1987).

A 75 mm long plug of the sandstone was ground on a diamond lap to be a close fit in a 12.5 mm diameter gold capsule, the latter incorporating a cup-shaped cap with a 2 mm diameter gold tube welded in the centre. A 25 mm length of the plug was cut off for the clay precipitation experiment as shown in Plate 5.1, while the remainder was retained for a mercury intrusion and scanning electron microscopy (SEM) study of the untreated sandstone. One end of the capsule was crimped and welded with a DC arc, and 0.3 g of an amorphous gel of composition $Al_2O_3.2SiO_2$ was placed in it. The sandstone plug was then placed on top of the gel. Potassium hydroxide solution was added through

Plate 5.1 Plug used for the clay precipitation

Plate 5.2 Sectioned plug

the small tube in the cap (1 mL, 0.1 M), which was then welded without boiling the solution. The sealed capsule was placed in a 15 mm diameter hydrothermal pressure vessel, and maintained at 350 °C and 1 kbar for 23 days.

Following this hydrothermal treatment the capsule was opened so that the crystallised gel and the sandstone plug could be recovered. X-ray diffraction (XRD) showed that the gel itself had crystallised mainly into kaolinite, but there were indications that illite-smectite and illite were present. The outside surface of the sandstone plug was coated in a deposit which was identified as kaolinite, but with a greater proportion of illite-smectite than the gel sample. The 25 mm long plug was sectioned longitudinally and transversely as shown in Plates 5.2, 5.3 and 5.4. Plate 5.3 shows a transverse section of the plug and Plate 5.4 shows a longitudinal segment of the section shown in Plate 5.3. The extent and nature of the clay precipitation in these various segments were examined by SEM. Plate 5.5 shows the clean quartz grains of the untreated Fontainebleau sandstone sample. Plate 5.6 shows the clay-precipitated sample at a section plane 2mm from the end of the plug. Kaolinite was identified with the aid of energy dispersive X-ray spectra. It forms blocky shaped grains a few μm wide, and was mixed with finer-grained lath-shaped crystals which are illite or illite-smectite. Clay precipitation is much less well developed away from the outer surface of the plug (Plate 5.7), where only a few illite and kaolinite particles are observed. Plate 5.7 is however representative of the sandstone sample used for mercury porosimetry.

5.4.2 *Mercury intrusion results*

Mercury intrusion experiments were carried out on both an untreated sample and a clay-precipitated sample. Fig. 5.18 shows the resulting mercury intrusion curves for both. The upper shoulder for the clay-precipitated sample is less pronounced than that for the untreated sample. The equivalent throat diameter at 50 % pore volume intruded is also

Plate 5.3 Sectioned plug

Plate 5.4 Sectioned plug

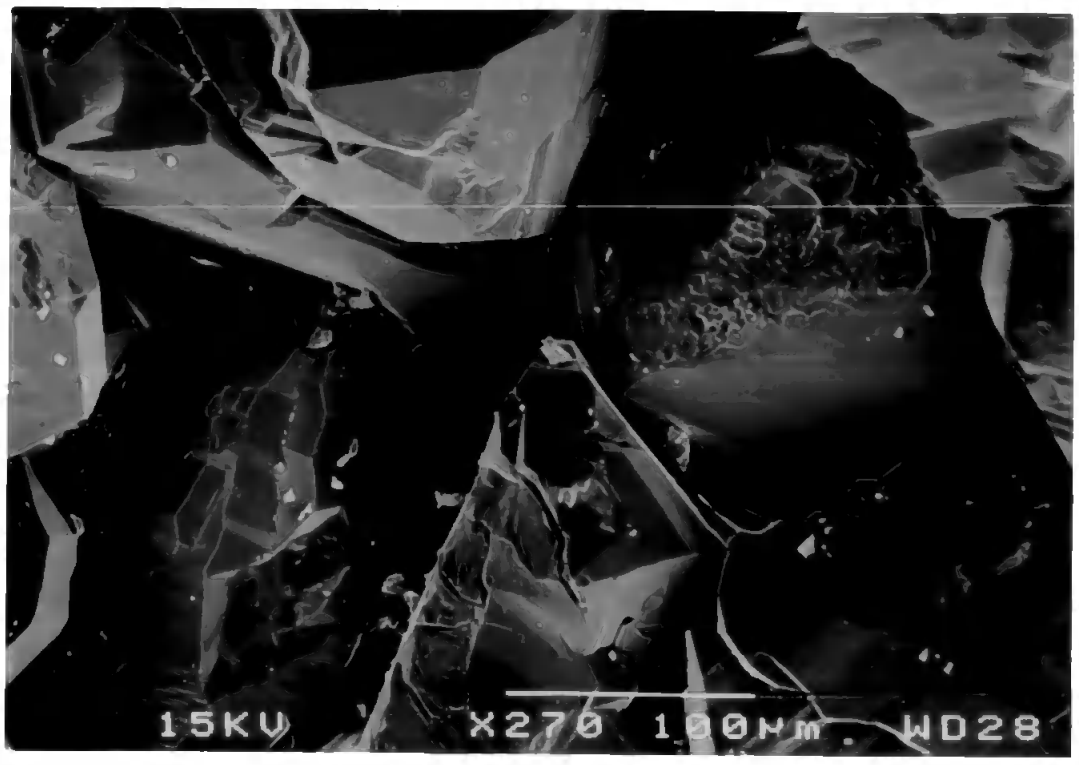

Plate 5.5 Electron micrograph of clean quartz grains of untreated Fontainebleau sandstone sample

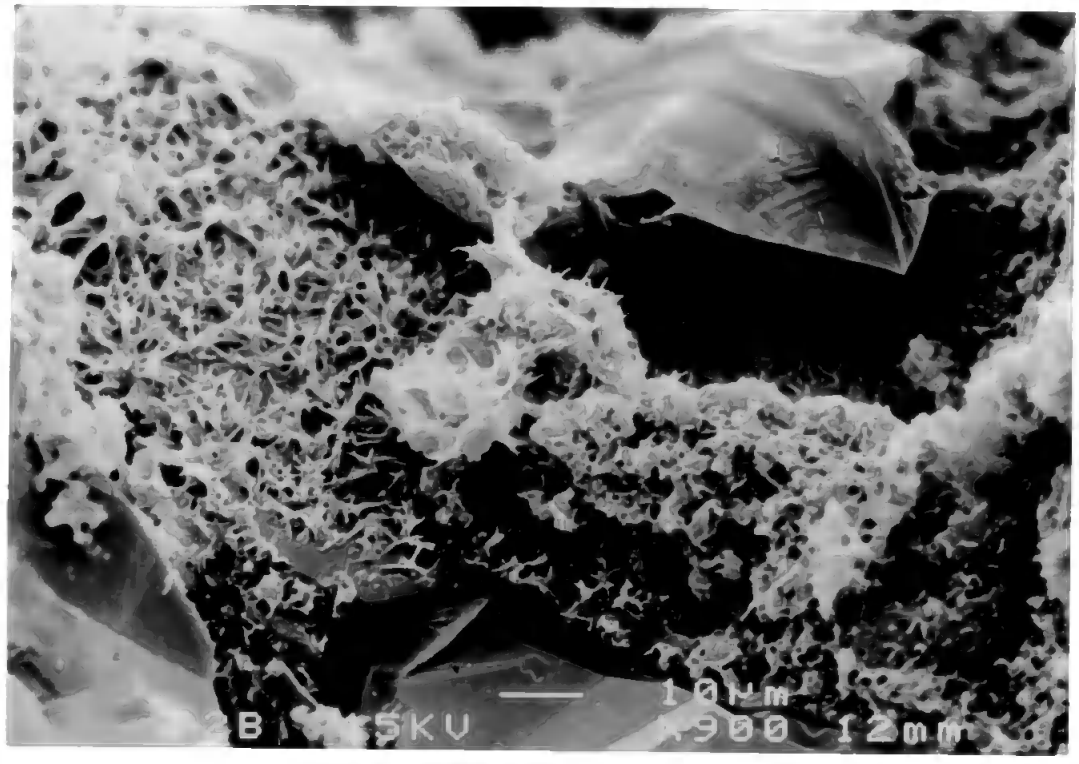

Plate 5.6 Electron micrograph of clay-precipitated sample from the end 2 mm of the plug

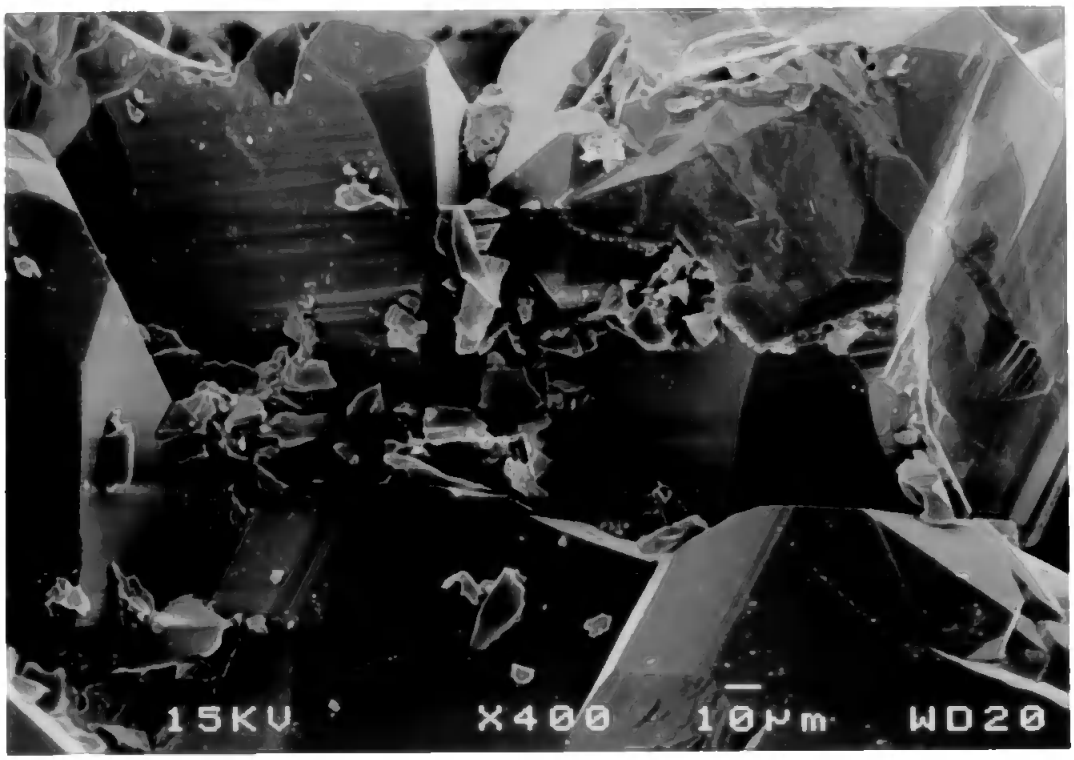

Plate 5.7 Electron micrograph of clay-precipitated sample used for the mercury intrusion

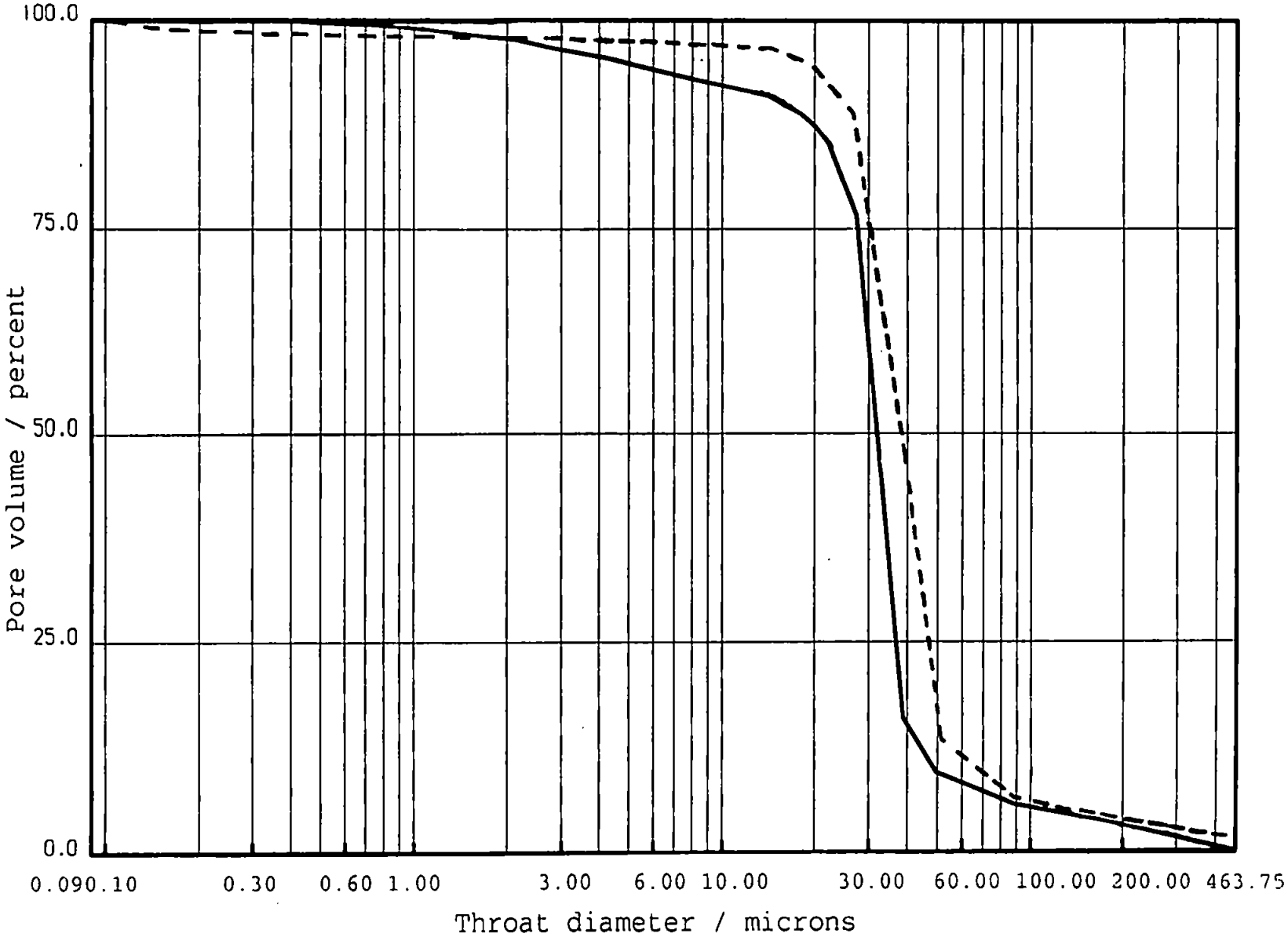

Figure 5.18 Mercury intrusion curve for untreated and clay precipitated samples of Fontainebleau sandstone: ----- untreated, —— clay precipitated

reduced. These differences are typical of clay precipitation or 'formation damage'.

The porosities of these samples were obtained from measurements of the volume of mercury intruded into the sample and the volume of the sample itself. They were corrected for mercury compression and also for the expansion of the penetrometer (Gane *et al.* 1995). Both samples had a porosity of 17 %, indicating that any porosity variation due to clay precipitation was less than the precision of the porosity measurement.

5.4.3 *Modelling of Fontainebleau sandstone samples*

The experimental mercury intrusion curves for these two samples were modelled by Pore-Cor using the linear top fit method; the resulting simulated and experimental curves are shown in Figs. 5.19 and 5.20. The least squares deviations between the experimental and simulated throat diameters in the upper, fitted, regions of the curves are shown in Table 5.4. The pore and throat size distributions which generate the simulated curves in Figs. 5.19 and 5.20 are shown in Figs 5.21 and 5.22 respectively. The porosity is correctly modelled to within the experimental accuracy of 0.1 % , as confirmed in Table 5.4.

It can be seen from Table 5.4 that the skew of the simulated throat size distribution is larger for the precipitated sample simulation than it is for the untreated. An increase in skew corresponds to an increase in the number of small pores and throats and a consequential reduction in the number of large pores and throats. The connectivity of the precipitated sample simulation is slightly lower than that of the untreated sample. These differences are what might be expected from clay precipitation.

An alternative simulation method is to reduce the size of each throat (and hence pore) in the untreated sample simulation, while maintaining the same skew and connectivity. The minimum and maximum throat sizes in the new throat size distributions are shown in Table 5.4, together with the deviation between simulation and experiment,

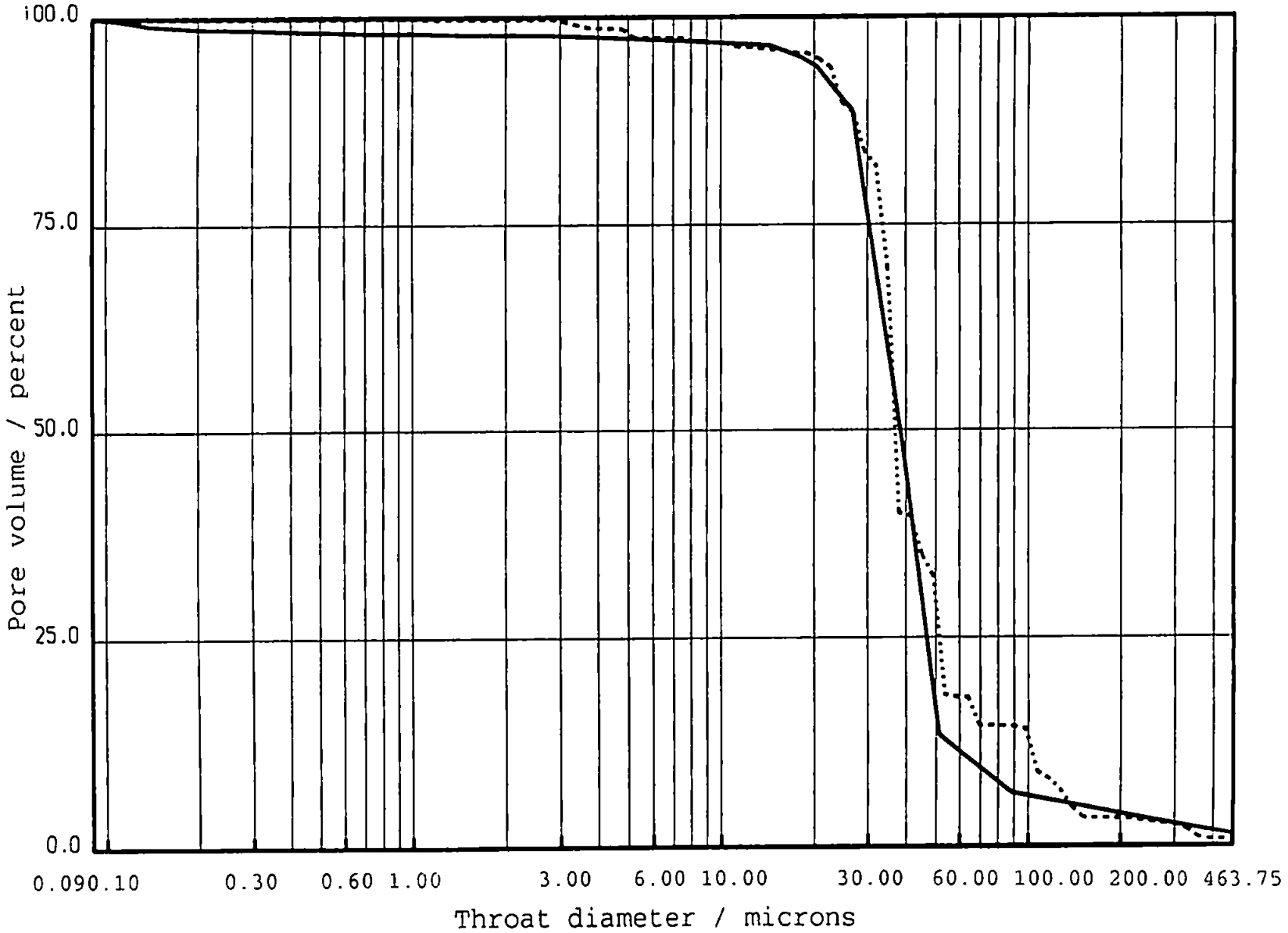

Figure 5.19 Mercury intrusion curves for untreated sample: —— experimental, ----- simulation

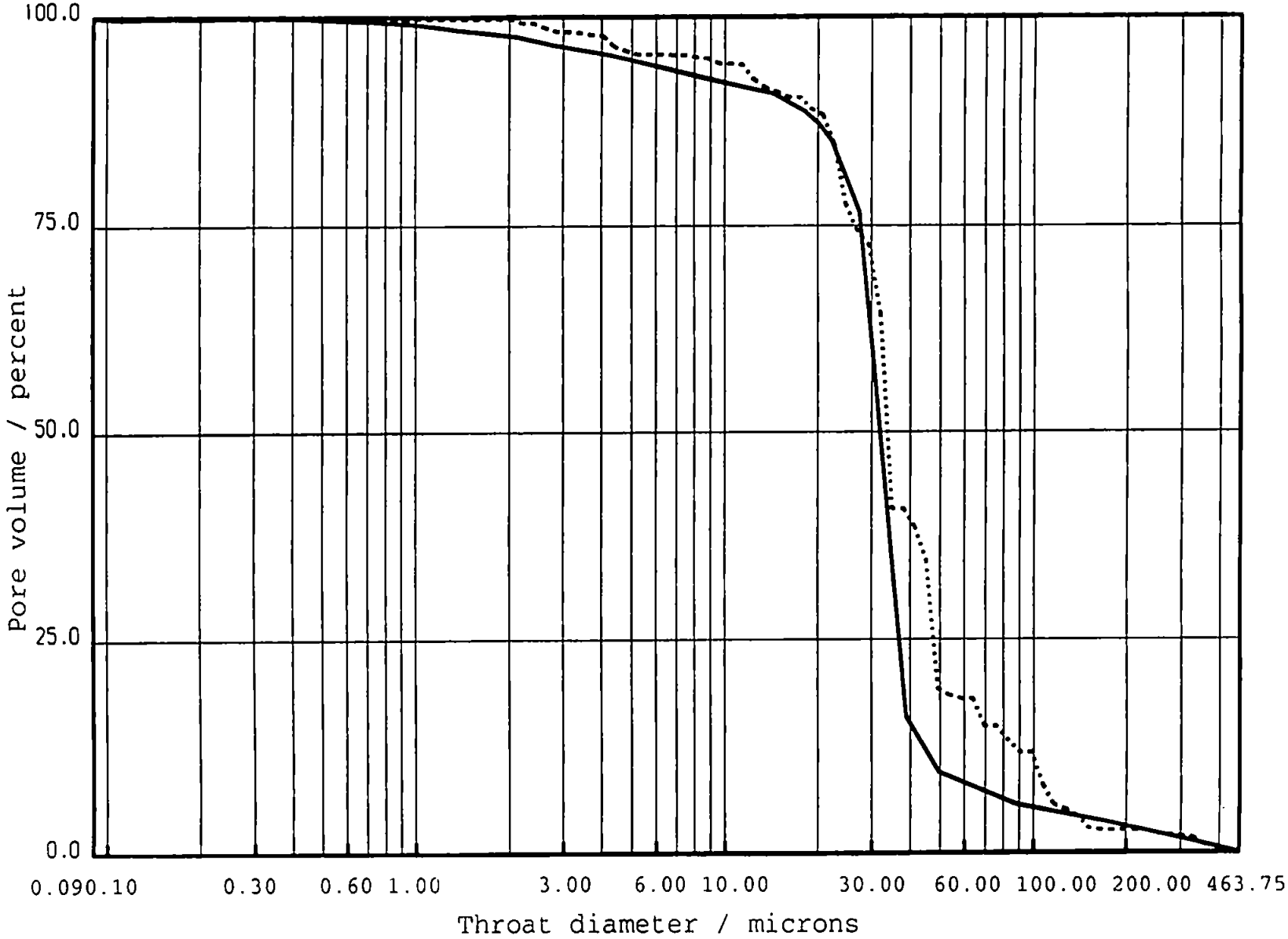

Figure 5.20 Mercury intrusion curves for clay precipitated sample: —— experimental, ----- simulation

	Experimental and simulated (identical)	Simulated				
Sample	Porosity / %	Minimum throat diameter / μm	Maximum throat diameter / μm	Skew	Connectivity	Deviation / μm
Untreated	17	0.09	463.75	-0.12	3.0	5.4
Precipitated	17	0.09	463.75	0.02	2.9	3.5
Reduced size range untreated simulation fitted to precipitated experimental curve	17	0.09	463.75	-0.12	3.0	65.7
	17	0.08	425.00	-0.12	3.0	38.2
	17	0.07	390.00	-0.12	3.0	22.2
	17	0.06	358.00	-0.12	3.0	16.1
	17	0.05	328.00	-0.12	3.0	18.7

Table 5.4 Fitted mercury intrusion parameters for untreated and clay-precipitated samples of Fontainebleau sandstone

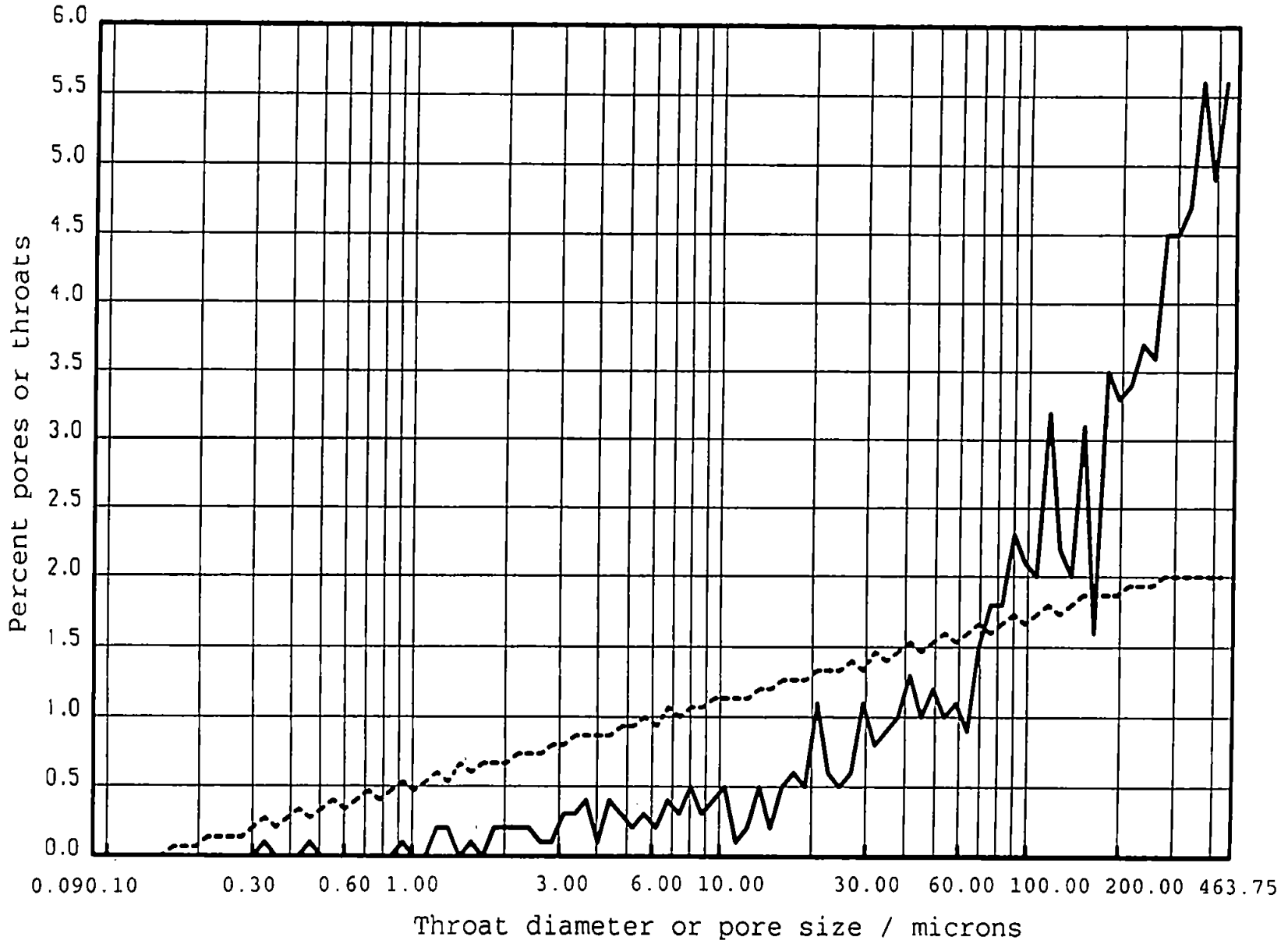

Figure 5.21 Negative skewed (-0.12 %) throat diameter distribution with pore size distribution for untreated sample: —— pores, ----- throats.

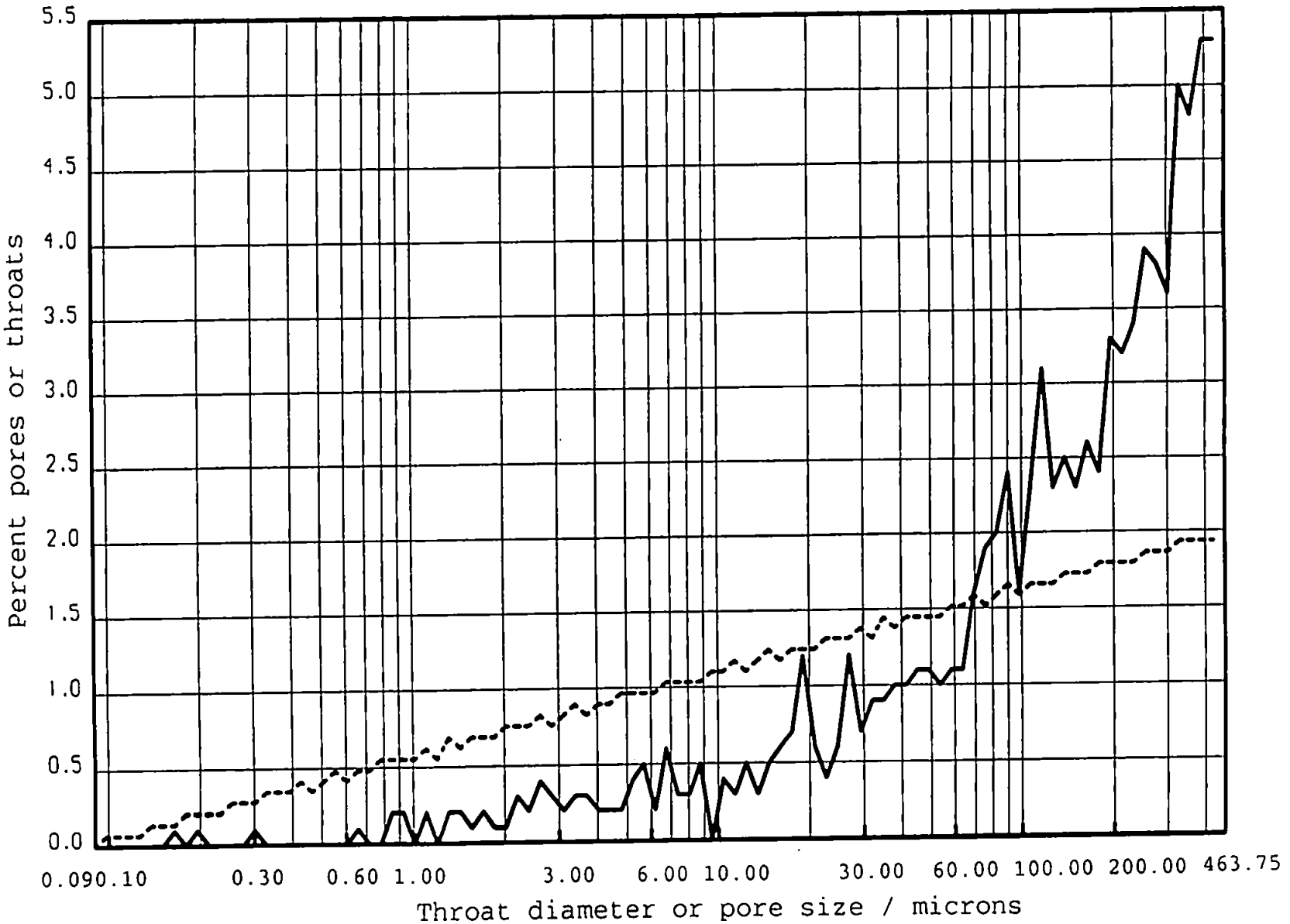

Figure 5.22 Skewed (0.02 %) throat diameter distribution with pore size distribution for clay precipitated sample: —— pores, ----- throats.

calculated as described previously in Chapter 2. The deviations show that the fit is improving as the size range is reduced, reaching a minimum of 16.13 μm at a size range of 0.6 - 358 μm. The mercury intrusion curve for this size range is shown in Fig. 5.23. However, the deviation of this simulation is considerably higher than that of the simulation curve with optimised skew and connectivity. It may thus be regarded as confirmed that the clay precipitation either causes void- size reductions that are different from those of the simple size reduction procedure, or that it causes a reduction of connectivity, or both.

5.4.4 *Tortuosity and permeability*

The samples of untreated and treated sandstone were small and irregular in shape, which made the experimental measurement of tortuosity impossible. The median together with the first and third quartile values Q(1) and Q(3), of the simulated tortuosities are shown in Table 5.5. The simulated tortuosity of the clay-precipitated sample is larger than that of the untreated sample. This is due to the lower connectivity which decreases the availability of the more direct paths through the unit cell, forcing a tortuous path to be taken instead. The connectivity reduction would also be expected if some of the pathways through the sample were blocked by clay.

The alternative unit cell, where the reduced size range has been used, has the same median tortuosity as the unit cell of the untreated material, but the upper and lower quartile values show that the alternative unit cell has a much wider spread of tortuosity.

As mentioned above, the samples of untreated and treated sandstone were small and irregular in shape, which also made the experimental measurement of permeability impossible. However, Pore-Cor can simulate the permeabilities of the void space structures derived from the fitting of the simulated mercury intrusion curve to the experimental curve. The simulated permeabilities of the three unit cells are shown in Table 5.5. The untreated sample has a simulated permeability of 7.0 mD. The clay-precipitated

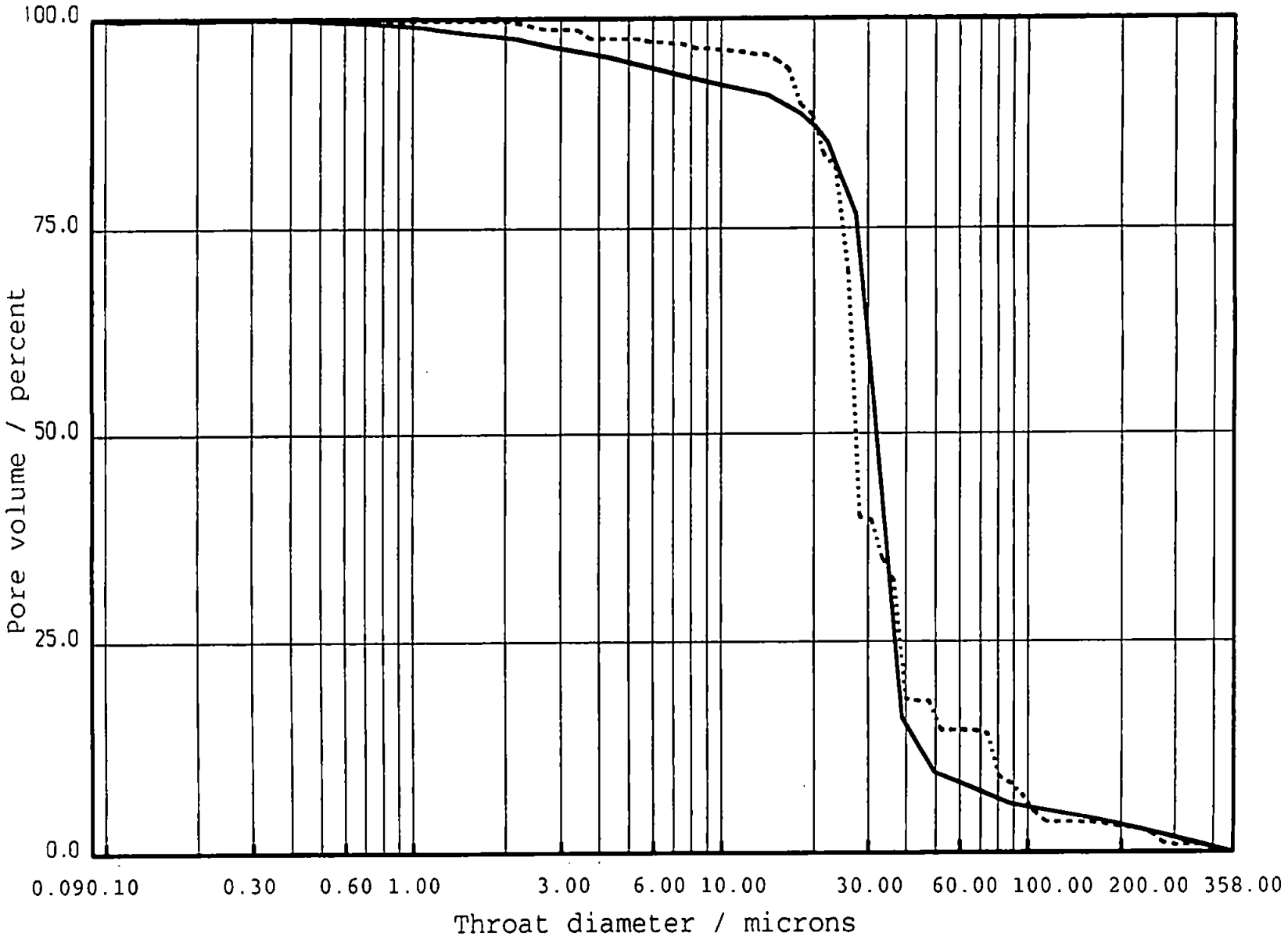

Figure 5.23. Mercury intrusion curves for clay precipitated sample with reduced untreated sample throat diameter and pore size distribution: —— experimental, ----- simulation

Sample	Tortuosity			Permeability / mD
	Q(1)	median	Q(3)	
Untreated sample	3.0	3.0	3.2	7.0
Clay precipitated sample	3.7	3.9	4.3	3.0
Reduced size range	2.2	3.0	3.6	4.0

Table 5.5 Tortuosity and permeability for untreated and clay-precipitated samples of Fontainebleau sandstone

sample with the optimised pore and throat size distribution has a simulated permeability of 3.0 mD, whilst the reduced size range sample has a value of 4.0 mD. These permeabilities only represent relative values which can be used to define the trend between the untreated and clay-precipitated samples; the actual permeability is likely to be significantly higher than these values (Matthews *et al.* 1993). The two clay-precipitated samples have lower permeabilities than the untreated sample indicating that the simulated structures can correctly model the trends in permeability caused by clay inclusions in the sample. The results show that Pore-Cor can be used to model the effects of clay precipitation, and even though they were too small for a change in porosity to be observed, their values could be compared and their trends are realistic.

5.5 Hysteresis

Void-space networks, with the correct porosity, have been used to simulate the hysteresis which occurs when the mercury is withdrawn. The effects of contact angle hysteresis and trapping within wide pores adjacent to narrow throats have been demonstrated. Considerable trapping of mercury has been found to occur because of snap-off effects, without invoking any dead-end pores.

5.5.1 *Hysteresis simulations*

As an example of the secondary imbibition simulation, the reservoir sandstone sample 212B was modelled, using the parameters listed in Table 5.3 which were obtained by the linear optimisation of the simulated onto the experimental intrusion curve .

Fig. 5.24 shows the effect of contact angle hysteresis. (The values of pressure on the abscissa are related to the throat diameters by eqn [1.2], although eqn [1.1] must be used for the secondary imbibition.) As the contact angle θ is reduced from 140° to 130° and then to 120°, the mercury meniscus becomes flatter, i.e. the mercury is more difficult

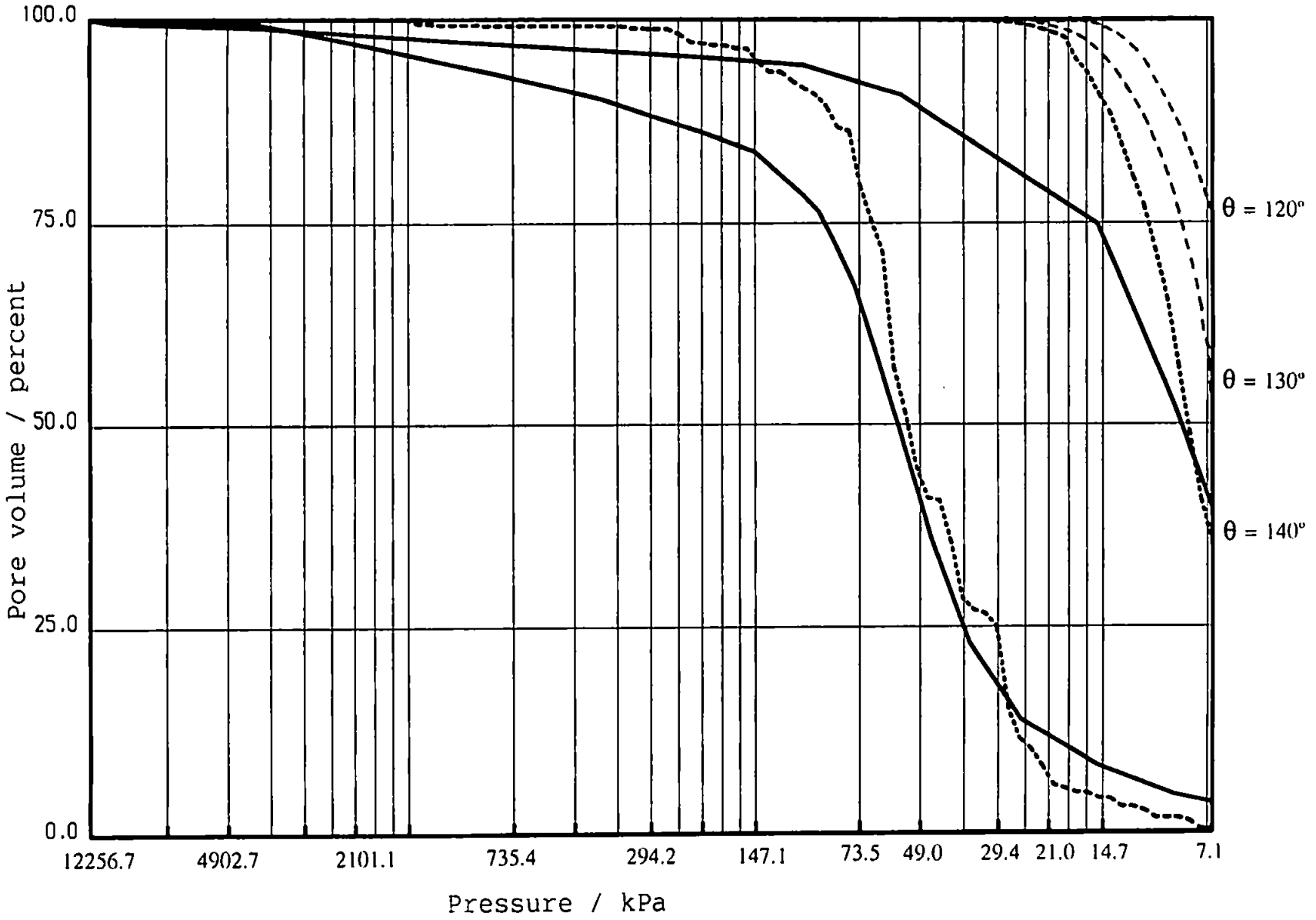

Figure 5.24 Effects of contact angle, θ, on hysteresis for R=5: —— experimental, ----- simulation

extract. It can be seen that the residual saturation at a pressure of 7.1 kPa increases substantially, from 35.1 % to 57.5 % and then to 77.0 %. The trapping ratio R was set at a value of 5, which is a realistic value for sandstone, because smaller values lead to a rapid increase in trapping reaching 100 % at a value of 1.

In Fig. 5.25 the contact angle has been set at 140°. As R was arranged to take values of 2, 5 and 100, the residual saturation decreased to 39.1 %, 35.1 % and 28.6 %. The correct residual saturation at 7.1 kPa occurred at θ = 140° and R = 2. The correct residual saturation could also be achieved with other combinations of θ and R values. However, all the imbibition curves shown in Figs. 5.24 and 5.25 exhibit a later and more sudden decrease in trapping with decreasing pressure than is observed experimentally.

Varying θ and R causes similar effects in other imbibition simulations. For example, Fig. 5.26 shows the experimental imbibition curve for the Clashach sandstone sample, together with simulations for θ = 120° and R = 5, and θ = 140° and R = 2.

5.5.2 *Discussion*

Some light can be thrown on the nature of the imbibition curves by comparing them to a 'total-pathway' secondary imbibition curve (or total-pathway intrusion curve) in which there is no pathway limitations, i.e. one in which each individual pore and throat independently empties (or fills) at a pressure determined by eqn [1.1]. An imbibition curve of this type is shown in Fig. 5.27 for θ = 140°. It is drawn as a long-dashed curve, but over most of its length it is identical to the secondary imbibition curve with θ = 140° and R = 5 based on the algorithm described above. A comparison of the curves reveals two effects. Firstly, the requirement for withdrawal of mercury to begin on the unit cell's lowest row of pores causes a retention of mercury, as might be expected. The total-pathway curve passes through 99.90 % pore volume at a pressure of 115 kPa (d=12.8 μm) whereas when the lowest row constriction is applied it does not descend through 99.90 %

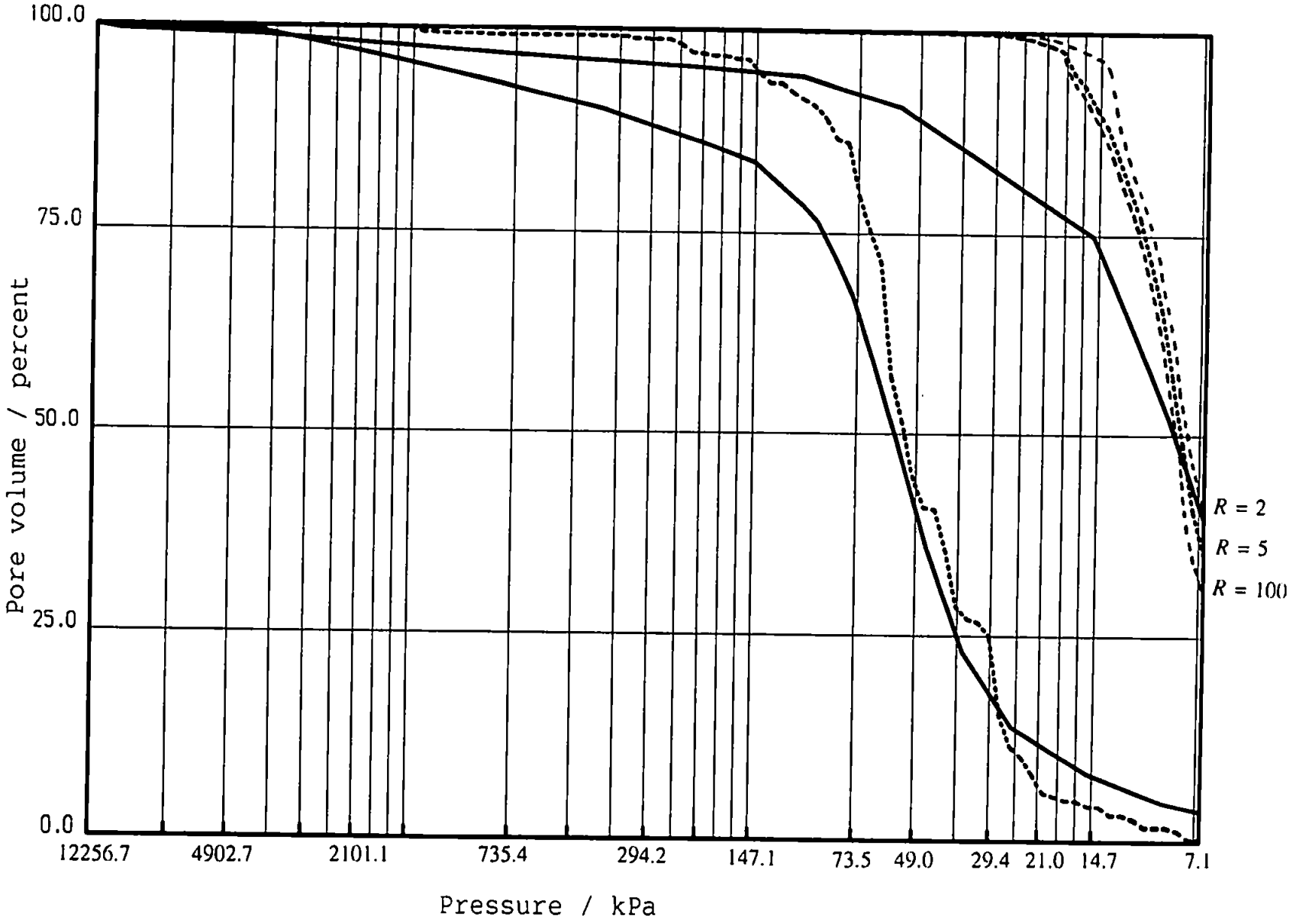

Figure 5.25 Effects of pore size : throat diameter ratio, R, on hysteresis for θ=140°: —— experimental, ----- simulation

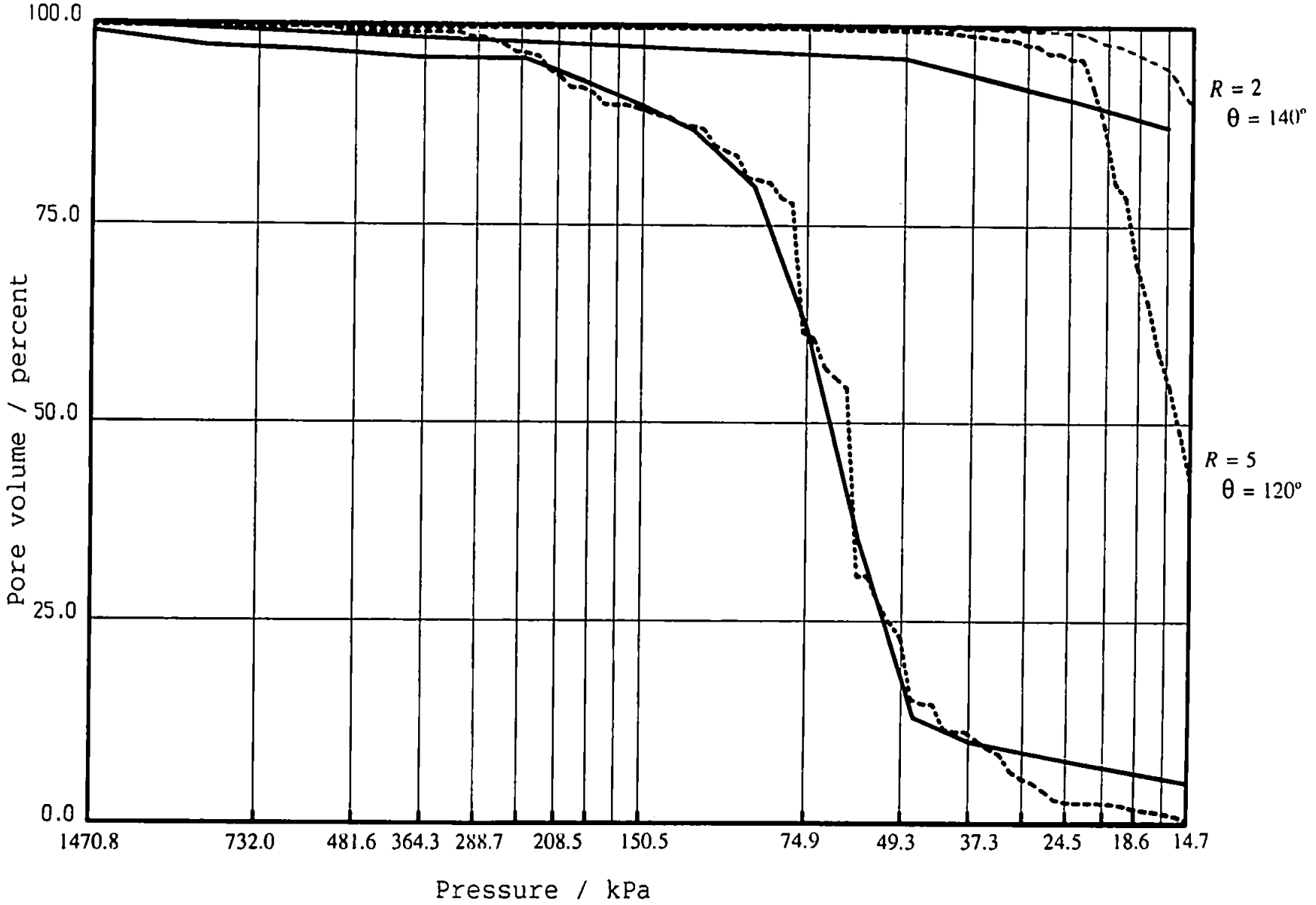

Figure 5.26 Hysteresis curves for Clashach: —— experimental, ----- simulation

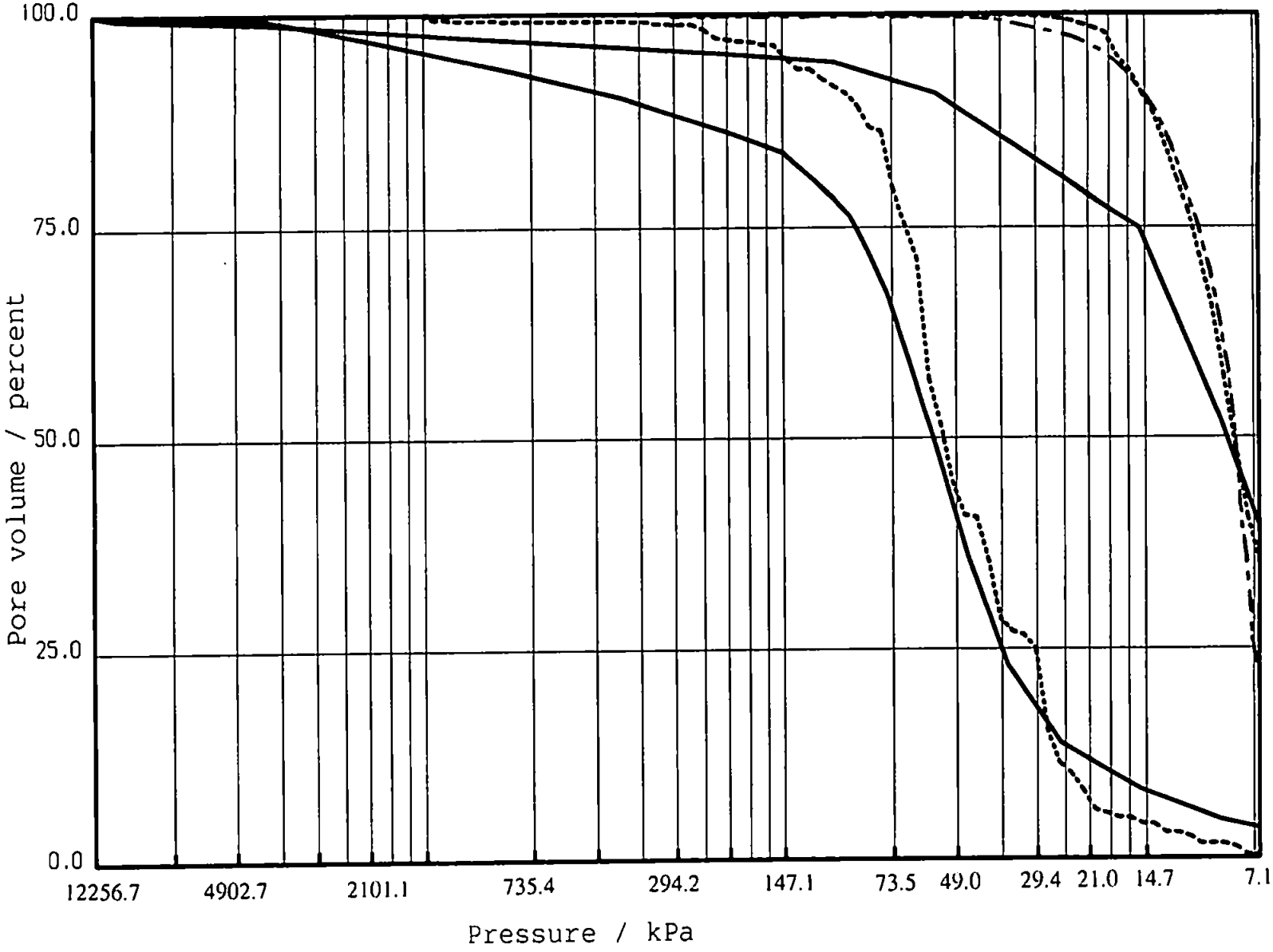

Figure 5.27 Mercury intrusion and extrusion hysteresis, with and without shielding for sample 212B, - - - - - with shielding effects, ———— without shielding effects.

until the pressure has decreased to 37.2 kPa (d=39.5 μm). Secondly, snap-off effects cause mercury to be trapped in some large pore-throat-pore systems. This makes itself apparent as a slight discrepancy between the two curves at the lowest pressure. Snap-off causes a trapping extent of 21 % for the total-pathway simulation as compared with 35 % at a pressure of 7.1 kPa (d= 207.2 μm). The 35 % of the mercury which is trapped at this pressure is shown black in Fig. 5.28.

The experimental secondary imbibition curve of Fig.5.27 lies, for the most part, between the simulated intrusion and secondary imbibition curves. Remembering that in the simulation it is assumed that intrusion is controlled by the size of throats and secondary imbibition by the size of pores, it would be easy to suppose that imbibition was part throat-diameter and part pore-size controlled. An alternative explanation would be based upon the simplistic geometry of pores and throats of the model. Cebeci (1980), for example, has shown that conical pores fill at a lower pressure than expected. However, such ease of filling is accompanied by a corresponding difficulty of emptying, and therefore does not change the extent of hysteresis. Conversely, the spherical shape of a pore can hinder mercury intrusion (Tsakiroglou *et al.* 1991), but again, no hysteresis occurs because of the geometry alone.

The most likely explanation of the discrepancy between the simulated and experimental imbibition curves lies in the fact that the experimental imbibition curve for Clashach sandstone lies closer to the top axis before it descends, i.e. lies closer to the simulation of Fig. 5.26. The discrepancy can be attributed to the principal difference between Clashach and reservoir sandstones, namely the clay inclusions in the latter. These increase the complexity of the geometry of the void volume and indicate the necessity of increasing the complexity of the simulation geometry.

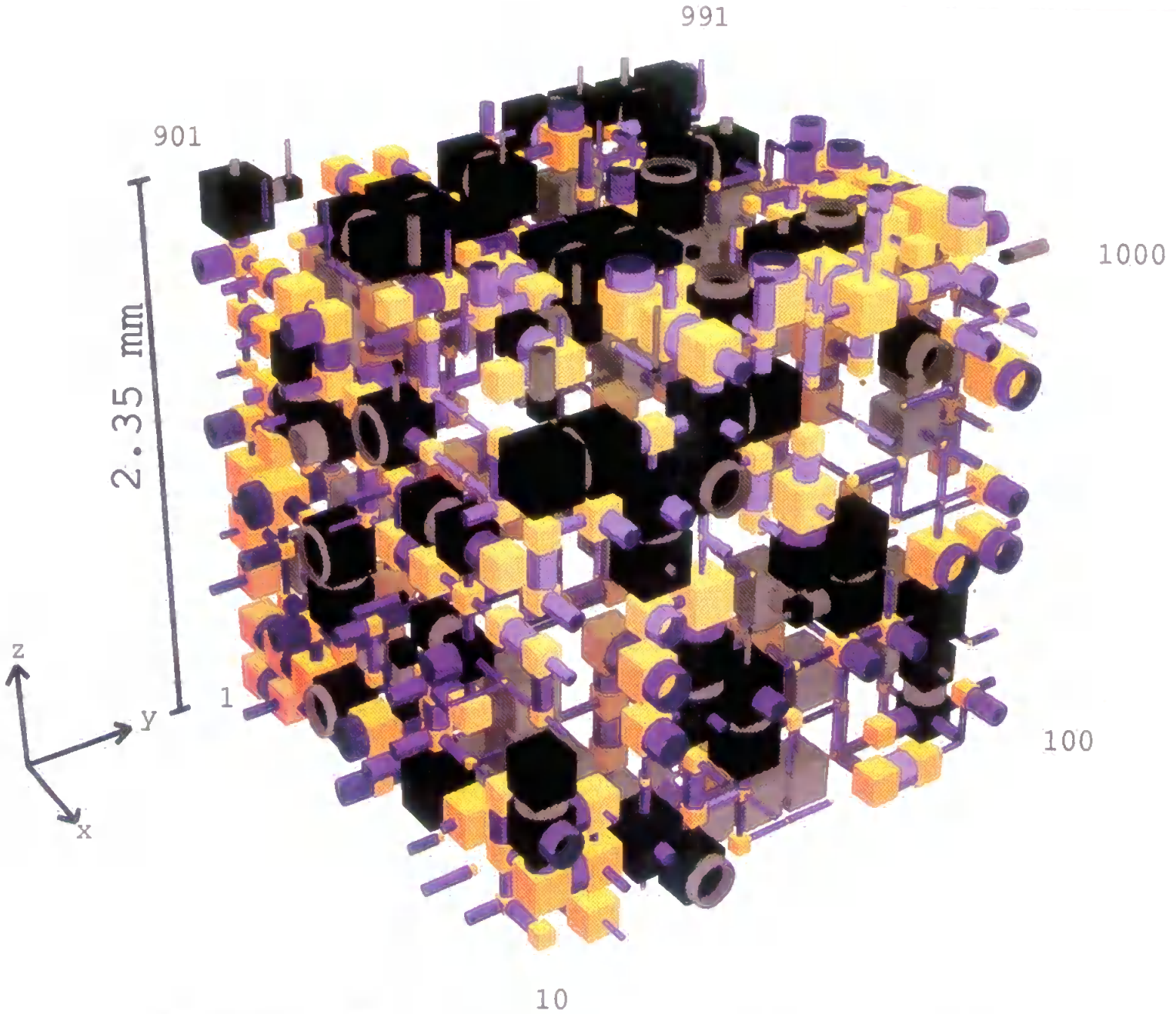

Figure 5.28 Unit cell for 212B pores filled with residual mercury shown in black

CHAPTER 6

PAPER COATING MEASUREMENTS

In Chapter 4 the correction terms for mercury and sample compression and penetrometer expansion were described, which have been incorporated into the Pore-Comp program. This chapter illustrates the use of Pore-Comp for nine different paper coating samples. Also shown are the effects of different drying conditions for clay/latex and clay/starch samples, and the interesting hysteresis curves which were generated. The hysteresis effects led on to an investigation of where exactly the mercury was trapped. Three samples were investigated by using the cryo-stage of the University's JEOL 6100 Scanning Electron Microscope and the results are illustrated.

6.1 Description of samples used to illustrate Pore-Comp

The calcium carbonate samples were produced by ECC International Europe, and have the trade names Carbital 90, Carbital 60 and LX 60, (see Table 6.1). Carbital 90 is a fine paper-coating grade of calcium carbonate made from ground marble which has 90 % by weight of its particles finer than 2 μm. In Carbital 60, 60 % of the particles are finer than 2 μm. LX 60 is made from limestone and has 60 % finer than 2 μm, but also has fewer fine particles than a conventional carbonate pigment, i.e. it has a steeper particle-size distribution. Fig. 6.1 shows the different particle-size distributions for these three calcium carbonates, as measured with a Micromeritics Sedigraph by John Kettle.

A study has also been made of Carbital 90 mixed with 12 parts per hundred (pph) by weight, relative to 100 parts of dry pigment, of three different latex binders. The first was an Acronal[1] styrene-acrylic copolymer latex (S801), with a glass transition temperature

[1]Acronal is a tradename of BASF, P.O. Box 4, Earl Road, Cheadle Hulme, Cheshire.

Type of Sample	Commercial name	Sample characteristics	Sample weight / g	Characteristic pressure P_{50}	Porosity ϕ^1, $\phi_{mercury}$, ϕ_{calc}	Compressibility ψ_m / 10^{-10} Pa^{-1}	Bulk modulus M_m
Dried slurry; finely ground calcium carbonate	Carbital 90	90% by weight < 2 μm	1.2777	23 MPa	26.2%, 28.4%, 26.1%	0	∞
	Carbital 60	60% by weight < 2 μm	1.6972	11 MPa	28.8%, 29.3%, 28.7%	0.51	20 GPa
	LX 60	60% by weight < 2 μm, steeper distribution	1.5738	5 MPa	40.9%, 42.0%, 39.7%	2.4	4.1 GPa
Dried coating colour; Carbital 90 with added latex binder	Carbital 90 + 12 pph Acronal S801	Styrene / acrylic latex T_g = 26 - 44 °C	0.7690	13 MPa	19.4%, 24.9%, 22.5%	0	∞
	Carbital 90 + 12 pph Revinex 95L10	Styrene-butadiene latex T_g = 5 °C	0.6757	16 MPa	19.3%, 22.7%, 19.2%	0.48	21 GPa
	Carbital 90 + 12 pph DL 950	Styrene-butadiene latex T_g = 8 °C	0.7539	15 MPa	21.3%, 25.2%, 20.5%	0.72	14 GPa
Plastic pigment	Lytron 2601	Solid polydisperse polystyrene spheres, av. diam. = 0.612 μm. For gloss	0.352	9 MPa	27.9%, 32.5%, 30.0%	0.87	12 GPa
	Lytron 2301	Solid polydisperse polystyrene spheres, av. diam. = 0.316 μm. For gloss	0.3552	35 MPa	23.2%, 30.7%, 25.1%	1.4	6.9 GPa
	Ropaque HP91	Hollow spheres, mean diam. 1.012 μm For gloss & opacity	0.1159	5 MPa	32.9%, 41.1%,40.1%	6.4	1.6 GPa

Table 6.1 Paper coating sample details

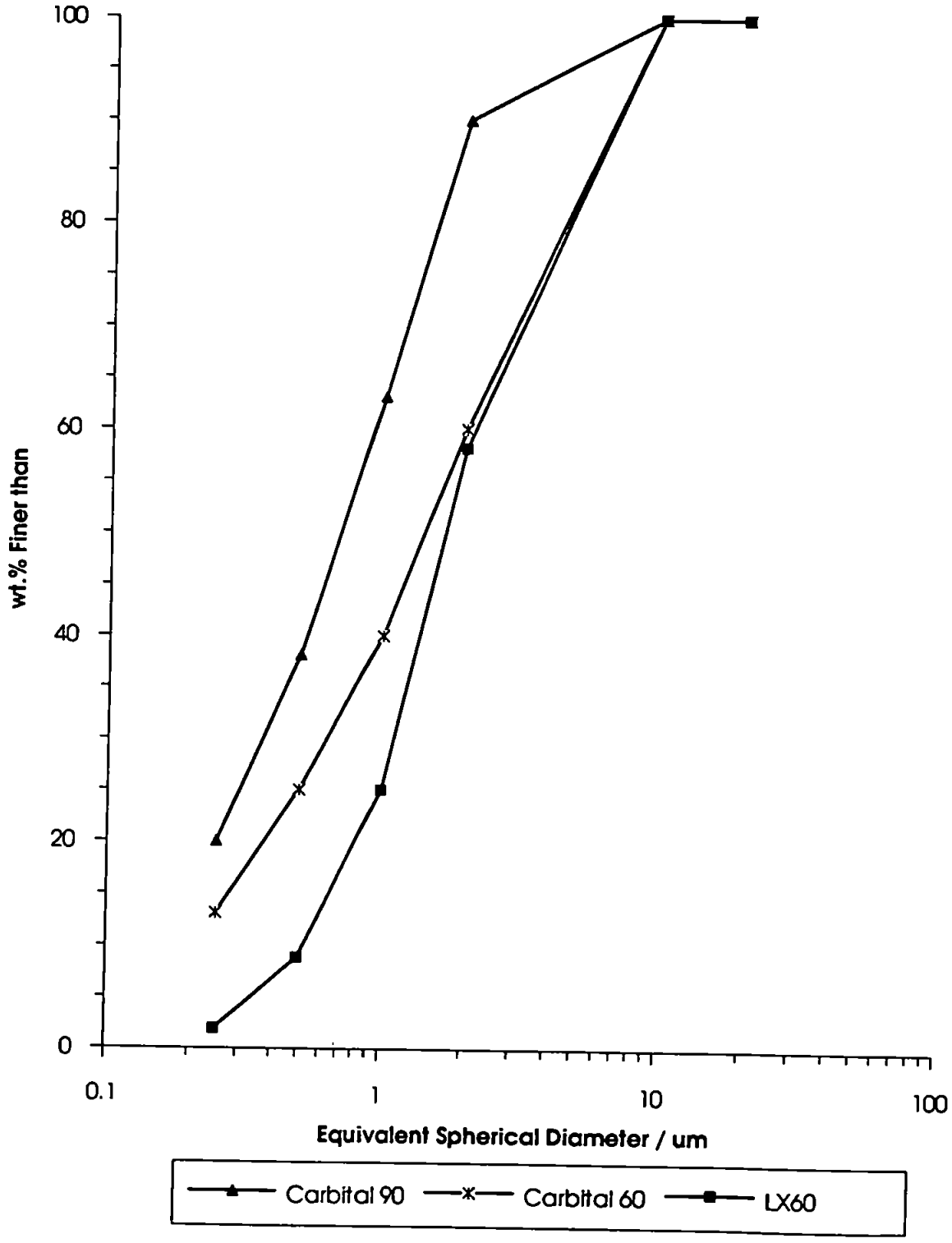

Figure 6.1 Particle size distribution of dispersed calcium carbonates

T_g in the range 26 - 44°C, and a pH of 8 to 8.5. The second binder was a Revinex[2] styrene-butadiene latex (95L10), with a T_g around 5°C. The third, DL 950[3], was a carboxylated styrene-butadiene copolymer, with a T_g of 8°C, and a pH of 5.5.

Three synthetic pigments were also studied. Two of them, designed to enhance gloss, consist of aqueous dispersions of solid spheres made from styrene copolymer: Lytron 2301[4], which has a quoted mean particle diameter of 0.3 μm, and Lytron 2601 with a quoted mean particle diameter of 0.6 μm. The pH values of these pigments are in the range of 8.7 - 9.3 and their T_g values are greater than 60°C. The third pigment, Ropaque HP91[5] developed to impart both gloss and opacity to paper coatings, is an aqueous suspension of water-filled styrene-acrylic copolymer spheres which dehydrates to form a dry, consolidated coating of hollow spheres with a mean diameter of 1 μm. The glass transition temperature of Ropaque HP91 is quoted as being greater than 95°C. The pH of the suspension is 9.5, its wet density is 1.03 g mL^{-1}, and dry density is 0.55 g mL^{-1}. The mean diameters of the three plastic pigments were measured as 0.32 μm, 0.61 μm and 1.01 μm respectively by photon correlation spectroscopy, and the Ropaque HP91 was shown to be essentially monosized by electron microscopy.

All the samples in this study were homogeneous lumps of dried coating material. Although such lumps are never encountered in paper making, their study provides a basis for understanding the properties of paper coating constituents; Alince and Lepoutre, for example, have studied the porosity and opacity of clay coated onto a transparent polyester film (Alince *et al.* 1980b), and of a coating made solely from plastic pigments (Alince *et*

---

[2]Revinex is a tradename of Doverstrand Ltd, Temple Fields, Harlow, Essex.

[3]Dow Chemical Company, Lakeside House, Stockley Park, Uxbridge, Middlesex.

[4]Lytron is a tradename of Morton International Ltd., Speciality Chemicals Group, Greville House, Hibernia Road, Hounslow, Middlesex.

[5]Ropaque is a tradename of Rohm & Haas Company, Lennig House, 2 Mason's Avenue, Croydon, Surrey.

al. 1980a). We have examined typical lump samples by electron microscopy, which shows the expected void size range and film-forming characteristics.

6.2 Porosimetry results and discussion

The mercury porosimetry experiments reported in this study were carried out using a Micromeritics 9320 porosimeter, which has an upper pressure limit of 207 MPa (30000 psi). In order to obtain results of sufficient accuracy, it was necessary to impose two important restrictions on the operating conditions of this instrument, which are also relevant when using other porosimeters. Firstly it was found that if the mercury pressure was increased too quickly, equilibrium was not achieved at each step. As a consequence, when the applied pressure was decreased from its maximum value to measure the hysteresis curve, the intruded volume initially continued to increase. To avoid this, the applied pressure had to be held for at least 1 minute at each pressure setting. Therefore, to be certain of complete equilibrium, the porosimeter was in fact held at each applied pressure for 4 minutes before measuring the intruded volume and changing the pressure.

Secondly, it was found that the expansion characteristics of the glass penetrometers could change between runs, so that it was impossible to obtain a totally reliable value of the blank volume δV_{blank} for any particular experimental run. Lee *et al.* (1973) reported problems with blank runs on a Micromeritics 903-1 porosimeter, and overcame them by means of a consideration of the precise geometry of the penetrometer, and the subsequent matching of empirical factors to experiment. Sufficient accuracy was obtained by using sample weights large enough for δV_{blank} to be less than 10 % of V_{int} at the highest applied pressure, and by re-measuring δV_{blank} for a particular penetrometer every few runs.

6.3 Calcium carbonate lump samples

The calcium carbonate samples Carbital 90, Carbital 60 and LX 60 were supplied in a fully dispersed slurry form containing 75 % solids by weight. Each slurry was stirred to ensure homogeneity. An amount between 5-10 g of each slurry was coated onto aluminium foil and dried at room temperature in order to form a consolidated slab of pigmented coating. Approximately 1 g of each consolidated sample was broken from the slab to produce a lump that was the full depth of the dried slab. The 1 g piece was then placed in the penetrometer.

The mercury intrusion and extrusion curves for these samples are shown in Fig. 6.2. The graphs show the apparent volume of mercury intruded against the applied mercury pressure P. The volume axis is in absolute units, and the total volume intruded is, therefore, dependent on the mass of a sample and its porosity, shown in Table 6.1. As can be seen, as the pressure increases, there is a sudden increase in pore volume intrusion. The characteristic intrusion pressures P_{50} at which 50 % of the void volume of each is intruded are shown in Table 6.1. (P_{50} is insensitive to the exact measure of 100 % pore volume intruded.) It can be seen that P_{50} decreases in the order C90, C60 and LX 60, in agreement with the coarsening of the particle size distribution in this series.

The graphs show the observed intrusion V_{obs} (■) and extrusion (□), which are then corrected for penetrometer expansion and mercury compression, eqn [4.8], to give the volume V_{int} for intrusion (♦) and extrusion (◊). For Carbital 90, the corrected extrusion curve diverges from the intrusion curve immediately the applied pressure is reduced. Carbital 90 is, therefore, assumed to be incompressible, according to the criteria discussed previously, as indicated by the values for ψ_{ss} and M_{ss} in Table 6.1. (The simulated intrusion curves (⊙) shown in this and subsequent figures are discussed later.)

Also shown are the Carbital 90 porosity, ϕ^1 at atmospheric pressure, eqn [4.19], and the uncorrected and corrected porosities, ϕ_{uncorr} and ϕ_{corr} , eqns [4.21] and [4.22],

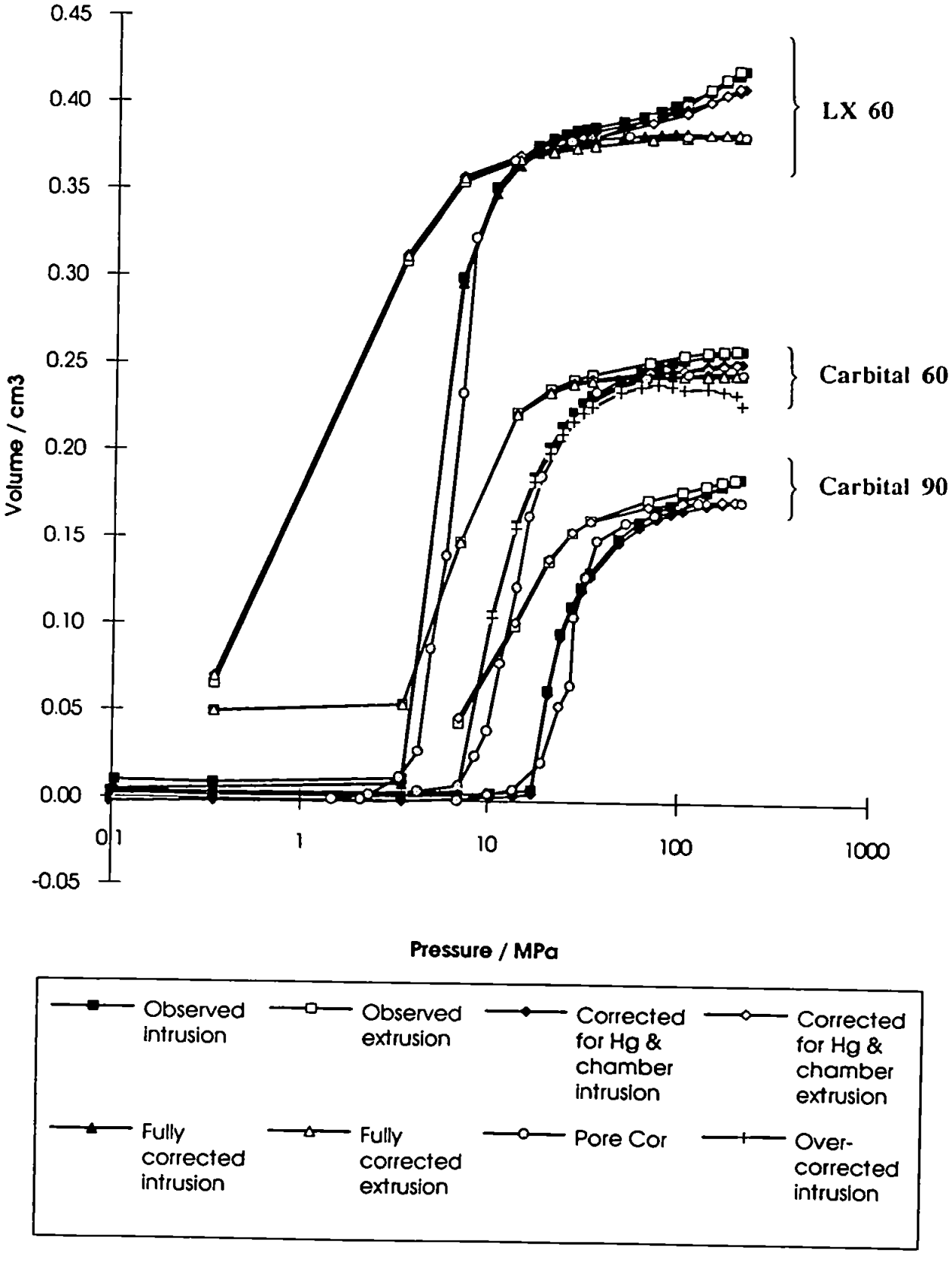

Figure 6.2 Mercury intrusion and extrusion curves for Carbital 90, Carbital 60 and LX 60

determined at the maximum applied pressure. Their values are 26.2 %, 28.4 % and 26.1 %; the close agreement between ϕ^1 and ϕ_{corr} brought about by application of the correction terms provides an independent validation of the correction procedure.

The corrected extrusion curve for Carbital 60 coincides with the intrusion curve, to within experimental uncertainty, at pressures above a P^2 value of around 130 MPa, (Fig. 6.2). Also, the coincident curves increase with pressure above P^2. Thus Carbital 60 is compressible, and the intrusion and extrusion curves may be interpreted using to eqns [4.13] and [4.18] to give a solid phase compressibility ψ_{ss} of 0.51 x 10^{-10} Pa^{-1} and a solid phase bulk modulus M_{ss} of 20 GPa. Correction of the intrusion and extrusion curves for compressibility via eqn [4.18] gives the fully corrected intrusion (▲) and extrusion (△) curves, which also satisfy eqn [4.13]. Also shown in Fig. 6.2 is the effect of over-correcting the intrusion curve (+) by using a compressibility of 2 x 10^{-10} Pa^{-1} (bulk modulus = 5 GPa). The obvious error that results gives a visual measure of the sensitivity of the method in measuring compressibility.

The corresponding results for LX 60 are also shown in Fig. 6.2 and listed in Table 6.1. For both Carbital 60 and LX 60, the ϕ_{corr} values include the correction for compressibility, and their similarity with the ϕ^1 values confirms the derived compressibilities and bulk moduli.

Samples in the present study which have an infinite solid phase bulk modulus are referred to as incompressible, those with a bulk modulus between 10 GPa and 100 GPa as medium compressible, and those with a bulk modulus less than 10 GPa as very compressible. It can be seen from Table 6.1 that Carbital 90 is incompressible, Carbital 60 is medium compressible and LX 60 very compressible. Calcite in its crystalline form might be expected to be incompressible. However, as discussed previously, mineral samples are seldom formed from single macro-crystals, and the medium compressibility of Carbital 60 may be attributable to compression at microcrystalline boundaries within an

internal mosaic structure. It is more compressible than solid glass, which typically has a bulk modulus of around 40 GPa (Cook *et al.* 1993). LX 60, by contrast, is made from limestone, and its high compressibility can be attributed to its formation from the remains of marine organisms, together with a significant organic content.

6.3.1 *Carbital 90 samples with added latex binder*

The effects on Carbital 90 of adding 12 parts per hundred by weight of three different latex binders have also been investigated. The coating colour was prepared by pouring the Carbital 90 slurry, at 75 % solids by weight, into a high speed mixer, adding 12 parts per hundred by weight of the latex, and adjusting to pH 9 with sodium hydroxide. The mixture was then passed through a 53 μm screen, coated onto aluminium and oven dried at 100° C. Since this temperature is much higher than any of the glass transition temperatures, it might be expected that the latex would form a film after the coating colour reached the first critical concentration. This has been confirmed by electron microscopy.

The mercury intrusion and extrusion curves for these preparations can be seen in Figs 6.3 - 6.5. The characteristic intrusion pressures P_{50} are similar for the three samples. The atmospheric pressure porosities are all around 20 %, and once again the corrections improve the agreement between the high pressure porosities and those at atmospheric pressure. The major difference between the samples is that the Carbital 90 / Acronal S801 coating colour is incompressible, as indicated by its horizontal intrusion curve at high pressure, (see Fig. 6.3). The coating colours containing the latices 95L10 and DL 950 are medium compressible. A possible explanation of this is that the compressibility of the latter two samples is influenced by the fact that the latex forms interstices with high surface-to-volume ratio at the calcite grain contact points as the coating colour passes through the first critical concentration, whereas the Acronal S801, with a higher T_g , does not. However, this cannot be proved from the electron micrographs, because the latex

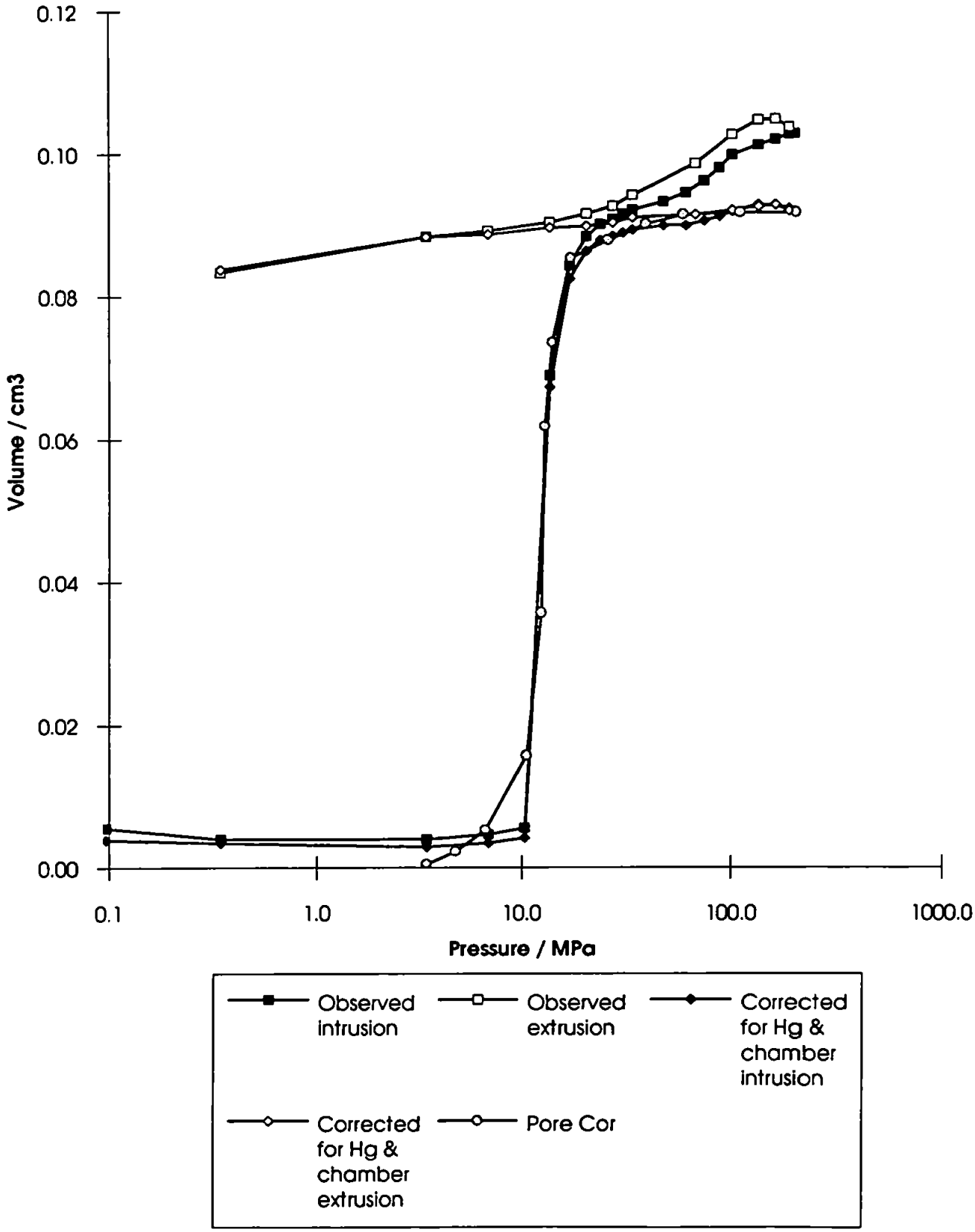

Figure 6.3 Mercury intrusion and extrusion curves for Carbital 90 + Acronal S801

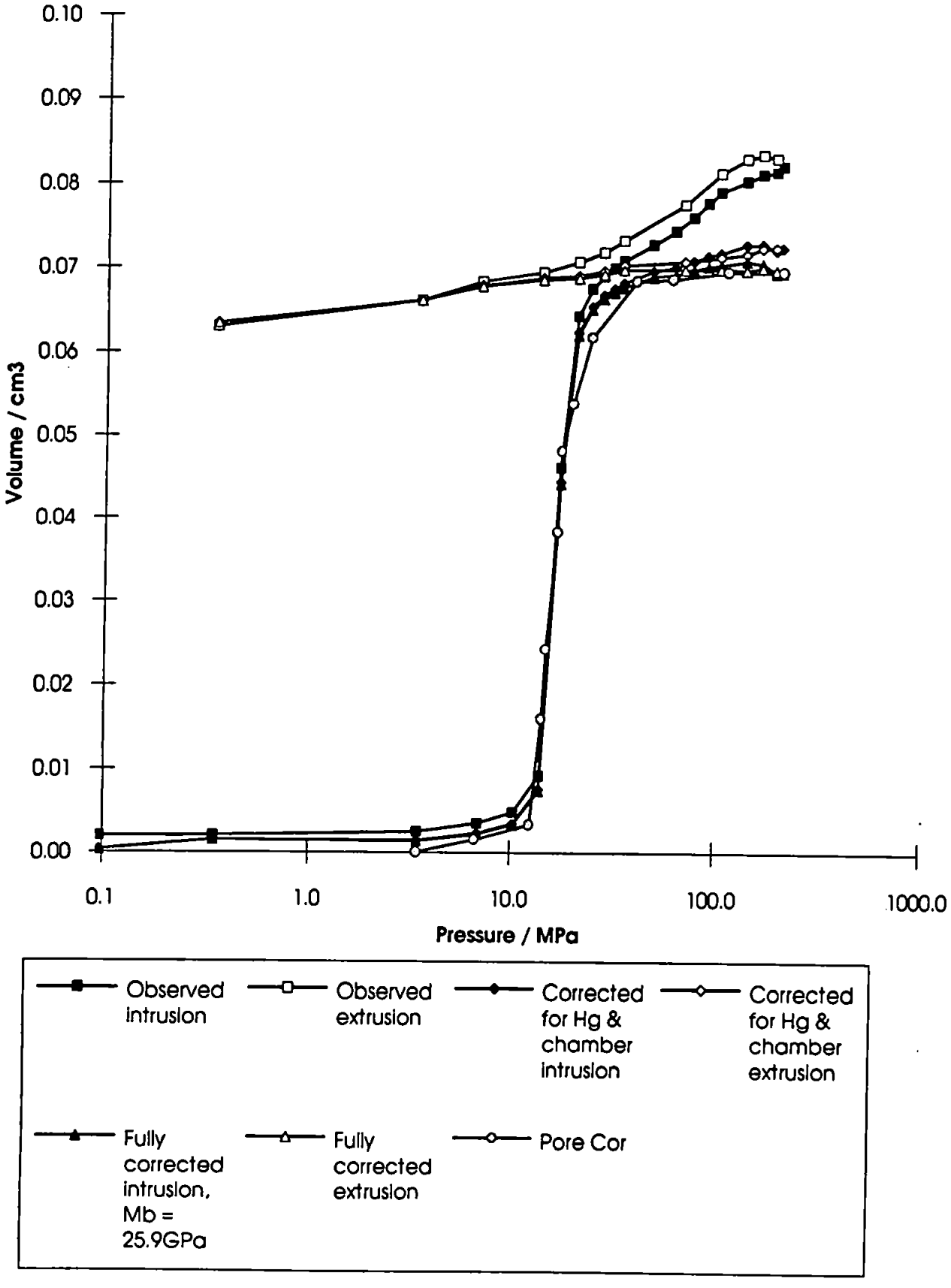

Figure 6.4 Mercury intrusion and extrusion curves for Carbital 90 + latex 95L10

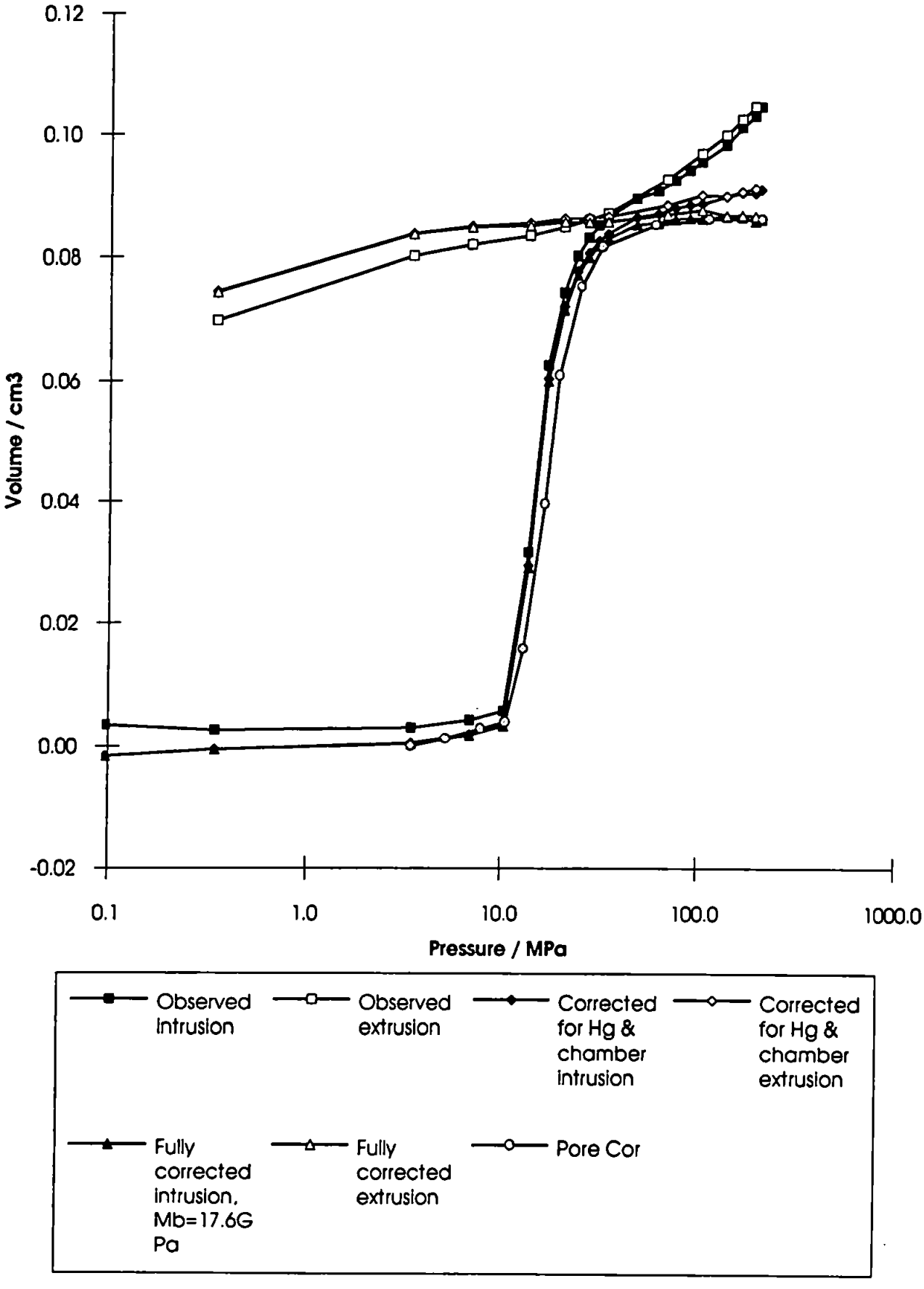

Figure 6.5 Mercury intrusion and extrusion curves for Carbital 90 + DL 950

films mask the grain contact points.

6.3.2 *Plastic pigments*

The plastic pigments studied were Lytron 2601 (solid spheres, mean diameter 0.612 μm), Lytron 2301 (solid spheres, 0.316 μm) and Ropaque HP91 (hollow spheres, 1.012 μm). Samples of emulsions of the pigments weighing 10 g were dried in a desiccator for 48 hours at room temperature. Samples of the consolidated material weighing approximately 0.2 g were used for the mercury porosimetry.

The results for the Lytron products are shown in Fig. 6.6, and Table 6.1. The characteristic intrusion pressures P_{50} for Lytron 2601 and Lytron 2301 are 9 MPa and 35 MPa respectively. The smaller particle size (and compressibility) of the Lytron 2301 affects the first critical concentration (Watanabe *et al.* 1982), and leads to a structure with smaller void spaces.

The intrusion and extrusion curves for the Ropaque HP91 pigment are shown in Fig. 6.7. The intrusion curve has a double sigmoid shape with two points of inflection, at 5 MPa and 41 MPa. The first results from intrusion into the spaces between the spheres, and the second from the compression of the hollow spheres themselves. As can be seen, the extrusion curve is nearly horizontal, demonstrating that the high pressure collapse of the hollow spheres is irreversible.

The porosities of the Lytron pigments, (Table 6.1), again tend to validate the correction methods. However, there is a discrepancy between the Ropaque HP91 porosity values of ϕ'_{atm} = 32.9 % and ϕ_{corr} = 40.1 %. The most likely explanation is that the effective dry density is 0.65 g mL^{-3} rather than 0.55 g mL^{-3} as quoted, which would change the porosity values to 43.2 % and 44.1 % respectively, via eqns [4.17], [4.18] and [4.20].

The solid phase bulk moduli of the plastic pigments decrease in the order Lytron 2601, Lytron 2301 and Ropaque HP91, corresponding to an increase in compressibility

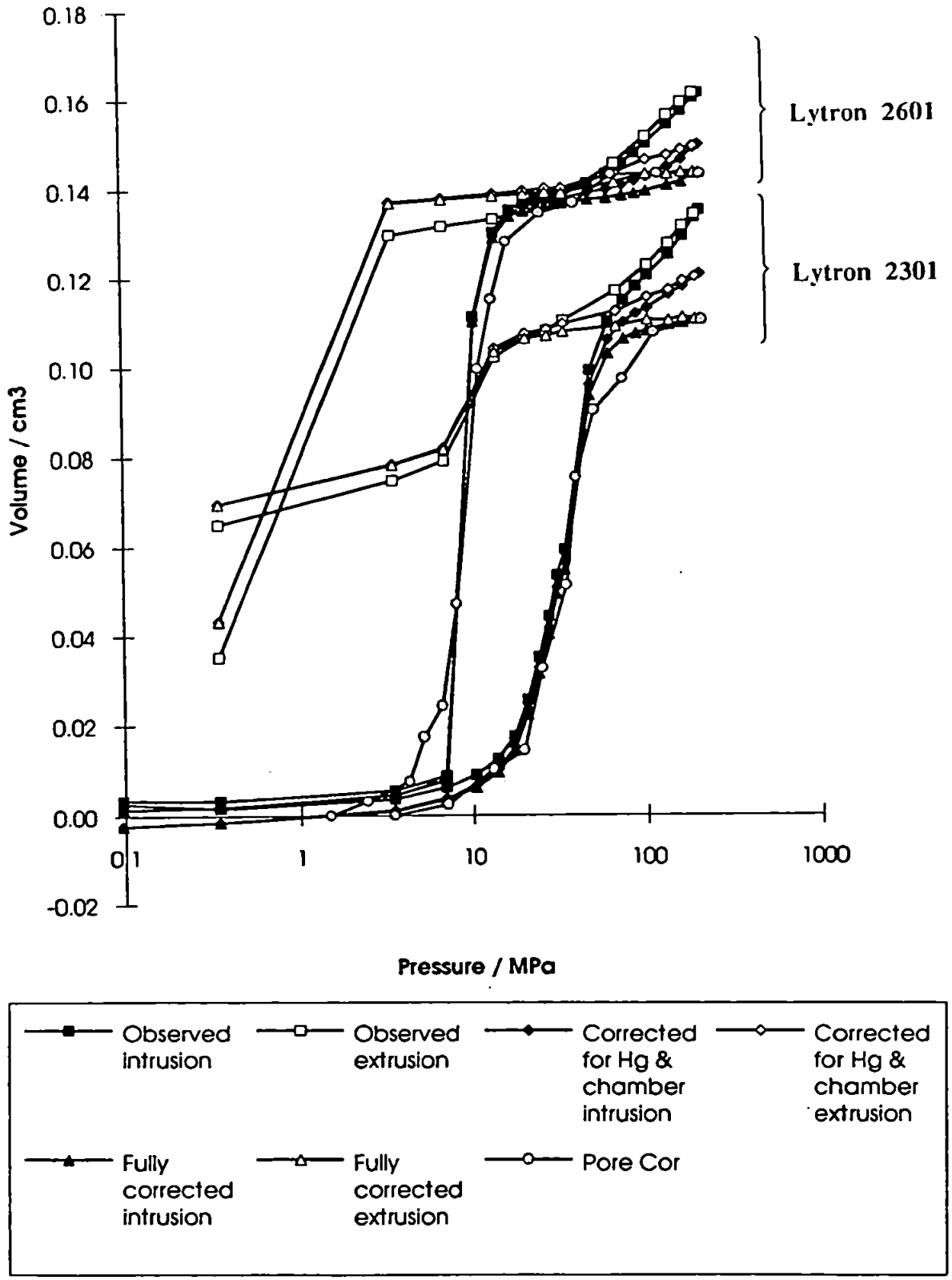

Figure 6.6 Mercury intrusion and extrusion curves for Lytron 2601 and Lytron 2301

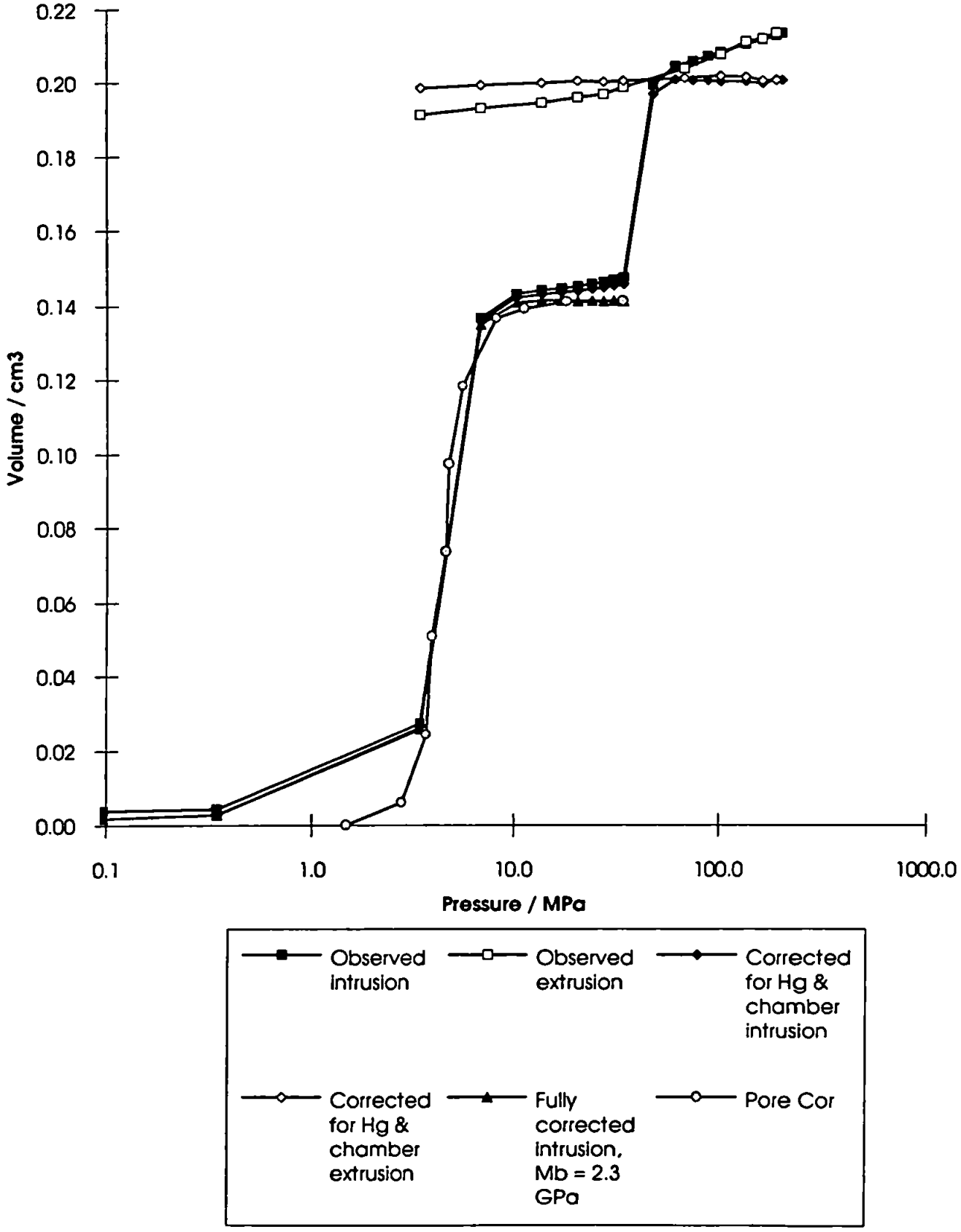

Figure 6.7 Mercury intrusion and extrusion curves for Ropaque HP91

from medium to very compressible, (Table 6.1). It thus appears that agglomerates of the smaller Lytron spheres are rather more compressible than those containing the larger spheres, and, as expected, the agglomerates of hollow spheres are much more compressible than those of solid spheres. For comparison, the bulk modulus of solid nylon is around 5.3 GPa, similar to that of Lytron 2301 (Cook *et al.* 1993)).

6.4 The calculation of permeability

Permeabilities have been calculated with both liquid and air at one atmosphere pressure being used as permeating fluids, by a method described previously in section 3.2 (Matthews *et al.* 1993,1995a). It was assumed that in a liquid, there is a negligible mean free path length, λ, between collisions in the fluid phase, and that the mean free path length of air is the same as that of nitrogen, i.e. 0.0698 μm. Permeability is very dependent on connectivity and correlation effects, which are difficult to characterise well for reasons that have already been described. The permeability calculations are the best available with the current state of knowledge, but should be used for ranking the samples rather than as absolute values.

6.5 Void space modelling results

The corrected intrusion data have been simulated by the Pore-Cor computer program. The resulting simulated intrusion curves (⊙) all match the corrected experimental curves closely, as can be seen in Figs. 6.2 - 6.7.

6.5.1 *Fine ground calcium carbonates*

The pore- and throat-size distributions which were used to generate the mercury intrusion curves for Carbital 90, Carbital 60 and LX 60 are summarised in Table 6.2. It can be seen that in this series, the percentages of pores and throats below 0.03 μm

Type of Sample	Commercial name	Min. throat diam. / μm	Max. throat diam. / μm	Skew	Connectivity	Unit cell length l_{cell} / μm	Porosity ϕ / %	Permeability / μD liquid, air
Dried slurry of finely ground calcium carbonate	Carbital 90	0.007	0.213	0.54	2.9	2.43	26.2	0.37, 6.38
	Carbital 60	0.007	0.427	0.09	2.8	4.74	28.8	1.83, 15.5
	LX 60	0.007	0.7	0.10	4.0	7.20	40.9	33.3, 154
Dried coating colour; Carbital 90 with added latex binder	Carbital 90 + Acronal S801	0.007	0.427	0.02	3.0	5.80	19.4	1.55, 13.3
	Carbital 90 + latex 95L10	0.007	0.427	0.74	3.5	5.36	19.3	1.02. 8.67
	Carbital 90 + DL 950	0.007	0.427	0.67	3.3	5.11	21.3	0.51, 5.72
Plastic pigment	Lytron 2601	0.007	1.0	0.46	2.9	10.14	27.9	0.85, 6.16
	Lytron 2301	0.007	0.427	0.84	2.7	4.46	23.2	0.033, 0.73
	Ropaque HP91	0.04	1.0	0.47	3.3	11.05	32.9	43.4, 159

Table 6.2 Paper coating simulation results

decrease, and the percentages of the large sizes increase (noting the different maximum sizes). These values are in agreement with the relative sizes of the void spaces which would be expected between particles of the sizes shown in Fig. 6.1. The unit cell of LX 60 is shown in Fig. 6.8, whilst Figs. 6.9 and 6.10 show an equal sized cubical sample (7.20 μm) of the simulated void-space structure of Carbital 90 and Carbital 60. The unit cell size varies for these samples as shown, and so more than one unit cell is included. As shown in Table 6.2, a higher connectivity (4.0) is required to simulate the steeper intrusion curve of LX 60, which also has a higher porosity (all experimental and simulated porosities match exactly). Overall, the simulated permeabilities increase by two orders of magnitude from Carbital 90 to LX 60. Slip flow causes a 17-fold relative increase in permeability for Carbital 90, and an absolute increase of 6 μD. For the more permeable samples, the absolute increase caused by slip flow is greater, but the relative effect is smaller.

6.5.2 *Carbital 90 with added latex binder*

The three coating colour samples have the throat diameter and pore size distributions shown in Table 6.2, each covering the range 0.007 - 0.427 μm. The Carbital 90 + Acronal S801 has a smaller skew and more large pores than the other two samples. The porosities of the three samples are all around 20 %. The unit cell of the Carbital 90 + Acronal S801 is similar to that of Carbital 60, (Fig. 6.10), although the unit cell sizes differ. Carbital 90 + latex 95L10 has a unit cell similar to that of Carbital 90 + DL 950. These three structures have a threefold range in permeability which is small in comparison to the range of simulated permeabilities in the previous section.

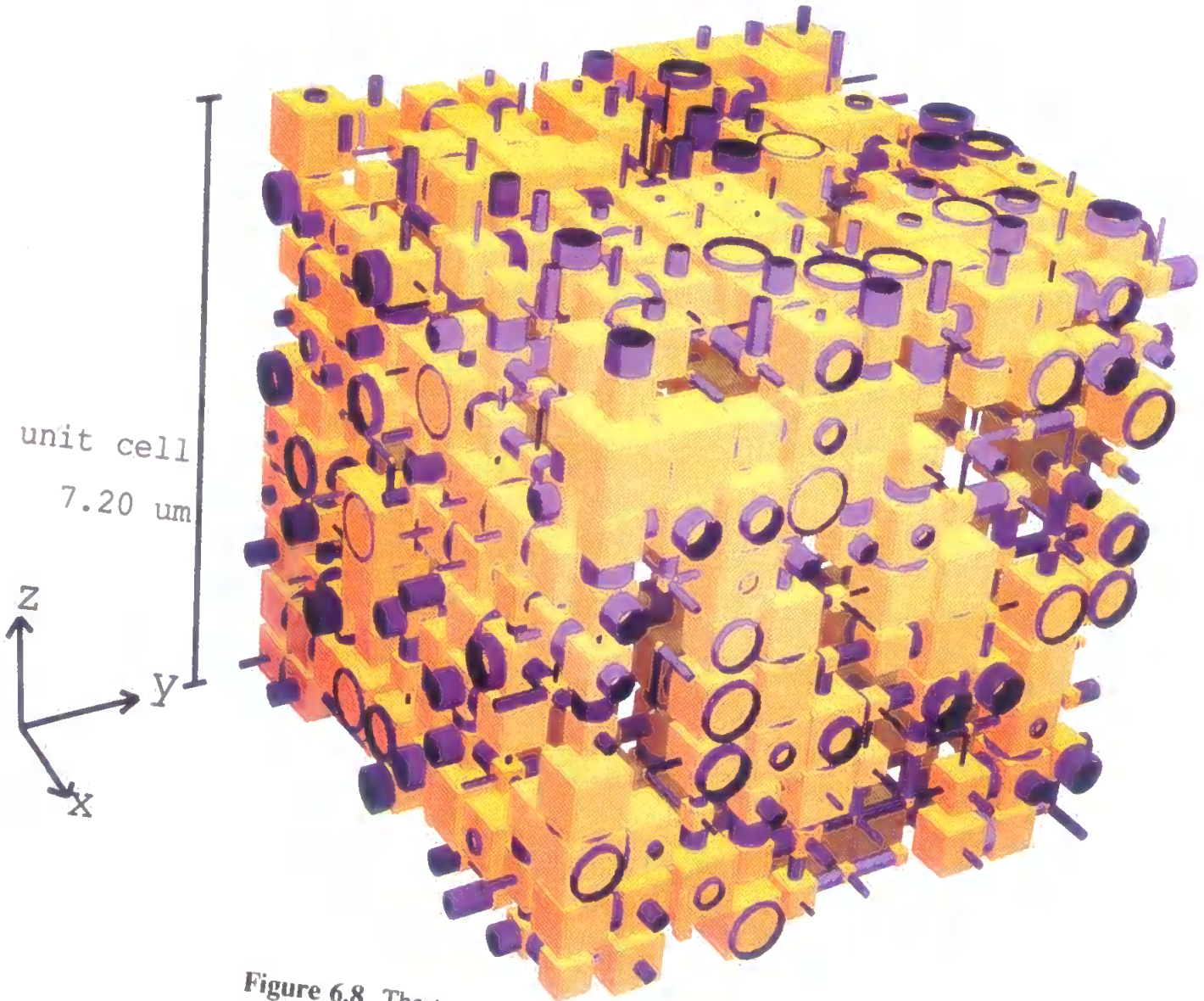

Figure 6.8 The two outermost layers of the unit cell of LX 60

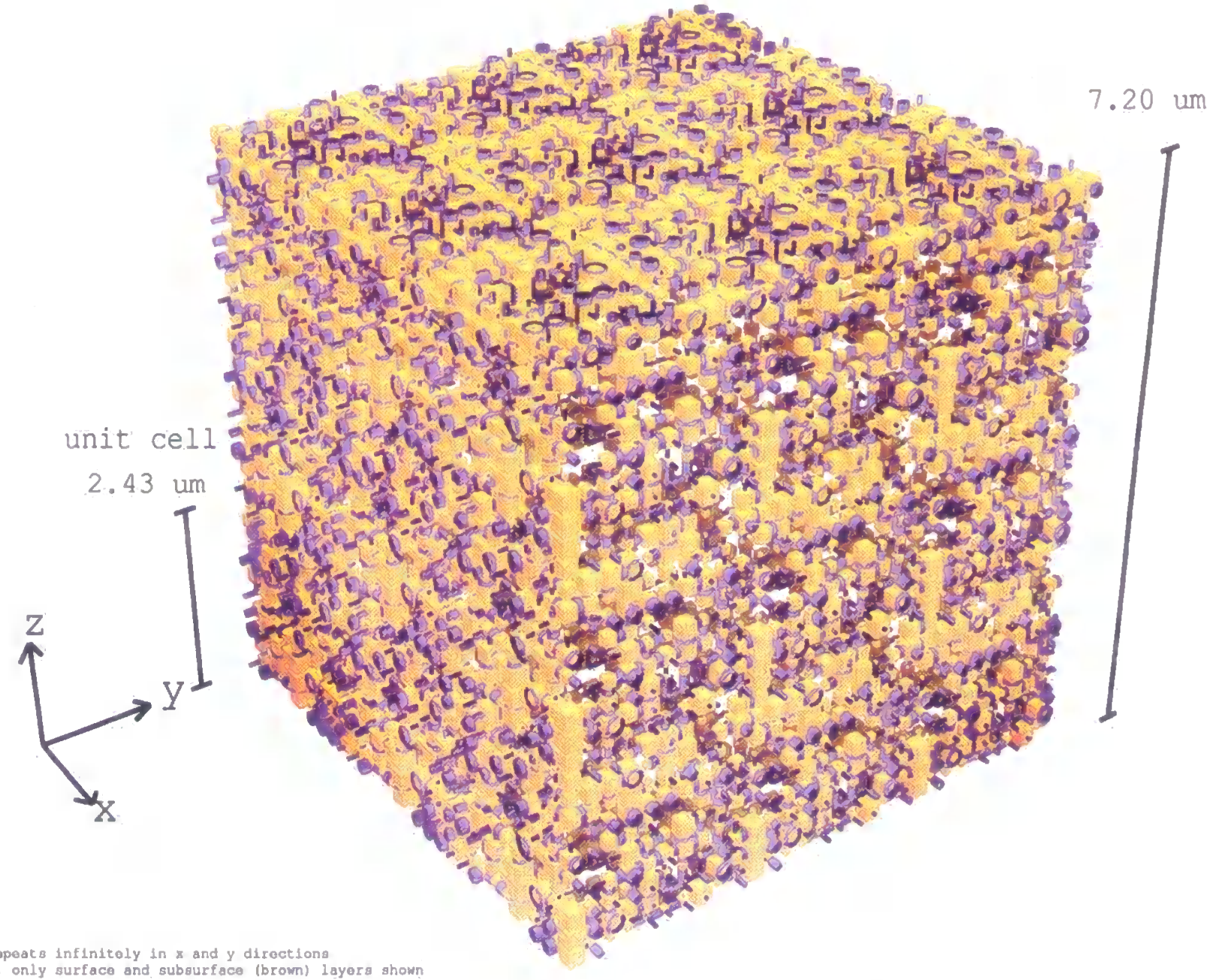

Figure 6.9 The two outermost layers of the unit cell of Carbital 90

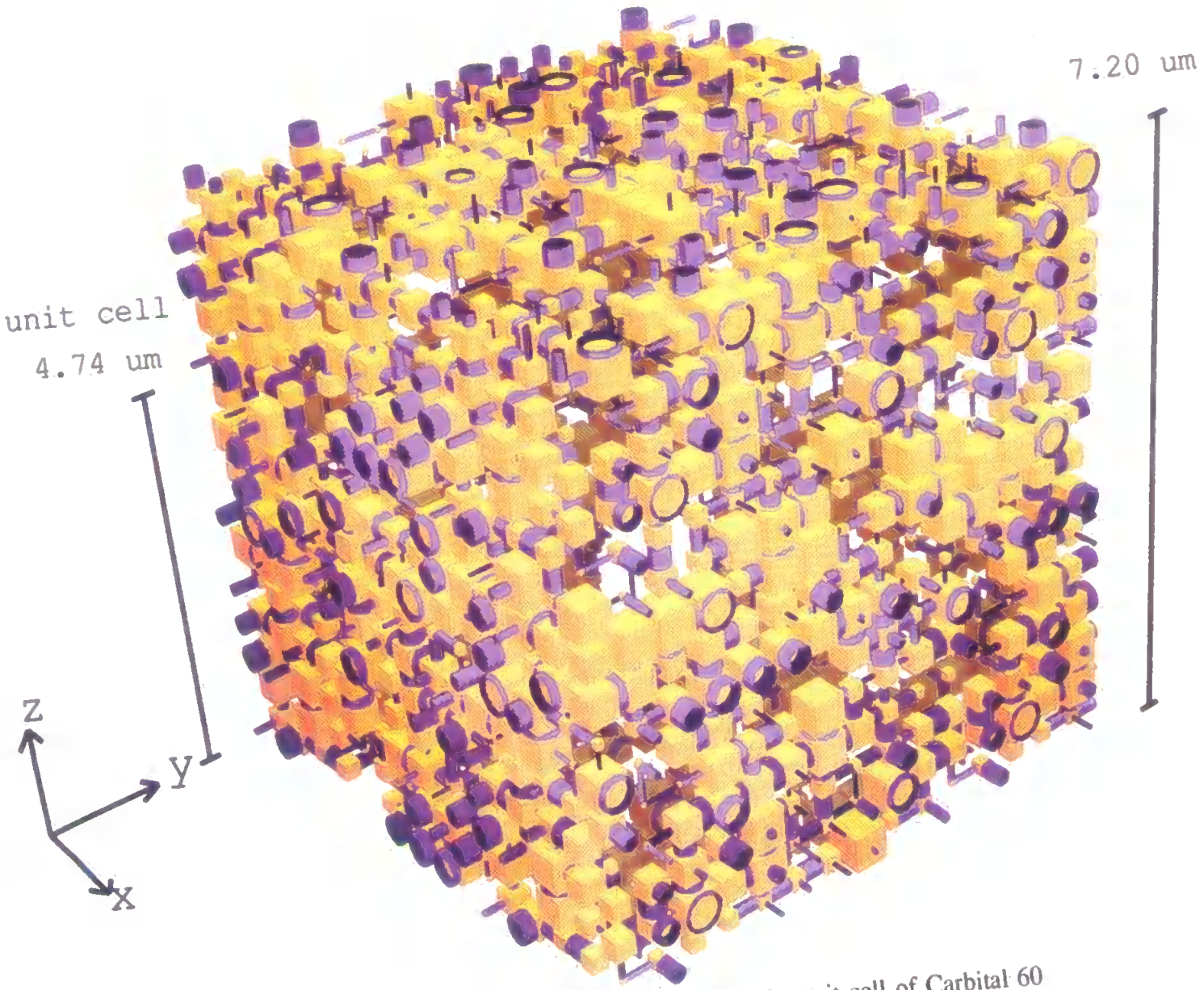

Figure 6.10 The two outermost layers of the unit cell of Carbital 60

6.5.3 *Plastic pigments*

The two solid plastic pigments have different sizes of particle; this is reflected in the modelling by the different throat-diameter and pore-size ranges. The maximum simulated throat diameter for Lytron 2601 is twice that of Lytron 2301, and its unit cell is also twice as large. Lytron 2601 has a simulated permeability of 0.850 μD compared to Lytron 2301 with a value of 0.033 μD. The differences between the throat-diameter and pore-size distributions, and between the simulated permeabilities of the two Lytron samples are in line with the differences between their experimental particle sizes and porosities, (Table 6.1).

The inter-particle void-space structure of Ropaque HP91 before the collapse of its polystyrene spheres has been simulated. The throat-diameter and pore-size distribution covers a range from 0.04 to 1.0 μm, the minimum throat diameter being much larger than the minimum throat diameter of the other samples. The simulated permeability of the Ropaque sample is higher than that of any of the previous structures, being 43.4 μD for liquid and 159 μD for air, because of its larger minimum throat diameter, coupled with a skew towards larger sizes.

6.6 Doverstrand samples

Investigation using different techniques for preparing paper coatings has been carried out in collaboration with John Kettle at ECCI plc. R&D, St Austell. Having carried out the mercury intrusion and extrusion experiments, further analysis of the samples involved looking at the fractured samples on the cryo-stage of the electron microscope. Sections 6.6.1 and 6.6.2 give details of mercury porosimetry carried out by John Kettle, and 6.6.3 the electron microscopy carried out by the author.

Mercury porosimetry has been used to characterise the void fraction and pore size distribution of dried lump samples of clay/latex and clay/starch formulations. It has been

possible, using this technique, to characterise the structures formed using different drying conditions and binder types.

The structures of consolidated coatings have been shown to be influenced by factors including the level and type of binder. This work describes the use of mercury porosimetry for the characterisation of the pore structure of consolidated coatings, namely clay with either 15 wt % latex (a hard styrene-butadiene latex containing 25 % butadiene) or 4 wt % starch (Nylgum A55, a phosphate ester of a potato starch). The SPS slurry was blended with either the latex or starch to form coating colours that were dried under different conditions. A pressure cell was used for two samples of each colour. The pressure cell is a unique adaption (by Doverstrand R&D) of an 'Eklaund-style' dewatering system, and the samples were in the pressure cell for two hours at a pressure of 3 bar. The pressure cell treated samples were either oven dried at 110°C or allowed to air dry. Two other samples of each colour were not pressure cell treated but were dried at either ambient or elevated temperatures.

6.6.1 *Intrusion data*

Mercury intrusion and extrusion curves have been measured for the dried lump samples. The porosity at atmospheric pressure and at elevated pressure has been determined for each of the samples, Table 6.3. The intrusion curves for the clay/latex samples are shown in Fig 6.11. The sample containing latex that had been air dried had the largest characteristic throat diameter and the highest porosity. By drying this system at 110°C more shrinkage has occurred and both the porosity and the median pore size are reduced. The pressure cell treatment with air drying reduced the sample porosity and effectively halved the characteristic throat diameter compared with the structure formed just by air drying. The most significant change occurred when both the pressure and heat were applied to the sample. This sample (1b) had the narrowest characteristic throat

Sample Description	Porosity Φ / % At P=atm	At P>atm	Median pore size d_{50} / μm
15 % clay/latex			
1a. PC (2 hr, 3 bar) air	17.5	17.8	0.028
1b. PC (2 hr, 3 bar) 110°C	17.8	14.6	0.022
1c. Air	22.6	19.5	0.055
1d. 110°C	19.4	18.4	0.044
15 % clay/starch			
2a. PC (2 hr, 3 bar) air	34.4	35.9	0.142
2b. PC (2 hr, 3 bar) 110°C	38.8	38.0	0.144
2c. Air	42.0	36.0	0.157
2d. 110°C	40.8	39.1	0.153

Table 6.3 Porosity and median pore size measurements for the Doverstrand samples

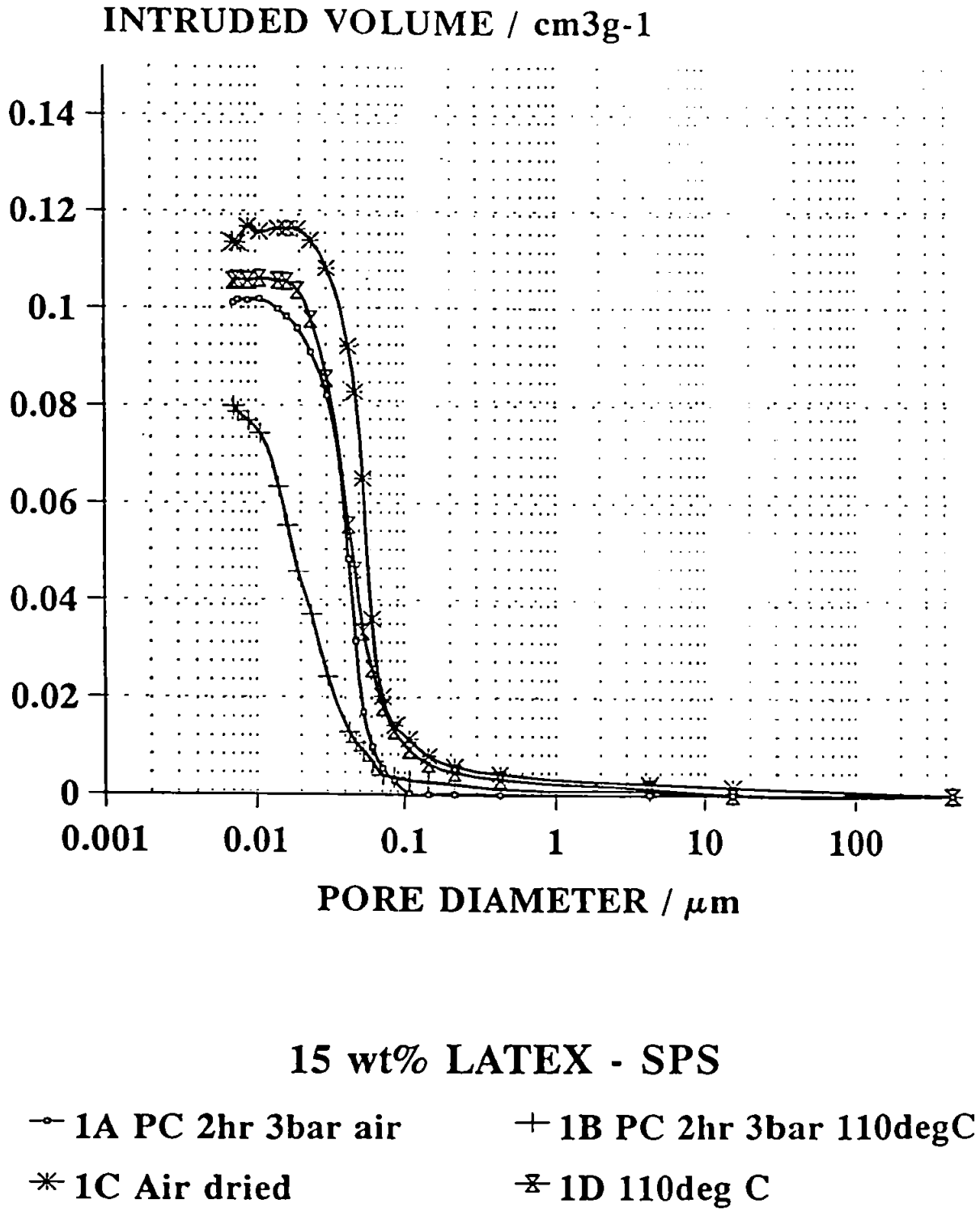

Figure 6.11 Mercury porosimetry intrusion data for clay/latex samples

and the smallest sample porosity.

The porosities of the clay/starch samples were larger than those for the clay/latex samples. The characteristic throat diameter and porosity of the clay/starch samples that were pressure cell treated were virtually constant and not altered by heat. The characteristic throat diameter and porosity of the samples that were dried without the use of the pressure cell were slightly larger, but once again in contrast to the samples containing latex, were unaffected by drying temperature (Fig.6.12).

The comparison between the latex containing samples and the starch containing samples highlights the packing properties of the latex spheres at room temperature and subsequent film formation associated with shrinkage at elevated temperatures. Starch is film forming at all temperatures studied and no significant progressive structural change is apparent under pressure and/or at elevated temperature.

All of the intrusion curves are plotted in Fig. 6.13 to illustrate the significant difference that binder type and binder level can have upon the pore structure of the consolidated lump.

6.6.2 *Extrusion data*

The extrusion data for the latex containing samples are shown in Fig. 6.14 and it is clear from these data that the use of heat has produced a structure that entraps mercury upon depressurisation of the porosimeter. This may be due to the presence of latex that has film-formed to produce 'elastic' diaphragms within the interconnected pore network which can be penetrated by mercury during the pressurisation part of the cycle. However upon depressurisation mercury cannot 'manoeuvre' around these 'partially reformed' diaphragms and mercury remains trapped within the pore structure of the sample.

The samples that contained starch did not entrap significant quantities of mercury upon depressurisation Fig. 6.15. This may be due to the lower level of binder and the fact

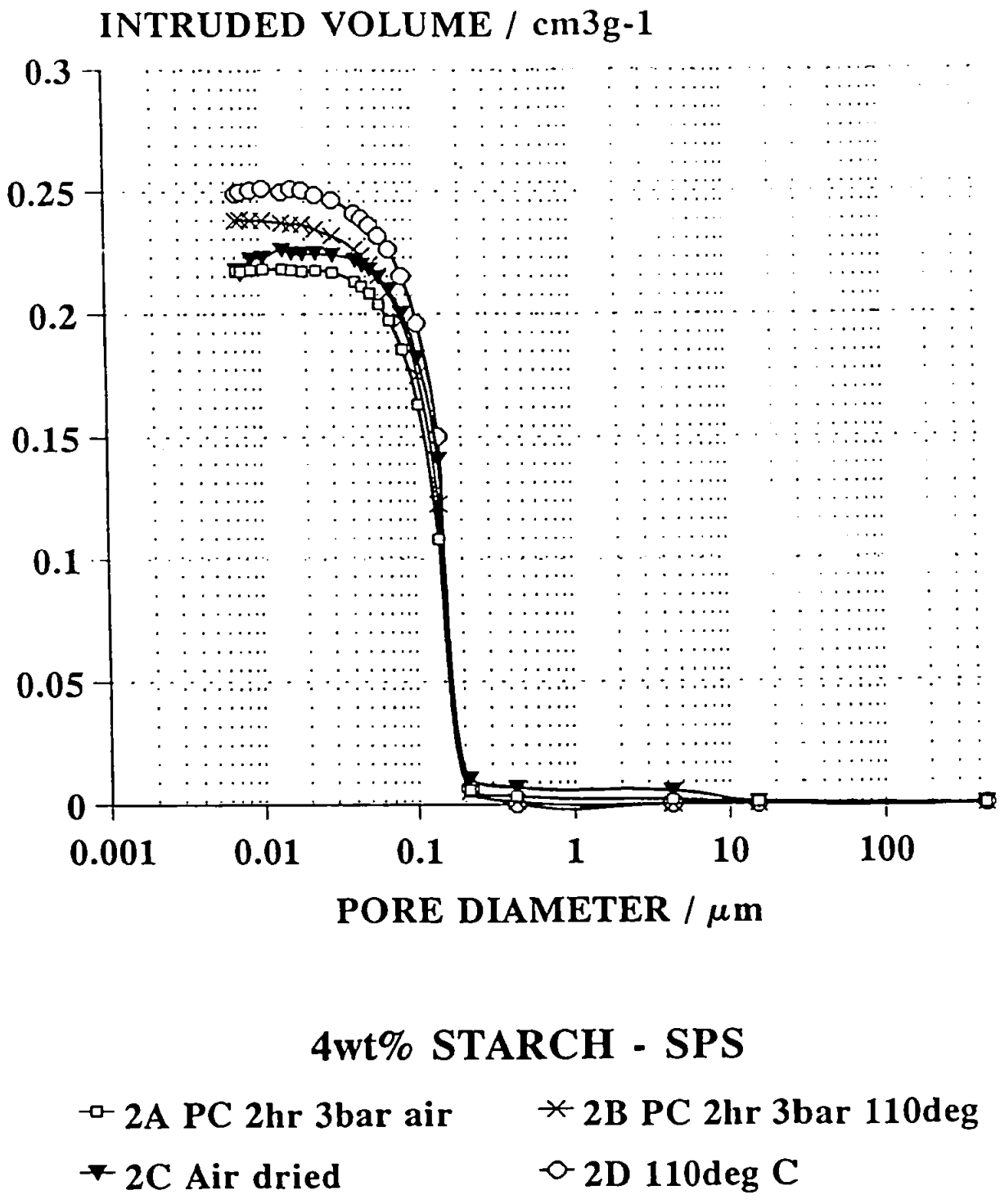

Figure 6.12 Mercury porosimetry intrusion data for clay/starch samples

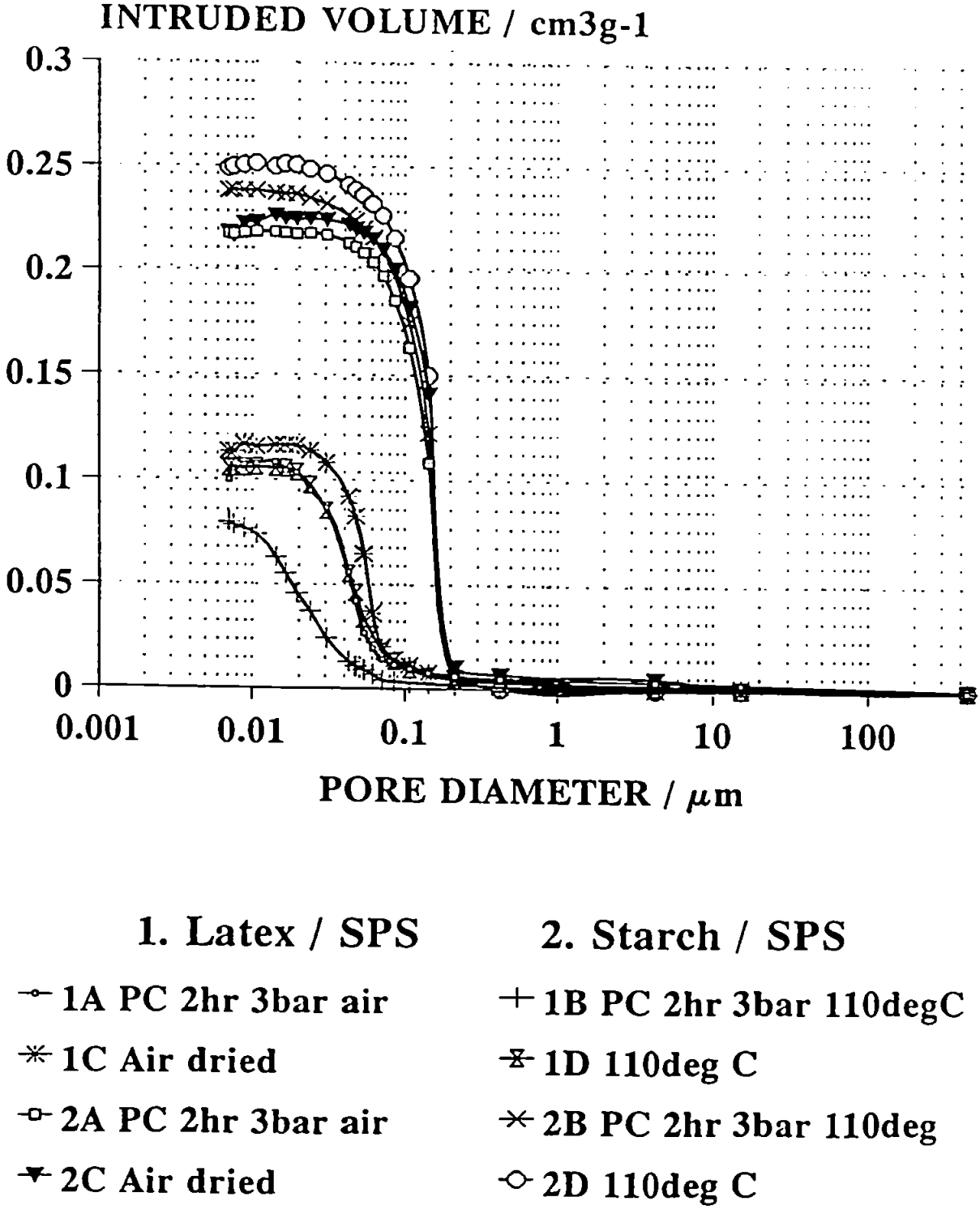

Figure 6.13 Mercury porosimetry intrusion data for clay/latex samples and clay/starch samples

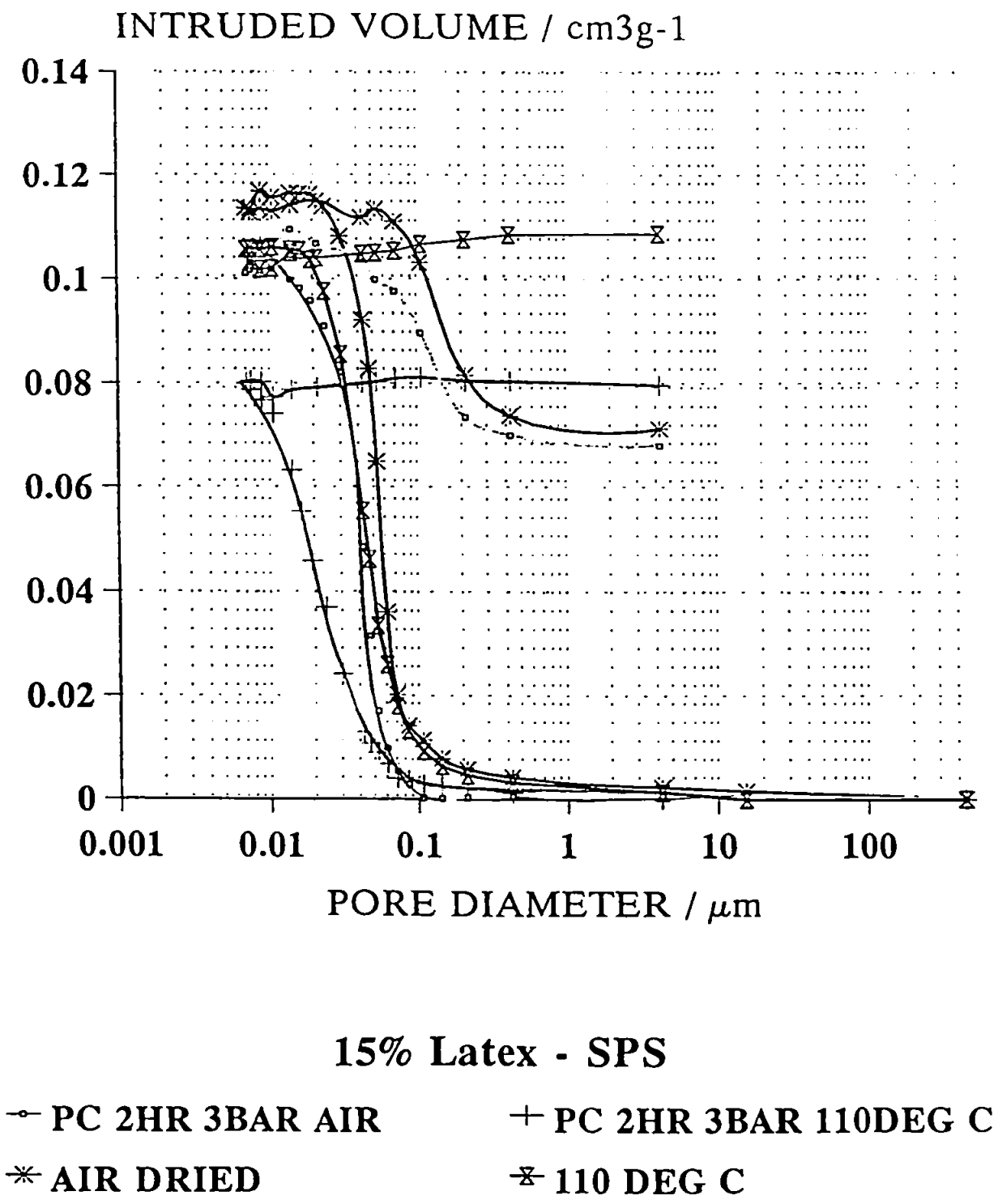

Figure 6.14 Mercury porosimetry intrusion and extrusion data for clay/latex samples

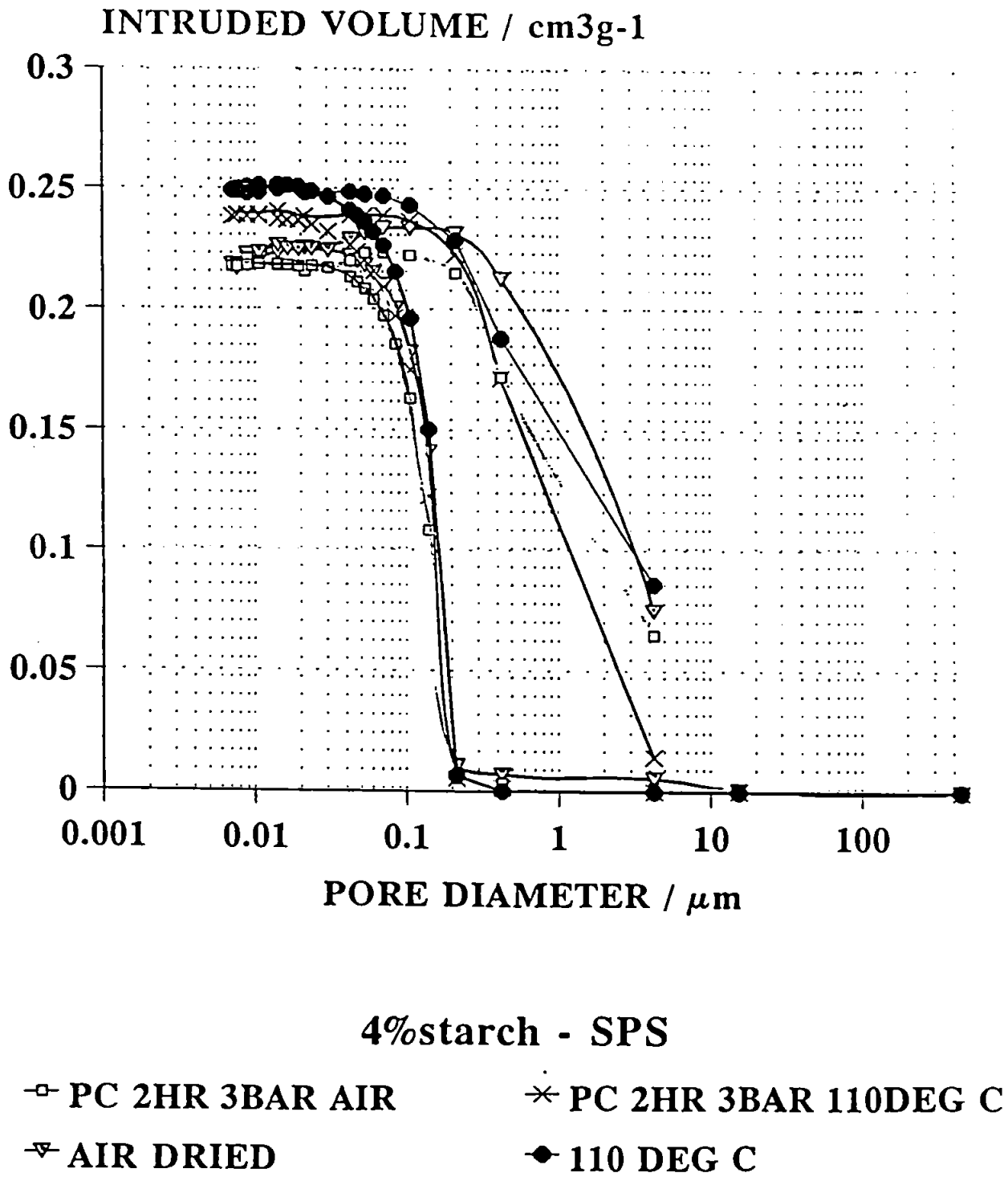

Figure 6.15 Mercury porosimetry intrusion and extrusion data for clay/starch samples

that if the binder had formed diaphragms within the interconnected pore network then they would probably be inelastic, as starch films tend to be brittle, and once penetrated, would not reform to hinder the extrusion of mercury.

6.6.3 *Electron micrographs*

Plate 6.1 shows samples of the consolidated colour coating before the mercury intrusion experiments had been carried out. The piece on the left is the clay/latex sample dried at 110 °C and the room temperature dried sample is on the right. Plate 6.2 shows the original clay/starch sample, also dried at room temperature. These samples have all been pressurised in their making. After mercury extrusion experiments had been carried out a very interesting situation was found on breaking of the extruded samples. It was clear that the mercury had penetrated through the air dried samples, Plate 6.3. However, when the heat dried clay/latex sample was broken the centre of the sample was still pure white as can be seen in Plate 6.4. It is shown that the mercury has not penetrated to the centre of the sample. This is a sample that showed no extrusion data, i.e. it had 100 % trapping.

Fragments of the samples were first frozen in liquid nitrogen and then broken before being placed on the cryo-stage of the electron microscope. Plates 6.5-6.10 are of the clay/latex room temperature dried sample. It is clear that the mercury has broken through the surface of the sample during the intrusion of mercury and filled pockets (perhaps created during the drying of the sample) within the sample. Plate 6.5 shows the cracked surface falling inwards and the mercury extruding. These globules were visible on the surface of the sample. Rubbing with tweezers did not cause the mercury to snap-off. Plate 6.6 shows a more detailed view of the tail end of the mercury in Plate 6.5. The mercury is visibly extruding from the smaller cracks around the main hole. Plate 6.7 shows mercury which is trapped in a space beneath the surface, the cracking around the

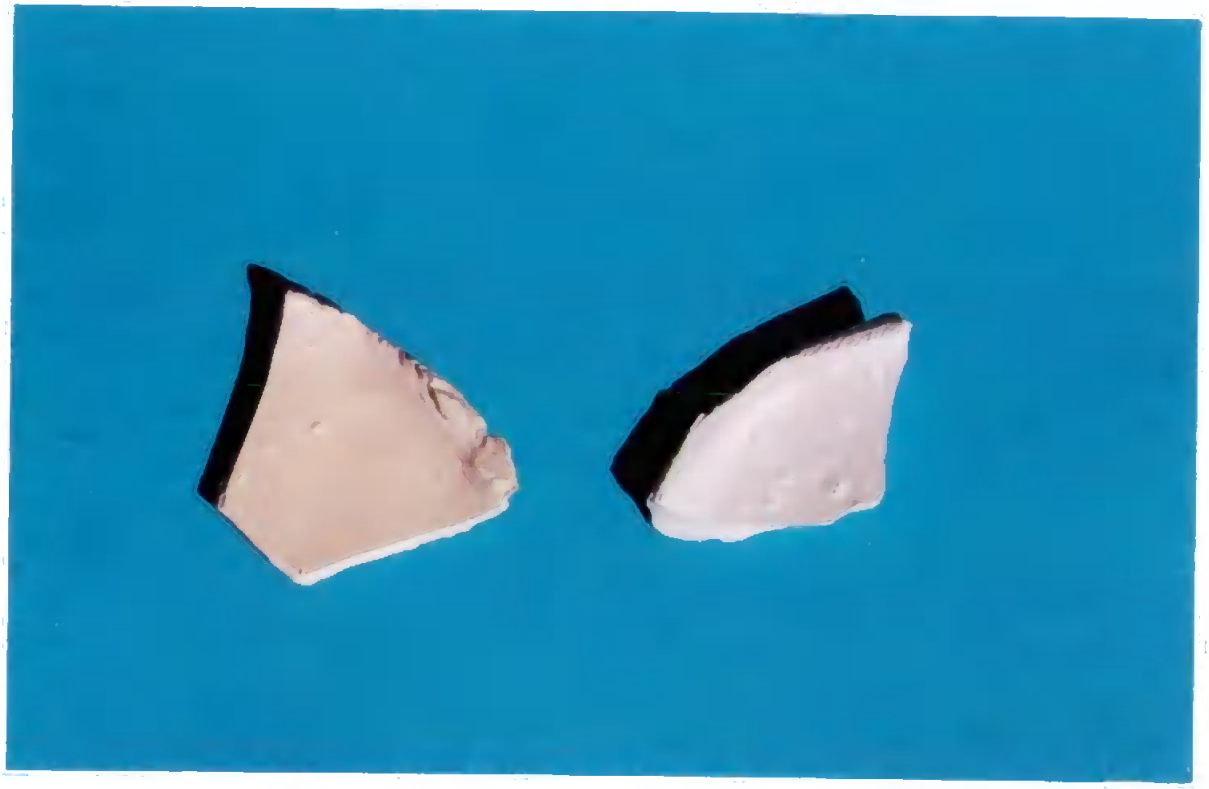

Plate 6.1 Dried lump samples of clay/latex formulations

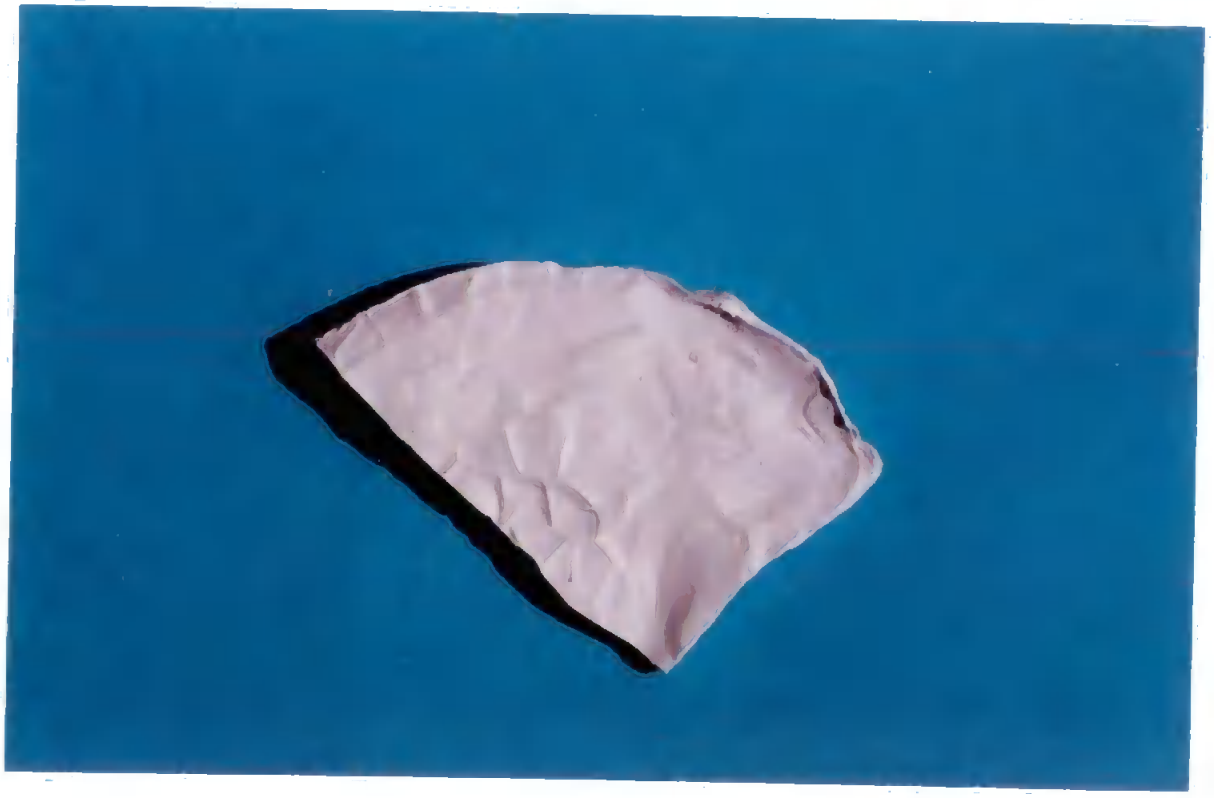

Plate 6.2 Dried lump sample of clay/latex formulation

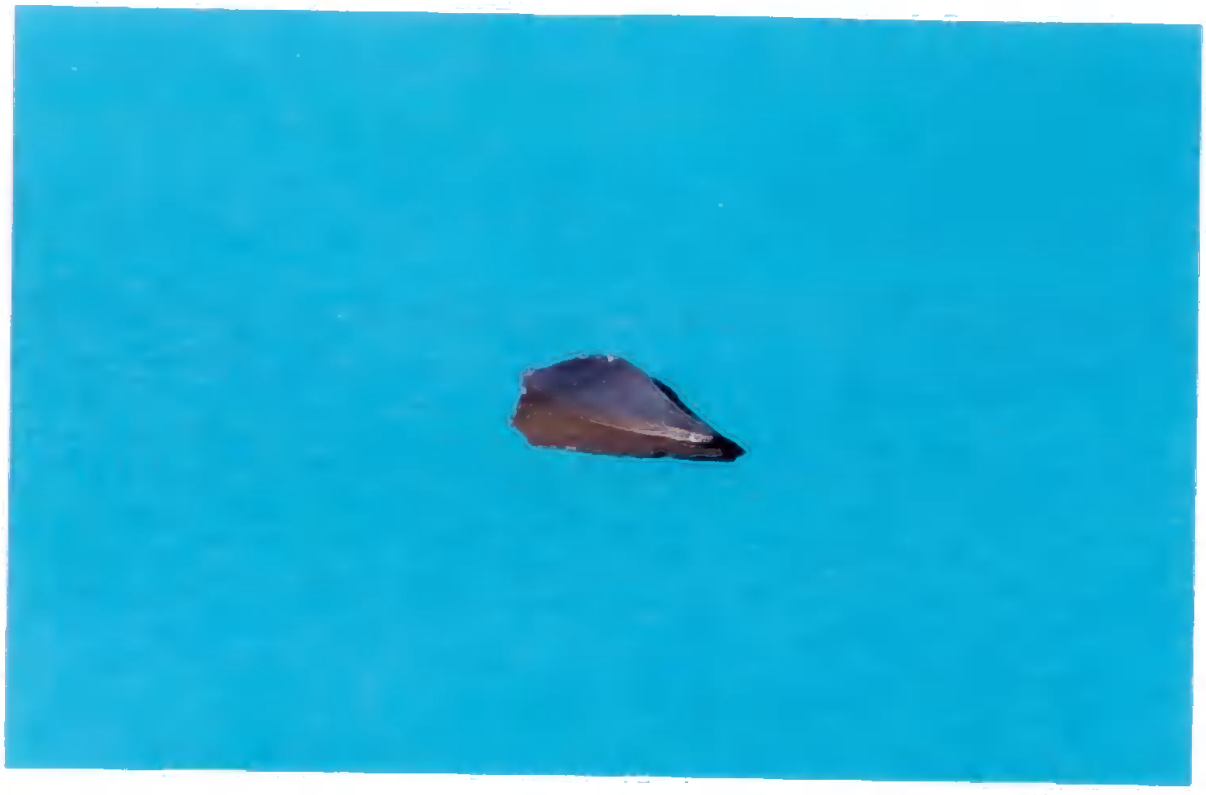

Plate 6.3 Mercury intruded clay/latex formulation - air dried

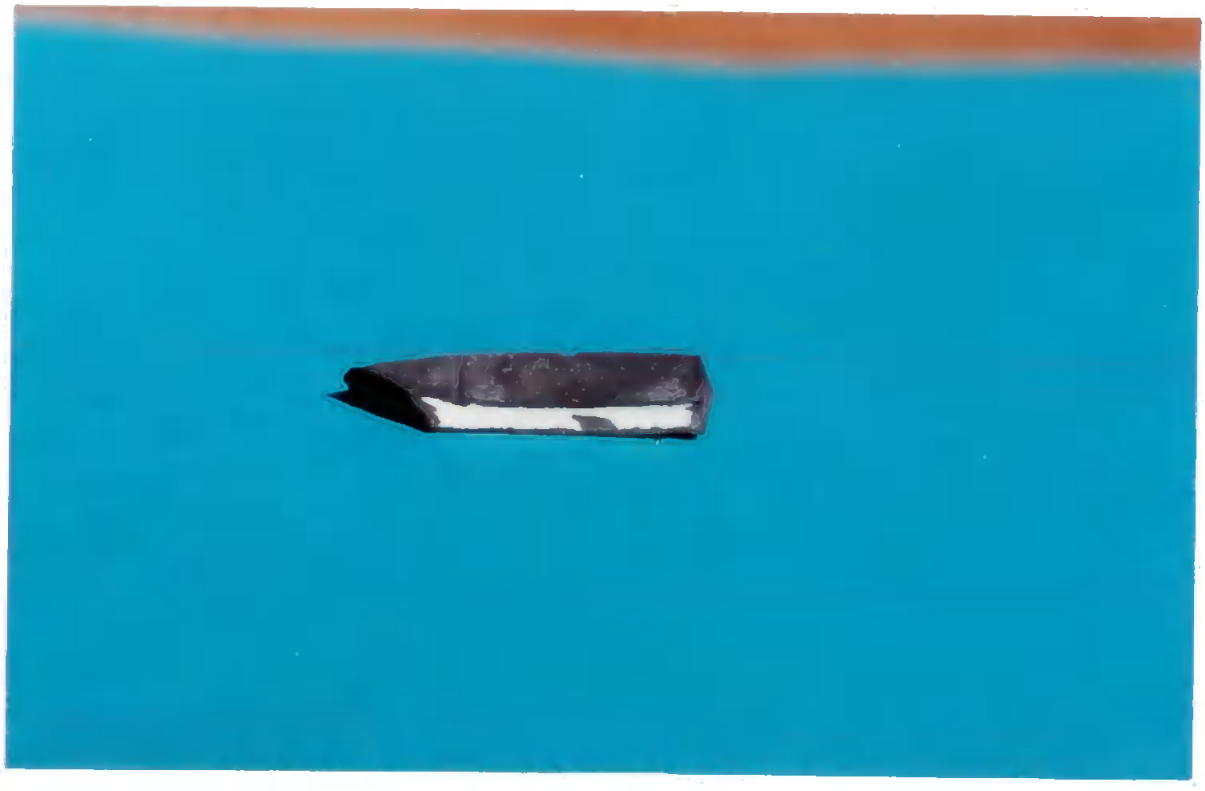

Plate 6.4 Mercury intruded clay/latex formulation - heat dried

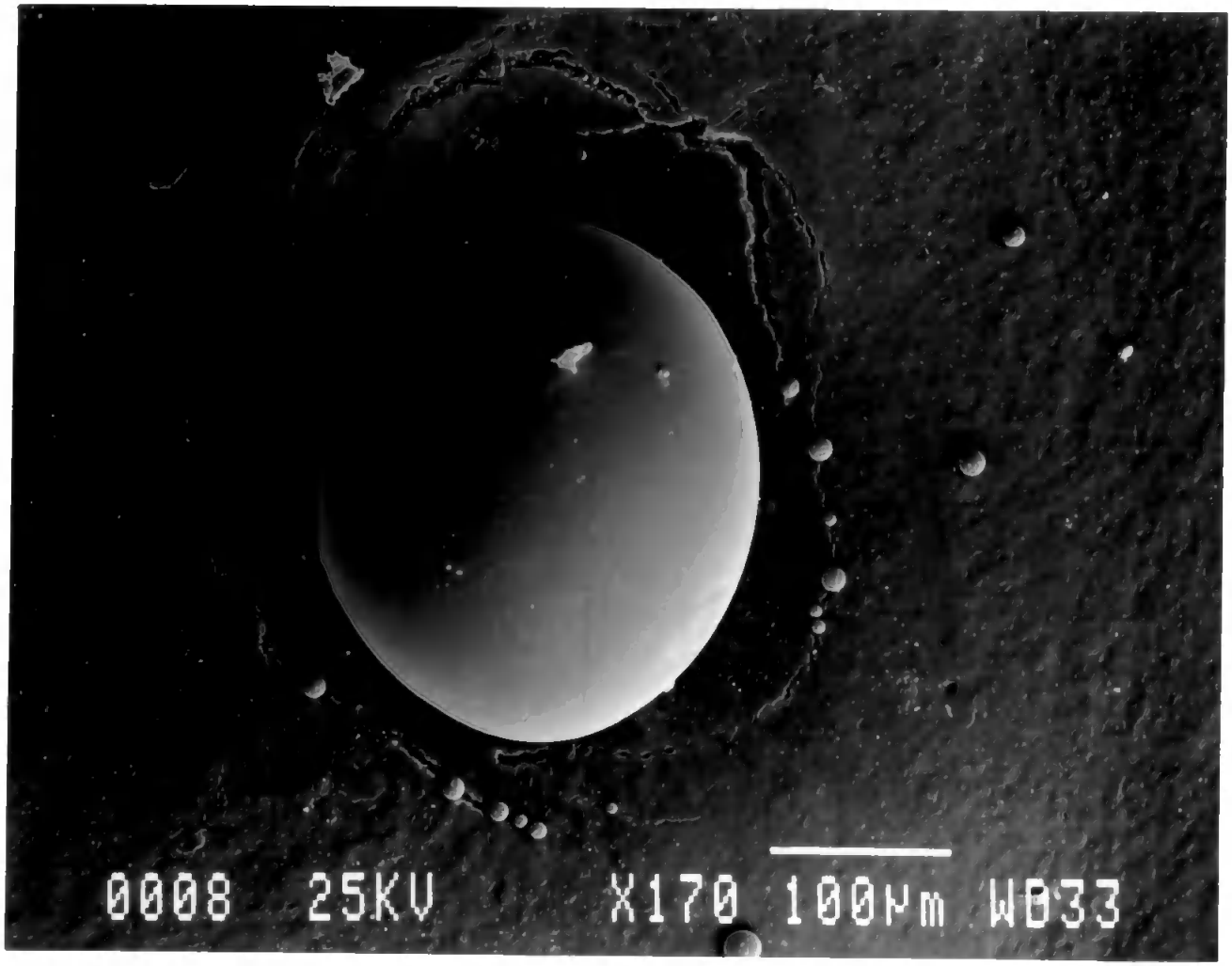

Plate 6.5 Electron micrograph of clay/latex formulation - air dried

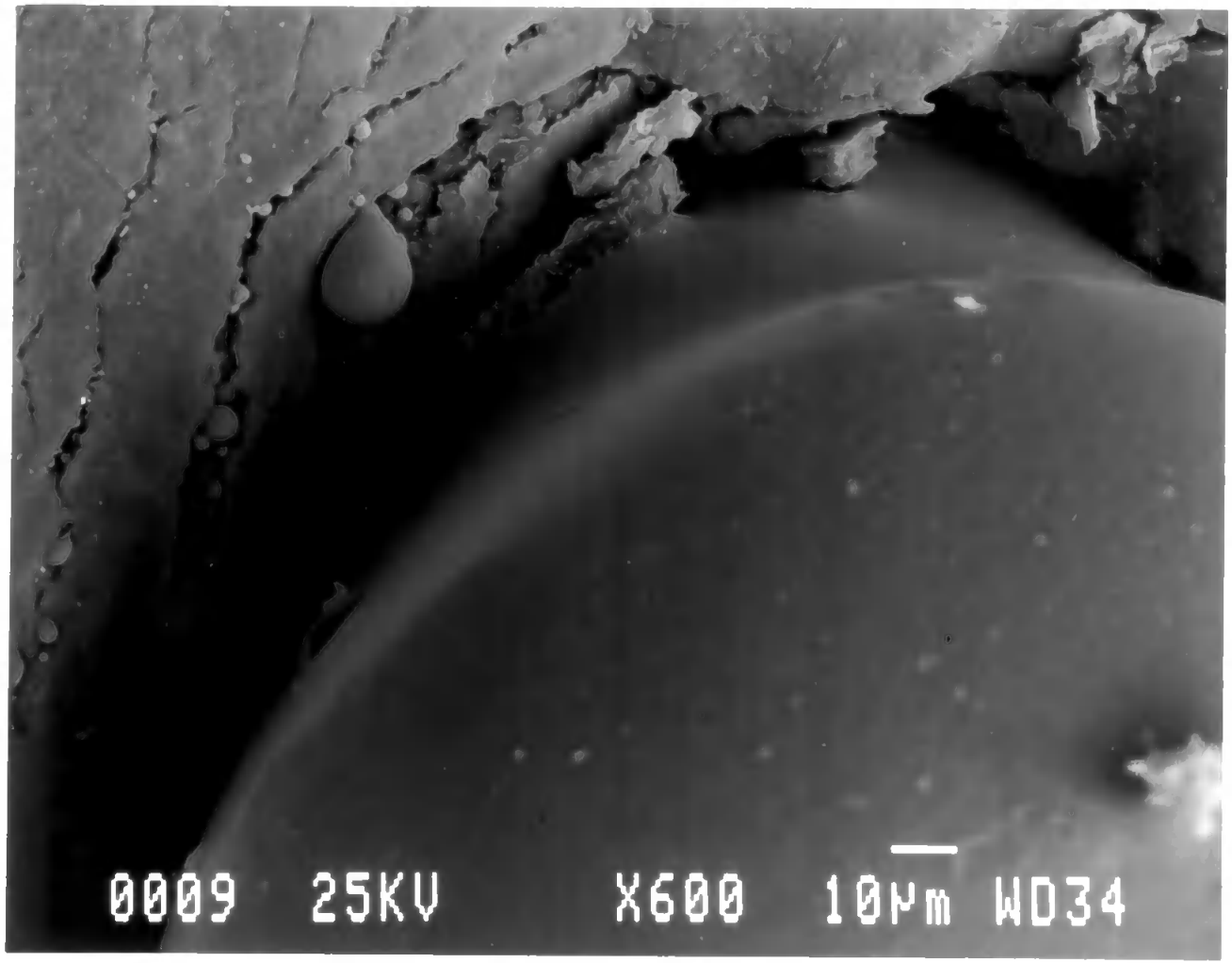

Plate 6.6 Electron micrograph of clay/latex formulation - air dried

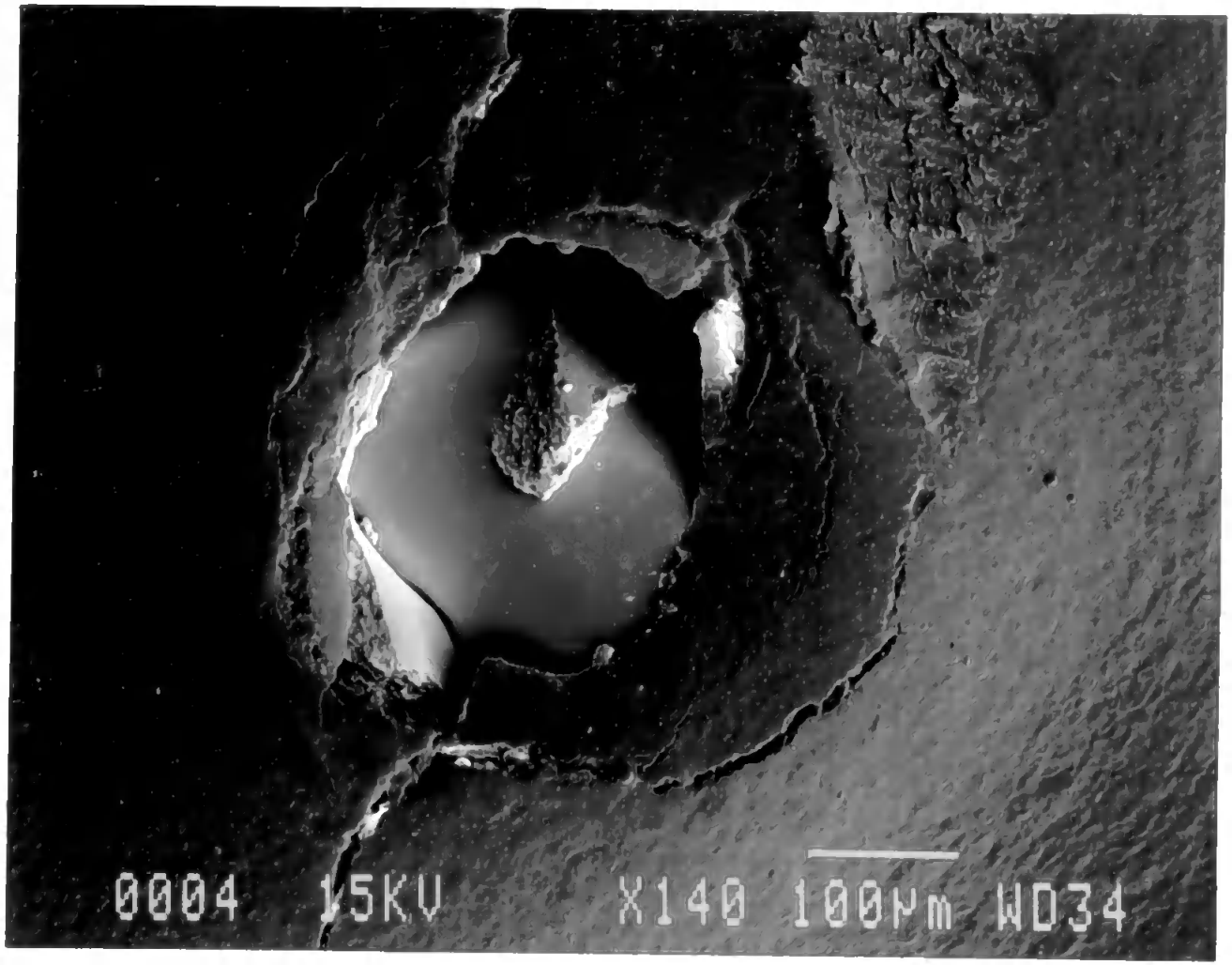

Plate 6.7 Electron micrograph of clay/latex formulation - air dried

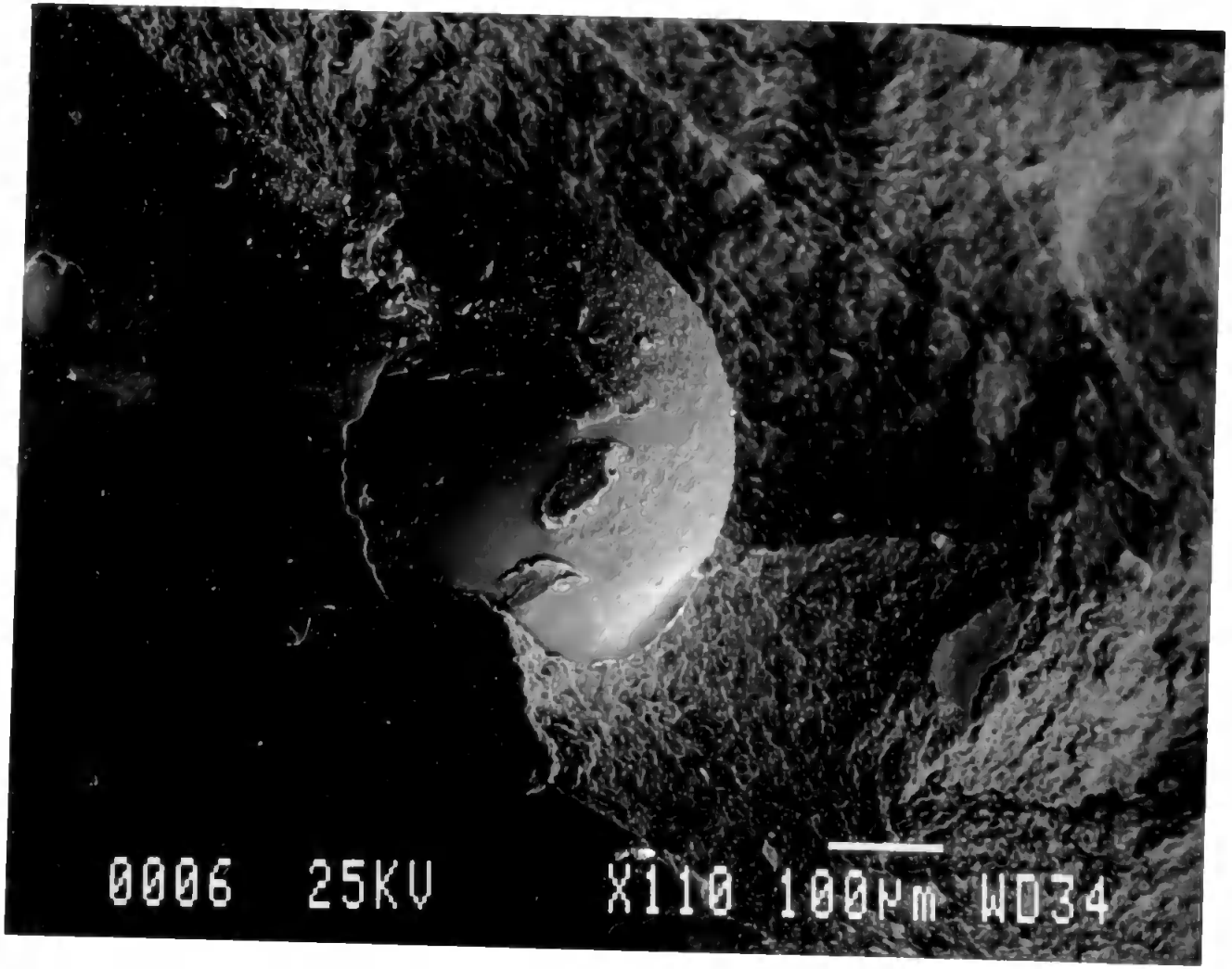

Plate 6.8 Electron micrograph of clay/latex formulation - air dried

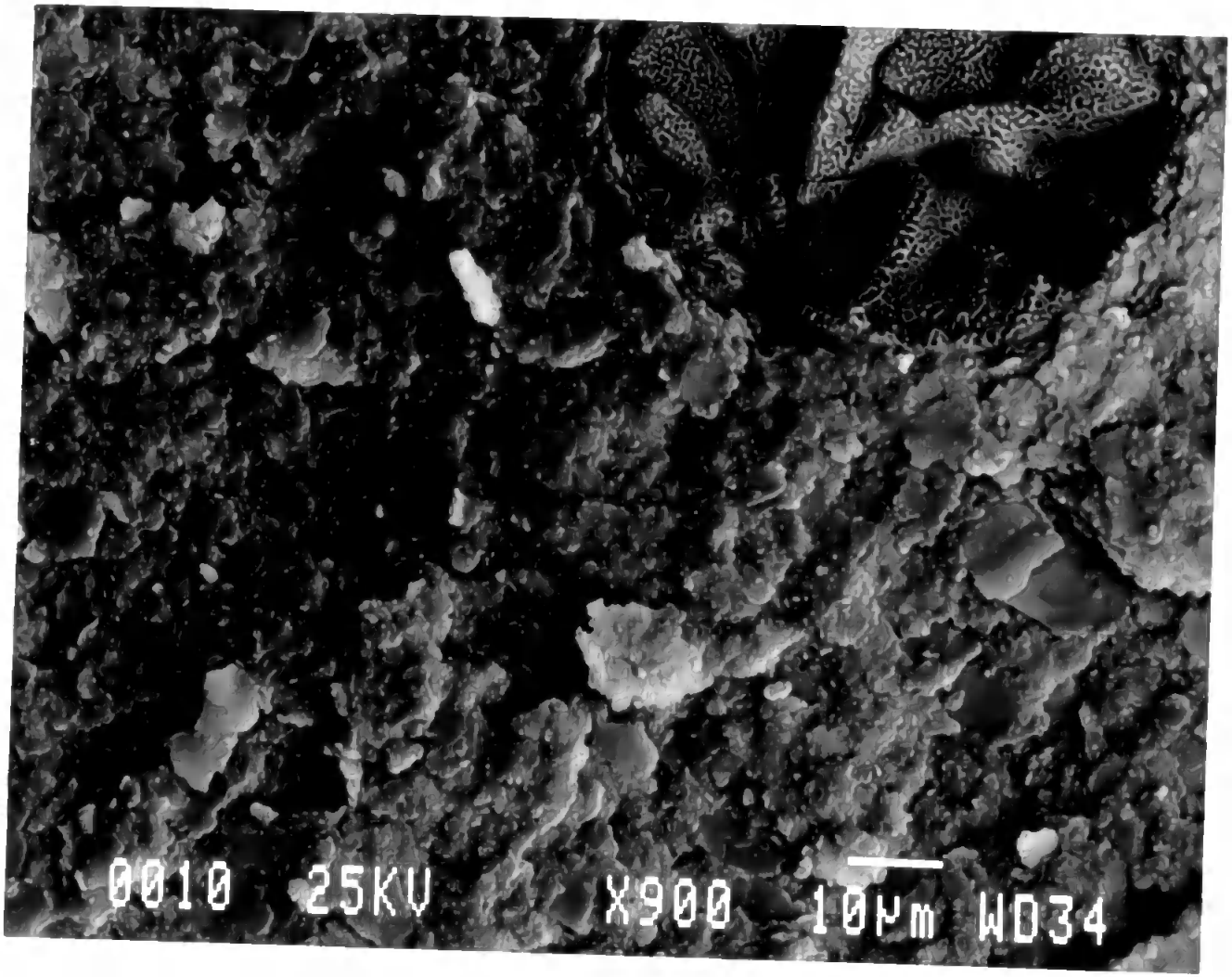

Plate 6.9 Electron micrograph of clay/latex formulation - air dried

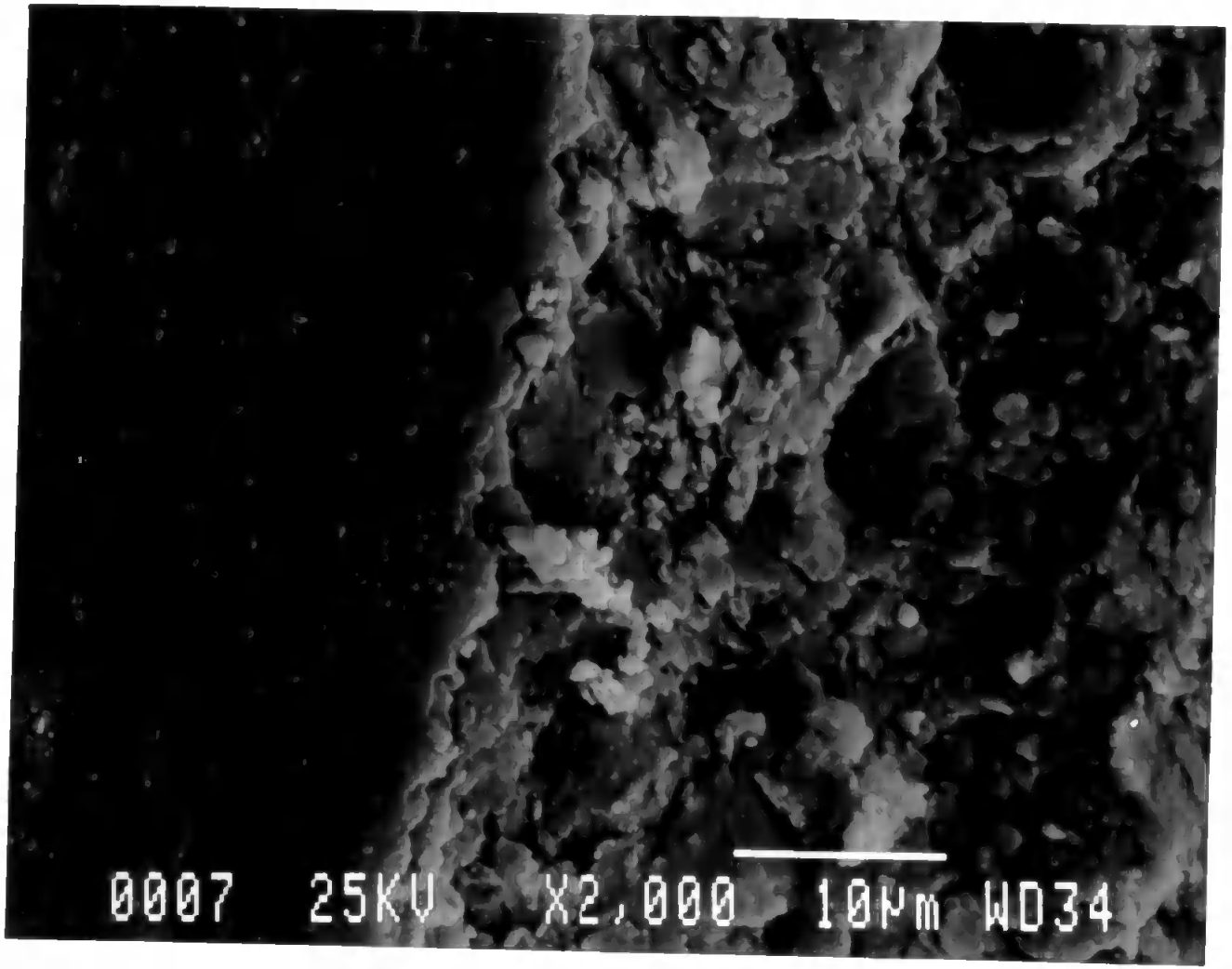

Plate 6.10 Electron micrograph of clay/latex formulation - air dried

hole again points towards the breakage occurring during intrusion. Plate 6.8 shows a globule of mercury trapped under the surface of the sample. Plate 6.9 has an irregular form in the top right hand corner. This is a snapped, frozen globule of mercury. Plates 6.9 and 6.10 both show the fractured surface of the clay/latex sample dried at room temperature.

The heat dried clay/latex sample also has a cracked surface and globules of mercury can be seen on the surface, as shown in Plates 6.11 and 6.12. During mercury intrusion only the surface layers were penetrated. The depth of intrusion can be seen in Plate 6.13 where the structure of the sample becomes more defined. Pictures were taken of the two areas, i.e. where the mercury intruded and where the sample was still clean. These pictures are at a much higher magnification and the results are seen in Plates 6.14 and 6.15. Plate 6.14 shows mercury globules and a few strands of latex, whereas Plate 6.15 has no mercury present and the strands of melted latex are very obvious. These strands of latex form *diaphragms* over the throats which can be penetrated by the intrusion of mercury but not on extrusion. The diaphragms of latex may be preventing the intrusion of mercury into the void space at the centre of the sample. The heat drying may also induce capillary force effects and hence tighten up the central void space structure.

The starch sample analysis showed no breakage through the surface, Plates 6.16 and 6.17. The pictures showed that no pockets were formed, but the mercury could lodge behind cracks in the structure, see Plate 6.18.

6.6.4 *Discussion*

Mercury porosimetry has been used to characterise the void fraction and pore size distribution of dried lump samples supplied by Doverstrand and it has been possible to identify effects caused by different drying conditions and binder types. A clay/latex system has a much smaller void fraction and a pore size distribution that starts at narrower

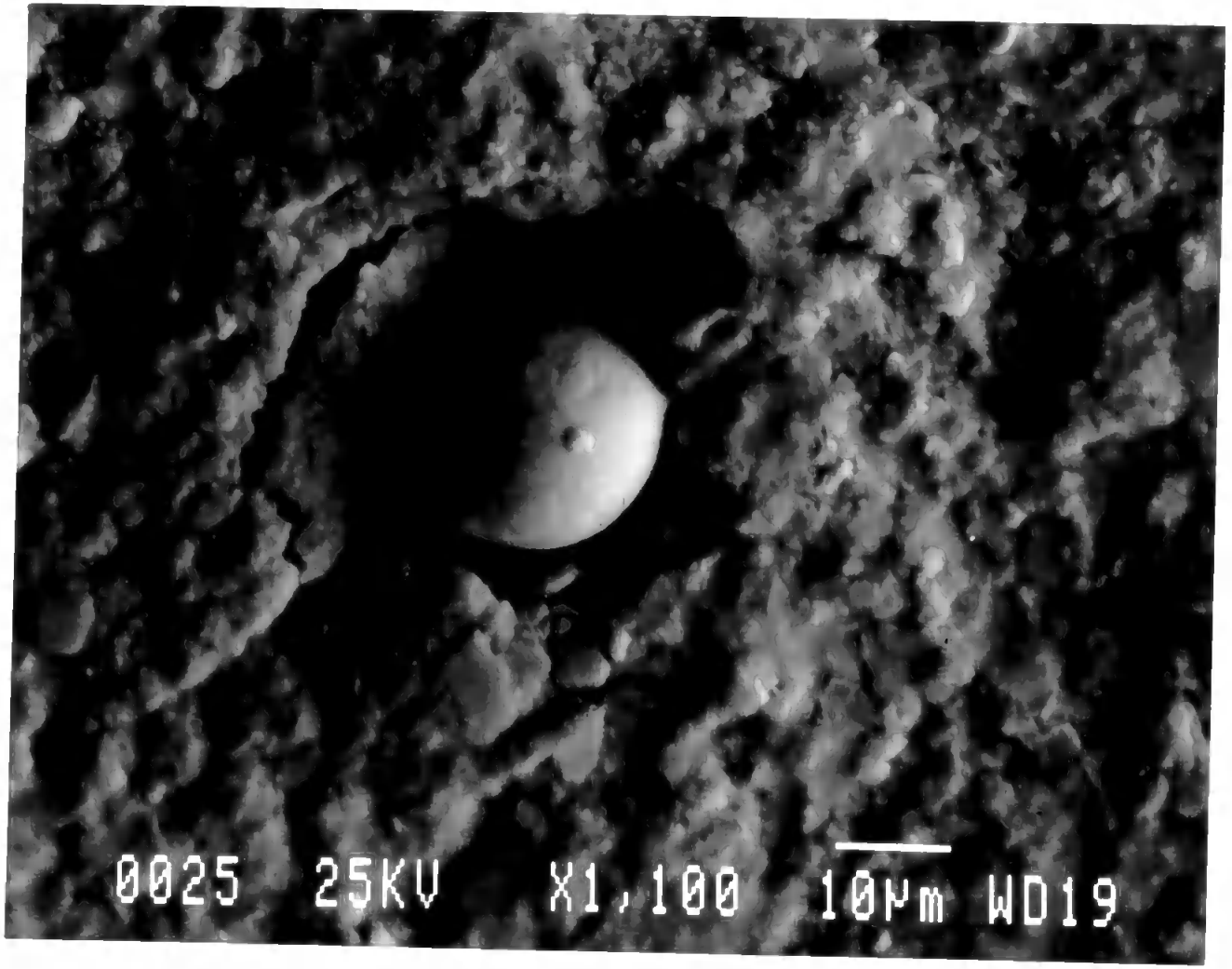

Plate 6.11 Electron micrograph of clay/latex formulation - heat dried

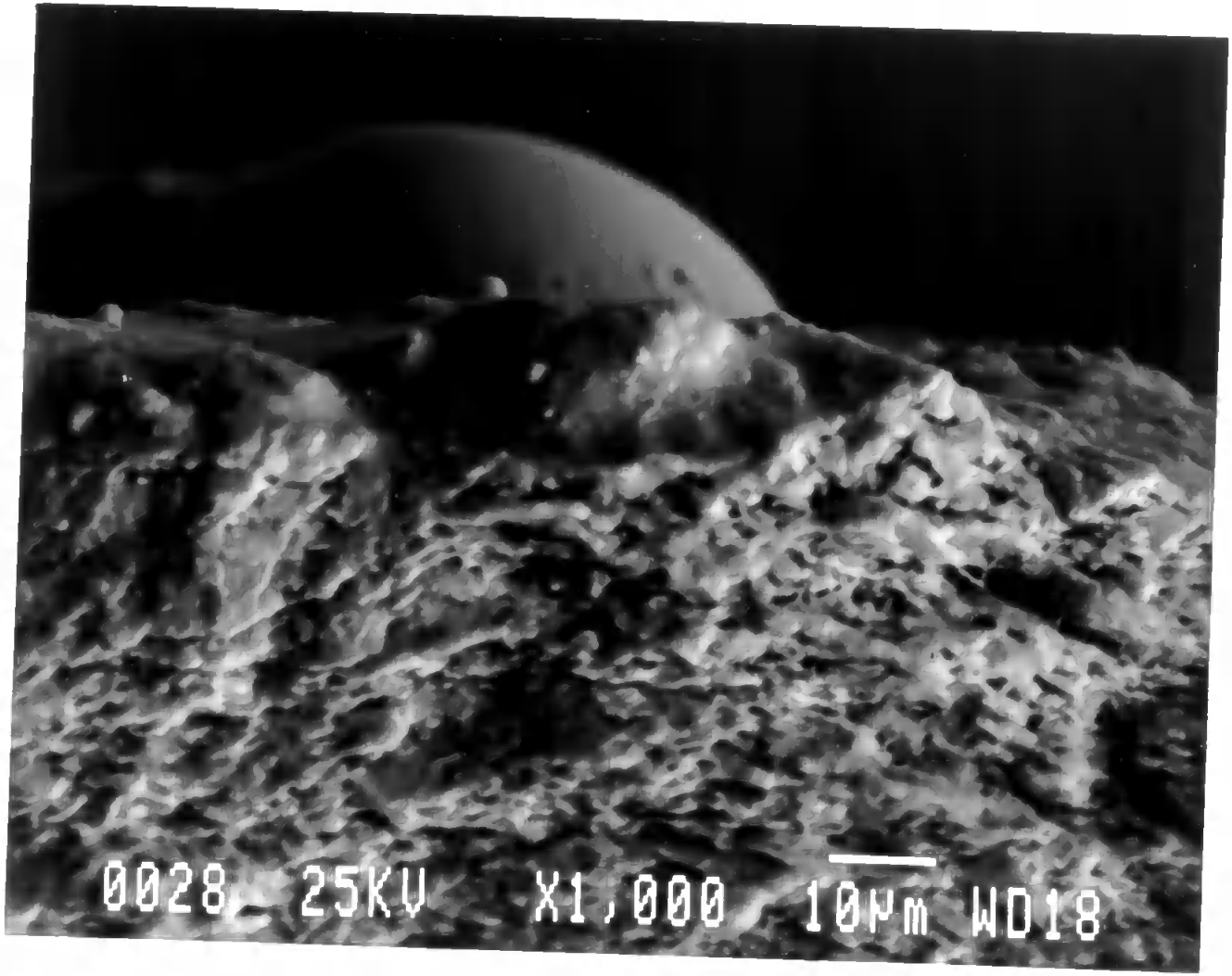

Plate 6.12 Electron micrograph of clay/latex formulation - heat dried

Plate 6.13 Electron micrograph of clay/latex formulation - heat dried

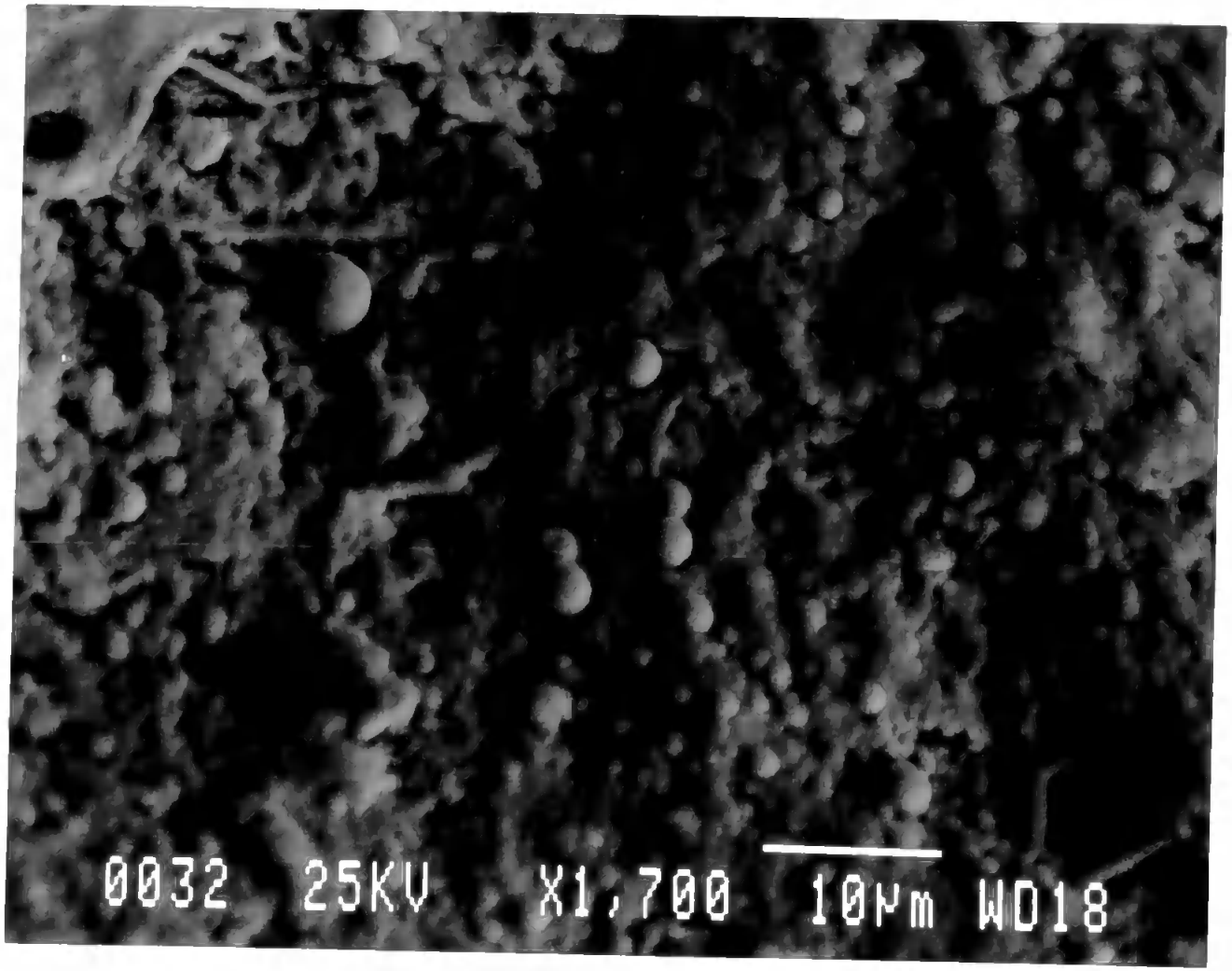

Plate 6.14 Electron micrograph of clay/latex formulation - heat dried

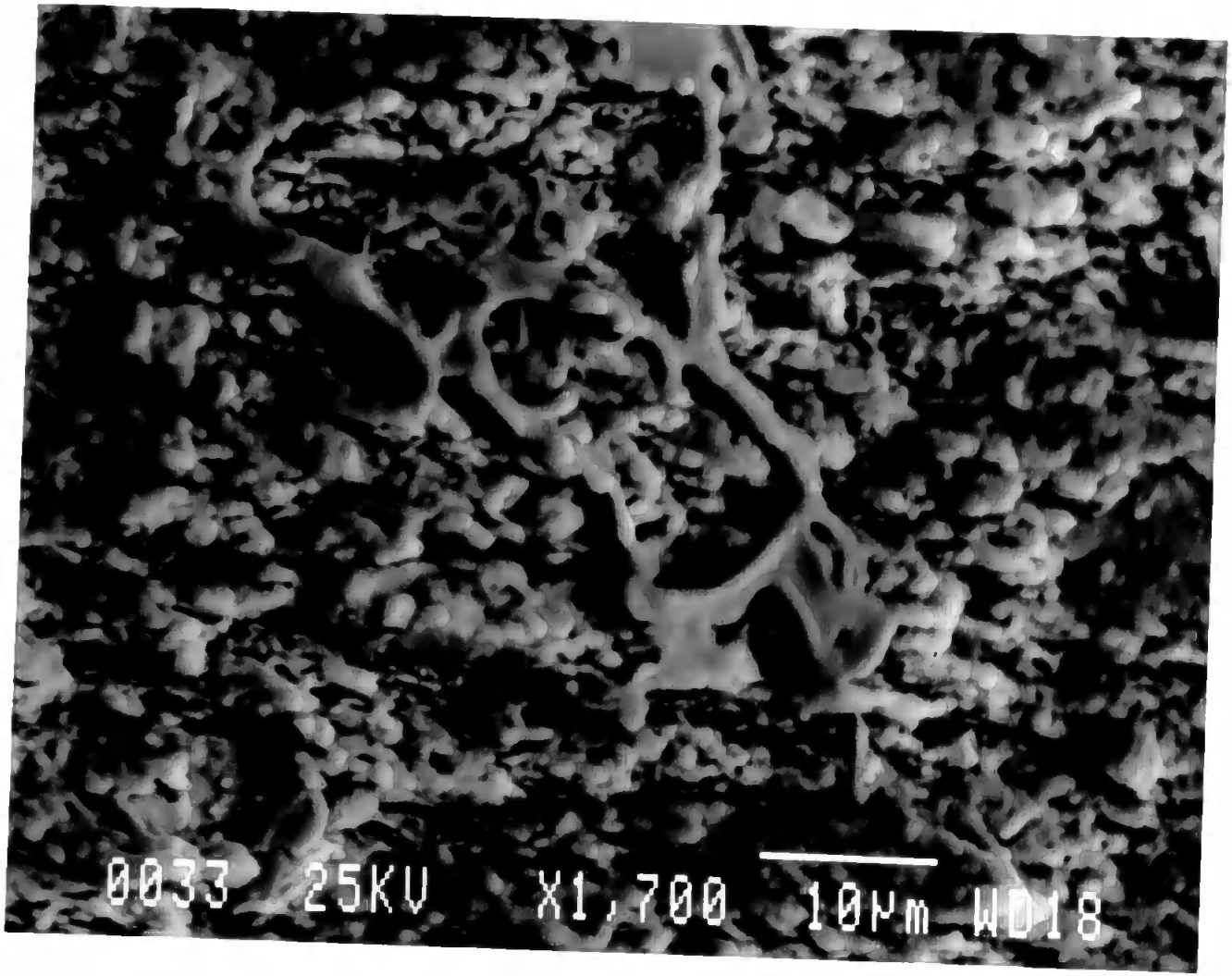

Plate 6.15 Electron micrograph of clay/latex formulation - heat dried

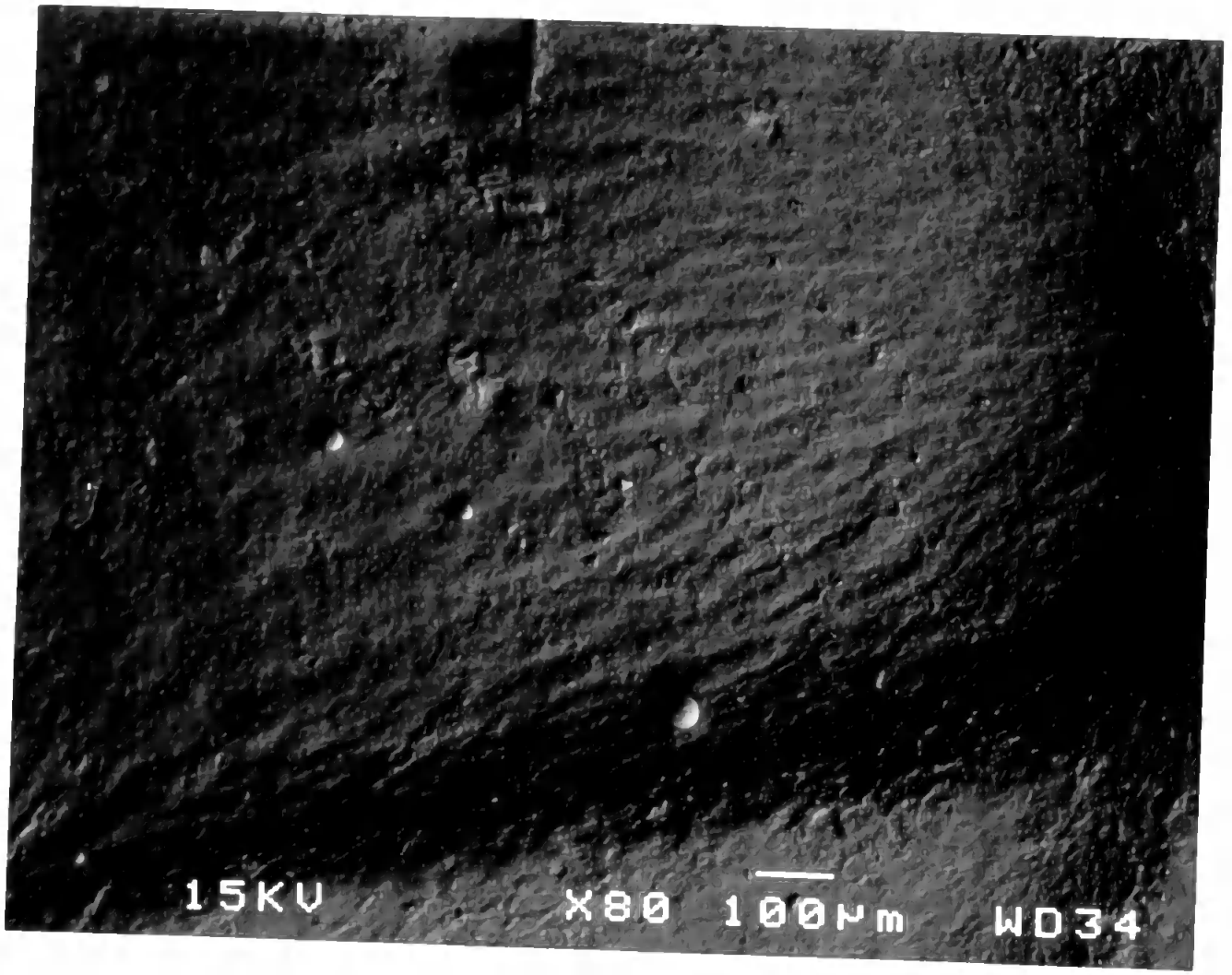

Plate 6.16 Electron micrograph of clay/starch formulation - air dried

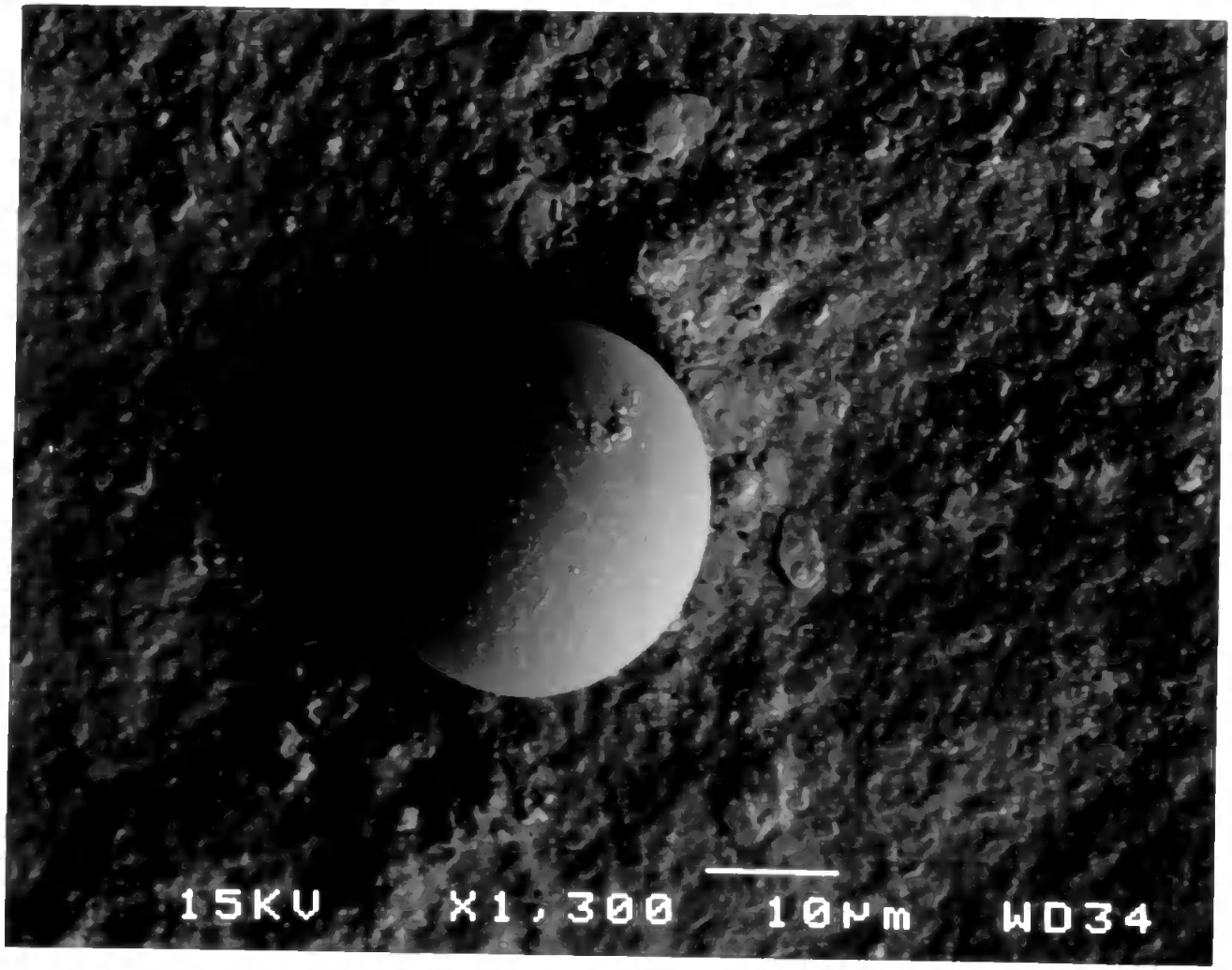

Plate 6.17 Electron micrograph of clay/starch formulation - air dried

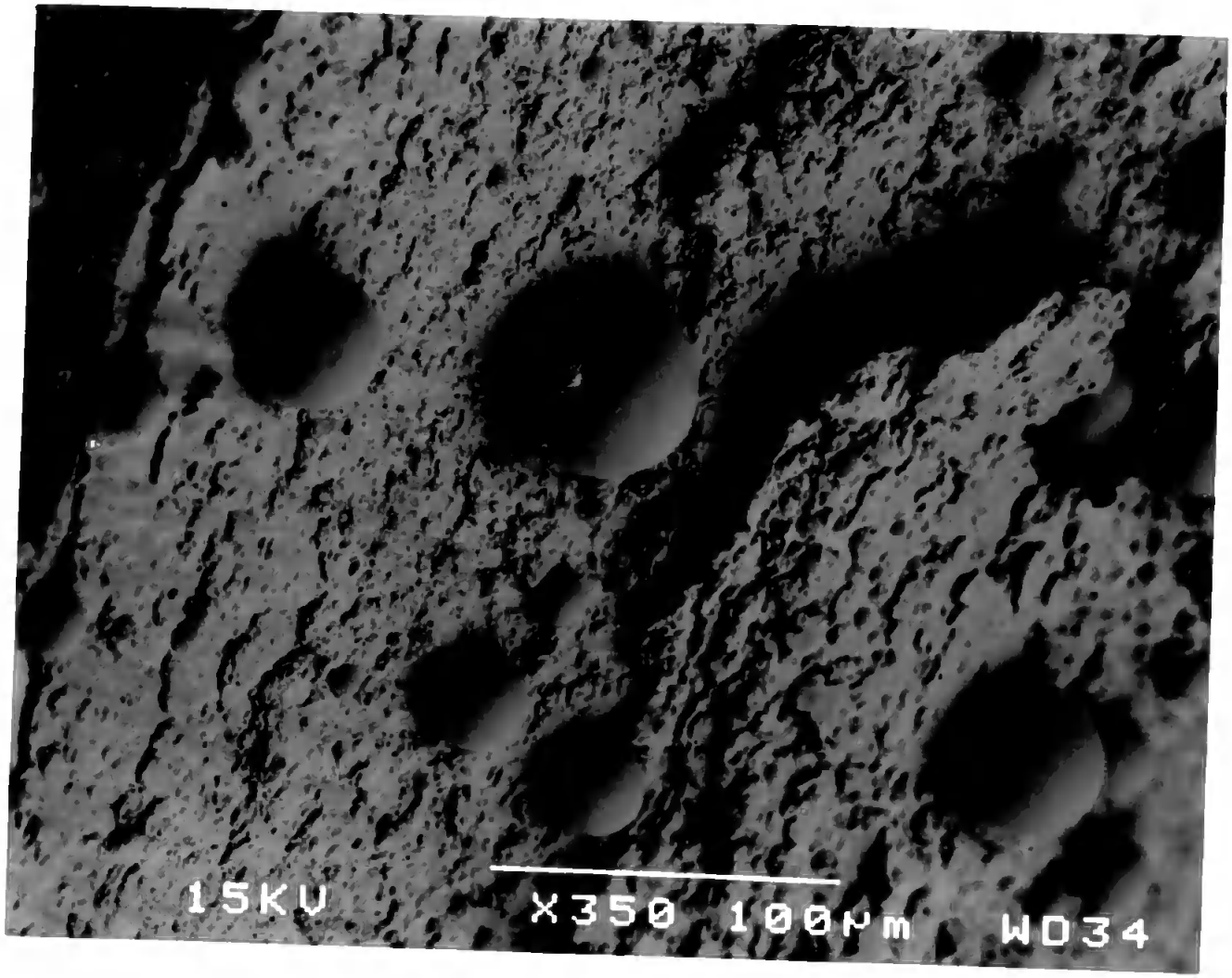

Plate 6.18 Electron micrograph of clay/starch formulation - air dried

pore diameters than the same clay with an addition of starch. The consolidation regimes had a significant effect upon the porous structure of the consolidated clay/latex samples but only a limited effect on the samples that contained starch. The shrinkage effects were most severe for the clay/latex sample that had been subjected to both pressure and heat. The use of heat in the consolidation process of the clay/latex samples produced a structure that had more mercury entrapment upon depressurisation. It is thought that drying at 110°C has assisted the formation of latex films within the porous structure that act as diaphragms over the throats. These diaphragms can be penetrated during the pressurisation cycle, but during the depressurisation the mercury thread snaps entrapping mercury in the pore structures. This effect was not evident for the clay/starch samples probably due to the lack of any compressible film formation within these structures.

From these results it is apparent that the characteristics of pigment/starch systems, such as low calendering, cracking tendency etc. can be related in part to structural packing derived from solution starch. In comparison integral latex spheres can contribute to voidage in-fill. The formation of a permanent compression and heat resistant structure during starch film formation is in marked contrast to the 'softer' structural nature imparted by latex during forming at elevated pressure and/or temperature.

CHAPTER 7

CONCLUSIONS

7.1 Work carried out

The end result of the work reported in this thesis is a greatly improved version of the computer program Pore-Cor. The presentation of the three dimensional unit cell has been improved, a user interface has been incorporated and the program runs much more rapidly with an automatic convergence routine that was written as part of this thesis. The automatic convergeance routine has four different fitting options; the 50% fit, the linear fit, the logarithmic fit or the linear top fit. All methods are weighted to fitting different sections of the simulated to experimental mercury intrusion curves. It is the operators choice as to which method will be most appropiate.

The permeability calculation was previously carried out on the mainframe network system, but is now an integral part of the Pore-Cor program. The DINIC network analysis algorithm in Pore-Cor results in the calculation time being reduced from ten minutes to several seconds.

The models employed as a basis for the computer simulations have been improved in order to be able to handle non-homogeneous structures of various types. These diverge somewhat from a completely random arrangement of the pores and throats, and include banded structures, clustered arrangements where the large pores are either at the centre or the periphery of the clusters, and stuctures where all the pores are of the same large size. These structures can be used to represent layered samples, clay included samples, vuggy soil samples and extremely open high-voidage fibrous mats.

The mercury extrusion curves have been simulated and the effects of contact angle hysteresis and trapping within wide pores adjacent to narrow throats have been demonstrated. The extrusion curves of the simulated structures have too high retention in

the middle of the experimental pressure range. This is a result of the geometry of the unit cell.

An additional program Pore-Comp has been developed which corrects experimental mercury intrusion data for mercury compression and penetrometer expansion. This program also takes into consideration any sample compression and can be used to calculate the bulk modulus of the sample. The capabilities of this program have been demonstrated using nine paper coating formulations.

An investigation into the trapping of mercury after hysteresis was carried out by using the cryo-stage of the electron microscope. The samples examined were blends of clay/latex and clay/starch dried at different temperatures and pressures. The most interesting result discovered was the unintruded centre of the clay/latex sample which was dried at an elevated temperature and under pressure. The results are shown in a series of electron micrographs at the end of Chapter 6.

Detailed results have been presented throughout the thesis. Mercury intrusion curves have been successfully simulated and other properties modelled. The simulated permeability values are rather low due to the restrictions of the network. However, the simulated porosity can always be matched to the experimental value.

7.2 Future work

Three consultancy projects have been undertaken as the result of an article that appeared in the Micromeritics report. Having read this article, forty industrial companies asked for further information about Pore-Cor and its capabilities. The consultancy studies carried out so far have been for the fibrous mat structure and the selection of building materials (granite, marble, slate, York stone, Bath stone and Portland stone). Consultancy work at the present time is concentrating on sintered tantalum slugs, which are used for capacitors of the smallest size for use in mobile phones, computers and other electronic

equipment. Porosity measurements and associated simulations are available for all the above but due to confidentiality requirements the results cannot be given in this thesis.

7.2.1 *Experimental*

For further development of Pore-Cor it would be advantageous to investigate samples such as sandstones with larger amounts of clay inclusions, perhaps known, or shown, to accumulate in certain areas giving rise to sections with grouped small void spaces together. The experimental mercury intrusion curve could then be modelled using the optimisation routine and the structure with small pores and throats in the centre. Similarly a sample, such as a vuggy soil, could be investigated and modelled using the structure with large pores and throats in the centre. In the work to date the only actual correlated samples investigated have been the banded reservoir sandstone samples.

The actual measurement of correlation in specific samples is a study currently part of a different PhD project. This work is closely related to this project and will be a very useful measure in choosing deciding the type and level of correlation to use. The work to date has been submitted for publication (Adams, J.M. *et al.* 1995)

For full clarity of the capabilities of Pore-Cor it would be very useful to have full sets of data (experimental intrusion and extrusion curves, porosity, permeability, tortuosity, Archies coefficients) for a range of samples. Preliminary work has been carried out on simulating Archies first, second and third coefficients. A grant application is being reviewed for such a set of data to be collected for a range of Fontainebleau sandstone samples of varying porosities. The three main experimental values needed are the intrusion and extrusion data, the porosity and the permeability, any other measurements are simply further clarification that the simulated structure is close to the actual void space structure, although still only a representation.

An area where mercury porosimetry has been used, and which could benefit from

Pore-Cor analysis is within the concrete industry (Cabrera, J.G., *et al.* 1993; Penttalla, V.E. 1994).

7.2.2 *Computational improvements*

Computational developments for the future would be to increase the unit cell size. The main limitation on this is the algorithm for calculating the maximum capacity of the unit cell. This algorithm could cope with at the most a 30 x 30 x 30 unit cell, however, if the unit cell was increased to this size the Pore-Cor program would then have to be altered throughout its entirety. Such an enlargement would increase the amount of computing in both memory size and time, which runs counter to another improvement which would to be enable Pore-Cor to run on a desk top computer. This would be a great advantage, not least because it would produce a marketable product.

Current optimisation routines are somewhat limited on both overall capability and computational time. It should be possible to use comparatively recent techniques such as a Simulated Annealing / Simplex algorithm to examine a hypersurface in several dimensions, hunting for maxima and minima while changing several variables at once. Examples of such variables are the skew, connectivity, random number seed, type of structure and level of correlation. The Simplex method is a trusted parameter optimisation technique, but because of the vastness of any hyperspace with more than three dimensions it is necessary to use Annealing to ensure that the program homes in on a global maximum or minimum and does not get trapped in a small local extremum.

7.3 Summary

The main achievements of this project have been the development of the optimisation routine for fitting the simulated mercury intrusion data to the experimental, the improvement of the permeability routine to incorporate the whole calculation into Pore-

Cor and reduce the time taken for the calculation and to develop the non-homogeneous structures for the modelling of a much wider range of porous materials. At the start of the project only outcrop sandstone, and reservoir sandstone to a lesser extent, had been successfully modelled. Now these sandstones, as well as Fontainebleau sandstone with and without clay inclusions, a range of building materials, paper coatings, fibrous mats, battery separators and tantalum slugs for capacitors have all been successfully simulated with the development of further structures. The program Pore-Comp has been created to produce improved porosity and experimental mercury intrusion measurements.

LIST OF SYMBOLS

A	cross-sectional area of unit cell normal to flow
Cu	size of cubic pore
d	throat diameter
d_c	characteristic throat diameter
D	fractal dimension
dV/dt	volumetric flow rate
δV_{blank}	total change in mercury volume during blank run
δV_{Hgpen}	increase in mercury volume due to compression of a volume of mercury which fills the empty penetrometer
δV_{pen}	increase in mercury volume due to penetrometer expansion
δV_{Hg}	increase in mercury volume due to compression of mercury during sample run
δV_{Hgbulk}	compression of mercury volume corresponding to sample bulk volume
δV_{sample}	increase in mercury volume caused by the compression of the sample
δV_{ss}	compression of continuous solid phase of sample
δV_{su}	compression of solid into unintruded void space
F	formation factor
h	throat length
k	absolute permeability
l	length
m_{sample}	mass of sample
M_{ss}	solid phase bulk modulus
n	number of experimental points
P	applied mercury pressure
P^1	atmospheric pressure
P_{50}	pressure at which 50 % pore volume is intruded
P^2	applied pressure at which accessible pore volume is fully intruded
P^{max}	maximum experimentally attainable applied pressure
r	throat radius
R	pore-size : throat-size ratio for trapping
t	time
T_g	glass transition temperature

V	volume of mercury intruded
V^1_{bulk}	bulk volume of sample at one atmosphere pressure
V_{obs}	observed volume of mercury intruded
V_{int}	volume intruded into sample
V^1_{blank}	volume of mercury used in the blank experiment at one atmosphere pressure
V^1_{pen}	volume of the penetrometer at one atmosphere pressure
V^1_{Hg}	total volume of mercury in filled penetrometer (with sample) at one atmosphere pressure
V^1_{Hgpen}	volume of mercury in filled penetrometer (no sample) at one atmosphere pressure
V^1_{Hgbulk}	volume of mercury equal to the bulk volume of sample at one atmosphere pressure
V^z_{ss}	volume of the continuous solid phase of the sample at zero void pressure
V^1_{solid}	volume of solid at one atmosphere pressure calculated from composition and constituent densities
$w_{pigment}$	relative weight of pigment in parts per hundred
w_{binder}	relative weight of binder in parts per hundred
x,y,z	Cartesian coordinates

Greek letters

β	number of tubes in z direction in a unit cell
γ	mercury interfacial tension
Δ	deviation between simulation and experiment
θ	mercury/solid/air contact angle
λ	mean free path length between molecular collisions in the fluid
μ	fluid viscosity
$\rho_{pigment}$	density of pigment
ρ_{binder}	density of binder
τ	tortuosity
ϕ^1	porosity at one atmosphere pressure
ϕ_{uncorr}	porosity uncorrected for compressibility
ϕ_{corr}	corrected porosity
ψ_{ss}	solid phase compressibility
Ω	network averaging operator

REFERENCES

Adams, J.M., Mathews, T., Matthews, G.P., Moss, A.K., and Ridgway, C.J., *Transport in Porous Media*, 1995, submitted for publn.

Adler, P.M., Jacquin, C.G. and Quiblier, J.A., *International Journal of Multiphase Flow*, 1990, **16**, 691.

Alince, B. and Lepoutre, P., *Journal of Colloid and Interface Science*, 1980a, **76**, 182.

Alince, B. and Lepoutre, P., *Journal of Colloid and Interface Science*, 1980b, **76**, 439.

Androutsopoulos, G.P. and Mann, R., *Chemical Engineering Science*, 1979, **34**, 1203.

Bell, W.K., Van Brakel, J. and Heertjes, P.M., *Powder Technology*, 1981, **29**, 75.

Blunt, M. and King, P., *Physical Review A*, 1990, **42**, 4780.

Blunt, M. and King, P., *Transport in Porous Media*, 1991, **6**, 407.

Bryant, S.L., Mellor, D.W. and Cade, C.A., *AIChE Journal*, 1993, **39**, 387.

Cabrera, J.G., Claisse, P.A. and Lynsdale, C.J., *Materials And Structures*, 1993, **26**, 587.

Cebeci, O.Z., *Journal of Colloid and Interface Science*, 1980, **78**, 383.

Chatzis, I. and Dullien, F.A.L., *Powder Technology*, 1981, **29**, 117.

Chatzis, I. and Dullien, F.A.L., *International Chemical Engineering*, 1985, **25**, 47.

Climpson, N.A. and Taylor, J.H., *Tappi Journal*, 1976, **59**, 89.

Conner, W.C., Blanco, C., Coyne, K., Neil, J., Mendioroz, S. and Pajares, J., *Characterization of Porous Solids*, 1988a, 273.

Conner, W.C., Horowitz, J. and Lane, A.M., *AIChE Symposium Series*, 1988b, **84**, 29.

Constantinides, G.N. and Payatakes, A.C., *Chemical Engineering Comm*, 1989, **81**, 55.

Cook, R.A. and Hover, K.C., *ACI Materials Journal*, 1993, **March/April**, 152.

Dawe, R.A. and Egbogah, E.O., *Contemporary Physics*, 1978, **19**, 355.

Day, M., Parker, I.B., Bell, J., Fletcher, R., Duffie, J., Sing, K.S.W. and Nicholson, D.,

Characterization of Porous Solids III. 1993, 225.

Deer, W.A., Howie, R.A. and Zussman, J., *Introduction to Rock Forming Minerals.* Longman, 1992, 476.

Dunmore, J.M.and Schols, R.S., *Society of Petroleum Engineers Journal*, 1974, **October**, 437.

Friesen, W.I. and Laidlaw, W.G., *Journal of Colloid and Interface Science*, 1993, **160**, 226

Gane, P.A.C. and Seyler, E.N., *Tappi Coating Conference Proceedings*, 1994.

Gane, P.A.C., Kettle, J.P., Matthews, G.P. and Ridgway, C.J., *Industrial and Engineering Chemistry Research*, 1995, submitted for publn.

Garboczi, E.J., *Powder Technology*, 1991, **67**, 121.

Gavrilenko, P. and Gueguen, Y., *Geophysics Journal International*, 1989, **98**, 159.

Good, R.J. and Mikhail, R.S., *Powder Technology*, 1981, **29**, 53.

Haines, W.B., *Journal of Agricultural Science*, 1927, **17**, 264.

Hamlen, R.C. and Scriven, L.E., *Tappi Coating Conference Proceedings*, 1991.

Hampton, J.H.D., Savage, S.B. and Drew, R.A.L. *Chemical Engineering Science*, 1993, **48**, 1601.

Hirasaki, G.J., *Interfacial Phenomena in Petroleum Recovery*, Marcel Dekker, New York, 1990, 77.

Ioannidis, M.A. and Chatzis, I., *Journal of Colloid and Interface Science*, 1993a, **161**, 278.

Ioannidis, M.A., Chatzis, I. and Sudicky, E.A., *Water Resources Research*, 1993b, **29**, 1777.

Jerauld, G.R. and Salter, S.J., *Transport in Porous Media*, 1990, **5**, 103.

Kent, H., Climpson, N., Gane, P., Coggon, L. and Hooper, J., *Tappi Coating Conference Proceedings*, 1986.

Kettle, J.P. and Matthews, G.P., *Advanced Coating Fundamentals Symposium*, 1993.

Kloubek, J., *Powder Technology*, 1981, **29**, 63.

Kloubek, J., *Journal of Colloid and Interface Science*, 1994, **163**, 10.

Koplik, J., Lin, C. and Vermette, M., *Journal of Applied Physics*, 1984, **56**, 3127.

Larrondo, L. and St-Amour, S., *Tappi Coating Conference Proceedings*, 1992.

Lee, J.A.and Maskell, W.C., *Powder Technology*, 1973, **7**, 259.

Lenormand, R., Touboul, E. and Zarcone, C., *Journal of Fluid Mechanics*, 1988, **189**, 165.

Lenormand, R., *Proc R Soc Lond A*, 1989, **423**, 159.

Lepoutre, P. and Rezanowich, A,. *Tappi Journal*, 1977, **60**, 86.

Li, Y., Laidlaw, W.G. and Wardlaw, N.C., *Advances in Colloid and Interface Science*, 1986a, **26**, 1.

Li, Y. and Wardlaw, N.C., *Journal of Colloid and Interface Science*, 1986b, **109**, 461.

Li, Y. and Wardlaw, N.C., *Journal of Colloid and Interface Science*, 1986c, **109**, 473.

Li, Y. and Wardlaw, N.C., *Interfacial Phenomena in Petroleum Recovery*, Marcel Dekker, New York, 1990, 101.

Lymberopoulos, D.P. and Payatakes, A.C., *Journal of Colloid and Interface Science*, 1992, **150**, 61.

Mann, R., Androutsopoulos, G.P. and Golshan, H., *Chemical Engineering Science*, 1981, **36**, 337.

Mason, G., Morrow, N.R. and Walsh, T., *Characterization of Porous Solids*, 1988, 243.

Mason, G. and Mellor, D.W., *Characterization of Porous Solids II*, 1991, 41.

Mathews, T., Matthews, G.P., Moss, A.K. and Powell, G., *Journal of the Society of Petroleum Engineers: Formation Evaluation pre-prints*, 1994.

Matthews, G.P. and Spearing, M.C., *Marine and Petroleum Geology*, 1992, **9**, 146.

Matthews, G.P., Moss, A.K., Spearing, M.C. and Voland F., *Powder Technology*, 1993,

76, 95.

Matthews, G.P. and Ridgway, C.J., *Computer Modelling of the Void structure of a Non-Bonded Fibrous Network*, 1994.

Matthews, G.P., Moss, A.K. and Ridgway, C.J., *Powder Technology*, 1995a, **83**, 61.

Matthews, G.P., Ridgway, C.J.and Spearing, M.C., *Journal of Colloid and Interface Science*, 1995b, **171**, 8.

Matthews, G.P. and Ridgway, C.J., *Preliminary Mercury Porosimetry Study of Building Materials to test feasibility of use in the study of sealer pigment migration*, 1995c.

Matthews, G.P. and Ridgway, C.J., *Feasibility Study of the Void Space Modelling of AVX Tantalum Capacitors using Pore-Cor*, 1995d.

Moss, A.K and Matthews, G.P., *Geofluids '93*, 1993.

Penttala, V.E., *Magazine of Concrete Research* 1994, **44**, 87.

Pickell, J.J., Swanson, B.F. and Hickman, W.B., *Society of Petroleum Engineers Journal*, 1966, 55.

Portsmouth, R.L. and Gladden, L.F., *Chemical Engineering Science*, 1991, **46**, 3023.

Postek, M.T., *Scanning Electron Microscopy - A Student's Handbook*, Burlington, Vermont, LADD Research Industries Inc., 1980.

Ranger, A.E., *Fundamental Properties of Paper Related to Its Uses*, 1983.

Ringrose, P.S., Pickup, G.E., Jensen, J.L. and Sorbie, K.S., *3rd European Conference on the Mathematics of Oil Recovery, DELFT*, 1992, 15.

Shaw, D.J., *Introduction to Colloid and Surface Chemistry*, third edition, Butterworth, London, 1986.

Shinohara, K., *Powder Technology Handbook*, Marcel Dekker, New York, 1990, 481.

Small, J.S., Hamilton, D.L. and Habesch, S., *Journal of Sedimentary Petrology*, 1992a, **62**, 508.

Small, J.S., Hamilton, D.L. and Habesch, S., *Journal of Sedimentary Petrology*, 1992b,

62, 520.

Spearing, M.C. and Matthews, G.P., *Computer Modelling in the Environmental Sciences*. Oxford University Press, Oxford, 1991a, 139.

Spearing, M.C. and Matthews, G.P., *Transport in Porous Media*, 1991b, **6**, 71.

Templeton, C., *Petroleum Transactions AIME*, 1954, **201**, 161.

Thiry, M. and Millot, G., *Journal of Sedimentary Petrology*, 1987, **57**, 343.

Thompson, A.H., Katz, A.J. and Raschke, R.A.., *62nd Annual Technical Conference and Exhibition of the Society of Petroleum Engineers*, 1987.

Tsakiroglou, C.D. and Payatakes, A.C., *Journal of Colloid and Interface Science*, 1990, **137**, 315.

Tsakiroglou, C.D. and Payatakes, A.C., *Journal of Colloid and Interface Science*, 1991, **146**, 479.

Tsakiroglou, C.D. and Payatakes, A.C., *Journal of Colloid and Interface Science*, 1993, **159**, 287.

Van Brakel, J., *Powder Technology*, 1975, **11**, 205.

Van Brakel, J., Modry, S. and Svata, M., *Powder Technology*, 1981, **29**, 1.

Vizika, O., Avraam, D.G., and Payatakes, A.C., *Journal of Colloid and Interface Science*, 1994, **165**, 386.

Wardlaw, N.C. and Taylor, R.P., *Bulletin of Canadian Petroleum Geology*, 1976, **24**, 225.

Wardlaw, N.C. and Cassan, J.P., *Bulletin of Canadian Petroleum Geology*, 1979, **27**, 117.

Wardlaw, N.C. and McKellar, M., *Powder Technology*, 1981, **29**, 127.

Wardlaw, N.C., Li, Y. and Forbes, D., *Transport in Porous Media*, 1987, **2**, 597.

Wardlaw, N.C., *North Sea Oil and Gas Reservoirs - II*, Graham and Trotman, Tronheim, Norway, 1990, 229.

Warren, N. and Nashner, R., *The Physics and Chemistry of Minerals and Rocks*, John Wiley & Sons, London, 1976, 197.

Watanabe, J. and Lepoutre, P., *Journal of Applied Polymer Science*, 1982, **27**, 4207.

Wilson, M.D. and Pittman, E.D., *Journal of Sedimentary Petrology*, 1977, **47**, 3.

Yamazaki, H. and Munakata, Y., *Oxford Fundamental Research Symposium Proceedings*, 1993.

Yanuka, M., Dullien, F.A.L. and Elrick, D.E., *Journal of Colloid and Interface Science*, 1986, **112**, 24.

Yuan, H.H. and Swanson, B.F., *Society of Petroleum Engineers Formation Evaluation*, 1989, 17.

Zgrablich, G., Mendioroz, S., Daza, L., Pajares, J., Mayagoitia, V., Rojas, F. and Conner W.C., *Langmuir*, 1991, **7**, 779.

APPENDIX 1

FURTHER PORE-COR GRAPHIC DEVELOPMENTS

A new logo for Pore-Cor has been designed by James Matthews and is shown in Plate A1.1. A button operated user interface screen has been developed and incorporated into the program by Joseph Matthews. Initially Pore-Cor ran on a purely question / answer format to set up the pore and throat size distribution. A mouse controlled window was then used to display the further options. These included the viewing or printing of the mercury intrusion/extrusion curves, the pore and throat size distributions or the three-dimensional unit cell. Other options from this window included colloidal blocking of the unit cell, polymer pore plugging of the unit cell or tortuosity. The permeability option could only be carried out on exiting the program. This was initially the case as the permeability calculation was carried out on the University network system. The new user interface now allows all data input options and output options to be accessible from the one screen, see Fig. A1.1. The red boxes indicate the initial input data needed to set up the unit cell. It is also possible to use the default button which will input all the initial data which has been previously stored into a default file. Once the data is entered the buttons all turn orange, next either the manual or auto button needs to be selected. The auto button requires the user to select a method of fit which have been described previously. The manual button also requires the user to select a measure of fit but this is purely for comparison purposes between different mercury intrusion curves. The next stage is for all the buttons to turn green, this indicates that the options are all available and it is then possible to choose an option to investigate the simulated structure further. One of the major advantages of this user screen is that the permeability calculation is now incorporated into Pore-Cor which is very time saving. It is also possible to just change one of the initial input parameters and reconstruct the unit cell without having to re-input

Plate A1.1 Pore-Cor logo

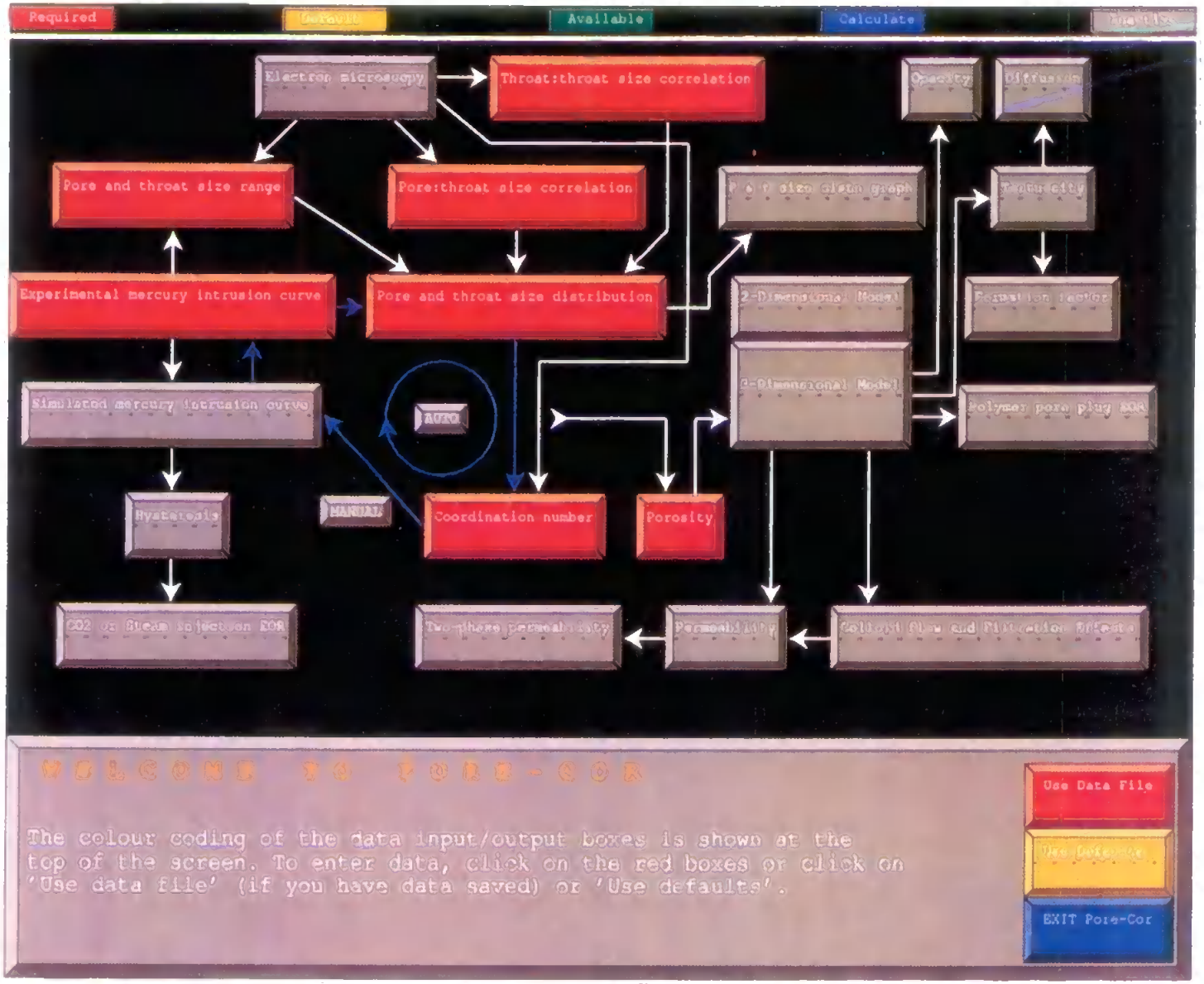

Figure A1.1 Pore-Cor User Interface

the whole set of data.

The three-dimensional unit cells of the correlated structures shown in this thesis have been complete unit cells and the central structure has not been visible. For graphical purposes only it is possible to view only half of the unit cell, and hence the internal layout of pores and throats. Half of the fully correlated unit cell with small pores and throat in the centre is shown in Fig. A1.2, and half of the fully correlated unit cell with large pores and throat in the centre is shown in Fig. A1.3

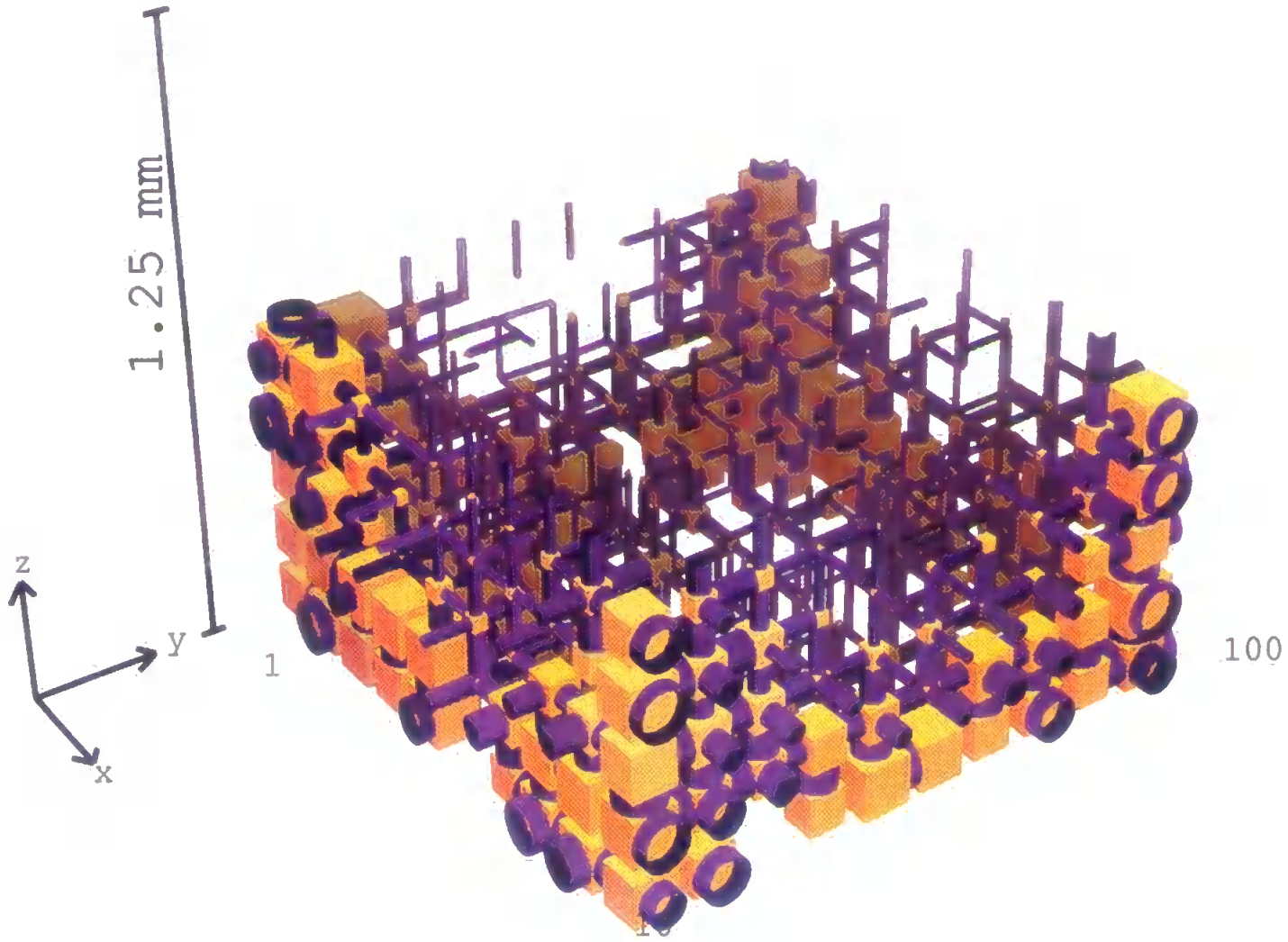

Figure A1.2 Half of the totally correlated unit cell with small pores and throats in the centre

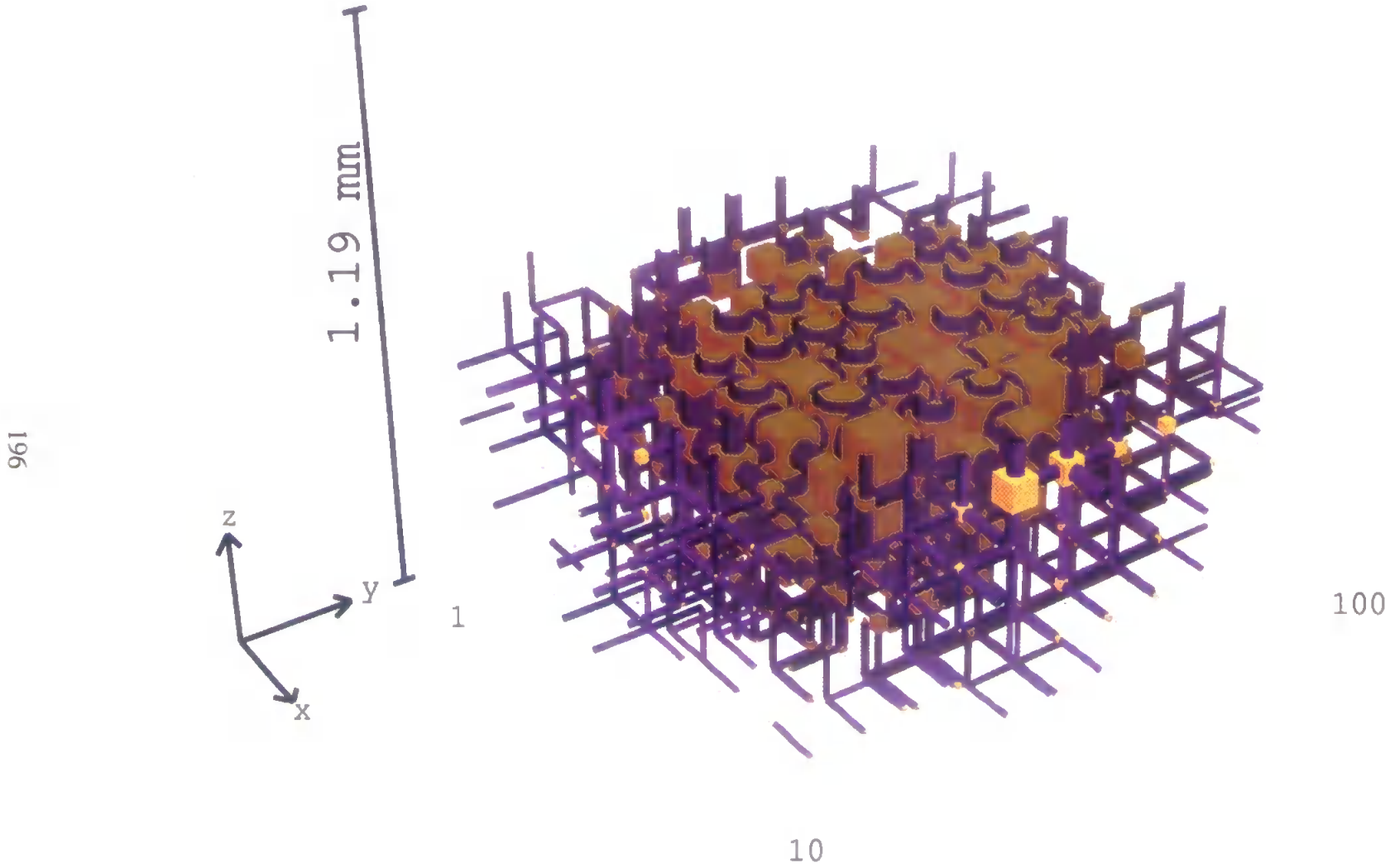

Figure A1.3 Half of the totally correlated unit cell with large pores and throats in the centre

APPENDIX 2

MERCURY POROSIMETRY

Mercury intrusion / extrusion cycles were mainly performed at English China Clay International plc. R&D, St Austell on a Micromeritics PoreSizer 9320 Mercury Porosimeter. The PoreSizer 9320 is a 30,000 psia (207 MPa) mercury porosimeter covering the pore diameter range from approximately 360 to 0.006 μm. The unit has two built-in low pressure ports and one high pressure chamber. Data collection, data reduction, and data display are processed by the optional control module. All aspects of the high pressure analysis are also managed by the control module. Fig. A2.1 shows the general appearance of the mercury porosimeter.

The PoreSizer measures the volume distribution of pores in materials by mercury intrusion or extrusion. Mercury has a high surface tension and is non-wetting to all materials with the exception of a few noble metals. These properties cause a mercury surface in contact with a solid to assume the minimum surface area and largest radius of curvature possible at a given pressure. An increase in pressure on the mercury shifts the balance between surface tension and surface area causing the radius of curvature of the mercury contacting the solid to become smaller. When the radius is equal to that of a pore entrance (throat), mercury fills the volume within the pore. A thorough discussion of the theory of porosimetry is given previously.

Initial information needs to be input into the control module; penetrometer volume, penetrometer weight, sample weight, mercury density, etc. The low pressure run is carried out manually and then the high pressure run is controlled according to a selected pressure table with a specified equilibrium time by the control module. An example of the output data can be seen in Figs. A2.2 - A2.4. The summary sheet is shown in Fig. A2.2, the porosimetry data is shown in Fig. A2.3 and Fig. A2.4 shows the graph of cumulative

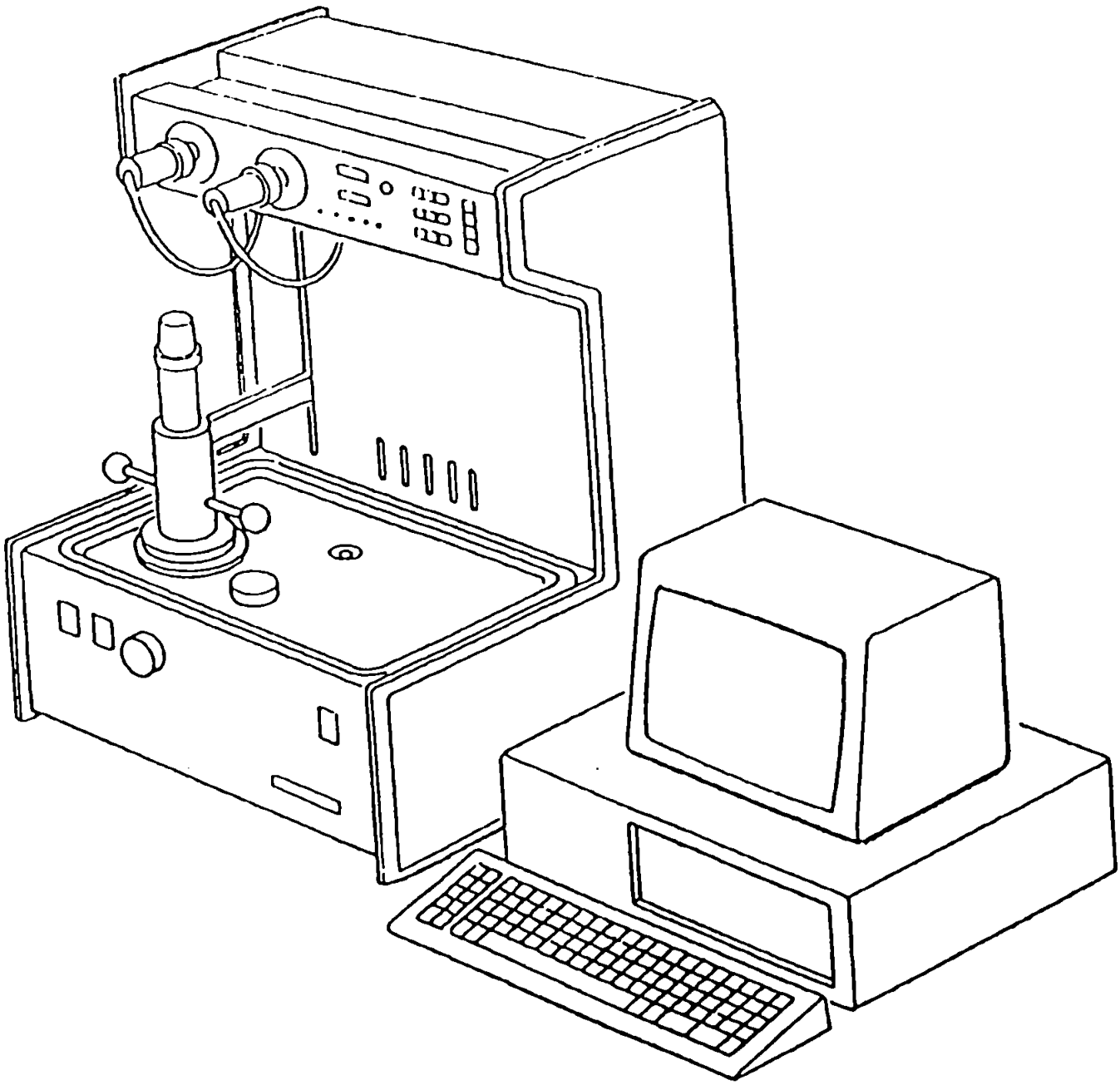

Figure A2.1 Micromeritics PoreSizer 9320 Mercury Porosimeter

Mercury porosimetry for dried lump samples

```
PORESIZER 9320 V1.00                                              PAGE   1

SAMPLE DIRECTORY/NUMBER: JPK94    /66
OPERATOR:                                          LP   07:04:02 07/20/94
SAMPLE ID: F2 sandstone                            HP   09:57:17 07/20/94
SUBMITTER:                                         REP  19:26:02 11/25/95

PENETROMETER NUMBER: 413                  ADVANCING CONTACT ANGLE: 140.0 deg
PENETROMETER CONSTANT:  10.79 µL/pF       RECEDING CONTACT ANGLE:  130.0 deg
PENETROMETER WEIGHT:    78.4163 g         MERCURY SURFACE TENSION: 485.0 dyn/cm
STEM VOLUME:             0.3960 mL        MERCURY DENSITY:        13.5359 g/mL
MAXIMUM HEAD PRESSURE: 4.4500 psi         SAMPLE WEIGHT:           0.7857 g
PENETROMETER VOLUME:   15.5710 mL         SAMPLE+PEN+Hg WEIGHT: 284.9500 g

LOW PRESSURE:
        MERCURY FILLING PRESSURE:  0.1533 psia
        LAST LOW PRESSURE POINT: 15.0960 psia

HIGH PRESSURE:
        RUN TYPE:                  AUTOMATIC
        RUN METHOD:                EQUILIBRATED
        EQUILIBRATION TIME:        240 seconds
```

INTRUSION DATA SUMMARY

TOTAL INTRUSION VOLUME =	0.0767	mL/g
TOTAL PORE AREA =	0.021	sq-m/g
MEDIAN PORE DIAMETER (VOLUME) =	32.8341	µm
MEDIAN PORE DIAMETER (AREA) =	0.8793	µm
AVERAGE PORE DIAMETER (4V/A) =	14.8097	µm
BULK DENSITY =	2.1188	g/mL
APPARENT (SKELETAL) DENSITY =	2.5299	g/mL
STEM VOLUME USED =	15	% ****

Figure A2.2 Fontainebleau sandstone sample summary sheet

Mercury porosimetry for dried lump samples

PORESIZER 9320 V1.00 PAGE 2

SAMPLE DIRECTORY/NUMBER: JPK94 /66
OPERATOR:
SAMPLE ID: P2 sandstone
SUBMITTER:

LP 07:04:02 07/20/94
HP 09:57:17 07/20/94
REP 19:26:02 11/25/95

PRESSURE psia	PORE DIAMETER µm	CUMULATIVE VOLUME mL/g	% OF TOTAL INTRUSION VOLUME
0.15	1405.7240	0.0000	0.0000
1.25	172.4585	0.0035	4.5952
2.43	88.6710	0.0053	6.9624
4.31	50.0122	0.0087	11.3984
5.50	39.1756	0.0143	18.6195
7.80	27.6451	0.0655	85.3988
9.64	22.3640	0.0730	95.2059
10.56	20.4156	0.0747	97.4537
11.78	18.2998	0.0762	99.3038
15.10	14.2782	0.0785	102.4070
25.26	8.5334	0.0783	102.0688
50.48	4.2745	0.0783	102.0290
75.93	2.8387	0.0778	101.4919
100.77	2.1391	0.0776	101.1339
154.44	1.3957	0.0772	100.6962
203.27	1.0604	0.0770	100.4177
302.10	0.7135	0.0769	100.2984
406.61	0.5301	0.0767	99.9801
503.11	0.4284	0.0766	99.8210
750.78	0.2871	0.0764	99.5624
1002.61	0.2150	0.0761	99.2839
1495.78	0.1441	0.0761	99.2640
1998.95	0.1078	0.0762	99.3236
2501.78	0.0862	0.0767	100.0000
2000.28	0.0904	0.0761	99.2839
1502.79	0.1204	0.0755	98.4683
1003.13	0.1803	0.0746	97.2548
750.63	0.2409	0.0738	96.2204
500.97	0.3610	0.0732	95.3849
401.81	0.4501	0.0726	94.6887
300.49	0.6019	0.0714	93.0774
200.16	0.9036	0.0703	91.7048
100.34	1.8025	0.0693	90.4118
71.01	2.5471	0.0689	89.8349
49.18	3.6775	0.0682	88.8801

Figure A2.3 Fontainebleau sandstone sample mercury porosimetry data

Mercury porosimetry for dried lump samples

PORESIZER 9520 V1.00

SAMPLE DIRECTORY/NUMBER: JPK94 /66
OPERATOR:
SAMPLE ID: FE sandstone
SUBMITTER:

LP 07:04:02 07/20/94
HP 09:57:17 07/20/94
REP 19:26:02 11/25/95

CUMULATIVE INTRUSION vs DIAMETER

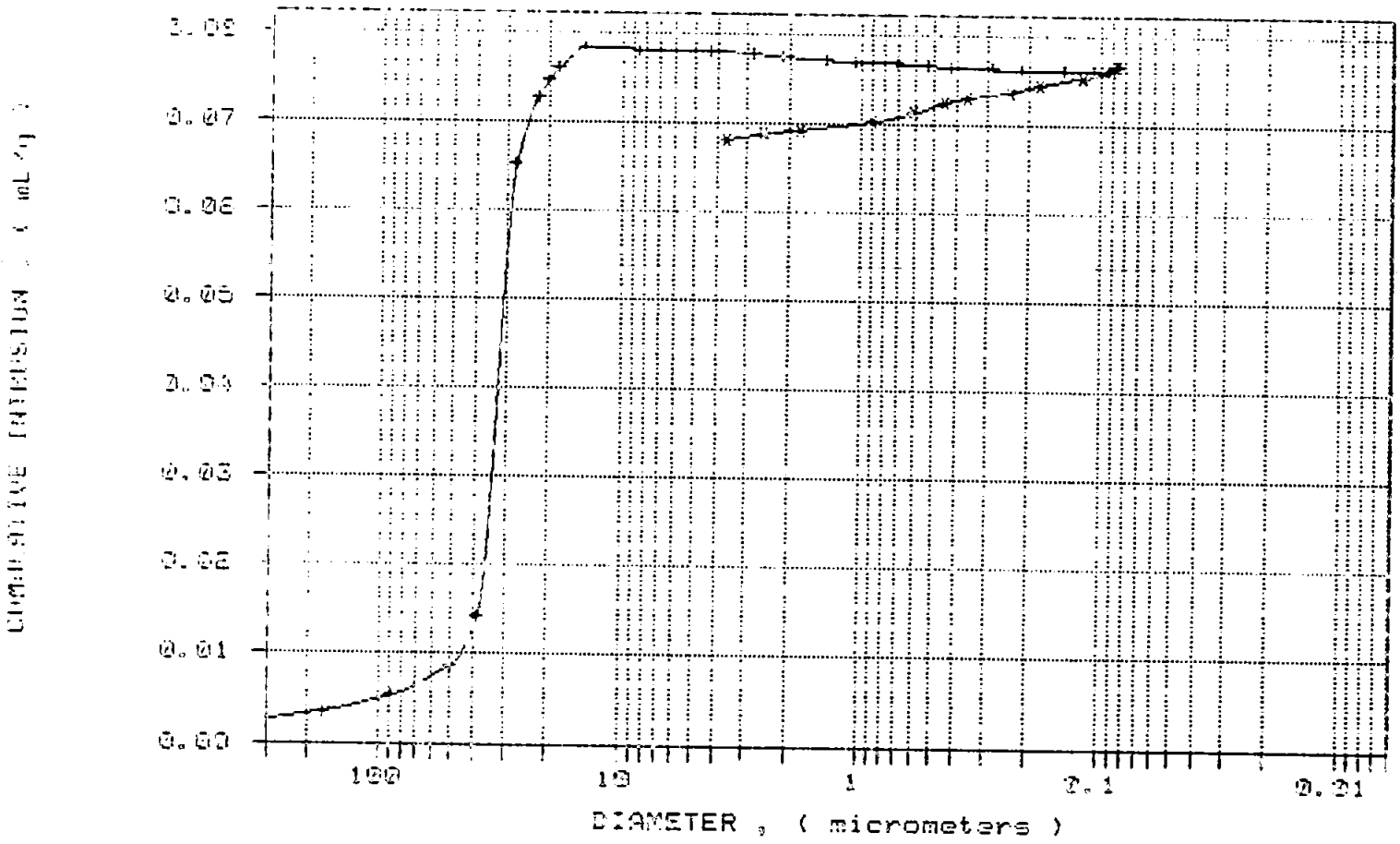

Figure A2.4 Cumulative volume intruded against throat diameter for Fontainebleau sandstone sample

volume intruded against throat diameter. For each run, an equivalent blank run was carried out to enable the corrections for mercury compression and penetrometer expansion. An example of the data obtained for a blank run can be seen in Figs. A2.5 -A2.7. These figures are the summary sheet, porosimetry data and cumulative volume intruded against throat diameter respectively. The corrections to the experimental run are carried out using the software package Pore-Comp. Fig. A2.8 shows the initial input information for Pore-Comp for a Fontainebleau sandstone sample and Fig. A2.9 shows the calculation stages for correcting the observed data for the mercury compression and penetrometer expansion. Figs. A2.10 and A2.11 show the same information from Pore-Comp but for a combination of a binder and pigment.

Mercury porosimetry for dried lump samples

PORESIZER 9320 V1.00 PAGE 1

SAMPLE DIRECTORY/NUMBER: JPK94 /69
OPERATOR:
SAMPLE ID: blank run for sample 413
SUBMITTER:

LP 13:59:43 07/20/94
HP 09:44:26 07/21/94
REP 19:50:14 11/25/95

PENETROMETER NUMBER:	413	ADVANCING CONTACT ANGLE:	140.0 deg
PENETROMETER CONSTANT:	10.79 µL/pF	RECEDING CONTACT ANGLE:	130.0 deg
PENETROMETER WEIGHT:	78.3950 g	MERCURY SURFACE TENSION:	485.0 dyn/cm
STEM VOLUME:	0.3960 mL	MERCURY DENSITY:	13.5291 g/mL
MAXIMUM HEAD PRESSURE:	4.4500 psi	SAMPLE WEIGHT:	0.0010 g
PENETROMETER VOLUME:	15.5710 mL	SAMPLE+PEN+Hg WEIGHT:	289.0100 g

LOW PRESSURE:
MERCURY FILLING PRESSURE: 0.1688 psia
LAST LOW PRESSURE POINT: 14.5484 psia

HIGH PRESSURE:
RUN TYPE: AUTOMATIC
RUN METHOD: EQUILIBRATED
EQUILIBRATION TIME: 240 seconds

INTRUSION DATA SUMMARY

TOTAL INTRUSION VOLUME	=	-5.3345 mL/g
TOTAL PORE AREA	=	2.780 sq-m/g
MEDIAN PORE DIAMETER (VOLUME)	=	1276.6693 µm
MEDIAN PORE DIAMETER (AREA)	=	0.1879 µm
AVERAGE PORE DIAMETER (4V/A)	=	-7.6760 µm
BULK DENSITY	=	0.2842 g/mL
APPARENT (SKELETAL) DENSITY	=	0.1129 g/mL
STEM VOLUME USED	=	0 % ****

Figure A2.5 Blank run summary sheet

Mercury porosimetry for dried lump samples

PORESIZER 9320 V1.00 PAGE 2

SAMPLE DIRECTORY/NUMBER: JPK94 /69
OPERATOR:
SAMPLE ID: blank run for sample 413
SUBMITTER:

LP 13:59:43 07/20/94
HP 09:44:26 07/21/94
REP 19:50:14 11/25/95

PRESSURE psia	PORE DIAMETER µm	CUMULATIVE VOLUME mL/g	% OF TOTAL INTRUSION VOLUME
0.17	1276.6693	0.0000	0.0000
1.65	155.4780	0.2997	-5.6180
3.15	68.3797	0.4795	-8.9888
4.64	44.5866	0.6953	-13.0337
6.16	33.7685	0.7912	-14.8315
7.72	27.3160	1.0070	-18.8764
9.26	21.6332	1.2347	-23.1461
10.79	19.9843	1.3546	-25.3933
12.36	18.6124	1.4745	-27.6405
14.55	14.8157	1.8101	-33.9326
24.95	8.6407	0.4196	-7.8652
50.16	4.2996	-1.3186	24.7191
75.81	2.8432	-2.4815	46.5169
101.15	2.1309	-3.3326	62.4719
151.66	1.4212	-4.1597	77.9775
204.17	1.0557	-4.6992	88.0899
305.01	0.7067	-5.0708	95.0562
404.01	0.5335	-5.3465	100.2247
501.85	0.4295	-5.5623	104.2697
749.35	0.2876	-5.7421	107.6405
1001.85	0.2151	-5.8500	109.6629
1495.69	0.1441	-5.8620	109.8876
2008.52	0.1073	-5.6342	105.6180
2497.18	0.0863	-5.3345	100.0000
1996.52	0.0906	-6.1617	115.5056
1500.21	0.1206	-7.6481	143.3708
1000.88	0.1807	-8.0797	151.4607
751.38	0.2407	-8.4513	158.4270
497.55	0.3635	-9.0867	170.3371
400.22	0.4519	-9.3504	175.2809
301.40	0.6001	-10.2495	192.1348
200.91	0.9002	-10.8489	203.3708
99.24	1.8224	-11.2924	211.6854
68.75	2.6309	-11.4962	215.5056
49.75	3.6355	-11.8318	221.7978

Figure A2.6 Blank run mercury porosimetry data

Mercury porosimetry for dried lump samples

PAGE 3

SAMPLE DIRECTORY/NUMBER: JPK94 /69

LP 13:59:43 07/20/94
HP 09:44:26 07/21/94
REP 19:50:14 11/25/95

CUMULATIVE INTRUSION vs DIAMETER

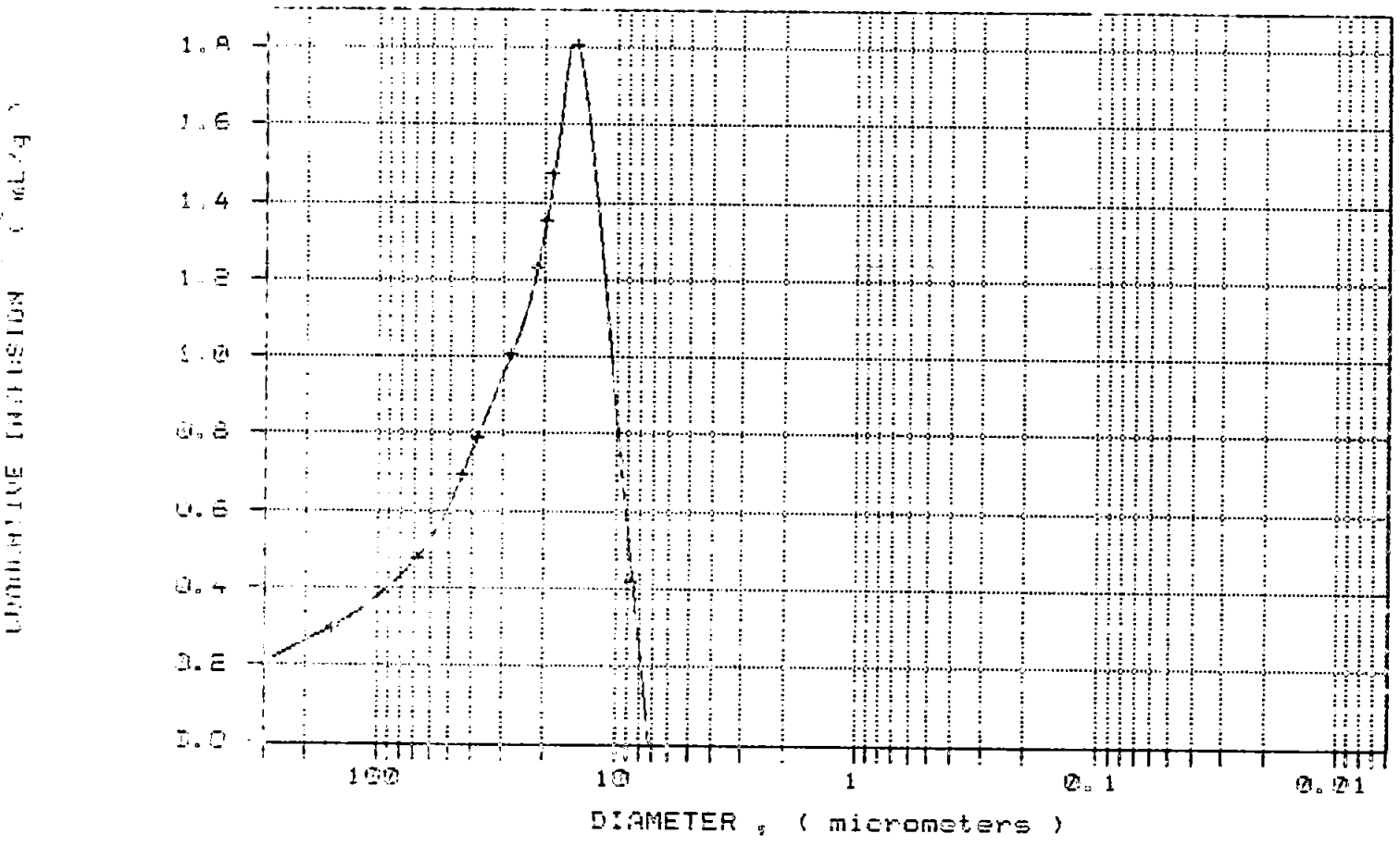

Figure A2.7 Cumulative volume intruded against throat diameter for blank run

Porosimeter run ref:		Small sample
Sample description:		Fontainebleau sandstone with clay precipitation
Specific gravity of solid phase		2.65 g/cm3
Penetrometer reference number		413
Maximum pressure		2500 psi
Sample weight		0.7900 g
Penetrometer + assembly		78.4200 g
Penetrometer + assembly + sample		79.2100 g
Penetrometer + assembly + sample + mercury		284.9500 g
Mercury weight in penetrometer containing sample		205.7400 g
Mercury Temperature		25.6 degC
Mercury Density		13.53 g/cm3
Blank: Penetrometer + assembly + mercury		289.0100 g
Blank: Mercury weight in penetrometer without sample		210.5900 g
Blank: Volume of penetrometer without sample		15.5710 cm3
Blank: Nominal weight		0.0010 g
Volume of mercury in penetrometer containing sample		15.2062 cm3
Bulk volume of sample (1 atm)		0.3648 cm3
Reciprocal density volume of sample		0.4618 cm3/g
Reciprocal density of solid phase of sample (1 atm)		0.2981 cm3/g
Maximum observed intrusion	Vobs	0.0767 cm3/g
Maximum intruded volume corrected for Hg & chamber	Vuncompmax	0.0838 cm3/g
Fully corrected maximum intruded volume	Vcompmax	0.0838 cm3/g
Porosity at atm		18.28 %
Porosity based on observed data		16.61 %
Porosity corrected for Hg & chamber		18.14 %
Porosity fully corrected corrected for compressibility		18.14 %

Figure A2.8 Initial Fontainebleau sandstone sample set up data for Pore-Comp

PRESSURE /psi	PRESSURE / Mpa	V blank /cm3g-1	V blank /cm3	V obs /cm3g-1	V obs /cm3	dV"Hg /cm3	Vint+dVs /cm3	PORE DIAM / um	% Pore vol
0.15	0.0010	0.0000	0.0000	0.0000	0.0000	1.575E-08	1.575E-08	1422.1511	0.0000
1.25	0.0086	0.2997	0.0003	0.0035	0.0028	1.313E-07	2.465E-03	170.6581	3.7248
2.43	0.0168	0.4100	0.0004	0.0053	0.0042	2.552E-07	3.777E-03	87.7871	5.7068
4.31	0.0297	0.6181	0.0006	0.0087	0.0069	4.527E-07	6.255E-03	49.4948	9.4507
5.50	0.0379	0.7912	0.0008	0.0143	0.0113	5.777E-07	1.051E-02	38.7859	15.8733
7.80	0.0538	1.0070	0.0010	0.0655	0.0517	8.192E-07	5.074E-02	27.3491	76.6575
9.64	0.0665	1.2347	0.0012	0.0730	0.0577	1.012E-06	5.644E-02	22.1289	85.2654
10.56	0.0728	1.3546	0.0014	0.0747	0.0590	1.109E-06	5.766E-02	20.2010	87.1134
11.78	0.0812	1.4745	0.0015	0.0762	0.0602	1.237E-06	5.872E-02	18.1089	88.7228
15.10	0.1041	1.8101	0.0018	0.0785	0.0620	1.586E-06	6.021E-02	14.1273	90.9614
25.26	0.1742	0.4196	0.0004	0.0783	0.0619	2.653E-06	6.144E-02	8.4451	92.8251
50.43	0.3477	-1.3186	-0.0013	0.0783	0.0619	5.296E-06	6.318E-02	4.2301	95.4552
75.93	0.5235	-2.4815	-0.0025	0.0778	0.0615	7.974E-06	6.395E-02	2.8095	96.6195
100.77	0.6948	-3.3326	-0.0033	0.0776	0.0613	1.058E-05	6.465E-02	2.1169	97.6705
154.44	1.0648	-4.1597	-0.0042	0.0772	0.0610	1.622E-05	6.516E-02	1.3813	98.4512
203.27	1.4015	-4.6992	-0.0047	0.0770	0.0608	2.134E-05	6.555E-02	1.0495	99.0354
302.10	2.0829	-5.0708	-0.0051	0.0769	0.0608	3.171E-05	6.585E-02	0.7061	99.4931
406.61	2.8035	-5.3465	-0.0053	0.0767	0.0606	4.267E-05	6.598E-02	0.5246	99.6875
503.11	3.4688	-5.5623	-0.0056	0.0766	0.0605	5.279E-05	6.613E-02	0.4240	99.9095
750.78	5.1764	-5.7421	-0.0057	0.0764	0.0604	7.874E-05	6.618E-02	0.2841	99.9816
1002.61	6.9127	-5.8500	-0.0059	0.0761	0.0601	1.051E-04	6.607E-02	0.2128	99.8264
1495.78	10.3130	-5.8620	-0.0059	0.0761	0.0601	1.567E-04	6.614E-02	0.1426	99.9224
1998.95	13.7822	-5.6342	-0.0056	0.0762	0.0602	2.092E-04	6.604E-02	0.1067	99.7769
2501.78	17.2491	-5.3345	-0.0053	0.0767	0.0606	2.615E-04	6.619E-02	0.0853	100.0000
2000.28	13.7914	-6.1617	-0.0062	0.0761	0.0601	2.093E-04	6.649E-02	0.1066	100.4547
1502.79	10.3613	-7.6481	-0.0076	0.0755	0.0596	1.574E-04	6.745E-02	0.1420	101.9059
1003.13	6.9163	-8.0797	-0.0081	0.0746	0.0589	1.052E-04	6.712E-02	0.2127	101.4048
750.63	5.1754	-8.4513	-0.0085	0.0738	0.0583	7.873E-05	6.683E-02	0.2842	100.9715
500.97	3.4541	-9.0867	-0.0091	0.0732	0.0578	5.257E-05	6.697E-02	0.4258	101.1758
401.81	2.7704	-9.3504	-0.0094	0.0726	0.0574	4.217E-05	6.675E-02	0.5309	100.8424
300.49	2.0718	-10.2495	-0.0102	0.0714	0.0564	3.154E-05	6.669E-02	0.7099	100.7524
200.16	1.3800	-10.8489	-0.0108	0.0703	0.0555	2.101E-05	6.641E-02	1.0658	100.3292
100.34	0.6918	-11.2924	-0.0113	0.0693	0.0547	1.054E-05	6.605E-02	2.1260	99.7899
71.01	0.4896	-11.4962	-0.0115	0.0689	0.0544	7.457E-06	6.593E-02	3.0041	99.6157
49.18	0.3391	-11.8318	-0.0118	0.0682	0.0539	5.165E-06	6.571E-02	4.3376	99.2838

Figure A2.9 Fontainebleau sandstone sample data corrections for mercury compression and penetrometer expansion

Porosimeter run ref:		Binder and pigment	
Sample description:		Carbital 90 with 12 pph latex 95L10	
Specific gravity of pigment		2.71	g/cm3
Specific gravity of binder		1.05	g/cm3
pph of pigment		100	
pph of binder		12	
Total pph		112	
Specific gravity of solid phase of composite		2.32	g/cm3
Volume of solid composite		0.43	cm3/g
Penetrometer reference number		423	
Maximum pressure		30000	psi
Sample weight		0.6757	g
Penetrometer + assembly		77.6426	g
Penetrometer + assembly + sample		78.3183	g
Penetrometer + assembly + sample + mercury		280.8700	g
Mercury weight in penetrometer containing sample		202.5517	g
Mercury Temperature		23	degC
Mercury Density		13.5389	g/cm3
Blank: Penetrometer + assembly + mercury		285.1300	g
Blank: Mercury weight in penetrometer without sample		207.4874	g
Blank: Volume of penetrometer without sample		15.3219	cm3
Blank: Nominal weight		0.0010	g
Volume of mercury in penetrometer containing sample		14.9607	cm3
Bulk volume of sample (1 atm)		0.3612	cm3
Reciprocal density volume of sample		0.5345	cm3/g
Reciprocal density of solid phase of sample (1 atm)		0.4315	cm3/g
Maximum observed intrusion	Vobs	0.1214	cm3/g
Maximum intruded volume corrected for Hg & chamber	Vuncompmax	0.1047	cm3/g
Fully corrected maximum intruded volume	Vcompmax	0.1025	cm3/g
Porosity at atm		19.2727	%
Porosity based on observed data		22.7117	%
Porosity corrected for Hg & chamber		19.5967	%
Porosity fully corrected corrected for compressibility		19.1687	%

Figure A2.10 Initial C90 with latex 95L10 set up data for Pore-Comp

PRESSURE /psi	PRESSURE / Mpa	V blank /cm3g-1	V blank /cm3	V obs /cm3g-1	V obs /cm3	dV"Hg /cm3	Vint+dVs /cm3	PORE DIA / um	%pore vol	modulus, log method	Full corr V int log method, / cm 3
14	0.0965	1.6903	0.0017	0.0032	0.0022	1.456E-06	0.0005	15.2373	0.6688	0.3612	0.0005
50	0.3447	0.5514	0.0006	0.0030	0.0020	5.199E-06	0.0015	4.2665	2.0923	0.3612	0.0015
500	3.4474	1.1268	0.0011	0.0037	0.0025	5.195E-05	0.0014	0.4266	2.0136	0.3612	0.0014
1000	6.8947	1.3426	0.0013	0.0052	0.0035	1.038E-04	0.0023	0.2133	3.2140	0.3611	0.0022
1500	10.3421	1.5824	0.0016	0.0071	0.0048	1.555E-04	0.0034	0.1422	4.7621	0.3611	0.0033
2000	13.7895	1.8941	0.0019	0.0136	0.0092	2.072E-04	0.0075	0.1067	10.6000	0.3611	0.0074
2500	17.2368	2.0739	0.0021	0.0681	0.0460	2.588E-04	0.0442	0.0853	62.4476	0.3611	0.0441
3000	20.6842	2.3975	0.0024	0.0949	0.0641	3.102E-04	0.0620	0.0711	87.6479	0.3610	0.0619
3500	24.1316	2.6375	0.0026	0.0997	0.0674	3.616E-04	0.0651	0.0609	91.9637	0.3610	0.0649
4000	27.5789	2.8651	0.0029	0.1019	0.0689	4.128E-04	0.0664	0.0533	93.8148	0.3610	0.0662
4500	31.0263	3.1168	0.0031	0.1033	0.0698	4.640E-04	0.0671	0.0474	94.8680	0.3609	0.0669
5000	34.4737	3.3446	0.0033	0.1045	0.0706	5.151E-04	0.0678	0.0427	95.7640	0.3609	0.0675
7000	48.2631	4.1597	0.0042	0.1074	0.0726	7.184E-04	0.0691	0.0305	97.6682	0.3608	0.0688
9000	62.0526	5.6582	0.0057	0.1098	0.0742	9.203E-04	0.0695	0.0237	98.1274	0.3607	0.0690
11000	75.8421	6.8210	0.0068	0.1122	0.0758	1.121E-03	0.0701	0.0194	99.0588	0.3606	0.0695
13000	89.6315	8.3075	0.0083	0.1148	0.0776	1.320E-03	0.0706	0.0164	99.7218	0.3605	0.0699
15000	103.4210	9.5902	0.0096	0.1168	0.0789	1.517E-03	0.0708	0.0142	100.0979	0.3604	0.0701
20000	137.8947	10.6091	0.0106	0.1187	0.0802	2.005E-03	0.0716	0.0107	101.1612	0.3601	0.0706
24000	165.4736	11.9158	0.0119	0.1199	0.0810	2.389E-03	0.0715	0.0089	101.0031	0.3599	0.0703
28000	193.0525	13.5341	0.0135	0.1204	0.0814	2.767E-03	0.0706	0.0076	99.7290	0.3597	0.0691
30000	206.8420	14.2054	0.0142	0.1214	0.0820	2.955E-03	0.0708	0.0071	100.0000	0.3596	0.0692
28000	193.0525	14.8527	0.0149	0.1228	0.0830	2.767E-03	0.0709	0.0076	100.1572	0.3597	0.0694
24000	165.4736	14.7449	0.0147	0.1234	0.0834	2.389E-03	0.0710	0.0089	100.3473	0.3599	0.0698
20000	137.8947	14.3972	0.0144	0.1227	0.0829	2.005E-03	0.0705	0.0107	99.6278	0.3601	0.0695
15000	103.4210	12.2874	0.0123	0.1201	0.0812	1.517E-03	0.0704	0.0142	99.4376	0.3604	0.0696
10000	68.9473	8.2835	0.0083	0.1145	0.0774	1.021E-03	0.0701	0.0213	99.0470	0.3607	0.0696
5000	34.4737	3.7042	0.0037	0.1081	0.0730	5.151E-04	0.0699	0.0427	98.6927	0.3609	0.0696
4000	27.5789	2.7811	0.0028	0.1060	0.0716	4.128E-04	0.0693	0.0533	97.8476	0.3610	0.0691
3000	20.6842	2.1098	0.0021	0.1044	0.0705	3.102E-04	0.0687	0.0711	97.1236	0.3610	0.0686
2000	13.7895	0.9460	0.0009	0.1025	0.0693	2.072E-04	0.0685	0.1067	96.8085	0.3611	0.0684
1000	6.8947	0.5275	0.0005	0.1009	0.0682	1.038E-04	0.0678	0.2133	95.7262	0.3611	0.0677
500	3.4474	0.0480	0.0000	0.0977	0.0660	5.195E-05	0.0660	0.4266	93.2755	0.3612	0.0660
50	0.3447	-0.3956	-0.0004	0.0932	0.0630	5.199E-06	0.0634	4.2665	89.5403	0.3612	0.0634

Figure A2.11 C90 with latex 95L10 data corrections for mercury compression and penetrometer expansion

APPENDIX 3

SCANNING ELECTRON MICROSCOPY

Scanning electron microscopes produce an image of the sample by interaction with an electron beam. The best possible resolution obtainable from light microscopes is 0.2 μm, using an electron beam instead of light, resolutions of 3 nm are attainable. Thus scanning electron microscopes are ideally suited to analysis of the samples studied in this thesis.

The primary electron beam is produced by heating a fine tungsten filament (Fig. A3.1). The electron beam accelerates towards the sample under the influence of a voltage of 5 - 30 KV. The beam is demagnified and focused by a series of electromagnetic lenses, to produce a fine beam which interacts with the sample. The apparatus must be maintained at vacuum (approximately 2 x 10^{-6} Torr) to allow electron beam formation, this restricts samples to only dry non-volatile substances. Upon collision with the sample surface, the electron beam causes a number of emissions (Fig. A3.2). Low energy electrons emitted from the sample surface are called Auger Electrons, this emission is not normally detected in S.E.M., the sample image is primarily formed by secondary electron emissions. Secondary electrons are emitted due to ionization when the electron beam collides inelastically with the sample surface. Secondary electrons have energies less then 50 EV.

Backscattered electrons have energies greater than 50 EV and normally produce signals of the same order as the primary electron beam 5 - 20 KV (Postek, 1980). Backscattered electrons are formed deep within the sample due to elastic collisions between the electron beam and the specimen nuclei or electrons. There is a correlation between backscattered electron production and atomic number of the sample. As atomic number increases, more backscattered electrons are emitted. Thus high atomic number

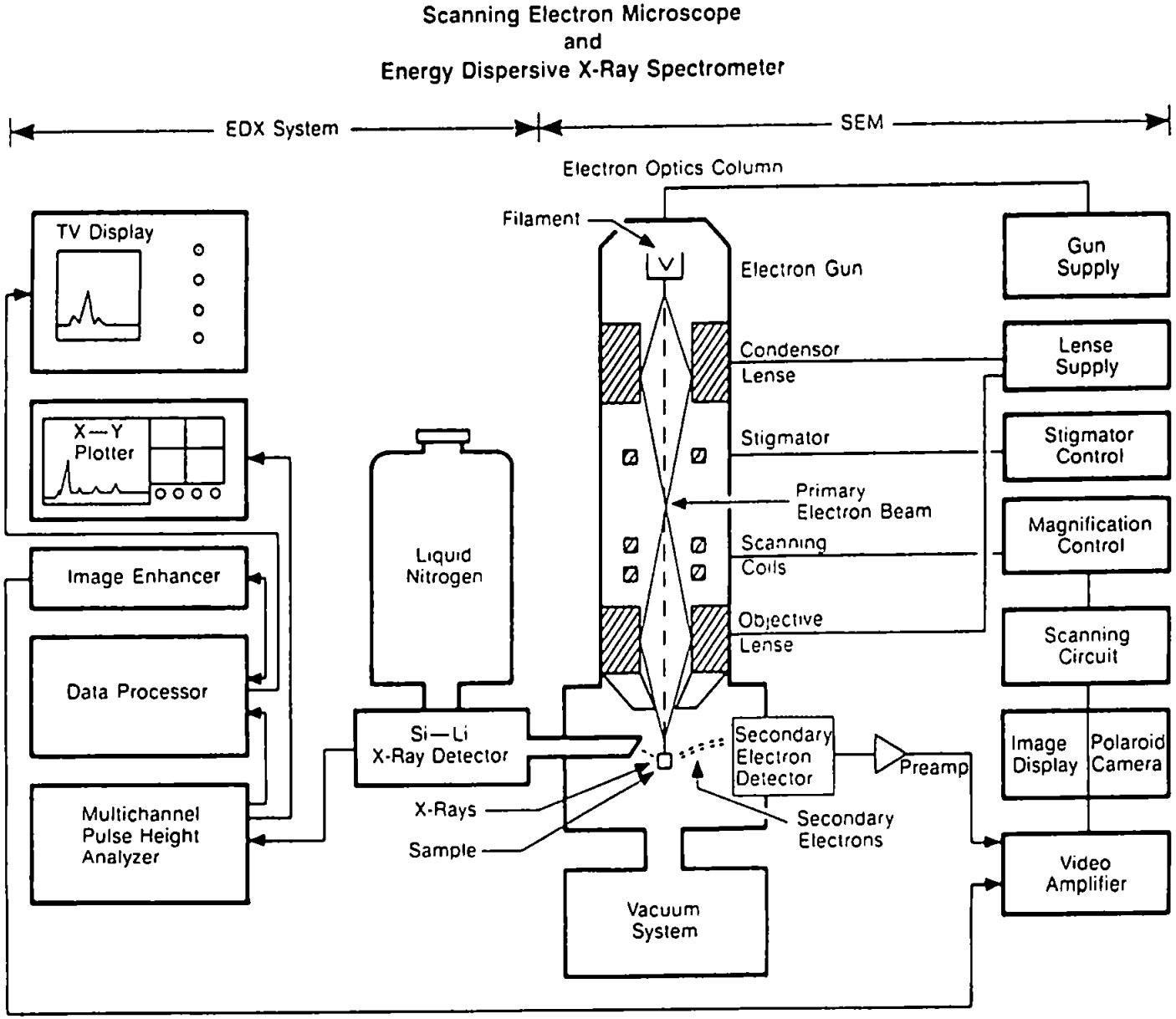

Figure A3.1 Schematic showing SEM / EDX system

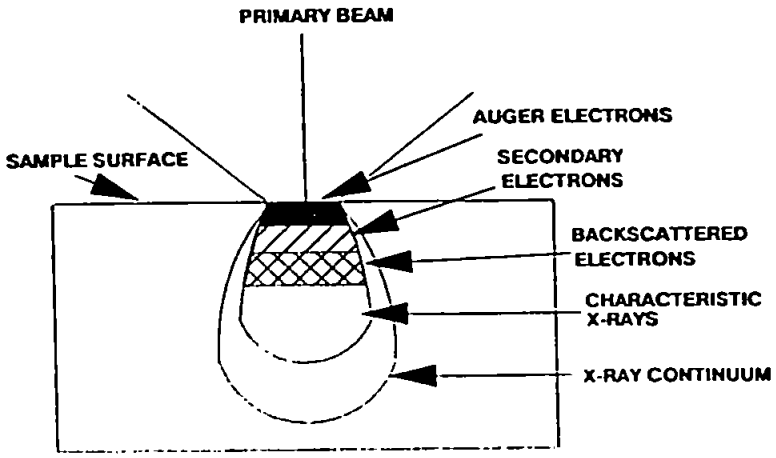

Figure A3.2 Interactions between an electron beam and sample

elements produce a strong emission and appear brighter in a backscattered electron image. This facility is used in the imaging of the low atomic number epoxy resin filled pore space, which appears black compared to the sandstone grains.

The cryo-stage that was used for the study of mercury entrapment in paper coating samples, is a chamber on the side of the electron microscope which is kept at a temperature of approximately -70°C by an interlocking liquid nitrogen system. The samples examined were frozen in liquid nitrogen before being mounted on a stub and placed into the cryo-stage.